Functional and Structural Studies on the *Atmungsferment* Cytochrome *c* Oxidase from *Paracoccus denitrificans*

Dissertation zur Erlangung
des Doktorgrades der Naturwissenschaften

vorgelegt beim Fachbereich 14
Biochemie, Chemie und Pharmazie
der Johann Wolfgang Goethe – Universität
in Frankfurt am Main

von **Heike Angerer**
aus Frankfurt am Main

Frankfurt (2008)
(D30)

Vom Fachbereich 14 Biochemie, Chemie und Pharmazie der Johann Wolfgang Goethe – Universität als Dissertation angenommen.

Dekan: Prof. Dr. Harald Schwalbe

1. Gutachter: Prof. Dr. Bernd Ludwig
2. Gutachter: Prof. Dr. Hartmut Michel

Datum der Disputation: 31.03.09

Diese Doktorarbeit wurde vom 01. April 2005 bis zum 30. Oktober 2008 unter Leitung von Prof. Dr. Hartmut Michel in der Abteilung für Molekulare Membranbiologie am Max-Planck-Institut für Biophysik in Frankfurt am Main durchgeführt.

Eidesstattliche Erklärung

Hiermit versichere ich, dass ich die vorliegende Arbeit selbstständig angefertigt habe und keine weiteren Hilfsmittel und Quellen als die hier aufgeführten verwendet habe.

Heike Angerer

Frankfurt am Main, den 30.10.08

Über Eisen, den sauerstoffübertragenden Bestandteil des Atmungsfermentes

Otto Heinrich Warburg, 1924

Publications

MacMillan, F., Budiman, K., Angerer, H., and Michel, H. (2006) The Role of Tryptophan 272 in the *Paracoccus denitrificans* Cytochrome *c* Oxidase, *FEBS letters* **580**, 5, 1345-1349

Dürr, K. L., Köpke, J., Hellwig, P., Müller, H., Angerer, H., Peng, G., Olkhova, E., Richter, O.-M. H., Ludwig, B., and Michel, H. (2008) A D-pathway mutation decouples the *Paracoccus denitrificans* cytochrome *c* oxidase by altering the side-chain orientation of a distant conserved glutamate, *JMB* (submitted)

Posters and oral presentations

Poster; Budiman, K., Kirchberg, K., Angerer, H., Müller, H., and Michel, H. (2005) Functional and Mechanistic Studies of Cytochrome *c* Oxidase from *Paracoccus denitrificans*; Biannual Meeting of the Advisory Board

Poster; Angerer, H., MacMillan, F., and Michel, H. (2006) Deeper Insights into Radical Formation in Cytochrome *c* Oxidase from *Paracoccus denitrificans*; "Membrane Proteins 2006" Symposium SFBs 431, 472 and 628

Poster; Angerer, H., Köpke, J., MacMillan, F., and Michel, H. (2007) Cytochrome *c* Oxidase from *Paracoccus denitrificans* – Novel Features of Function & Structure; Biannual Meeting of the Advisory Board

Poster and oral presentation; Angerer, H., MacMillan, F., and Michel, H. (2007) Formation of the Tyrosyl-167 Radical of Cytochrome *c* Oxidase from *Paracoccus denitrificans* upon an **F** state → **P** state Transition Induced by Catalase; Molecular & Cellular Bioenergetics, Gordon Research Conference (GRC)

Poster; Angerer, H., Köpke, J., MacMillan, F., and Michel, H. (2008) The Reversibility of **F** state → **P** state Transition Cytochrome *c* Oxidase from *Paracoccus denitrificans*; 2nd Joint German/UK Bioenergetics Conference - Integration of structures, spectroscopies and mechanisms, Edinburgh

Poster and oral presentation; Angerer, H., Köpke, J., MacMillan, F., and Michel, H. (2008) The Reversibility of **F** state → **P** state Transition Cytochrome *c* Oxidase from *Paracoccus denitrificans*; 15th European Bioenergetics Conference (EBEC), Dublin

CONTENTS

Table of Contents

Summary

Cytochrome *c* oxidase (C*c*O), also called Complex IV of the aerobic respiratory chain, is located in the plasma membrane of prokaryotes and in the inner mitochondrial membrane of eukaryotes. The redox energy of dioxygen reduction is used to translocate protons across the membrane resulting in an electrochemical proton gradient (proton motive force, pmf), however 50 % of the pmf also originates from the oxidation of reduced cytochrome *c* at the outer side of the membrane (electrons are delivered to dioxygen) and by the uptake of protons from the inside of the membrane, to form water. The generated electrochemical proton gradient is exploited by the adenosine-5'-triphosphate synthase. In this work, the bacterial four-subunit aa_3-Type C*c*O from *Paracoccus denitrificans* (ATCC 13543, 4 SU-wt ATCC C*c*O) was used for analyses.

1) The recombinant homologously produced four-subunit wild type C*c*O (4 SU-wt rec C*c*O) was functionally compared with the native 4 SU-wt ATCC C*c*O. The 4 SU-wt rec C*c*O shows a) lower enzymatic activity b) shifts in the redox difference absorption spectrum c) impaired induction of H_2O_2-derived intermediates as determined by difference absorption spectroscopy and d) a lower yield of Y167 radical species during intermediate states as determined by electron paramagnetic resonance (EPR) studies. Total X-ray Reflection Fluorescence measurements show in both wild type C*c*Os the same ratio of the redox-active Fe and Cu (2 Fe : 3 Cu) indicating full complement of the functional metals.

   The importance of subunit III for the structural and functional integrity of C*c*O was demonstrated using the 2 SU-wt rec C*c*O. If C*c*O contains only subunit I and II, it loses its functional integrity during continuous turnover activity. This so called *suicide inactivation* might be caused by the formation of an interhelical cross-link induced by reactive oxygen species. However, mass spectra have not shown a new covalent bond in *suicide inactivated* 2 SU-wt rec C*c*O, but the spectra have been used for the identification of the C*c*O. Crystallisation trials of *suicide inactivated* 2 SU-wt rec C*c*Os have been ineffective using standard crystallisation conditions. Crystals of *active* 2 SU-wt rec C*c*O (positive control) have been obtained under these conditions and this result indicates possible structural changes in *suicide inactivated* 2 SU-wt rec C*c*O. The structure of *active* 2 SU-wt rec C*c*O was determined to 2.25 Å resolution.

2) Terminal oxidases require four electrons for the cleavage of the dioxygen bond (O=O). In general, the catalytic cycle of C*c*O is described by the electron input and thus by the different redox states of the metal centres: the fully oxidised state is termed **O**, which can be reduced by one electron to form the **E** intermediate. Further electron input leads to the doubly reduced (*mixed valence*) **R** state. Doubly reduced C*c*O is able to bind dioxygen to form the **A** intermediate, a ferrous-oxygen adduct (Fe^{+II}-O_2). The two-electron reduced **R** intermediate is able to donate four electrons for dioxygen reduction forming the **P** state. The **P** intermediate

is an oxoferryl state implying the lack of an electron for the **R** → **P** transition, because the metal centres can only provide three electrons (Fe^{+II} forms Fe^{+IV} and Cu^{+II} forms Cu^{+I}). The **P** state, where the dioxygen bond is already broken, shows an oxoferryl state ($Fe^{IV}=O^{2-}$) and a nearby tyrosine is proposed to form a tyrosyl radical representing the donor of the missing electron. The uptake of a further electron leads to the three-electron reduced oxoferryl **F** state, which then relaxes via a further electron transfer back to the **O** state.

H_2O_2-induced artificial intermediates provide the opportunity to investigated different catalytic intermediates in detail. Mixing equimolar amounts of H_2O_2 to C*c*O in the **O** state induces the "two-electron" reduced $\mathbf{P_H}$ state at high pH and the electronically equal "two-electron" reduced $\mathbf{F^{\bullet}_H}$ state at low pH. The addition of an excess amount of H_2O_2 leads to the three-electron reduced $\mathbf{F_H}$ state. Functional studies using the 4 SU-wt ATCC C*c*O have demonstrated a bound peroxide (O^{-}-O^{-}) intermediate during the catalytic cycle and H_2O_2-induced reactions provided further insight into the overall mechanism. Using EPR it was previously shown that Y167 hosts a radical species in $\mathbf{P_H/F^{\bullet}_H}$ state which suggests that Y167 could provide this "missing electron" (MacMillan, F., Kannt, A., Behr, J., Prisner, T., Michel, H. (1999) "Direct Evidence for a Tyrosine Radical in the Reaction of Cytochrome *c* Oxidase with Hydrogen Peroxide" Biochemistry (38) 29, 9179-9184). While X-ray structural models of C*c*O and Fourier-transformed infrared (FTIR) measurements of oxygenated ("pulsed") 4 SU-wt ATCC C*c*O suggest a bound peroxide in the **O** state, UV-vis and EPR spectroscopic studies indicate that other intermediates may also contain such peroxide species. Equimolar and excess amounts of H_2O_2 induce the $\mathbf{P_H/F^{\bullet}_H}$ and $\mathbf{F_H}$ states, respectively and catalase treatment of the $\mathbf{F_H}$ state leads, contrary to the natural direction of the catalytic cycle, to the apparent transition of the $\mathbf{F_H} \rightarrow \mathbf{P_H/F^{\bullet}_H}$ states, which is accompanied by reappearance of an EPR signal from the $Y167^{\bullet}$ radical. The novel $\mathbf{P_{FH}/F^{\bullet}_{FH}}$ states are presented here and we postulate that the $\mathbf{F_H}$ state hosts a superoxide (or peroxide) adduct at Cu_B in the binuclear site.

In addition, the novel $\mathbf{P_{10}}$ state is also introduced having a maximum at λ = 612 nm in the difference absorption spectrum (*minus* the **O** state). The $\mathbf{P_{10}}$ state is induced by mixing C*c*O in the **O** state with a pH 10 buffer. This pH 10 induced state resembles standard **P** states such as $\mathbf{P_{CO}}$, $\mathbf{P_H}$ and $\mathbf{P_R}$. However, the $\mathbf{P_{10}}$ state evolves out of the **O** state without addition of reduction equivalents. Simply, the alkaline shift from pH 8 to 10 induces $\mathbf{P_{10}}$ state formation and the transition of the $\mathbf{P_{10}} \rightarrow \mathbf{F^{\bullet}}$ state shows an isosbestic point at λ = 592 nm and a pK_a value of 8. Using EPR spectroscopy it was shown that Y167 hosts a radical species in the $\mathbf{P_{10}}$ state such as in the $\mathbf{P_H}$ state. Variant W272F, which cannot form any stabilised radical, shows in the UV-vis difference absorption spectrum the reduction of the low-spin haem *a* and the possible reduction of Cu_B instead of $\mathbf{P_{10}}$ state formation. In summary, all functional data presented here provide evidence for a peroxide bound during the **O** state. Finally, a new model for the natural catalytic cycle is proposed. If the **O** state contains a peroxide, it is also

likely that the **E** and **R** state contain this species. Even the oxoferryl intermediates **P** and **F** states may complex a peroxide at Cu_B in the binuclear site.

3) The amino acid residue Y167, which hosts the radical in the $\mathbf{P_H/F^{\bullet}_H}$ states, is not directly part of the binuclear site of C*c*O. For identification of the primary electron donor, two tryptophan variants of C*c*O, W272F and W164F, which are located nearby the binuclear site, were produced. Evidence is provided that W272 is a kinetically fast electron donor for the O_2 molecule. The electron is replenished by Y167, or probably by Y280 in the natural cycle. The Y167 radical is detectable by EPR spectroscopy after treatment with equimolar amounts of H_2O_2 in the active variant W164F, but is absent in the inactive variant W272F.
4) C*c*O contains two proton conducting pathways, the D- and the K-pathway. Proteoliposomes of the variants H28A and D30N, mutations located at the entrance of the D-pathway, both show the identical proton pumping activity as the 4 SU-wt rec C*c*O (pumped $H^+/e^- = 1$). The variant N113D shows abolished proton pumping (pumped $H^+/e^- = 0$), but a relative high cytochrome *c* oxidation activity (63 %). G196D displays no cytochrome *c* oxidation and proton pumping activity. Overall, the addition or removal of a negative charge within the D-pathway such as in D124N, N131D, N113D and G196D leads to a decoupled phenotype indicating the high degree of electrostatic coupling in C*c*O.

Deutsche Zusammenfassung

Die Cytochrom *c* Oxidase (C*c*O) ist ein integrales Membranprotein, das in fast allen aeroben Organismen vorhanden ist und bildet den Komplex IV der aeroben Atmungskette. Die Redoxenergie der Sauerstoffreduktion wird durch die membranständigen Komplexe der Atmungskette ausgenutzt, um Protonen über die Membran zu transportieren und somit einen elektrochemischen Protonengradienten aufzubauen. Die Komplexe der prokaryotischen Atmungskette befinden sich in der Plasmamembran und die Protonen werden vom Cytosol ins Periplasma gepumpt, während die eukaryotische Atmungskette in der inneren Membran der Mitochondrien lokalisiert ist, und die Protonen von der Matrix in den Intermembranraum gepumpt werden. Zusätzlich zu den aktiv gepumpten Protonen werden weitere Ladungen an beiden Seiten der Membran verschoben: die Elektronen von reduzierten Cytochrom *c*s werden von der Aussenseite der Membran zum Sauerstoff weitergeleitet und die Substratprotonen für die Wasserbildung gelangen von der Innenseite der Membran zum Sauerstoff, und diese Ladungsverschiebungen und -neutralisationen machen insgesamt 50 % des elektrochemischen Potentials aus. Die gespeicherte Energie des produzierten elektrochemischen Protonengradienten wird von der Adenosin-5´-triphosphat (ATP) Synthase zur Synthese von ATP genutzt. Die redox-aktive C*c*O hat vier Metallzentren, die an den Redoxreaktionen beteiligt sind: Das dinukleare Cu_A-Zentrum, welches Elektronen von reduziertem Cytochrom *c* empfängt, das Häm *a* und das binukleare Häm a_3-Cu_B Zentrum. Im binuklearen Fea_3-Cu_B Zentrum findet die Sauerstoffreduktion zu zwei Wassermolekülen statt, bei der pro Sauerstoffmolekül vier Elektronen und vier Substratprotonen benötigt werden. Der katalytische Zyklus der C*c*O wird in verschiedene Intermediate aufgeteilt, die die einzelnen Redoxstufen des Enzyms widerspiegeln: der oxidierte **O** Zustand wird durch eine ein-Elektron Reduktion in den **E** Zustand überführt. Ein weiterer Reduktionsschritt führt zum zwei-Elektronen reduzierten **R** Zustand, welcher nach der Bindung von Sauerstoff, über den **A** Zustand, durch Elektronenumlagerung zum **P** Zustand reagiert. Der **P** Zustand ist nach einem putativen Peroxy-Intermediat benannt, ist aber tatsächlich ein nachgewiesenes Oxoferryl-Intermediat. Zusätzlich wurde im **P** Zustand ein Tyrosylradikal mittels elektronenparamagnetischer Resonanz-(EPR-)Spektroskopie identifiziert. Der nächste Reduktionsschritt, die Reduktion des Tyrosylradikals zum Tyrosinrest, führt zum Oxoferryl-Intermediat **F** Zustand. Das vierte Elektron führt die C*c*O zurück in ihren Grundzustand, dem **O** Zustand. Einige dieser katalytischen Zustände lassen sich künstlich durch Zugabe von H_2O_2 induzieren, wobei je nach zugegebener H_2O_2-Menge unterschiedliche Intermediate hervorgebracht werden. Equimolare Mengen an H_2O_2 induzieren bei hohem pH den $\mathbf{P_H}$ Zustand und bei niedrigem pH den protonierten $\mathbf{F^{\bullet}_H}$ Zustand. Beide Intermediate haben gleich viele Elektronen, d.h. den gleichen Redoxzustand, jedoch unterscheiden sie sich in ihrem Protonierungsgrad. Ein Überschuss an zugegebenem H_2O_2 induziert den $\mathbf{F_H}$ Zustand. H_2O_2-

induzierte, künstliche Intermediate ermöglichen den katalytischen Zyklus der C*c*O im Modell zu studieren. In dieser Arbeit wurde die Typ aa_3 C*c*O des Bodenbakteriums *Paracoccus denitrificans* (Stamm ATCC 13543) untersucht. *P. denitrificans* C*c*O besteht aus vier Untereinheiten gegenüber der Rinderherz-C*c*O, die aus 13 Untereinheiten zusammengesetzt ist. Die Kristallisation der funktionell aktiven zwei-Untereinheiten Form der *P. denitrificans* C*c*O zusammen mit einem Antikörperfragment (Fv Fragment) ermöglichte die Strukturbestimmung bei einer Auflösung von 2,7 Å (Ostermeier, C., Harrenga, A., Ermler, U., Michel, H. (1997) "Structure at 2.7 Å resolution of the *Paracoccus denitrificans* two-subunit cytochrome *c* oxidase complexed with an antibody Fv fragment." PNAS 94 (20): 10547-10553).

1) In dieser Arbeit wurde ein homologes Expressionssystem für die Produktion einer rekombinanten Wildtyp C*c*O genutzt. Das Gen der Untereinheit I (*cta*DIIβ) der C*c*O, das in dem *P. denitrificans* AO1-Deletionstamm über den Expressionsvektor pUP39 exprimiert wurde, ist ohne Affinitätsanhängsel kloniert worden. Die rekombinante Wildtyp C*c*O wurde auf gleiche Weise wie die native Wildtyp C*c*O mit Hilfe des Fv Fragments gereinigt. Die funktionellen Eigenschaften der rekombinant produzierten Wildtyp C*c*O wurden mit denen der nativen Wildtyp C*c*O verglichen. Es konnte gezeigt werden, dass rekombinant produzierte Wildtyp C*c*O gegenüber der nativen Wildtyp C*c*O a) weniger Aktivität b) Verschiebungen im Redox-Differenzabsorptionsspektrum c) niedrige Ausbeute an UV-vis spektroskopisch messbaren Intermediaten ($\mathbf{P_H}$, $\mathbf{F^{\bullet}_H}$ und $\mathbf{F_H}$ Zustände) und d) weniger Ausbeute an EPR spektroskopisch messbaren Tyrosylradikalen im $\mathbf{P_H/F^{\bullet}_H}$ Zustand aufwieß.

   Die beobachteten Unterschiede hätten durch das Fehlen von redox-aktiven Metallen in der rekombinanten Wildtyp C*c*O verursacht werden können. Die Überexpression des Gens der Untereinheit I der rekombinanten Wildtyp C*c*O könnte die Maschinerie der Proteinbiosynthese und die Rekrutierung von Kupfer- oder Hämgruppen-Einbauhilfsproteinen (Häm/Cu-Chaperone) überfordert haben. Die Untersuchung der Metallzusammensetzung der Wildtyp C*c*Os mittels Totalreflektions-Röntgenfluoreszenz-Analyse ergab für beide Proteine das korrekte Verhältnis der redox-aktiven Metalle von zwei Fe zu drei Cu.

   Für die Rinderherz-C*c*O konnte von einer anderen Gruppe dieses Forschungsfeldes gezeigt werden, dass sie aus dem Vorrat von Membranlipiden überwiegend Phosphatidylglycerin (PG) mit (18:1)-Δ^{11}-Vaccensäureresten selektiert, obwohl PG mit (18:1)-Δ^{9}-Ölsäureresten in der Membran viel häufiger vorkommt (Shinzawa-Itoh K. *et al.*, (2007) Structures and physiological roles of 13 integral lipids of bovine heart cytochrome *c* oxidase, EMBO, 26, 1713–1725). Der AO1-Deletionsstamm könnte durch sein verändertes Expressionsmuster eine andere Komposition von Lipiden in seiner

Biomembran aufweisen, was die reduzierte Funktion der rekombinanten Wildtyp C*c*O erklären könnte, da sie nicht-funktionelle Lipide gebunden haben könnte.

2) Die Bedeutung der Untereinheit III für die funktionelle Integrität der C*c*O wurde anhand von Untersuchungen der zwei-Untereinheiten Form der C*c*O aufgeklärt. Wenn C*c*O nur aus den Untereinheiten I und II besteht, dann fehlt die stabilisierende Wirkung von Untereinheit III. Aktivitätstests mittels Sauerstoffelektrode ermöglichen die Beobachtung der Selbst-Inaktivierung (*suicide inactivation*) des zwei-Untereinheiten Enzyms während des katalytischen Zyklus. Die Inaktivierungs-Reaktion verhält sich exponentiell entsprechend einer Kinetik erster Ordnung. Das Resultat der Selbst-Inaktivierung ist eine „tote" zwei-Untereinheiten C*c*O. Da eine strukturelle Veränderung als Ursache für die Inaktivierung vermutet wurde, sind massenspektrometrische Untersuchungen und Krisallisationversuche zur Strukturbestimmung durchgeführt worden. Zahlreiche Peptide von aktiver und selbst-inaktivierter C*c*O konnten zur Identifikation der C*c*O herangezogen werden, zeigten aber keine Unterschiede. Kristalle der Positivkontrolle (aktive C*c*O) sind reichlich erhalten worden, jedoch konnten unter Benutzung der gleichen Kristallisationsbedingungen keine Kristalle von selbst-inaktivierter C*c*O produziert werden. Kürzlich wurde vorgeschlagen, dass nicht das Fehlen der Untereinheit III, sondern die Abwesenheit konservierter Lipide, die Selbst-Inaktivierung verursacht (durch die resultierende Instabilität des aktiven Zentrums). Die Struktur der aktiven Positivkontrolle der Wildtyp C*c*O wurde mit einer Auflösung von 2,25 Å bestimmt.

3) Funktionelle Studien der nativen Wildtyp C*c*O ergaben weitreichende neue Erkenntnisse über die Mechanismen des katalytischen Zyklus und die Ergebnisse deuten auf die Anwesenheit eines Peroxids (O^{-}-O^{-}) in ihren katalytischen Intermediaten. Terminale Oxidasen benötigen zur Sauerstoffreduktion (Spaltung der O=O-Doppelbindung) vier Elektronen. Wie gezeigt wurde, ist der **P** Zustand bereits ein Oxoferryl-Intermediat (Fe^{IV}=O^{2-}) und da die redox-aktiven Metallzentren des binuklearen Zentrums der C*c*O im **R** Zustand nur drei Elektronen bereitstellen können, fehlt für die Sauerstoffspaltung bzw. die Bildung des **P** Zustands ein Elektron. EPR-Studien der H_2O_2-induzierten Modell-Intermediate $\mathbf{P_H/F^{\bullet}_H}$ Zustand zeigten ein organisches Radikalsignal, das mittels der Hyperfeinstruktur des Spektrums und Mutagenesestudien dem Rest Y167 zugeordnet werden konnte. Daher ist Y167 der Donator des fehlenden Elektrons (Budiman, K. *et al*., (2004) „Tyrosine 167: The Origin of the Radical Species Observed in the Reaction of Cytochrome *c* Oxidase with Hydrogen Peroxide in *Paracoccus denitrificans"* Biochemistry 43, 37, 11709-11716). Im nativen Zyklus gilt Y280 als Donator des fehlenden Elektrons, da es kovalent an einen Cu_B-Histidinliganden gebunden und damit Teil des aktiven Zentrums ist. Zusätzlich zeigt die Variante Y167F eine erstaunlich hohe Enzymaktivität, was die Beteiligung von Rest Y167 am natürlichen Zyklus fast ausschließt.

Während Röntgenstrukturanalyse der C*c*O und Fourier-Transform-Infrarotspektroskopie-Messungen der oxygenierten C*c*O (gepulst mit $^{16}O_2$ oder $^{18}O_2$) in dieser Arbeit auf ein Peroxidmolekül im **O** Zustand deuten, zeigten UV-vis und EPR-Messungen, dass die C*c*O auch in anderen Intermediaten Peroxid-Spezies gebunden haben könnte. Zugabe eines Überschusses von H_2O_2 im Verhältnis 1:500 induziert den $\mathbf{F_H}$ Zustand, und wird der H_2O_2 Überschuss mittels Katalase vom $\mathbf{F_H}$ Zustand entfernt, führt dies zu einem deutlichen Übergang vom $\mathbf{F_H}$ zurück zum $\mathbf{P_H/F^{\bullet}_H}$ Zustand. Dieser Übergang entgegen der Richtung des natürlichen Zyklus wird begleitet vom Wiederauftreten des EPR-aktiven Y167 Tyrosylradikals. Im Rahmen dieser Arbeit werden die $\mathbf{P_{FH}/F^{\bullet}_{FH}}$ Zustände vorgestellt (die Indices stehen für entferntes überschüssiges H_2O_2). Wir postulieren, dass der H_2O_2-induzierte $\mathbf{F_H}$ Zustand ein Superoxid (oder ein Peroxid) an Cu_B im aktiven Zentrum bindet. Die Entstehung der $\mathbf{P_{FH}/F^{\bullet}_{FH}}$ Zustände könnte durch eine superoxid-produzierende Seitenreaktion der C*c*O in Anwesenheit eines Überschusses an H_2O_2 erklärt werden. Mittels Sauerstoffelektrode konnte gezeigt werden, dass die C*c*O in Anwesenheit von überschüssigem H_2O_2 molekularen Sauerstoff produziert. Demzufolge scheint der induzierte $\mathbf{F_H}$ Zustand als „langsame“ Katalase zu fungieren, was auch zur Freisetzung von reaktiven Sauerstoffspezies (ROS) führen kann. ROS haben wiederum die Fähigkeit freie C*c*O teilweise zu reduzieren und somit können aktivierte (gepulste bzw. „schnelle“) Formen der C*c*O gebildet werden. Der $\mathbf{F_H}$ Zustand wird nun nach Zugabe von Katalase im Aussenmedium H_2O_2-frei, jedoch könnten vorher produzierte Superoxide oder andere ROS dazu führen, dass C*c*O in Gegenwart von Sauerstoff die neuartigen $\mathbf{P_{FH}/F^{\bullet}_{FH}}$ Zustände bilden kann.

Zusätzlich wird der in dieser Arbeit neuentdeckte $\mathbf{P_{10}}$ Zustand mit einem Maximum bei λ = 612 nm im Differenzabsorptionsspektrum *minus* dem **O** Zustand vorgestellt. Die spektralen Eigenschaften dieses Zustandes gleichen denen der standardmäßig induzierten **P** Zustände, die alle ein Maximum bei λ = 610 nm aufweisen: der CO-O_2 induzierte $\mathbf{P_{CO}}$ Zustand, der H_2O_2-induzierte $\mathbf{P_H}$ Zustand und der $\mathbf{P_R}$ Zustand, welcher durch Oxygenierung der total-reduzierten C*c*O induziert wird. Der $\mathbf{P_{10}}$ Zustand wird jedoch ohne Zugabe von Redoxequivalenten generiert und eine alleinige Verschiebung des pH Wertes von pH 8 nach 10 induziert den Übergang vom **O** zum $\mathbf{P_{10}}$ Zustand. Dieser Übergang folgt nicht einer Kinetik erster Ordnung und ist demnach keine einfache monomolekulare Reaktion. Der $\mathbf{P_{10}}$ Zustand lässt sich in den elektronisch identischen $\mathbf{F^{\bullet}}$ Zustand überführen, indem man den pH Wert von pH 10 auf 6 senkt. Der $\mathbf{P_{10}} \rightarrow \mathbf{F^{\bullet}}$ Übergang hat einen isobestischen Punkt bei der Wellenlänge λ = 592 nm und der pK_S-Wert dieser Titration liegt bei pK_S = 8. Mittels EPR-Spektroskopie konnte das Y167-Tysosylradikal auch während des $\mathbf{P_{10}}$ Zustands nachgewiesen werden, d.h. es stellt das identische Radikalsignal wie im $\mathbf{P_H}$ Zustand dar. Im Kontrast zur Wildtyp C*c*O zeigte die

Variante W272F, deren Elektronenweg von Y167 zum aktiven Zentrum blockiert ist und kein Y167-Tyrosylradikal stabilisieren kann, im $\mathbf{P_{10}}$ Zustand kein Maximum bei λ = 612 nm, jedoch ohne Zugabe von Reduktionsmitteln eine fotometrisch gemessene Umverteilung von Elektronen zum Häm *a* und möglicherweise zum Cu_B. Zusammengefasst lassen alle vorgestellten experimentell gemessene Effekte die Schlußfolgerung zu, dass sich eine Peroxid-Brücke während des **O** Zustandes im aktiven Zentrum befindet. Wenn der **O** Zustand der C*c*O ein gebundenes Peroxid enthält, dann ist es wahrscheinlich, dass auch andere Intermediate des natürlichen Zyklus ein Peroxid enthalten. Sogar die Oxoferryl-Intermediate **P** und **F** könnten ein gebundenes Peroxid an Cu_B enthalten. Basierend auf einen Peroxid-gebundenen **O** Zustand wird ein neues Modell des nativen katalytischen Zyklus vorgestellt.

4) Der Rest Y167 liegt in den $\mathbf{P_H}$ und $\mathbf{F^{\bullet}_H}$ Zuständen als Radikal vor, jedoch ist Y167 zu weit vom binuklearen Zentrum entfernt, um der primäre Elektronendonator des fehlenden Elektrons sein zu können. Zur Charakterisierung des Elektronenweges von Y167 bis zum binuklearen Zentrum wurde die Aminosäure W272 (Tryptophan 272), die eine Wasserstoffbrücke zu Y167 bildet und selbst zwischen Y167 und dem binuklearen Zentrum liegt, durch ein Phenylalanin (F) ersetzt. Zum Vergleich zweier Tryptophanvarianten wurde zusätzlich die Variante W164F produziert, welche zwischen dem Häm *a* und dem Häm a_3 liegt. Weitere Varianten (W272Y und W272H und die Doppelvarianten W272F/Y167F, W272Y/Y167F und W272H/Y167F) wurden hergestellt. Es konnte gezeigt werden, dass sämtliche W272-Varianten katalytisch inaktiv sind und auch die Bildung des Y167-Tyrosylradikals unterbunden ist. Bei den Varianten W272Y oder W272H konnten keine Radikale nachgewiesen werden. Dieses Ergebnis stellt die Bedeutung des konservierten Tryptophans an Position 272 hevor. Die Variante W164F zeigte eine vergleichsweise hohe Aktivität (20 %) und das Y167-Tyrosylradikalsignal. Die Varianten W272F und W164F zeigten jedoch Änderungen in den Redoxpotentialen ihrer Metallzentren, da die eingebrachten Elektronen der H_2O_2-induzierten $\mathbf{P_H}$ und $\mathbf{F^{\bullet}_H}$ Zustände auf Häm *a* und wahrscheinlich auf Cu_B umverteilt wurden.

5) C*c*O enthält zwei verschiedene Protonentransferkanäle, den D- und den K-Kanal, welche Protonen von der cytoplasmatischen Seite ins Innere des Enzyms leiten. Es wurden Protonenpumpexperimente mit D-Kanalvarianten durchgeführt, um Informationen über die Eigenschaften des D-Kanals zu erhalten. Die verschiedenen Varianten (H28A, D30N, G196D, S193Y und N113D) wurden in Liposomen rekonstituiert und das Verhältnis von gepumpten Protonen je injiziertem Elektron bestimmt. Die Aminosäurereste H28 und D30 wurden als essentielle Reste für die Protonentranslokation vorgeschlagen, jedoch zeigten die Varianten H28A und D30N das gleiche Verhätnis von einem gepumpten Proton je Elektron vergleichbar der Wildtyp C*c*O. Für die beiden Varianten N131D und N199D der

Asparagin-Triade konnte bereits bewiesen werden, das sie keine Protonen pumpen, aber volle Aktivität in der Cytochrom *c* Oxidation aufweisen. Es stellte sich heraus, dass N113D den gleichen Phänotyp zeigt wie die Varianten der anderen Mitglieder dieser Triade. Oberhalb der Triade liegt der Aminosäurerest G196. Dessen Variante G196D ist weder aktiv bezüglich der Cytochrom *c* Oxidation noch hat sie die Funktion der Protonentranslokation. Variante S193Y wurde entwickelt, um die Waserkette oberhalb der Asparagin-Triade zu blockieren, aber sie zeigte im Versuch 45 % Restaktivität und ein Verhältnis von einem halben gepumpten Proton pro Elektronen. Anhand dieser Daten lässt sich die Schlussfolgerung formulieren, dass jedes Einfügen oder Entfernen einer negativen Ladung (z.B. in D124N, N131D, N199D, N113D oder G196D) zu einer völligen oder teilweisen Entkopplung der Redoxchemie vom Protonenpumpen führt. Der katalytische Zyklus der C*c*O scheint eine starke elektrostatische Kopplung des Proteins vorrauszusetzen.

Abbreviations and Symbols

2 SU-wt ATCC C*c*O	Two-subunit native wild type cytochrome *c* oxidase
2 SU-wt rec C*c*O	Two-subunit recombinantly produced wild type cytochrome *c* oxidase
4 SU-wt ATCC C*c*O	Four-subunit native wild type cytochrome *c* oxidase
4 SU-wt rec C*c*O	Four-subunit recombinantly produced wild type cytochrome *c* oxidase
A	Alanine
ΔAbs	Absorption difference
Abs	Adenine
ADP	Adenosine diphosphate
Ab	Antibody
Ala	Alanine
Amp	Ampicillin
AP	Alkaline phosphatase
APS	Ammonium persulfate
Asn	Asparagine
Asp	Aspartic acid
ATP	Adenosine triphosphate
bp	Base pares
BSA	Bovine serum albumine
C	Cytosine
C	Cysteine
CCCP	Carbonyl cyanide 3-chlorophenylhydrazone
C*c*O	Cytochrome *c* oxidase
C*c*P	Cytochrome *c* peroxidase
cyt *c*	Cytochrome *c*
D	Aspartic acid
DNA	Desoxyribo-nucleic acid
E	Glutamic acid
ε	Extinction coefficient
EDTA	Ethylendiamin-tetra-acetate
F	Phenylalanine
Fv	Antibody fragment variable
G	Glycine
Glu	Glutamic acid
Gly	Glycine
h	Hour
H	Histidine
HEPES	N-2-hydroxyethylpiperazinethane sulfonic acid
His	Histidine
HPLC	High Performance Liquid Chromatography
IPTG	Isopropyl-β-D-thiogalactoside
K	Lysine
k_2	Turnover number (= k_{cat})
Kan	Kanamycin
kb	Kilo base pairs
kDa	Kilo Dalton
K_M	Michaelis-Menten constant
KP_i	Potassium phosphate buffer
L	Leucine
LB	Luria-Bertani medium
LDAO	N-N-dimethyldodecylamine-N-oxide
LM	n-Dodecyl-β-D-maltopyranoside
UM	n-Undecyl-β-D-maltopyranoside

M	Methionine
min	Minute
mV	Milivolt
NADH	Nicotineamide adenine dinucleotide
N	Asparagine
OD	Optical density
ORF	Open reading frame
o.n.	Over night
ox	oxidised
P	Proline
P_i	Inorganic phosphate
PAGE	Polyacrylamide gel electrophoresis
PCR	Polymerase chain reaction
Phe	Phenylalanine
Q	Glutamine
R	Asparagine
red	reduced
Rif	Rifampicin
rpm	Rounds per Minute
RT	Room temperature
s	Second
S	Serine
Ser	Serine
SDS	Sodium dodecyl sulfate
Sm	Streptomycin
SU	Subunit
Tris	Tetramethylbutyl-phenylpolyoxyethylene
T	Thymine
T	Threonine
TMH	Transmembrane helix
Trp	Tryptophan
TY	Trypton Yeast
Tyr	Tyrosine
V	Valine
Vol	Volume
W	Tryptophan
Y	Tyrosine

1 INTRODUCTION

1.1 Respiratory chain of mitochondria and prokaryotes

Nature's universal energy currency is the energy-rich molecule adenosine-5'-triphoshate (ATP), and the exergonic hydrolysis of ATP to adenosine-5'-diphoshate (ADP) and inorganic P_i fuels many metabolic pathways. ATP-hydrolysis, a "downhill" reaction, is enzymatically coupled to endergonic "uphill"-running reactions, and thus a constant pool of stored ATP has to be maintained in sufficient amounts to supply the energy requirements of living cells.

Substrate-level phosphorylation is a type of chemical reaction that results in the formation of ATP by the direct transfer of a P_i group to ADP from a reactive intermediate. In cells, substrate-level phosphorylation occurs in the cytoplasm under both aerobic and anaerobic conditions in the metabolic reactions of glycolysis and anaerobic fermentation, respectively. Glycolysis, the degradation of glucose to pyruvate, was discovered by Gustav Embden, Otto Meyerhof and Jakub Parnas (Embden and Zimmermann, 1927; Meyerhof and Kiessling, 1933). Metabolic fermentation is a process which is based on the conversion of pyruvate to ethanol and is well known from the production of beer and wine. Lactic acid fermentation by microorganisms was described by Louis Pasteur, who was able to prove that metabolic reactions lead to biologically usable chemical energy (Pasteur, 1860).

However, organisms can only extract a limited amount of energy from the metabolism of nutrients without the ability to use dioxygen as the final electron acceptor, and the exploitation of dioxygen as electron acceptor was a successful evolutionary development providing an effective process of energy conversion for the production of high levels of ATP.

It was Karl Lohmann who isolated ATP from muscle cells and thus demonstrated the natural existence of the nucleotide ATP as an energy-rich molecule (Lohmann, 1929). Prior to this, Otto Warburg had characterised the *Atmungsferment* (respiration ferment) (Warburg, 1924), and Herman Kalckar had later shown the link between the *Atmungsferment* and ATP synthesis (Kalckar, 1944; Saraste, 1999). These findings connected the phenomenon of "air" respiration with the ATP-producing energy metabolism.

In eukaryotes, the utilisation of dioxygen as a means of powerful energy extraction takes place in a specialised organelle, the mitochondrion. After transport from the cytosol into the mitochondrion, nutrients are completely oxidised to carbon dioxide and water. The energy resulting from the extremely exergonic dioxygen reduction ($\Delta G'^0 = -2880$ kJ/mol) is predominantly stored in an electrochemical proton gradient across the inner mitochondrial membrane. The chemiosmotic theory of oxidative phosphorylation describes the energy storage in a proton electrochemical gradient, the proton motive force ($pmf = \Delta\Psi - 2.3\ RT/F\ \Delta pH$), as the central concept of energy

accumulation in biological cells (Mitchell and Moyle, 1967; Saraste, 1999) and the mitochondrial enzyme ATP synthase utilises the pmf for driving the synthesis of ATP from ADP and P_i.

Mitochondria are specialised organelles within eukaryotic cells and according to the endosymbiont theory these organelles are believed to have evolved from an incorporated eubacterium (Margulis, 1970). Evidence for this theory is provided by the double membrane of mitochondria, by the existence of independent mitochondrial DNA (mtDNA) and by the autonomous machinery for protein biosynthesis in mitochondria (Haldar *et al.*, 1966; Hatefi, 1985; Castresana and Saraste, 1995).

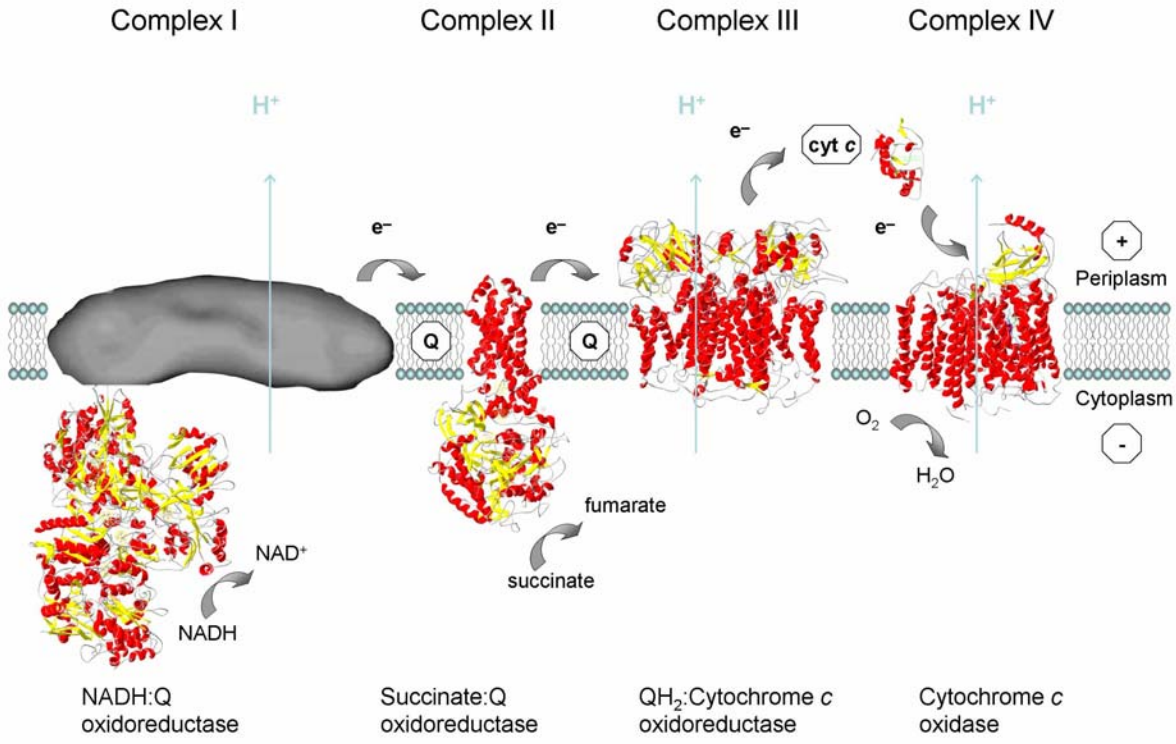

Figure 1.1-1 Picture of the mitochondrial-like prokaryotic respiratory chain. Complex I represents a composite of the crystal structure of the soluble domain (*Thermus thermophilus*, pdb-file 2fug, Sazanov and Hinchliffe, 2006) and the electron microscopic electron density of the transmembrane domain (*E. coli*, Guénebaut *et al*., 1998). Complex II is represented by the monomeric form (*E. coli*, pdb-file 1nek, Yankovskaya *et al*., 2003). The dimeric structure model of Complex III (*Rhodobacter capsulatus*, pdb-file 1zrt, Berry *et al*., 2004) and a structural model of Complex IV (*P. denitrificans*, pdb-file 1qlr, Iwata *et al.*, 1995) are depicted. The soluble cyt *c* (*R. capsulatus*, pdb-file 1c2r, Bennning *et al*., 1991) is the electron shuttle between Complex III and IV.

The Gram-negative α_3-proteo- (and soil-) bacterium *Paracoccus denitrificans* was proposed as a probable progenitor of the mitochondrion (John and Whatley, 1975), because some *P. denitrifcans* respiratory pathways are similar to the mitochondrial respiratory chain. In general, the prokaryotic respiratory chain is composed of the same membrane complexes as that of the mitochondrion, but the prokaryotic complexes contain fewer subunits, mainly consisting of the respective mitochondrially encoded *core subunits*. However, other pathways also play important

roles in their energy metabolism (see also chapter 1.6), because the prokaryotic respiratory chain is normally branched, for example more input pathways are available such as electrons from other respiration substrates and more output pathways for these electrons by the usage of several terminal oxidases.

The generally accepted model of the respiratory chain (mitochondria-based) consists of four redox-active membrane protein complexes, Complex I to IV (Figure 1.1-1): the nicotinamide adenine dinucleotide (NADH):quinone oxidoreductase (Complex I); the succinate:quinone oxidoreductase (Complex II); the quinol:ferrocytochrome *c* oxidoreductase (Complex III); and the cytochrome *c* oxidase (C*c*O, Complex IV) (Schägger, 2002). The redox potential difference between electrons from reduced NADH ($\Delta E^{0'}$ = – 0.315 V) and dioxygen ($\Delta E^{0'}$ = + 0.815 V) provides the redox energy for proton-translocation by Complexes I, III and IV. Complex I, III and IV are redox-driven proton-translocating enzymes and only Complex II does not pump protons, but rather provides quinol molecules for oxidation by Complex III. The nano-motor ATP synthase is often called Complex V of the respiratory chain and it is driven by the electrochemical proton gradient generated by the proton pumping complexes (Walker and Dickson, 2006). The complexes of the mitochondrial respiratory chain are highly regulated in order to fine-tune the energy requirements of the eukaryotic cell resulting in a high number of accessory subunits, however the prokaryotic complexes are less regulated and contain fewer accessory subunits next to the *core subunits*. Interestingly, many genes for these *core subunits* are still mitochondrially encoded in eukaryotic cells and are highly conserved in aerobic organisms, but the respective eukaryotic accessory proteins are mainly encoded by nuclear DNA. The analysis of the basic respiratory complexes was facilitated by study of the complexes of prokaryotes (bacteria and archaea), because their complexes are predominantly composed of the *core subunits*. *P. denitrificans* was suggested to contain directly-related complexes of the mitochondrial respiratory chain and has been called a “free living mitochondrion”, resulting in a scientific focus on this organism as well as on beef heart mitochondria.

1.2 Cytochrome *c* oxidase

C*c*O belongs to the group of haem and copper containing proteins which comprise the superfamily of haem-copper oxygen reductases. However, the atmosphere of earth was mainly anaerobic until photosynthesis driven organisms produced an excess of dioxygen. Thus, the evolution of haem-copper oxidases is linked to enzymes involved in the anaerobic nitrogen cycle, especially to the N_2O and NO reductases (NOR), and both NOR and haem-copper oxygen reductases comprise this haem-copper superfamily (Castresana and Saraste, 1995). Based on the specific amino acids of the *core subunits* I and II which form different proton pathways and bind prosthetic groups, the members of the haem-copper oxidase superfamily are classified by

three main families, here emphasised on C*c*Os (Pereira *et al.*, 2001): mitochondrial-like C*c*Os (Type A1 and A2); *ba*$_3$-like C*c*Os (Type B) and *cbb*$_3$-like C*c*Os (Type C) (Figure 1.2-1).

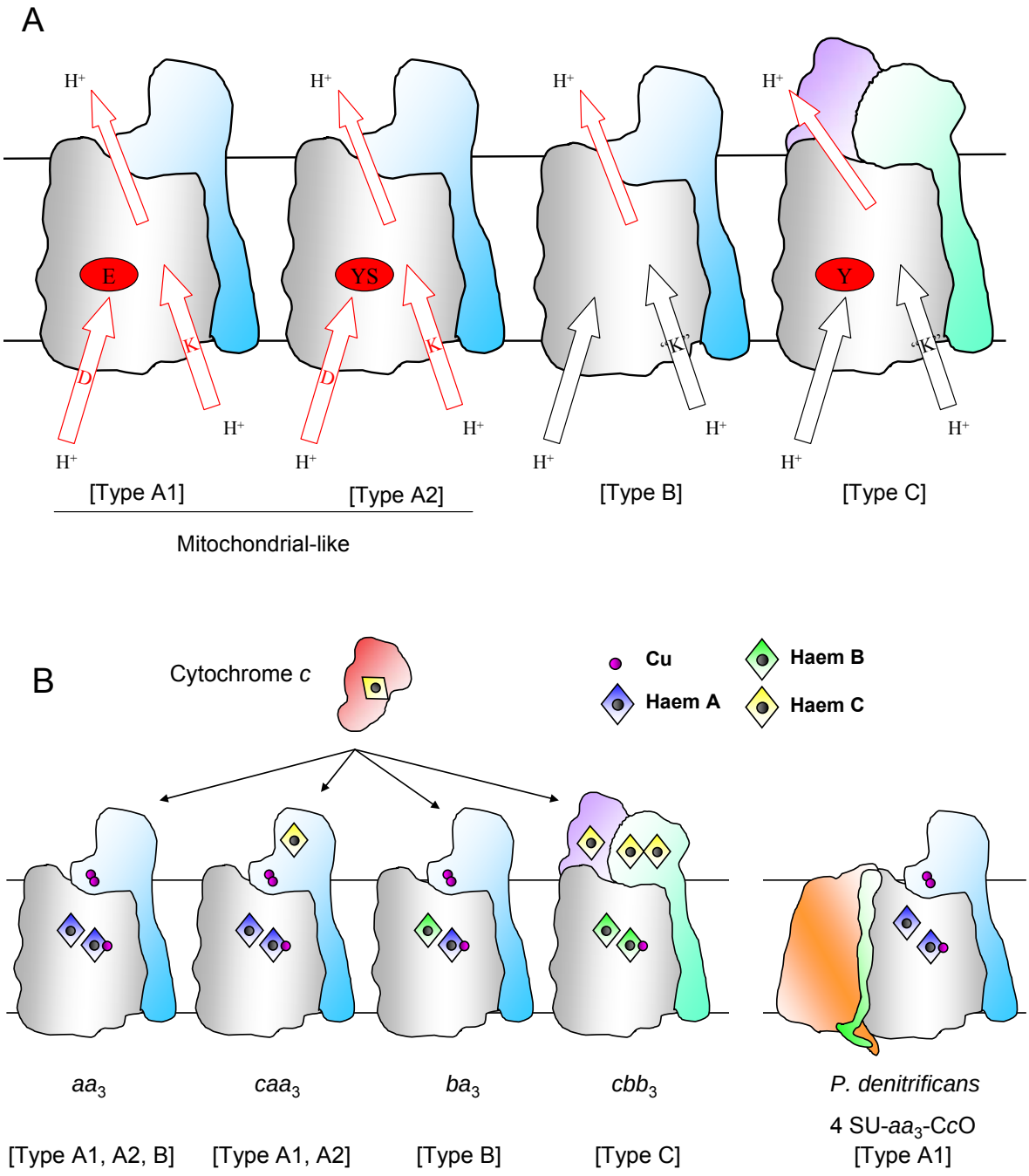

Figure 1.2-1 Schematic model of the *core subunits* I (grey) and II (blue) from the haem-copper superfamily. (A) Mitochondrial-like C*c*O (Type A1 and A2); *ba*$_3$-like C*c*O (Type B) and *cbb*$_3$-like C*c*O (Type C) are shown. (B) Different types of C*c*Os based on their haem composition: Type *aa*$_3$, *caa*$_3$, *ba*$_3$ and *cbb*$_3$ (containing the dihaemic FixP subunit (green) instead of subunit II and an additional monohaemic subunit (violet)). In addition, the whole four-subunit (4 SU) *aa*$_3$-C*c*O from *P. denitrificans* is depicted.

The Type A group of haem-copper C*c*Os is divided into two subfamilies, the Type A1 and A2, according to one of their two proton pathways starting at the cytoplasmic side of the membrane (the so called D- and K-pathway, Figure 1.2-1 A). Type A1 C*c*Os contain a glutamate residue at the end of the D-pathway, while Type A2 C*c*Os contain instead a tyrosine-serine motif at this position. In Type B C*c*Os the residues forming the D- and K-pathway are not conserved, however a "K"-pathway homologue is most probably present (Figure 1.2-1 A). The third subfamily, the Type C C*c*Os, seems to contain only a part of the alternative "K"-pathway and a specific tyrosine residue at the position of the Type A2 tyrosine-serine motif. In addition, Type C C*c*Os contain a dihaemic subunit called FixP (green, Figure 1.2-1 A and B) instead of subunit II of Type A and B C*c*Os and an additional monohaemic subunit (violet, Figure 1.2-1 A and B).

P. denitrificans mitochondrial-like C*c*O is a Type A1 member of the haem-copper C*c*Os (Figure 1.2-1 B) and it represents the terminal complex of the respiratory chain catalysing the four-electron reduction of dioxygen to water. C*c*O is a redox-driven proton pump producing an electrochemical proton gradient across the membrane from the negative side (N) to the positive side (P). The net reaction of C*c*O is formulated as (cyt *c* = cytochrome *c*) (Wikström, 1977):

$$4\ \text{cyt}\ c^{+II} + O_2 + 8\ H^+_{(N)} \rightarrow 4\ \text{cyt}\ c^{+III} + 2\ H_2O + 4\ H^+_{(P)}$$

The equation shows that C*c*O takes for one catalytic cycle four electrons and four chemical protons per reduced dioxygen molecule forming two molecules of water and the redox energy is used to pump four protons across the membrane from the cytoplasm to the periplasm. However, 50 % of the resulting electrochemical proton gradient also originate from the oxidation of reduced cytochrome *c* at the P-side, and from the uptake of protons from the N-side, to form water.

In general, the structural details of a protein provide the basis for the analysis of its enzymatic functions. To determine the structure of C*c*O had been a big challenge in order to understand the nature of the mechanism of its catalytic cycle.

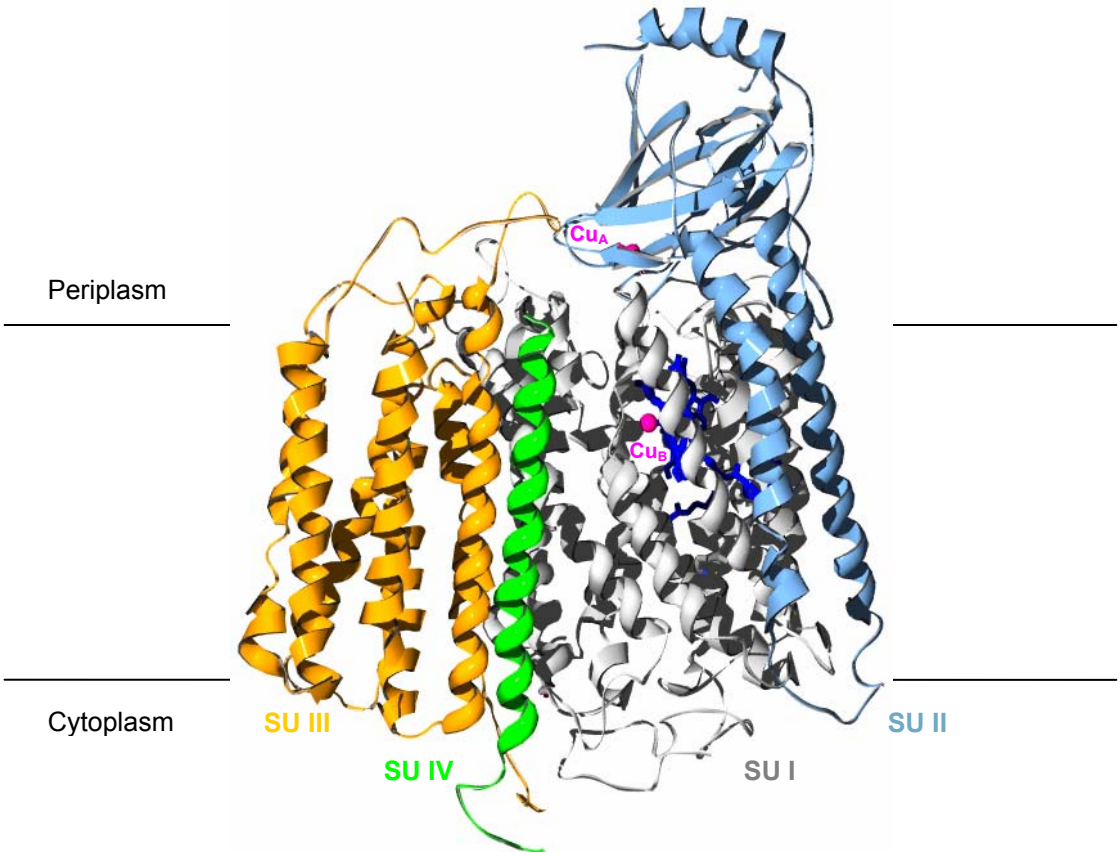

Figure 1.2-2 Model of the 4 SU-C*c*O (*P. denitrificans*, pdb-file 1qlr). Copper ions (magenta) form the dinuclear Cu_A centre located in subunit II. Two haem A groups in subunit I (dark blue) form either the haem *a* or the binuclear haem a_3-Cu_B centre.

Accordingly, the C*c*Os of *Bos taurus* (bovine heart), *P. denitrificans* (see Figure 1.2-2) and *Rhodobacter sphaeroides* have been sucessfully crystallised and their structures determined by X-ray chrystallography (Iwata *et al.*, 1995; Tsukihara *et al.*, 1996; Ostermeier *et al.*, 1997; Yoshikawa *et al.*, 1998; Qin *et al.*, 2006).

The four-subunit C*c*O (4 SU-C*c*O) of *P. denitrificans* shows an apparent molecular mass of 126 kDa as determined by SDS polyacrylamide electrophoresis ($M_{W\ theoretical}$ = 131.2 kDa) (Ludwig and Schatz, 1980; Haltia *et al.*, 1988) and its subunits I, II and III are remarkably similar to the eukaryotic mitochondrially encoded *core subunits*.

The two-subunit C*c*O (2 SU-C*c*O, the "holoenzyme"), comprised of subunits I and II, contains the redox-active metal centres that exclusively comprise the electron pathways from reduced cyt *c* to O_2 (see Figure 1.2-3). Purified 2 SU-C*c*O possesses enzymatic activity as determined by catalytic activity assays.

Subunit I (SU I), representing a hydrophobic cytochrome aa_3, contains twelve transmembrane helices and shows an apparent molecular mass of 45 kDa as determined by SDS polyacrylamide electrophoresis ($M_{W\ theoretical}$ = 62.4 kDa). It contains the low-spin haem A and the

binuclear site, which is composed of the high-spin haem A_3 and the copper B ion forming the Fea_3-Cu_B binuclear centre. In addition, subunit I contains redox-inactive metal centres such as a complexed Ca^{2+} ion (Pfitzner *et al.*, 1999; Lee *et al.*, 2002a) and a Mn^{2+} or Mg^{2+} ion (Witt *et al.*, 1997).

Subunit II (SU II), which is membrane-anchored by two transmembrane helices, displays a molecular mass of 28 kDa as determined by SDS polyacrylamide electrophoresis ($M_{W\ theoretical}$ = 32.5 kDa) and it harbors the first electron acceptor within the C*c*O, the dinuclear copper A (Cu_A) centre (Panskus *et al.*, 1988). The Cu_A centre is embedded in a β-sheet folded domain of the extracellular, hydrophilic part of SU II (see Figure 1.2-2).

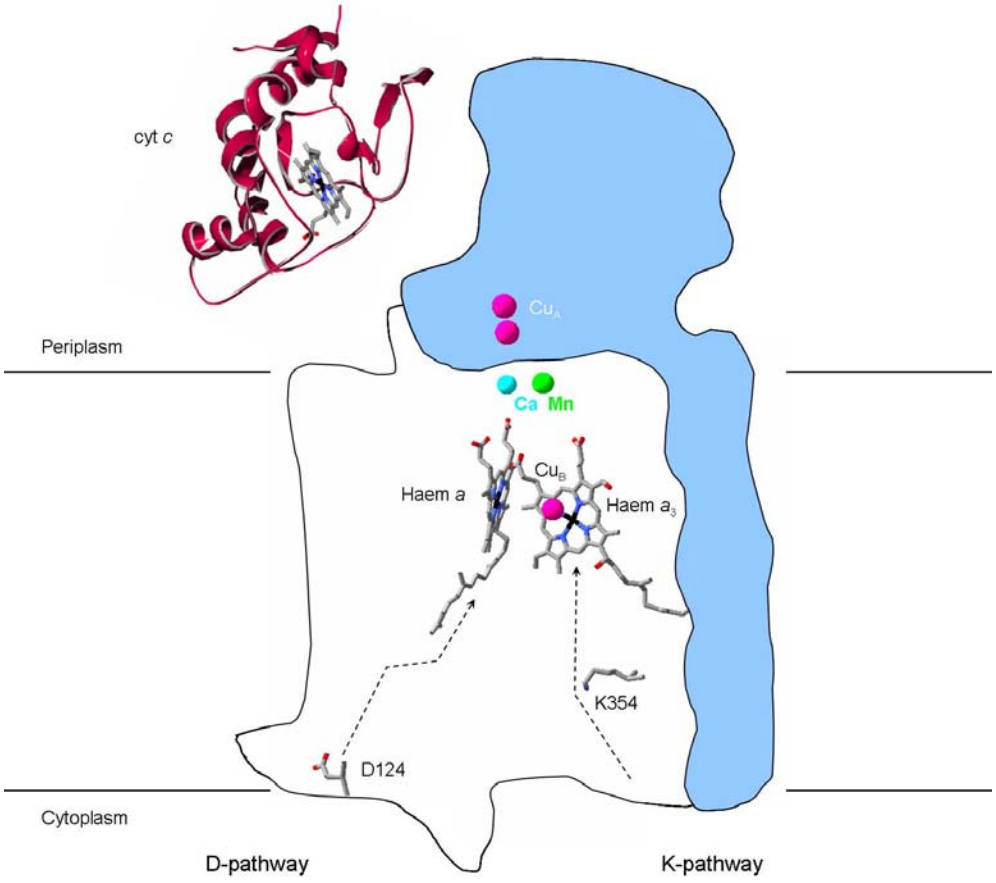

Figure 1.2-3 Metal centres of C*c*O from *P. denitrificans* and the soluble cyt *c*. The 2 SU-C*c*O contains four redox-active transition metal centres next to other redox-inactive metal centres (haem groups in grey; Cu in magenta; Ca in light blue and Mn/Mg in green). The dinuclear Cu_A centre is the entrance for the stepwise input of electrons from cyt *c*. The binuclear centre, composed of haem a_3-Cu_B, is the "burning chamber" of C*c*O, where dioxygen reduction takes place (pdb-file 1ar1, Ostermeier *et al*., 1997; and *R. capsulatus*, pdb-file 1c2r, Bennning *et al*., 1991). The key residues of the D-(124) and K-(354)-pathway are depicted.

Reduced cyt *c*s, which exhibit a relatively low redox potential (see Table 1.2-1), inject electrons into the electron pathway of C*c*O successively. The electrons are transfered to the Cu_A centre having a higher redox potential, and then via the low-spin haem A to the binuclear haem a_3 Fe-Cu_B centre. The O_2 reduction takes place in the binuclear site driven by the high redox potential of

the dioxygen molecule (Moser *et al.*, 2006).

Table 1.2-1 Redox potentials of the redox-active metal centres of cyt *c* and C*c*O in direction of the electron transfer (Hellwig *et al.*, 1999; Voet *et al.*, 1999).

	$\Delta E^{0'}$ in V	Reference
cyt *c*	0.235	Voet *et al.*, 1999
Cu_A centre	0.245	Voet *et al.*, 1999
Haem *a*	0.22 +/- 0.04	Hellwig *et al.*, 1999
Haem a_3	-0.03 +/- 0.01	Hellwig *et al.*, 1999
Cu_B	0.340	Voet *et al.*, 1999
O_2	0.815	Voet *et al.*, 1999

The properties of the different catalytic redox states of the metal centres and their coupling to the proton transfer and the protonation states within C*c*O are still intensively investigated. First, it had been necessary to identify the key residues which provide the metal ion binding or which form the electron and proton transfer pathways.

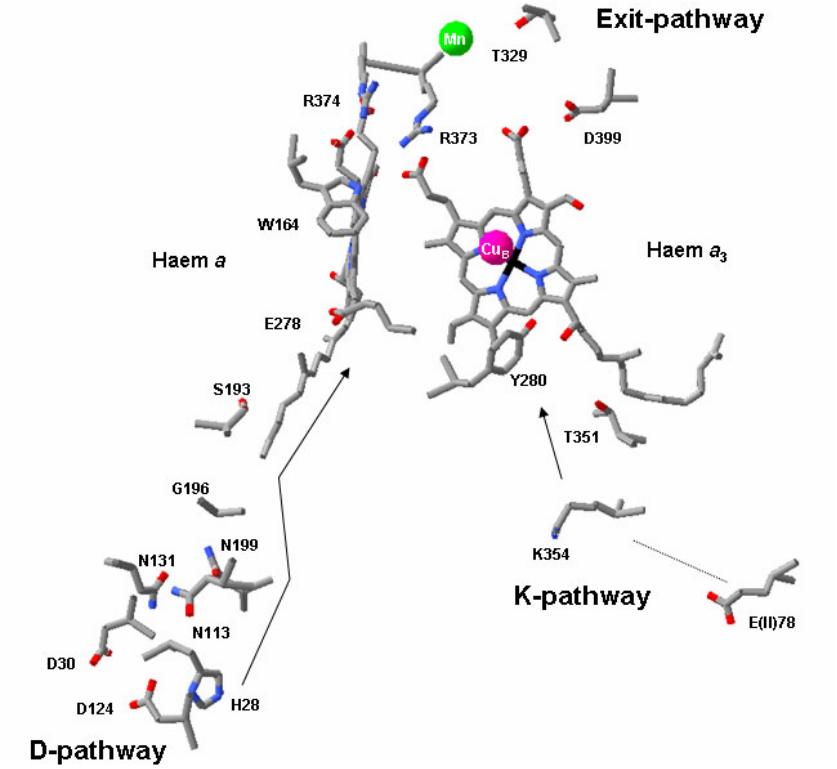

Figure 1.2-4 Proton transfer pathways of C*c*O from *P. denitrificans*. The figure shows several amino acids that are important for functional proton transfer or line the pathways (pdb-file 1ar1, Ostermeier *et al*., 1997). Residues of the D-pathway are D124, N131, N113, N199, G196, S193, E278 (and W164). In addition, the putative proton conducting residues H28 and D30 are shown at the entrance of the D-pathway. The K-pathway is formed by the residues K354, T351 and Y280 (and E78 of subunit II in *R. sphaeroides* C*c*O). A putative exit pathway includes the haem propionates, R373/374, the Mg/Mn ion (green), T329 and D399.

Alignments of the amino acid sequences from Type A1 C*c*Os revealed several strictly conserved residues, for example D124, N131, E278, K354 and Y280, and suggested the binding motifs, which coordinate the haem A groups and the other metal ions (*P. denitrificans* numbering, Figure 1.2-4) (Chepuri *et al.*, 1990; Garcia-Horsman *et al.*, 1994; Pereira *et al.*, 2001). Furthermore, mutagenesis studies in these positions have identified the residues responsible for coordinating haem A groups and copper ions or involved in proton transfer (Lemieux *et al.*, 1992; Minagawa *et al.*, 1992; Shapleigh *et al.*, 1992; Hosler *et al.*, 1993; Thomas *et al.*, 1993a; Thomas *et al.*, 1993b; Thomas *et al.*, 1993c; Verkhovsky *et al.*, 2001a).
Moreover, the crystal structures have revealed many details, such as two pores. Based on the mutagenesis data, the X-ray structure has been interpreted to contain two proton pathways for the substrate and for pumped protons: the D- and the K-pathway (Figure 1.2-4) (Iwata *et al.*, 1995). In addition, a third H-pathway was proposed and an exit pathway in the case of the bovine enzyme (Tsukihara *et al.*, 1996; Gennis, 1998; Yoshikawa *et al.*, 1998).
The structures of C*c*Os have suggested the routes of the D- and K-pathway structurally, and mutagenesis studies of specific residues have proven the existence of these two independent proton pathways (Fetter *et al.*, 1995b; Ädelroth *et al.*, 1997a; Jünemann *et al.*, 1997a; Pfitzner *et al.*, 2000).

The K-pathway is named after the central lysine residue K354 (Fetter *et al.*, 1995a; Jünemann *et al.*, 1997b; Forte *et al.*, 2004a). This residue links the proton conductance pathway from the cytoplasmic side of the membrane to the binuclear site via the residues T351 and Y280 (Iwata *et al.*, 1995; Buse *et al.*, 1999; Pinakoulaki *et al.*, 2002). The K-pathway was proposed to provide all four substrate protons to the binuclear site. In deed, single point mutations of residues of the K-pathway can block dioxygen reduction chemistry at the binuclear site. However, the K-pathway is suggested to deliver only one to two substrate protons to the binuclear site during the reductive phase of the catalytic cycle, because this reductive phase is hindered in variant K354M only (Konstantinov *et al.*, 1997; Ädelroth *et al.*, 1998; Ruitenberg *et al.*, 2000a; Bränden *et al.*, 2001).

The D-pathway starts at the cytoplasmic side of the membrane with aspartic residue D124, which forms the entrance of the D-pathway (Iwata *et al.*, 1995; Pfitzner *et al.*, 1998; Pfitzner *et al.*, 2000; Forte *et al.*, 2004b; Olkhova *et al.*, 2005a). A chain of structural water molecules builds a proton wire from D124 to three asparagines N131, N113 and N199 and additional fixed water molecules conduct protons to residue E278 (Ädelroth *et al.*, 1997b; Brzezinski and Ädelroth, 1998; Hellwig *et al.*, 1998; Pfitzner *et al.*, 2000; Qin *et al.*, 2006). Since both the substrate (at least two) and all pumped protons are taken up through the D-pathway, there has to be a branching point distributing protons either to the binuclear site or to the pumping site (Smirnova *et al.*, 1999;

Karpefors *et al.*, 2000). Recent publications suggest a coupling of each electron input via haem *a* to an uptake of a substrate proton accompanied by a proton pumping step, likely gated by E278 (Iwata *et al.*, 1995; Wikström *et al.*, 2005; Wikström and Verkhovsky, 2007).

The variant D124N, targeting the entrance of the D-pathway, shows a very low turnover (Fetter *et al.*, 1995a; Pfitzner *et al.*, 2000), thus demonstrating the importance of a conserved protonatable group at the entrance of the D-pathway, far away from the binuclear centre (Smirnova *et al.*, 1999). Proton pumps such as C*c*O may require proton-attractive systems nearby the membrane bilayer. A proton-attracting antenna function of several histidines and aspartic residues (for an effective collection of protons around the entrance of proton pathways) could be shown for C*c*O and other proton translocating enzymes. Furthermore, Zn^{2+} ions can bind these patterns of amino acids and block proton pumping (Wikström, 1998; Aagaard and Brzezinski, 2001; Aagaard *et al.*, 2002; Ädelroth and Brzezinski, 2004).
Electrostatics calculations were performed on the D-pathway entrance. According to pK_a value determination by continuum electrostatics calculations, the residues H28 and D30 have been proposed to exhibit a function in protonation steps during proton pumping (Figure 1.2-4) (Olkhova *et al.*, 2005b).

Study of the variant N131D produced an interesting result concerning mutagenesis of the D-pathway. This variant shows full dioxygen reduction activity, but does not show proton pumping and is thus called a decoupled variant (Fetter *et al.*, 1995a; Pfitzner *et al.*, 1998). The intrinsic pK_a values of charged amino acids play an important role for functional proton translocation. FTIR measurements have determined the protonation states of residue E278 in wild type C*c*O (Hellwig *et al.*, 1998; Namslauer *et al.*, 2003a) and in the variant N131D (Namslauer *et al.*, 2003b) during the $\mathbf{P_R}$ state as determined by the pH dependence of the rate of $\mathbf{P_R} \rightarrow \mathbf{F}$ state transition (see chapter 1.3). The pK_a value of residue E278 shifts two units, from wild type $pK_a = 9$ up to a $pK_a = 11$ in variant N131D.
The doubly mutated variant N131D/D124N shows a decreased turnover. However, it shows full activity in proton pumping and it does not exhibit the increased pK_a value of residue E278 during the $\mathbf{P_R}$ state. The removal of one negative charge (D → N) within the D-pathway of the variant N131D/D124N shifts the pK_a value of E278 back to the value of wild type C*c*O (Bränden *et al*., 2006). The imbalance of negative charges inside the D-pathway such as in variant G196D decreases the dioxygen reduction activity of C*c*O (Han et al., 2005).

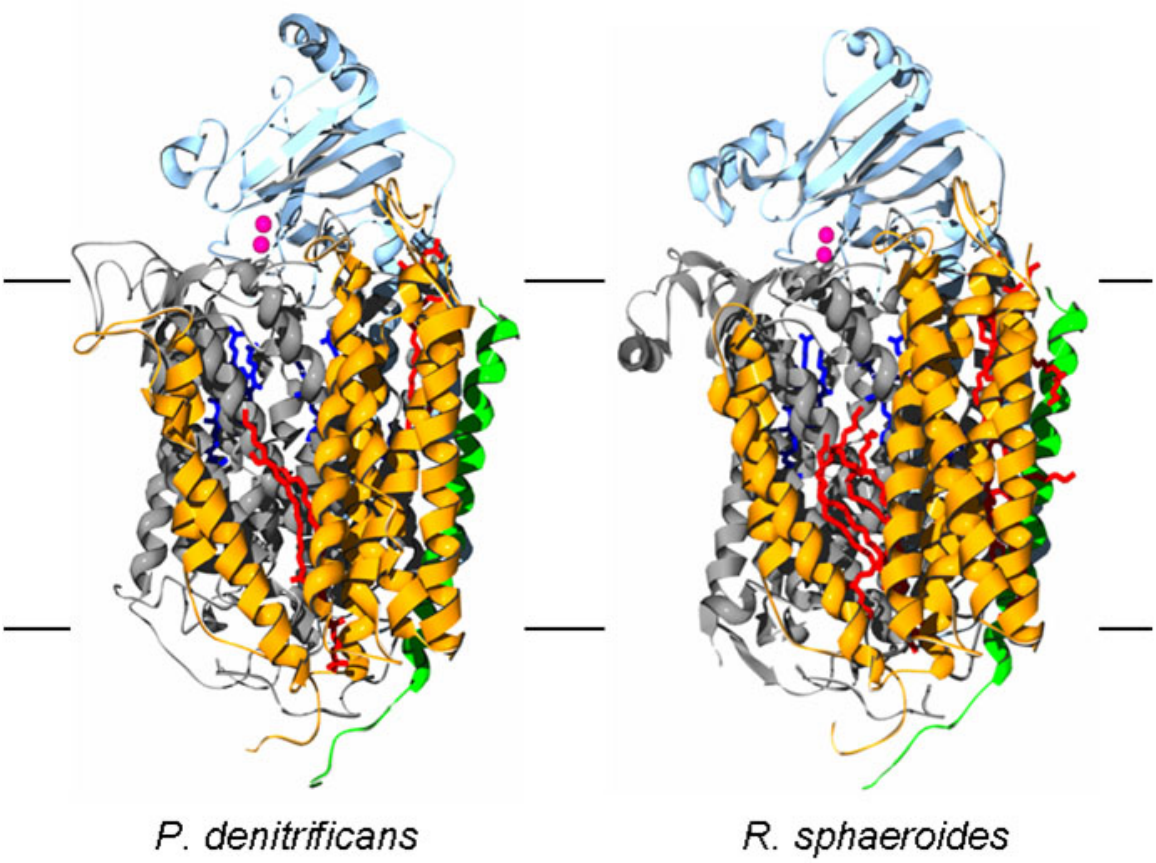

Figure 1.2-5 Model of the V-shaped cleft in subunit III of C*c*O from *P. denitrificans* and from *R. sphaeroides*. The 4 SU-C*c*O from *P. denitrificans* (1qle) and the 4 SU-C*c*O from *R. sphaeroides* (1m56) are depicted. Subunit III (orange) is composed of seven transmembrane helices, which provide lipid binding sites. SU I is shown in grey, SU II in light blue and SU IV in green. Lipids and detergent molecules are shown in red. Copper ions are depicted in magenta and haem groups in dark blue.

The variant W164F shows a D-pathway defective phenotype, although this residue is located above E278 (the structural end of the D-pathway) and thus is not part of the D-pathway (Ribacka *et al.*, 2005), but rather part of a putative exit pathway.

Accordingly, subunit I contains different metal ion binding sites for Ca^{2+} ions and Mn^{2+} or Mg^{2+} ions, respectively (Witt *et al.*, 1997; Puustinen and Wikström, 1999; Lee *et al.*, 2002b; Kirichenko *et al.*, 2005) (Figure 1.2-3) and the bound Mn^{2+} (or Mg^{2+}) is suggested to play a role in this putative exit channel of C*c*O (Schmidt *et al.*, 2003).

The existence of a proton conducting H-channel has been postulated in the case of the bovine enzyme (Yoshikawa *et al.*, 1998) but has not been proven for the bacterial C*c*O (Pfitzner *et al.*, 1998; Lee *et al.*, 2000).

Subunit III (SU III), which displays a theoretical molecular mass of 30.8 kDa, is a very hydrophobic polypeptide and contains seven transmembrane helices without bound prosthetic groups. Both subunits III and I provide an effective O_2 pathway and residue V279 of SU I is part of this O_2 pathway. Thus, variant V279I shows a decreased dioxygen reduction activity (Riistama *et al.*, 2000). In addition, subunit III forms a V-shaped structure comprised of a two α-helix bundle versus a five α-helix bundle. This V-shaped cleft provides potential structural space for a tight binding of conserved lipids (Figure 1.2-5) (Iwata *et al.*, 1995; Tsukihara *et al.*, 1996), however some naturally bound lipids have not yet been correctly assigned by X-ray crystallography, because several lipid binding sites are occupied by detergent moecules.

The importance of subunit III is still a matter of debate. It is considered as part of the *core subunits*, however the 2 SU-C*c*O (in the absence of SU III and IV) seems to form a functionally active enzyme (Haltia *et al.*, 1988; Haltia *et al.*, 1989).

SU III is suggested to provide structural stabilisation of C*c*O during catalytic turnovers and it has been observed that the 2 SU-C*c*O destroys itself during continuous turnover, a process termed *suicide inactivation* (Bratton *et al.*, 1999b; Mills and Hosler, 2005). The reason of this loss of function may originate from a structural change or in an increased flexibility of the binuclear site due to the lack of subunit III.

Subunit IV ($M_{W\ theoretical}$ = 5.5 kDa) does not show a catalytic function as determined by deletion of the gene coding for SU IV and thus 3 SU-C*c*O shows full enzymatic activity (Witt and Ludwig, 1997). SU IV is surrounded by lipid molecules within the membrane bilayer, suggesting a role in the structural integrity of the complex in its hydrophobic environment (Iwata *et al.*, 1995).

1.3 Catalytic intermediates

Cytochromes are redox-active metalloproteins and these proteins contain haem groups that reversibly alternate between their Fe(+II) and Fe(+III) oxidation states. The haem groups of reduced cytochromes show prominent absorption spectra containing of three maxima: The α, β, and γ (Soret) bands (Keilin, 1925).

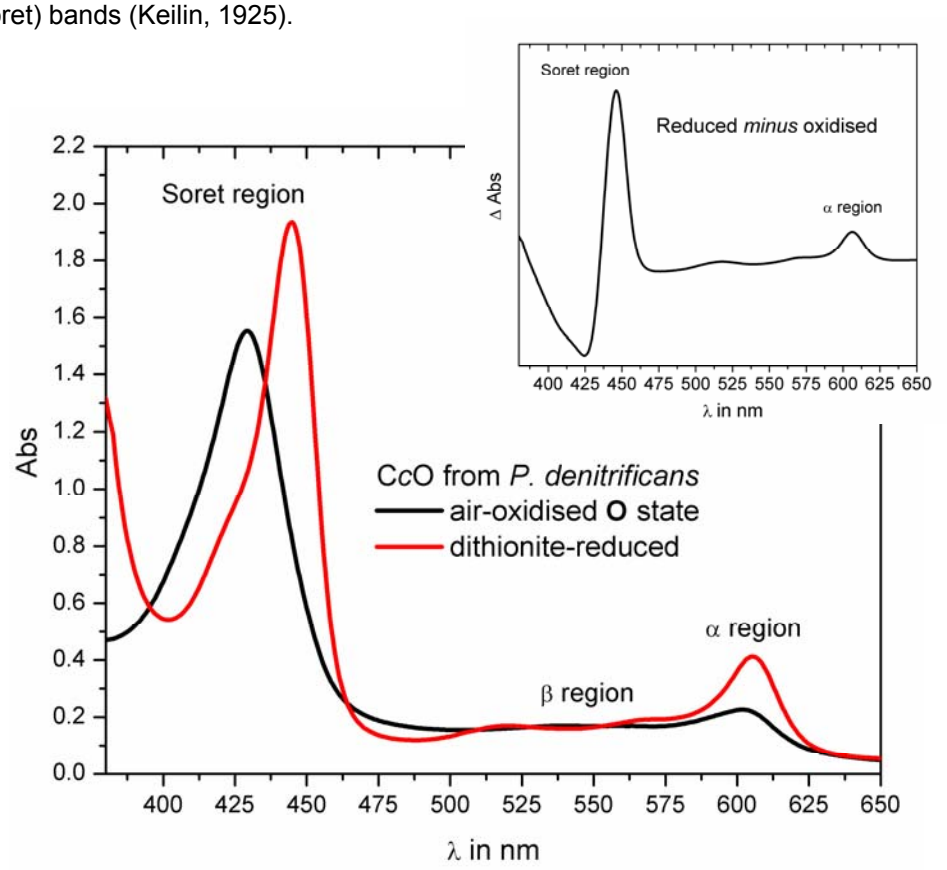

Figure 1.3-1 Absorption spectra from λ = 380 to 650 nm of C*c*O from *P. denitrificans* in the air-oxidised and dithionite-reduced state. The spectra show the Soret region ~ 427 nm and the α maximum at ~ 600 nm. The inset shows the reduced *minus* oxidised difference absorption spectrum.

The wavelength of the α maximum, which varies characteristically with the particular reduced cytochrome species (the α maximum is less prominent in the oxidised form of cytochromes), is useful in differentiating the various cytochromes (Figure 1.3-1). C*c*O binds non-covalently two Type A haems (cytochrome aa_3) and thus the protein shows the typical cytochrome *a* absorption in its (UV)-vis spectrum. In the absorbance spectrum of air-oxidised *P. denitrificans* C*c*O, the Soret peak absorbs in the range of λ = 427 nm with a high extinction coefficient (ε_{425}= 158 $mM^{-1}cm^{-1}$) and in contrast to the cytochromes *b* or *c* having additional β bands, there occurs only the α-peak of C*c*O in the area at λ ~ 605 nm. Again, the haem absorption is highly

dependent on the oxidation state of the complexed iron ion and the fully reduced *minus* oxidised difference absorption spectrum reveals the most extreme redox state dependent spectral changes of C*c*O. Absorption shifts of the intermediate states between this oxidised and fully reduced state are also analysed using difference absorption spectroscopy.

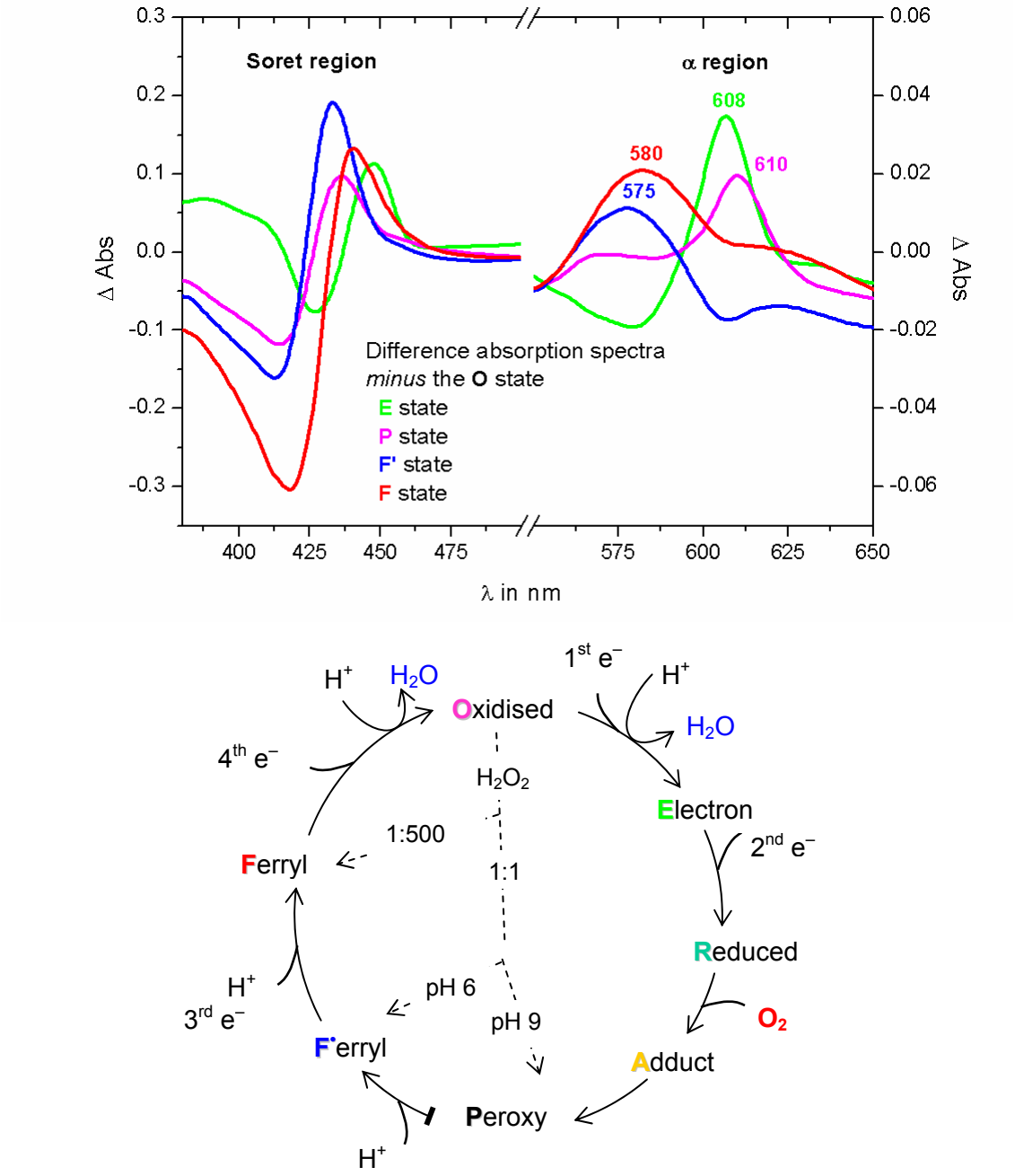

Figure 1.3-2 Catalytic intermediates of C*c*O from *P. denitrificans*. (A) Difference absorption spectra of single intermediate states (*minus* the O state). (B) Starting from the O state, the E state is formed via a one-electron input. Further electron uptake leads to the two-electron reduced R state. The A state is formed after dioxygen binding. Electronic reorganisation results in the P state and a protonation step leads to the F˙ state. The catalytic cycle moves on by two additional electron uptakes; thus the cycle relaxes via the F state back to ground state. The reaction with an equimolar amount (1:1 at pH 9 and pH 6) and an excess of H_2O_2 (1:500) is shown by the short cuts (dashed arrows).

ATP-energised mitochondria in an oxidative environment reveal a 607 nm maximum and a 580 nm maximum in the difference absorption spectra *minus* untreated mitochondria (Wikström, 1981). These absorption maxima represent thermodynamically stable intermediates of mitochondrially embedded C*c*O, termed the **P** state (at that time wrongly named Peroxy state) and the **F** state (Ferryl state), respectively. Figure 1.3-2 A shows the difference absorption spectra (*minus* the **O** state) of single intermediates of C*c*O from *P. denitrificans*.

In general, the catalytic cycle of C*c*O is described by the different redox states of the metal centres (Figure 1.3-2 B): the fully oxidised state is termed **O**, which can be reduced by one electron to form the **E** intermediate (Moody *et al.*, 1991). Further electron input leads to the doubly reduced (*mixed valence*) **R** state. This doubly reduced binuclear site is able to bind dioxygen to form the **A** intermediate, a ferrous-oxygen adduct (Fe^{+II}-O_2) that can only be observed in stable form at cryogenic temperatures (Chance *et al.*, 1975b; Chance *et al.*, 1975a).

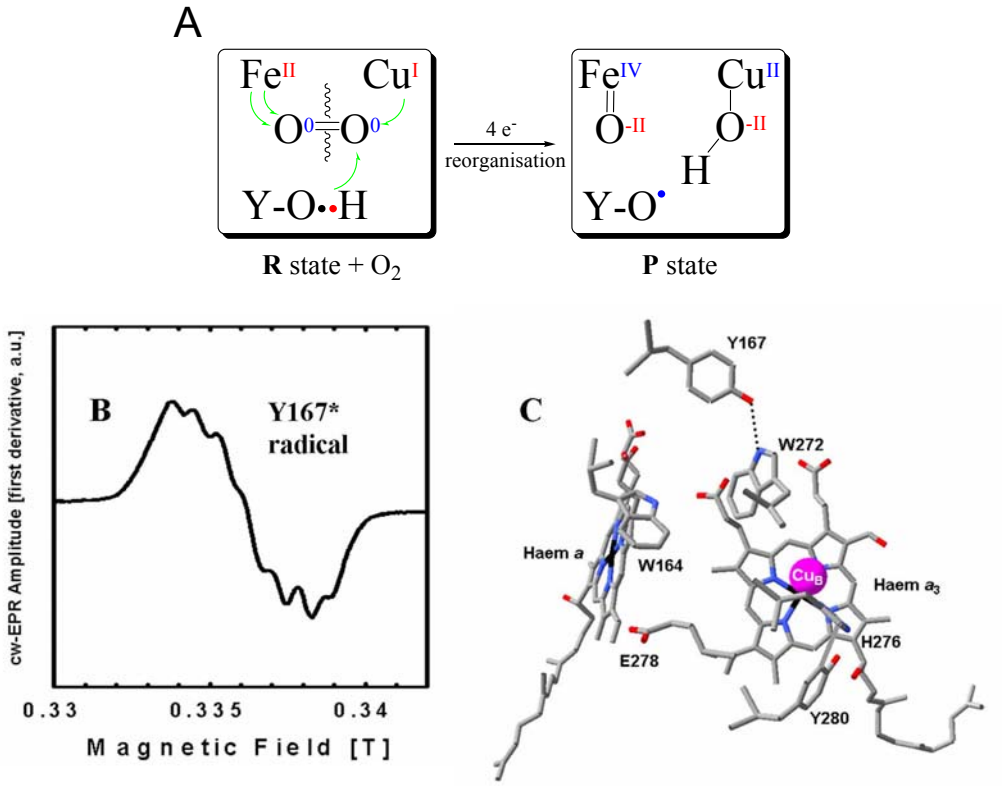

Figure 1.3-3 Formation of the organic radical hosted at a tyrosine during dioxygen reduction of the two-electron reduced C*c*O. (A) Reaction of R state + dioxygen → P state at the binuclear site. The binuclear site can only provide three electrons a_3-Fe^{II} → a_3-Fe^{IV} and Cu^{I}_{B} → Cu^{II}_{B}. The fourth "missing" electron is provided by a tyrosine Y-$O^{\bullet}$ (in the natural cycle probably Y280). (B) Hyperfine structure of the EPR signal from the tyrosyl 167 radical during $F^{\bullet}_{H}$ state recorded at 80 K (Kannt *et al.*, 1999). (C) Model of the binuclear haem a_3-Cu_B centre in context of the haem *a* and the residues of the end of D- and K-pathway (pdb-file 1ar1, Ostermeier *et al.*, 1997), H276 and Y280 are covalently linked.

The ability of C*c*O in this two-electron reduced **R** intermediate to donate four electrons for

dioxygen reduction was revealed by identification of the **P** state (Figure 1.3-3), where the dioxygen bond is already broken and an oxoferryl state ($Fe^{IV}=O^{2-}$) has been observed, and in addition, a tyrosyl (Y167$^{\bullet}$) radical has been observed during the artificially H_2O_2-induced $\mathbf{P_H}$ state (Fabian and Palmer, 1995; Proshlyakov *et al.*, 1996b; Proshlyakov *et al.*, 1996a; Fabian *et al.*, 1999; MacMillan *et al.*, 1999; Budiman *et al.*, 2004; Svistunenko *et al.*, 2004). The uptake of a further electron into the binuclear haem a_3-Cu_B site leads to the three-electron reduced oxoferryl **F** state, which then relaxes via a further electron transfer back to the **O** state.

The doubly reduced **R** state is able to react with dioxygen, regardless of its mode of formation. It has been shown previously that **P** states can be generated from the **O** state by: ATP-energised mitochondria (Wikström, 1981); by a CO-O_2 reaction ($\mathbf{P_{CO}}$ state) (Chance *et al.*, 1975b; Nicholls and Chanady, 1981); by oxygenation of the fully reduced state ($\mathbf{P_R}$ state) (Morgan *et al.*, 1996) or by equimolar amounts of a partially-reduced oxygen species such as H_2O_2 (see short cut in Figure 1.3-2 B, the $\mathbf{P_H}$ state) (Bickar *et al.*, 1982; Weng and Baker, 1991).

Table 1.3-1 Summary of natural and artificial catalytic intermediates from C*c*O. Maxima of intermediates from difference absorption spectra (*minus* the O state) are listed.

	Reduction state	Binuclear site (current model)	Mode of production	Maxi-mum	Reference
O state	-	Fea_3(III) Cu_B(II) Y280	As isolated	-	
E state	Single reduced	Fea_3(III) Cu_B(I) Y280	Ruthenium complexes or **F** state + CO	608 nm	Witt and Chan, 1987, Moody, 1991
R state	Double reduced	Fea_3(II) Cu_B(I) Y280	Fully reduced + O_2	-	Morgan, 1996
A state	Double reduced	Fea_3(II)-O_2 Cu_B(I) Y280	Fully reduced + O_2	590 nm	Chance, 1975
P state	"Double reduced"	Fea_3(IV)=O OH^--Cu_B(II) Y280(*)	Energised mitochondria	607 nm	Wikström, 1981
$\mathbf{P_{CO}}$ state	"Double reduced"	Fea_3(IV)=O OH^--Cu_B(II) Y280	CO + O_2	607 nm	Chance, 1975
$\mathbf{P_R}$ state	"Double reduced"	Fea_3(IV)=O OH^--Cu_B(II) Y280	Fully reduced + O_2	607 nm	Morgan, 1996
$\mathbf{P_H}$ state	"Double reduced"	Fea_3(IV)=O OH^--Cu_B(II) Y167*	Equimolar amounts of H_2O_2, pH 9	610 nm	Bickar, 1982
$\mathbf{F^{\bullet}_H}$ state	"Double reduced"	Fea_3(IV)=O H_2O-Cu_B(II) Y167*	Equimolar amounts of H_2O_2, pH 6	575 nm	Fabian & Palmer, 1995 Jünemann, 2000
F state	Triple reduced	Fea_3(IV)=O H_2O-Cu_B(II) Y280	Energised mitochondria	580 nm	Wikström, 1981
$\mathbf{F_H}$ state	Triple reduced	Fea_3(IV)=O H_2O-Cu_B(II) Y280	Excess H_2O_2	580 nm	Bickar, 1982

Using an excess of H_2O_2 the enzyme forms the three-electron reduced $\mathbf{F_H}$ state (Bickar *et al.*, 1982). Thus it was shown for bovine C*c*O that it is possible to define three different oxoferryl states simply by fine-tuning the concentration of H_2O_2 and by the apparent pH: the $\mathbf{P_H}$ state, a two-electron reduced $\mathbf{F^{\bullet}_H}$ state and the $\mathbf{F_H}$ state (Jünemann *et al.*, 2000).

These intermediates have different maxima in their difference absorption spectra (Figure 1.3-2). The $\mathbf{P_H}$ state, generated by equivalent amounts of H_2O_2 at pH 9, has a maximum at 610 nm in the difference absorption spectrum (*minus* the **O** state), which can be shifted to an electronically equivalent species, the $\mathbf{F^{\bullet}_H}$ state, with a maximum at 575 nm, simply by lowering the pH to pH 6 (Brittain *et al.*, 1996). This $\mathbf{F^{\bullet}_H}$ state is also directly inducible with equimolar amounts of H_2O_2 at pH 6, but is not convertible to the $\mathbf{P_H}$ state via alkalinisation (Brittain *et al.*, 1996). The addition of an excess of H_2O_2 (molar ratio 1:500) to either of these two species reduces C*c*O to the $\mathbf{F_H}$ state, which is characterised by a broad 580 nm maximum in the difference absorption spectrum (*minus* the **O** state) (Wikström, 1981; Vygodina and Konstantinov, 1988).

Furthermore electron paramagnetic resonance (EPR) spectroscopy has revealed the presence of a stable tyrosyl Y167 radical in both the $\mathbf{P_H}$ and $\mathbf{F^{\bullet}_H}$ states but not in the $\mathbf{P_{CO}}$ or $\mathbf{F_H}$ states (Figure 1.3-3) (MacMillan *et al.*, 1999; Budiman *et al.*, 2004; Siegbahn and Blomberg, 2004; Svistunenko *et al.*, 2004). This Y167 species is located too far away from the binuclear centre to be a direct electron donor and until now it is assumed that the primary donor of the “missing electron” for dioxygen reduction may be a tryptophan residue (Wiertz *et al.*, 2004). Residue Y280 was found by X-ray chrystallography to be covalently bound to H276 and it is therefore proposed as the radical hosting tyrosine during the natural catalytic cycle (Figure 1.3-3). Finally, a summary of all introduced states is listed in Table 1.3-1.

1.4 Coupling of intermediate transition to proton pumping

The proton translocation mechanism of C*c*O and its coupling to the different redox states of the metal centres is still controversially discussed. The electron flow in C*c*O can be partially reversed by high redox potentials in ATP-energised mitochondria (Wikström, 1981) and Marten Wikström gained data from titrations of oxidase intermediates with phosphorylation potentials in isolated rat liver mitochondria (Wikström, 1989). Interpreting this data, Wikström developed a model of the catalytic cycle and according to this model, the pumping of all four protons occurs after the binding of dioxygen to the reduced C*c*O and is exclusively coupled to the last two electron transfer steps (**P** → **F** and **F** → **O** state transition) (Figure 1.4-1, for a detailed mechanism see the appendices 6.1.1). The input parameters for this model had been: the intermediates are in thermodynamic equilibrium; the proton impermeability of the membrane; the electrochemical membrane potential is directly correlated to the ATP/ADP ratio; the same pH on both sides of the membrane; the binuclear centre is located in the centre of the dielectric and the consumption of two protons each in the **P** → **F** and **F** → **O** state transition. Furthermore an **O´** state had been introduced having two bound OH^- in the binuclear site (see appendices 6.1.1).

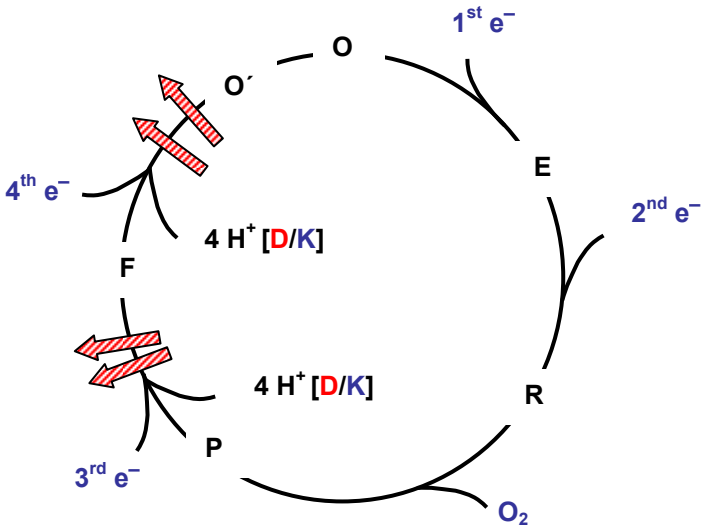

Figure 1.4-1 Simplified model for the catalytic cycle of C*c*O (Wikström, 1989).

However, there has been no verification of these input parameters. After reconsideration of the experimental data, Hartmut Michel criticised this classical model (Michel, 1998; Michel, 1999). He concluded that: 1) the ATP/ADP ratio does not directly correlate to the electrochemical gradient because of putative proton leakiness of the inner mitochondrial membrane; 2) the pH dependence of the ATP hydrolysis shifts the resulting equilibria; 3) and the formation of the **O´**

state is unlikely because of the electrostatic repulsion of the two negative charges from the two OH^- ions. In summary it was stated by Michel that the thermodynamic data do not provide any evidence for an exclusive coupling of proton pumping to the **P** → **F** and **F** → **O** state transitions.

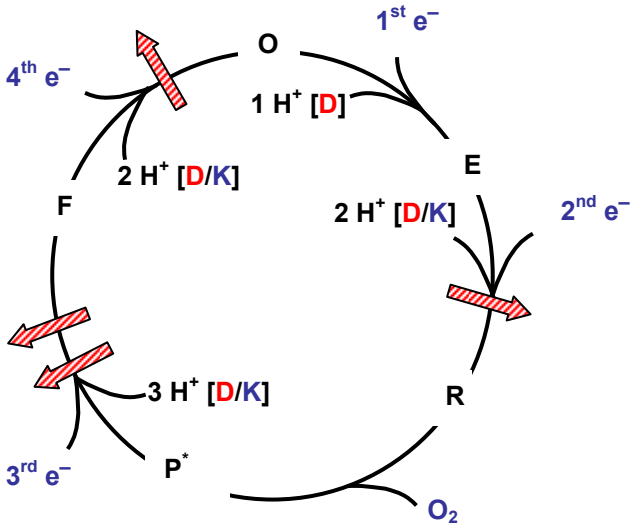

Figure 1.4-2 Simplified model for the catalytic cycle of C*c*O (Michel, 1999).

In addition, it has been observed that the (re-)reduction of C*c*O is accompanied by an uptake of two protons during the first two electron transfers (Mitchell and Rich, 1994) and in contrast to Wikström, Michel's model suggests (Figure 1.4-2 and appendices 6.1.2) that one proton is already pumped during the reductive phase of the catalytic cycle from either the **O** → **E** or **E** → **R** state transition (Michel, 1999).

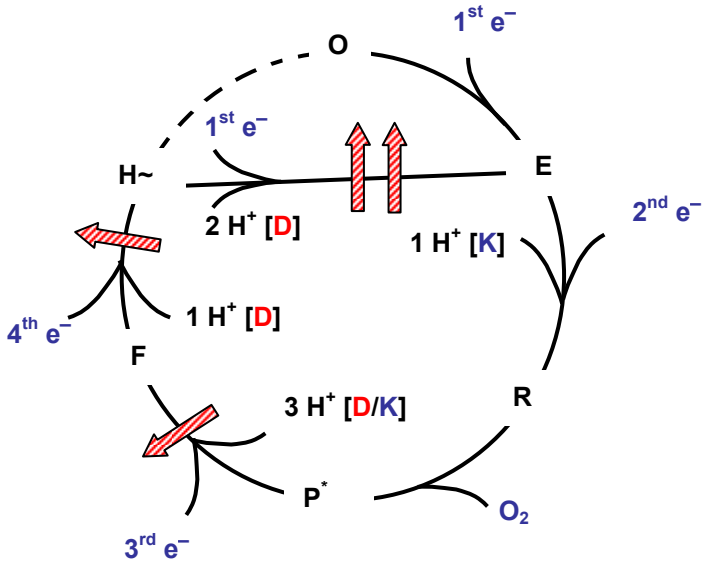

Figure 1.4-3 Simplified model for the catalytic cycle of C*c*O (Wikström, 2000).

This alternative model also satisfies the required electroneutrality principle (charge compensation between electron and proton) (Mitchell and Rich, 1994) and proposes that each haem *a* reduction is accompanied by a proton uptake to a protonation site close to the haem a_3-Cu_B binuclear centre (see appendices 6.1.2). Close to this protonatable cluster is the pumping site, which is a putative proton accepting site at the haem *a* propionates.

Wikström responded in 2000 to Michel´s criticism by introducing the new four-stroke histidine cycle (Figure 1.4-3 and appendices 6.1.3) (Verkhovsky *et al.*, 1999; Wikström, 2000). The original crystal structure of C*c*O (Iwata *et al.*, 1995) suggested this model because in this structure one Cu_B histidine ligand did not show a defined electron density in the oxidised state. The absence of an electron density from the histidine side chain was interpreted as a functional mobility of this histidine residue.

The Cu_B ligating histidine residue supports the proposal of a two proton storage in the active site by this amino acid (Wikström *et al.*, 1994). However, the 2000 model was disproven by parallel investigation of the crystal structure in the oxidised and the fully reduced state of the *P. denitrificans* C*c*O (Harrenga and Michel, 1999) and it was shown that the electron density for each Cu_B ligand is defined independently of the redox state of the binuclear centre.

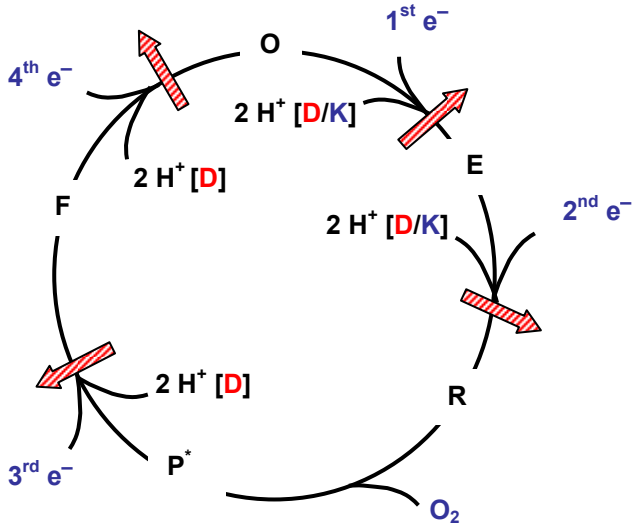

Figure 1.4-4 Wikström's current model for the catalytic intermediates of C*c*O. Starting from the O **state, the** E **state is formed via a one-electron input. Further electron uptake leads to the two-electron reduced** R **state. Electronic reorganisation results in the** P **state. The catalytic cycle moves on through two additional electron uptakes; thus the cycle relaxes via the** F **state back to the** O **state. Each electron input is coupled to an uptake of two protons; one substrate proton and one pumped proton (indicated by red arrows).**

Overall, more recent data do not provide further evidence supporting one or the other model. In fact, the proposed electroneutrality principle might indicate that another model is the most likely one. This current model suggests one pumped proton per each electron input (Mitchell and Rich, 1994; Verkhovsky *et al.*, 2001b; Wikström and Verkhovsky, 2007) and according to this model, the mechanism of proton pumping in C*c*O is less complicated than assumed by Wikström and Michel. Wikström's current model for the catalytic cycle is presented in Figure 1.4-4 (Bloch *et al.*, 2004; Salomonsson *et al.*, 2005; Verkhovsky *et al.*, 2006). However, a proton pumping step for the transition of the **O** → **E** state has not yet been observed by other groups (Ruitenberg *et al.*, 2000a) and these findings argue against Wikström's current model.

The proton pumping mechanism may be driven by electrostatic repulsion and the sequence of the charge inputs for each proton pumping step is assumed to be identical, however the respective pumping pathways might be different.

1.5 Peroxidase activity of cytochrome *c* oxidase

Peroxidase activity, the reduction of H_2O_2, is a well-known side reaction of C*c*O and it cannot be excluded that an H_2O_2 might be a natural intermediate in the mechanism of the catalytic cycle of C*c*O. The action of the aerobic respiratory chain leads to the generation of reactive oxygen species (ROS) such as $^{\bullet}O_2^-$, H_2O_2 or $^{\bullet}OH^-$ and ROS-metabolising enzymes such as peroxidases and superoxide dismutases provide protection against these cell-toxic oxygen species.

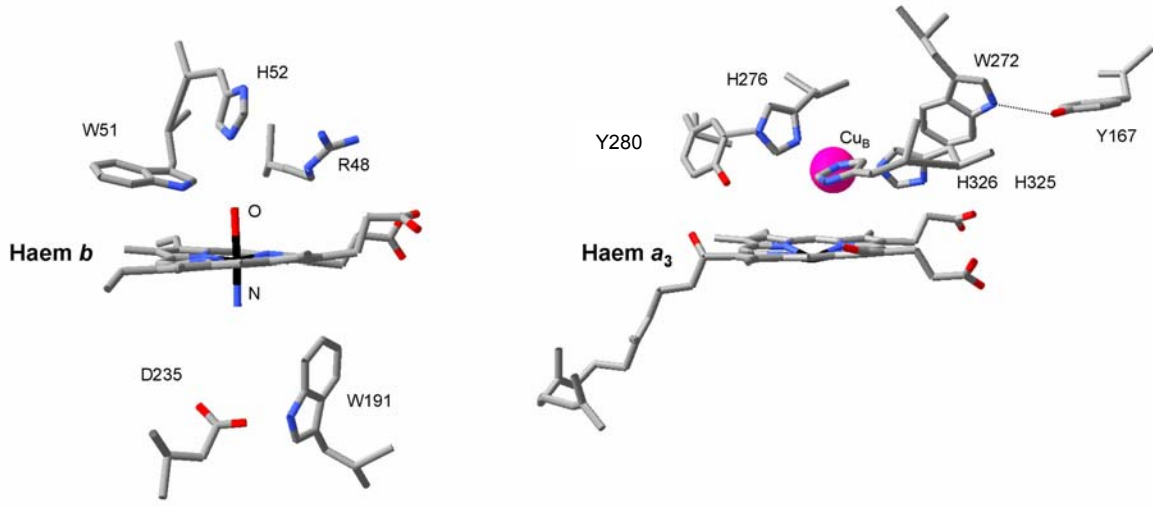

Cytochrome *c* peroxidase **Cytochrome *c* oxidase**

Figure 1.5-1 Active sites of *Saccharomyces cerevisiae* soluble mitochondrial C*c*P and *P. denitrificans* C*c*O. Catalytically important residues are shown; C*c*P: the catalytic triad of W51, H52 and R48 (Goodin and McRee, 1993); the radical hosting W191 next to the acid residue D235 (*S. cerevisiae*, pdb-file 2cyp, Finzel *et al.*, 1984); C*c*O: the Cu_B ligand H276 is covalently bound to Y280; Cu_B ligands H325/H326 and the radical hosting Y167 in H-bond distance to W272 (pdb-file 1ar1, Ostermeier *et al.*, 1997).

Yeast soluble mitochondrial cytochrome *c* peroxidase (C*c*P) is only related to C*c*O in having a high-spin haem B, and does not exhibit a Cu_B centre (Figure 1.5-1) (Finzel *et al.*, 1984), however both enzymes perform similar catalytic reactions. Obviously, only a haem-cytochrome is necessary for the H_2O_2 decomposition and single catalytic intermediates of C*c*P are related to the **P** and **F** state of C*c*O (Yonetani and Ray, 1965; Satterlee and Erman, 1981; Wikström, 1981).

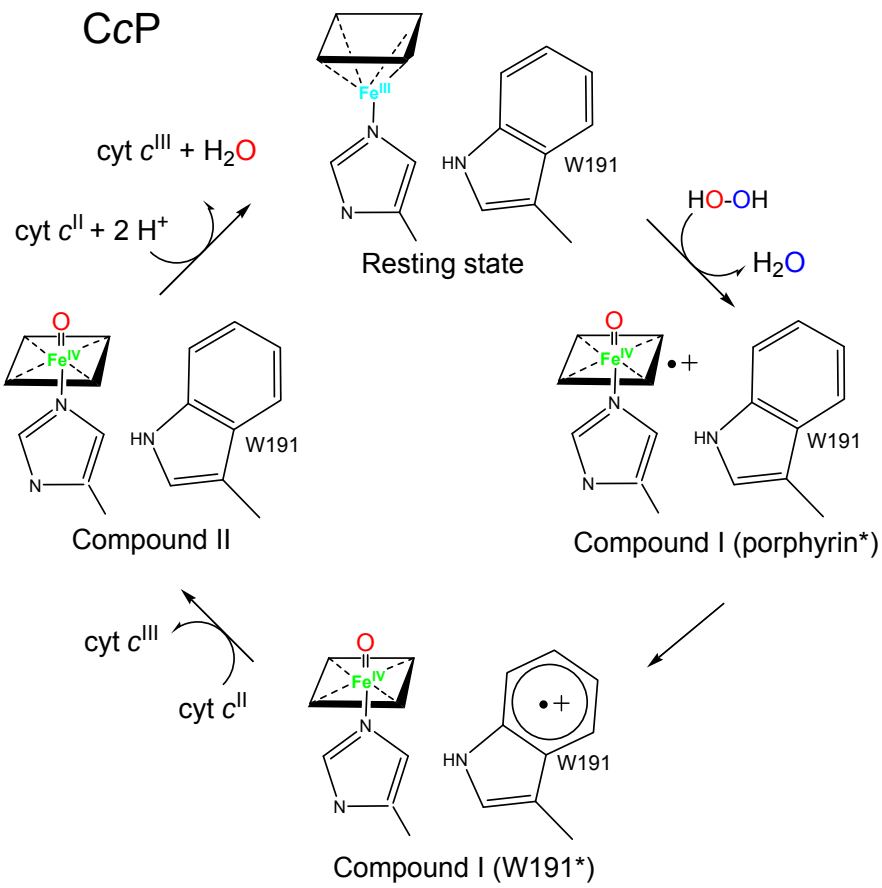

Figure 1.5-2 The active site of C*c*P and its schematic catalytic cycle. Compounds I and II of the C*c*P represent oxoferryl intermediates (Fe^{IV}=O).

C*c*P cleaves the O^--O^- bond of H_2O_2 to form Compound I as depicted in Figure 1.5-2 (Hiner *et al.*, 2002; Jones and Dunford, 2005), which contains an oxoferryl intermediate and additionally hosts a tryptophan W191 radical (Tsaprailis and English, 2003). Two reduction equivalents are required for cycling C*c*P back to the ground state. The first electron reduces W191 and forms Compound II resulting in the oxoferryl state exclusively (Satterlee and Erman, 1981). The second electron reduces the oxoferryl intermediate back to ferric haem *b*; the overall reaction requires two additional protons for the formation of water. C*c*O shows an analogous mechanism of reaction to C*c*P and the catalytic cycle of C*c*P follows the sequence **O** → "**P**" → "**F**"→ **O** state, whereas the C*c*O cycle has the order **O** → **E** → **R** → **P** → **F** → **O** state (see Figure 1.5-3). However, the

catalytic centres of the two enzymes are not structurally related to each other (Figure 1.5-1), and the haem *b* of C*c*P has a much lower redox midpoint potential than haem *a* ($\Delta E^{0'}$ ~ - 200 mV vs. ~ + 350 mV) (Conroy *et al.*, 1978; Wikström *et al.*, 1981).

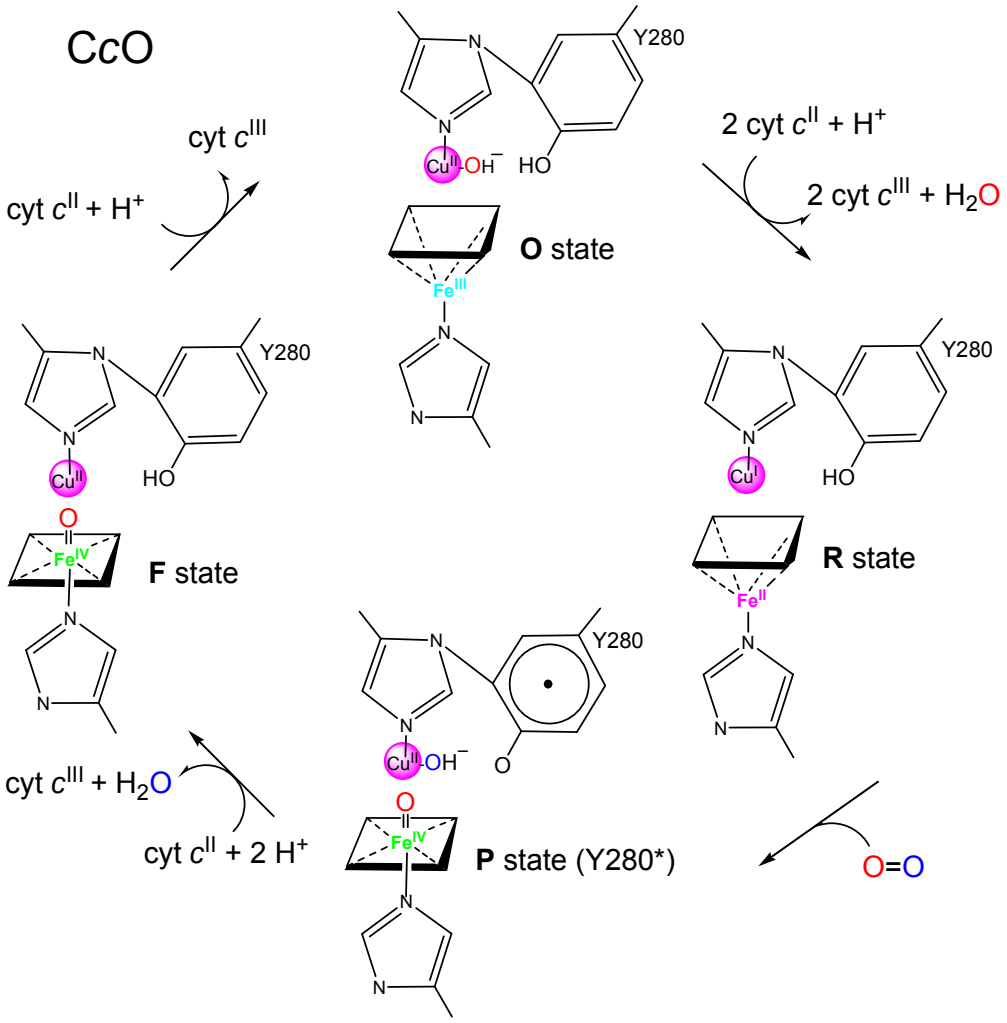

Figure 1.5-3 The active site of C*c*O and its simplified schematic catalytic cycle. The P **and** F **states of C*c*O represent oxoferryl imtermediates (Fe^{IV}=O).**

Both C*c*P and C*c*O undergo a range of extra reactions producing different types of products such as superoxide and peroxide. However, these additional reactions are much slower. For example, in an artificial environment of H_2O_2, Compound I of C*c*P and the **P** state of C*c*O react with a (further) molecule of H_2O_2 releasing a putative superoxide $^{\bullet}O_2^-$ (one-electron oxidation of H_2O_2) (Fridovich and Handler, 1961; Orii, 1982). The released $^{\bullet}O_2^-$ molecules are highly reactive and are able to introduce single electrons into oxidised C*c*P or C*c*O, generating a ferrous Fe(II) haem group. Dioxygen then binds the reduced Fe^{II}, forming the dioxygen-adduct (Fe^{II}-O_2) Compund III or the **A** state. However, only C*c*P releases superoxide more frequently, because of the low redox potential of haem *b*.

1.6 Expression hosts for the protein production

P. denitrificans is an α_3-proteobacterium from the sub-group of *Rhodobacterales* and members of this group of bacteria have been proposed to represent the precursor organisms of mitochondria (John and Whatley, 1975). The catalytic subunits of the membrane protein complexes in the respiratory chain from *P. denitrificans* show a high homology to those of the mitochondrial complexes. Thus, *P. denitrificans* is preferred as a bacterial model organism for the eukaryotic respiratory chain.

In addition, bacterial DNA expression systems have several advantages compared to genetic systems of eukaryotic cells. Tools of molecular biology are employed easily using bacteria, because the methods for mutagenesis and homologous recombination are well established.

The rapid cell proliferation of prokaryotes and the opportunity to use defined media for bacterial cell growth can provide high yields of the desired cell membranes. Secondly, methods for DNA manipulation and plasmid transfer into *P. denitrificans* result in a useful host for a homologous expression of C*c*O.

The free access to standard laboratory strains of *P. denitrificans* provided the possibility for the determination of several biochemical features of its respiratory chain and the analysis of its alternative bioenergetic pathways (Figure 1.6-1).

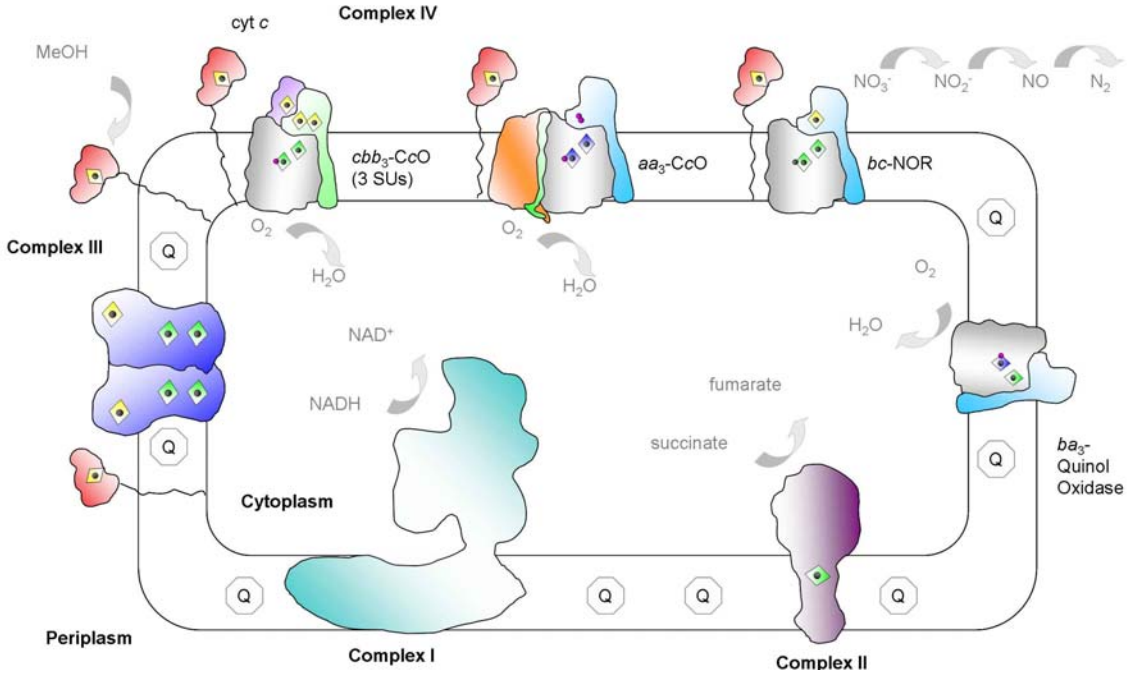

Figure 1.6-1 Respiratory chain and alternative terminal complexes of aerobic and anaerobic pathways from *P. denitrificans*.

The distinct ORFs coding for subunits of *P. denitrificans* aa_3-C*c*O are distributed at different loci in the genomic DNA (gDNA) (Figure 1.6-2). Two isoforms of subunit I exist, they are encoded by two independent genes (*cta*DIα and *cta*DIIβ), which are nearly 90 % identical to each other (Raitio *et al.*, 1990), however, the gene *cta*DIα seems to be a pseudogene and thus is not expressed under natural conditions. Subunits II, III and IV are encoded by the genes *cta*C, *cta*E and *cta*H, respectively, and *cta*C and *cta*E are found in an operon which also encodes several other proteins (*cta*CB-ORF2-*cta*GE). *P. denitrificans* possesses other terminal oxidases next to the mitochondrial-like aa_3-C*c*O: the ba_3 quinol oxidase (QOX) and the cbb_3-C*c*O. These alternative oxidases are also members of the haem-copper oxidase superfamily (Figure 1.6-1), but ba_3-QOX lacks the dinuclear Cu_A centre and cbb_3-C*c*O lacks subunit II, but contains additional subunits possessing haem C groups. The production of these three terminal oxidases depends on external conditions; for example, the gene of cbb_3-C*c*O is mainly expressed at a low partial pressure of dioxygen.

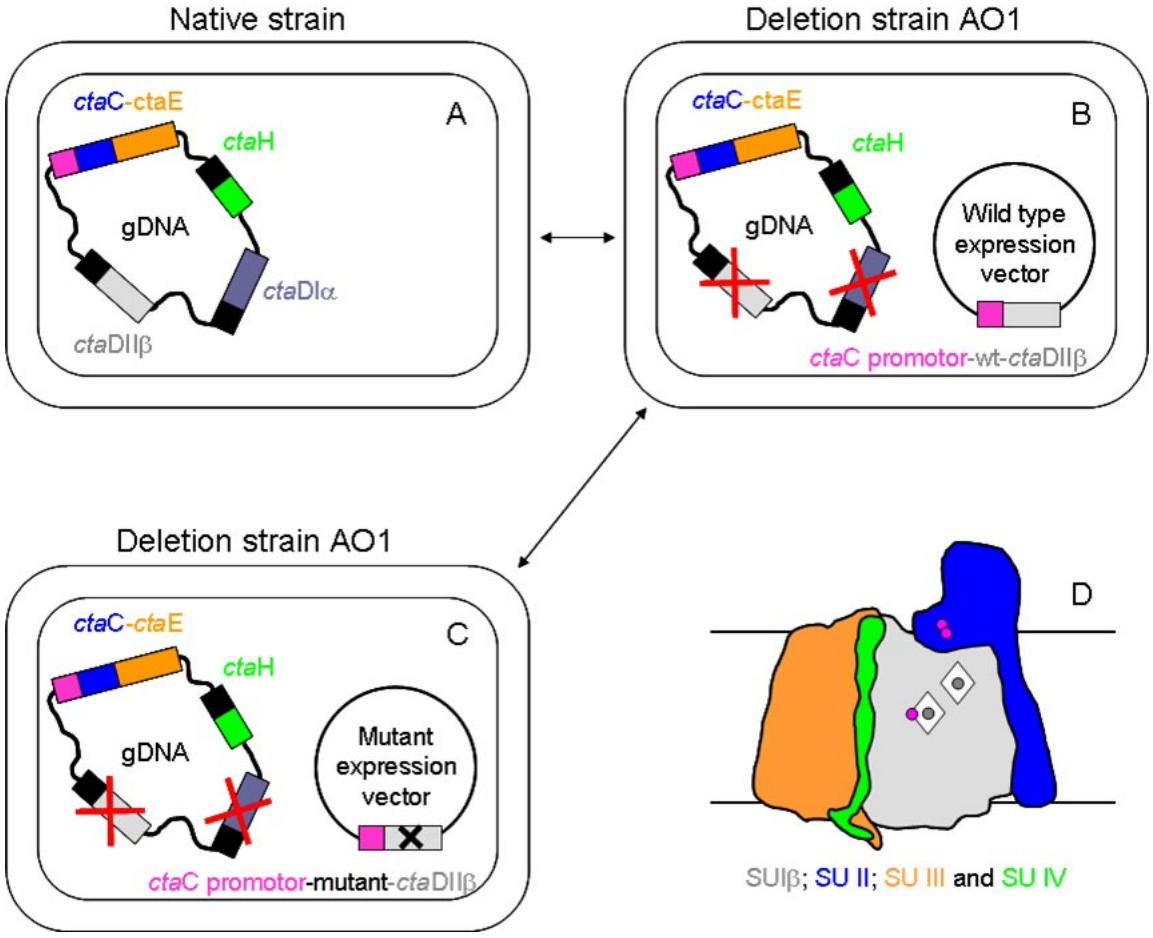

Figure 1.6-2 Expression system of aa_3-C*c*O from *P. denitrificans*. (A) Native Strain. (B) Deletion strain AO1 expressing the plasmid-encoded wt-*cta*DIIβ. (C) Deletion strain AO1 expressing the plasmid-encoded mutant-*cta*DIIβ. (D) Schematic model of produced subunits of C*c*O. Arrows indicate the relation of the produced C*c*Os.

Furthermore, *P. denitrificans* uses anaerobic bioenergetic pathways in the absence of dioxygen. This denitrifying organism is able to use nitrogenic compounds, for example NO_3^-; NO_2^-; N_2O or NO as electron acceptors. The NOR catalyses the last step of this pathway and converts NO to N_2 and H_2O. Both NOR and C*c*O/QOX belong to the same superfamily having a similar subunit composition. However, NOR does not have any bound Cu ions, the dinuclear Cu_A centre is missing and the Cu_B is replaced by Fe_B.

Overexpressed recombinant C*c*O is produced by homologous expression in a deletion strain using an expression vector. The *P. denitrificans* deletion strain AO1 (Figure 1.6-2 B) is a derivative of the *P. denitrificans* strain PD1222 exhibiting several deletions of oxidase genes as induced by homologous recombination (JWG University of Frankfurt, Dr. Richter). Thus, both genes coding for subunit I (*cta*DIα and *cta*DIIβ) and the genes coding for the *cbb*$_3$-C*c*O (*cco*N) are replaced by genes providing antibiotic resistance. The organism is forced to express plasmid-encoded wild type subunit Iβ to be able to perform cyt *c* oxidation and this expression system had been developed for the production of a recombinant wt C*c*O and for mutagenesis studies of C*c*O variants (Figure 1.6-2 C).

For decades, mitochondrial C*c*O has been purified applying classical strategies. Initially, purification protocols allowed the isolation of beef heart mitochondria from cell homogenates and further purification was mainly perfomed by salt precipitation and later by ion exchange chromatography steps.
Type *aa*$_3$-C*c*O from *P. denitrificans* was also purified using classical protocols and the purification had been performed by anion exchange chromatography and size exclusion chromatography. The generation and cloning of a C*c*O-binding Fv fragment (Fragment variable of an IgG) gave the opportunity for an affinity tag-based chromatographic purification (Kleymann *et al.*, 1995). Thus, membranes of the native *P. denitrificans* strain (for example available as ATCC 13543) offer a natively expressed form of C*c*O (Figure 1.6-2 A), which can be purified by using the Fv fragment. In addition, the Fv fragment-based purification protocol can also be employed for the purification of the recombinant wt C*c*Os (Figure 1.6-2 B and C).

1.7 Aim of this work

The aim of this work is to provide information about the mechanism of C*c*O by functional and structural studies. C*c*O from *P. denitrificans* is a four-subunit integral membrane protein (4 SU-wt C*c*O), however the redox-active haem A groups and the copper centres are located in subunits I and II exclusively.

The functionally active two-subunit form of wild type C*c*O (2 SU-wt C*c*O) was crystallised and its structure was determined at high resolution (2.7 Å). Homologously produced recombinant variants of C*c*O such as N131D and D124N (rec, plasmid-encoded SU Iβ) showed higher resolution (2.3 Å) than the native wt C*c*O (genome-encoded SU Iβ).

The improvement of the resolution of the wt C*c*O structure and further detailed functional studies might provide more information about the mechanism of this enzyme.

1) Cloning and production of a recombinant wt C*c*O (wt rec C*c*O) and its structural analysis (in comparison with the native wt C*c*O) will possibly provide more insights into the function of this enzyme, because the determined structures of the recombinantly produced variant C*c*Os exhibited better resolutions. Details obtained from structures of the wt C*c*Os might give more structural data such as orientations of certain amino acids, bound water molecules or a putatively bound peroxide molecule in the oxidised state (chapter 3.1 and 3.3).

2) The functional role of subunit III will be shown by a large scale *suicide inactivation* experiment and the structure of the *inactivated* 2 SU-wt recombinant C*c*O should provide information about the importance of subunit III (chapter 3.2 and 3.3).

Terminal oxidases such as the *P. denitrificans* C*c*O require four electrons (in the natural cycle provided by four reduced cytochrome *c* molecules) for the O_2 reduction reaction. The coupling of the redox states of the metal centres after electron inputs to the proton pumping is still under debate. The formation of stable intermediates has to be established in this work.

1) H_2O_2-induced states represent such reproducible intermediates and the properties of these intermediates have to be studied in more detail. The characterisation of the native 4 SU-wt C*c*O at different conditions may identify new intermediates. In addition, the functional peroxidase cycle of C*c*O (decomposition of H_2O_2) and its reactive oxygen species production have been described (Orii, 1982) and will be investigated in more detail (chapter 3.4).

2) The metal ions of C*c*O's active site donate only three electrons for the reduction of the dioxygen molecule. The 4^{th} electron is provided by residue Y167 in H_2O_2-induced model intermediates. This residue hosts a radical in these intermediates as determined by EPR spectroscopy. The substitution of the neighbouring residue W272 to other amino acids should prove the ability of W272 to act as an electron wire from Y167 to the binuclear site (chapter 3.5).

3) In order to characterise the function of one proton tansfer pathway of C*c*O, the D-pathway, proton pumping properties of the variants H28A, D30N, N113D, G196D and S193Y will be determined and compared to the results from the new recombinantly produced wt C*c*O (chapter 3.6).

Finally, the functional and structural information from all these experimental data will be used for the analysis of C*c*O's catalytic mechanism. The experiments presented here might have the potential to change the model of the mechanism of dioxygen reduction chemistry at the binuclear site.

The overall aim of this work is to investigate the putative role of peroxide in the catalytic cycle of C*c*O and to find out whether or not there is evidence for the presence of a peroxide molecule in the active site during different intermediate states of C*c*O. The results will be discussed in the context of the current model of the catalytic cycle.

2 MATERIAL AND METHODS

2.1 Devices

Device	Manufacturer
Autoklav	Holzner, Oberschleißheim, Germany
Centrifuges	Eppendorf, Hamburg, Germany Sigma, Taufkirchen,Germany Sorvall, Langenselbold, Germany
EPR spectrometer	Bruker BioSpin, Rheinstetten, Germany
Chromatography	In house made chromatography station
Homogenisator	Ultra Turrax T25 Basic IKA-Werke, Staufen, Germany
Incubator	Eppendorf, Hamburg, Germany
MALDI-TOF Omniflex Instrument	Bruker Daltonik, Bremen, Germany
4800 MALDI-TOF/TOF^{TM} Analyzer	Applied Biosystems, Darmstadt, Germany
Oxygen electrode	Hansatech, Reutlingen, Germany
pH electrode SevenEasy	Mettler, Toledo,
Polymerase chain reaction (PCR) machine	DNA Engine Dyad, Miami, U.S.A.
Shakers	Beckmann, Krefeld, Germany infors, Einsbach, Germany
Stopped flow apparatus SF-61X2 High-Tech Scientific	Wiggenhauser, Berlin, Germany
SDS-PAGE apparatus	Home-made
TXRF-Instrument	EXTRA IIA (Atomika Instruments)
Ultra Sonifier	Branson Sonifier 250, Schwäbisch Gmünd, Germany
UV-vis spectrophotometers	Ultrospec 2100 pro, Cambridge U.K., Perkin Elmer, Wellesley, U.S.A. Lambda 40, Agilent, Palo Alto U.S.A. PowerWaveX Bio-Tek Instruments, INC. Winooski, Vermont, U.S.A

2.2 Chemicals

Chemical	Company
Acetic acid	Roth, Karlsruhe, Germany
Acrylamide 30 % / Bisacrylamid 0.8 %	Roth (Protogel), Karlsruhe, Germany
Agarose	Roth, Karlsruhe, Germany
Agar	Roth, Karlsruhe, Germany
Ammoniumpersulfate	Koch-Light, Haverhill, U.K.
Ampicillin	Gerbu, Gaiberg, Germany
Ascorbate	Sigma, Taufkirchen,Germany
Asolectin (L-α-phosphatidylcholine Type II-S)	Sigma, Taufkirchen,Germany
Avidin	Gerbu, Gaiberg, Germany
Bacto-Trypton	Becton-Dickinson, Heidelberg, Germany
BCA assay	Perbio, Bonn, Germany
BSA	Roth, Karlsruhe, Germany
Boric acid	Merck, Darmstadt, Germany

Bromophenol blue Na salt	Roth, Karlsruhe, Germany
Buffers for resriction enzymes	Fermentas, St. Leon-Rot, Germany
Catalase (*Aspergillus niger*)	Sigma, Taufkirchen,Germany
Carbenicillin	Gerbu, Gaiberg, Germany
Cholic acid, Na salt	Sigma, Taufkirchen,Germany
CO	Air Liquide, Düsseldorf, Germany
Cytochrome *c* (horse heart)	Sigma, Taufkirchen, Germany
Deionised water	Milipore, Eschborn, Germany
N-N-Dimethyldodecylamin-N-oxide (LDAO)	Fluka, Sigma, Taufkirchen, Germany (CMC = 0.023% (w/v))
Desthiobiotin	IBA, Göttingen, Germany
DNA gel extraktion kit	Qiagen, Hilden, Germany
DNA markers, 100 b ladder and 1 kb ladder	New England Biolabs, Frankfurt am Main, Germany
n-Dodecyl-β-D-maltopyranosid (β-LM)	Glycon, Luckenwalde, Germany (CMC = 0.0087% (w/v))
n-Decyl-β-D-maltopyranosid (β-DM)	Glycon, Luckenwalde, Germany (CMC = 0.087% (w/v))
N-Dodecylphoscholin (FOS-12)	Anatrace, Maumee, U.S.A (CMC = 0.047% (w/v))
EDTA	Gerbu, Gaiberg, Germany
Ethanol	Roth, Karlsruhe, Germany
Ethidiumbromid solution	Roth, Karlsruhe, Germany
D-β-(+)-Glucose	Sigma, Taufkirchen,Germany
Glucose oxidase	Sigma, Taufkirchen,Germany
Glycerol	Gerbu, Gaiberg, Germany
Glycine	Gerbu, Gaiberg, Germany
IPTG	Gerbu, Gaiberg, Germany
HCl (0.1 M)	Merck, Darmstadt, Germany
HCl (1 M)	Roth, Karlsruhe, Germany
*Hind*III	New England Biolabs, Frankfurt am Main, Germany
H_2O_2	Sigma, Taufkirchen,Germany
Kanamycin	Gerbu, Gaiberg, Germany
K_2HPO_4	Merck, Darmstadt, Germany
KH_2PO_4	Merck, Darmstadt, Germany
Ligase kit	Epicentre, Bonn, Germany
Mes	Gerbu, Gaiberg, Germany
NaCl	Biotechnik GmbH, Gera, Germany
Na-dithionite	Fluka, Sigma, Taufkirchen, Germany
NaOH	Gerbu, Gaiberg, Germany
n-Octyl-β-D-glucopyranosid (β-OG)	Glycon, Luckenwalde, Germany (CMC = 0,53% (w/v))
Oligonucleotides	biomers.net, Ulm, Germany Invitrogen, Karlsruhe, Germany
Peptide standard	Bruker BioSpin, Rheinstetten, Germany
Pefabloc SC	Roche, Mannheim, Germany
2-Propanol	Merck, Darmstadt, Germany
Protein marker, prestained	New England Biolabs, Frankfurt am Main, Germany
PCR purifying kit	Qiagen, Hilden, Germany
Plasmid isolation kit	Qiagen, Hilden, Germany
Q sepharose F	Amersham Biosciences, Freiburg, Germany
Rifampicin	Gerbu, Gaiberg, Germany
Sigma catalase kit	Sigma, Taufkirchen,Germany
Sodium acetat	Roth, Karlsruhe, Germany

Streptomycine sulfate	Sigma, Taufkirchen, Germany
Superdex 200 prep scale	Amersham Biosciences, Freiburg, Germany
Superoxide dismutase	Sigma, Taufkirchen,Germany
Sucrose	Gerbu, Gaiberg, Germany
Tetramethylphenylen-diamine (TMPD)	Sigma, Taufkirchen,Germany
N,N,N,N-Tetramethyl-*p*-ethylendiamide (TEMED)	Koch-Light, Haverhill, U.K.
TSK gel G3000SW (TSK 3000)	TOSOH BIOSEP, Stuttgart, Germany
Tris	Roth, Karlsruhe, Germany
n-Undecyl-β-D-maltopyranosid (β-UM)	Glycon, Luckenwalde, Germany (CMC = 0.0087% (w/v))
Water soluble Coomassie, PageBlue	Fermentas, Fermentas, St. Leon-Rot, Germany
*Xba*I	New England Biolabs, Frankfurt am Main, Germany
Yeast extract	Merck, Darmstadt, Germany

2.3 Microorganisms

Strains of organisms used

Strain	**Genotype**	**Source and Reference**
E. coli DH5α	Φ 80 d *lac*^{q}ZDM15, *rec*A1, *end*A1, *gyr*A96, *thi*-1, *hsd*R17 ($r_{K-}m_{K+}$), *sup*E44, *rel*A1, *deo*R Δ(*lac*ZYA-*arg*F)U169	Bethesda Res. Lab., Inc., 1986
E. coli JM 83	pASK 68, Fv fragment 7E2	Ostermeier *et al.*, 1997
E. coli RP4-4	RP-4 derivative in J53 mit Amp^{r}, Tet^{r}, Km^{s}	JWG University of Frankfurt, Dr. Richter
P. denitrificans AO1	PD1222 derivative, Δ*cta*DIα::Km^{r}, Δ*cta*DIIβ::Tet^{r}, Δ*cco*N::Gm^{r}, Rif^{r}	JWG University of Frankfurt, Dr. Richter
P. denitrificans ATCC 13543	Wild type	American Tissue Culture Collection, LGC Promochem, Wesel, Germany

2.4 Nucleic acids

2.4.1 Plasmids

Plasmids used in this work

Plasmid	Relevant features	Reference
pRI2	pBBR1 MCS derivative, Sm^r, Cm^r	JWG University of Frankfurt, Dr. Richter
pUP39	pRI derivative, Sm^r, Cm^r, *cta*C2 promotor *Kpn*I/*Xba*I, *cta*DIIβ*Xba*I/*Hind*III, Δ*cta*DIIβPstI-fragment	JWG University of Frankfurt, Dr. Pfitzner
pUP6	Tet^r, *cta*C1 promotor (-148 to -39) *Kpn*I/*Xba*I, *cta*DIIβ*Xba*I/*Hind*III, in pAlter	JWG University of Frankfurt, Dr. Pfitzner
pUP39_D30N	pUP39 derivative, Sm^r,Cm^r, *cta*DIIβ_D30N, *Xba*I/*Hind*III	this work
pUP39_H28A	pUP39 derivative, Sm^r,Cm^r, *cta*DIIβ_H28A, *Xba*I/*Hind*III	this work
pUP39_H28A-N131D	pUP39 derivative, Sm^r,Cm^r, *cta*DIIβ_H28A-N131D, *Xba*I/*Hind*III	this work
pUP39_D30N-D124N	pUP39 derivative, Sm^r,Cm^r, *cta*DIIβ_D30N-D124N, *Xba*I/*Hind*III	this work
pUP39_G196D	pUP39 derivative, Sm^r,Cm^r, *cta*DIIβ_G196D, *Xba*I/*Hind*III	this work
pUP39_S193Y	pUP39 derivative, Sm^r,Cm^r, *cta*DIIβ_S193Y, *Xba*I/*Hind*III	this work
pUP39_W272F	pUP39 derivative, Sm^r,Cm^r, *cta*DIIβ_W272F, *Xba*I/*Hind*III	this work
pUP39_W272Y	pUP39 derivative, Sm^r,Cm^r, *cta*DIIβ_W272Y, *Xba*I/*Hind*III	this work
pUP39_W272H	pUP39 derivative, Sm^r,Cm^r, *cta*DIIβ_W272H, *Xba*I/*Hind*III	this work
pUP39_Y167F-W272F	pUP39 derivative, Sm^r,Cm^r, *cta*DIIβ_Y167F-W272F, *Xba*I/*Hind*III	this work

pUP39_Y167F-W272Y	pUP39 derivative, Sm^r,Cm^r, *cta*DIIβ_Y167F-W272Y, *Xba*I/*Hind*III	this work
pUP39_Y167F-W272H	pUP39 derivative, Sm^r,Cm^r, *cta*DIIβ_Y167F-W272H, *Xba*I/*Hind*III	this work
pUP39_W164F	pUP39 derivative, Sm^r,Cm^r, *cta*DIIβ_W164F, *Xba*I/*Hind*III	this work

2.4.2 Primers

List of used oligo nucleotides (mutated triplets are labelled)

No.	Name	Purpose	Sequence (5'-3')
1	D30N_para	Mutagenesis	GGTTCATGTCAACAAACCACAAGAATATCGGTATCCTTTACC
2	H28A_para	Mutagenesis	GTCGGTTCATGTCAACAAACCGCAAGGATATCGGTATCCTTTACC
3	W272F_para	Mutagenesis	CGGTGCTTTACCAGCACATCCTGTTTTTCTTCGGCCATCCCGAGG
4	W272Y_para	Mutagenesis	CGGTGCTTTACCAGCACATCCTGTACTTCTTCGGCCATCCCGAGG
5	W272H_para	Mutagenesis	CGGTGCTTTACCAGCACATCCTGCACTTCTTCGGCCATCCCGAGG
6	G196D_para	Mutagenesis	GGTGCCTCGTCGATCCTGGACGCGATCAACATCATCACC
7	S193Y_para	Mutagenesis	CCACGTCTCGGGTGCCTCGTATATCCTGGGCGCGATCAACATCATCACC
8	W164F_para	Mutagenesis	GGGTTCGGGCGTCGGCTTCGTGCTCTACCCGCCGC
9	*cta*DIIβ_Anfang	Sequencing	TCTAGAAACAGGCGAGTCC
10	*cta*DIIβ_550	Sequencing	CCTACTGGATGTATGTCTGC
11	*cta*DIIβ_1020	Sequencing	TCATCAGCCACGTCATC
12	*cta*DIIβ_1460	Sequencing	TACTGGATCGGCAAGATG

2.5 Antibiotics

Antibiotic stock solutions	[mg/mL]	Solvent
Streptomycin-sulfate 1000 x	25	50 % glycerol (v/v)
Rifampicin 500 x	30	methanol
Kanamycin 1000 x	25	50 % glycerol (v/v)
Ampicilin 1000 x	100	50 % glycerol (v/v)
Carbenicilin 1000 x	50	50 % glycerol (v/v)

2.6 Culture media

2.6.1 Luria-Bertani media

TY (Tryptone-Yeast) medium was composed of 0.8 % (w/v) peptone, 0.5 % (w/v) yeast extract, 0.5 % (w/v) NaCl, for shaking cultures. For plates 1.6 % (w/v) agar was added. LB medium contained 0.1 % (w/v) bacto tryptone, 0.5 % (w/v) yeast extract, 0.5 % (w/v) NaCl for culture medium and for LB-plates 1.6 % (w/v) agar was added. Cryo stock medium contained additional 15 % (v/v) glycerol in 2 x TY medium.

2.6.2 Succinate medium

Succinate medium was produced by preparation of a solution containing a final concentration of 25 mM succinate and 0.05 % (w/v) Na_2CO_3 in minimal medium at pH 7.
Minimal medium contained 1 x mineral salt solution, 1 x trace elements solution and 65 mM KP_i at pH 7.
Trace elements solution (1000 x) was composed of 100 mM $CaCl_2$, 10 mM $CoCl_2$, 5 mM $CuSO_4$, 90 mM $FeCl_3$, 5 mM H_3BO_3, 10 mM Na_2MoO_4, 25 mM $ZnCl_2$, in the presence or absence of 50 mM $MnCl_2$ in 50 % (v/v) HCl.
Mineral salt solution (10 x) contained 300 mM NH_4Cl, 3 mM $CaCl_2$, 8 mM $MgSO_4$, 6.5 mM $NaMoO_4$, 3 mM NTA (Triplex I).

2.7 Microbiological methods

2.7.1 Cultivation of microorganisms

E. coli cells were incubated in a shaker at 37°C and *P. denitrificans* cultures were incubated shaking at 32°C (5 mL cultures at 200 rpm, 600 mL at 180 rpm and 2 L at 160 rpm). Cultures of *E. coli* cells growing on agar plates were incubated at 37°C. Growing *P. denitrificans* cells were incubated on plates at 32°C. Storage temperature of the plates was 4°C for *E. coli* strains and RT for *P. denitrificans cells*. For cryo stock preparation cell pellets (centrifuged at max. 6000 g) were resuspended in 800 µL of 2 x TY medium and stored at - 80°C.

2.7.2 Site-directed mutagenesis of *cta*DIIβ

The *Hind*III/*Xba*I-wt-*cta*DIIβ DNA fragment, encoding isoform 2 of cytochrome *c* oxidase subunit Iβ, was first cloned from the plasmid pUP6 (pUP6wt-*cta*DIIβ kindly provided by Prof. Ludwig, JWG University of Frankfurt) into the *Hind*III/*Xba*I restriction sites of plasmid pASK75 (see Figure 2.7-1, all standard methods of molecular biology were performed after Sambrook and Russell (2001). The resulting plasmid pASK75wt-*cta*DIIβ was used for PCR-based mutagenesis employing primers 1 to 8 (chapter 2.4.2) using the MultiChange Quik mutagenesis kit (Stratagene).
Plasmids carrying the mutated *cta*DIIβ-mut gene (pASK75wt-*cta*DIIβ-mut) were isolated from *E. coli* cells using the DNA isolation kit (Qiagen, Germany). Mutated genes were sequenced in the particular gene section (in house or SeqLab, Germany) using primers 9 to 12 (chapter 2.4.2).

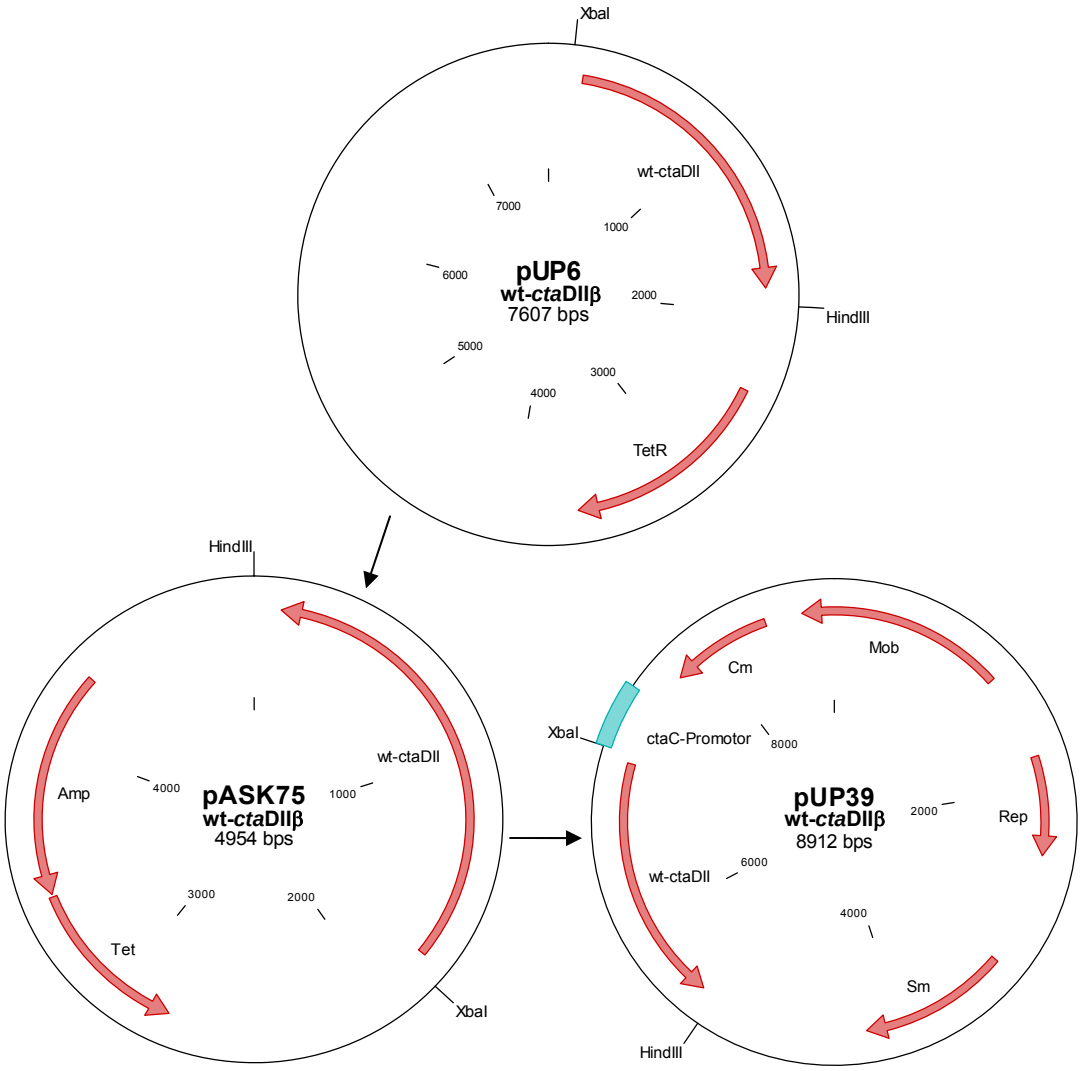

Figure 2.7-1 Plasmids pUP6wt-*cta*DIIβ, pASK75wt-*cta*DIIβ and pUP39wt-*cta*DIIβ. pASK75 (without insert ~ 3000 bp) was used for mutagenesis by PCR. pUP39 is a *P. denitrificans* low copy broad host range expression vector.

2.7.3 Cloning of the expression vector

*Hind*III/*Xba*I DNA fragments of pUP39 (kindly provided by Prof. Ludwig, JWG University of Frankfurt) and the insert DNA (*Hind*III/*Xba*I-wt-*cta*DIIβ-mut DNA fragment from pASK75) were separated via gel electrophoresis. DNA was extracted using the Gel extraction kit (Qiagen, Germany) and pUP39 was dephosphorylated using Calf instestine alkaline phosphatase (Fermentas, Germany). Vector pUP39 and the insert DNA were ligated using the Epicentre ligation kit (Promega). The resulting plasmids (2.4.1) were first transformed into *E. coli* DH5α cells,

and for homologous expression plasmids were transferred from *E. coli* to *P. denitrificans* cells by conjugation.

2.7.4 Triparental mating

Broad host range plasmids carrying the wt-*cta*DIIβ or the mutated *cta*DIIβ-mut genes were transferred into *P. denitrificans* cells by triparental conjugation ("Triple mating", Gerhus *et al.*, 1990). 2 mL o.n. cultures of the *P. denitrificans* AO1 (Rif^r, Kan^r); *E. coli* DH5α cells carrying the expression plasmid (Sm^r); and the *E. coli* RP4-4 helper strain (Amp^r) were harvested by centrifugation. Cells were resuspended in 500 μL LB medium each. Cells were mixed in a ratio of 1:1:3 (100 μL : 100 μL : 300 μL; *E. coli* DH5α : *E. coli*. RP4-4 : *P. denitrificans* AO1), centrifuged, resuspended in 100 μL LB medium, and plated on an agar plate and incubated at 32°C o.n.. The cell drop was scratched from the plate and resuspended in 1 mL LB medium. Cells were diluted to different concentrations (1:2; 1:4; 1:8 and 1:16) and plated on agar plates containing rifampicin, streptomycin and kanamycin.

2.7.5 Preparation of membranes from *P. denitrificans*

Both *P. denitrificans* native or mutated cells (chapter 2.3) grew in succinate medium in presence (+ Mn) or in absence of manganese (- Mn) for EPR sample preparation. Recombinant cells grew in the presence of the specific antibiotic (Sm, Kan). Cells were harvested by centrifugation (10000 g, JLA-8000 rotor, 6500 rpm, 4°C), resuspended using a chloride-free buffer (200 mM KP_i, 1 mM EDTA, pH 8, Pefabloc, DNase) and broken applying six cycles at the microfluidizer (ice cold, 1200 bar). Broken cells were centrifuged (SLA rotor, 5000 rpm, 45 min, 4°C) to remove unbroken cells. Membranes were prepared by ultracentrifugation (100000 g, 45Ti rotor, 42000 rpm, 4°C, 4 h or o.n.) and resuspended in 50 mM KP_i, 1 mM EDTA, pH 8 (chloride-free) or in 20 mM Tris-Cl, 100 mM NaCl, 1 mM EDTA, pH 8.

2.8 Biochemical methods

2.8.1 Protein purification

P. denitrificans membranes (~ 20 mg membrane protein / mL) were solubilised using ~ 3 % (w/v) LM in a chloride-free buffer (50 mM KP_i, 1 mM EDTA, pH 8, 0.25 mg/mL pefabloc, 0.02 mg/mL avidin) at 4°C for 12 min. The solubilisate was mixed in a ratio of 2:3 with prepared strep-tagged Fv fragments 7E2 (*E. coli* periplasm in 35 mM KP_i, 500 mM sucrose, 1 mM EDTA, pH 8) at 4°C for 12 min resulting in a final concentration of ~ 2 % (w/v) LM after dilution (Kleymann *et al.*, 1995), ultracentrifuged 1 h at 100000 g (70Ti rotor, 60000 rpm, 4°C), the supernatant was sterile filtrated (0.45 μM) and then applied to a streptavidin column equilibrated in 50 mM KP_i, 1 mM EDTA, pH 8, 0.05 % LM at 4°C. The column was washed using the same the buffer and the protein eluted with buffer containing 2.5 mM desthiobiotin. The eluted C*c*O was concentrated to 200 µM at 4°C using Centriprep, 50 kDa and then reduced with stoichiometric amouts of dithionite and reoxidised using the final air-containing 10 mM KP_i, 0.2 mM EDTA, pH 8, 0.01 % LM buffer (termed "pulsing"). The yield of the preparative purification was ~ 0.5 – 1.0 mg C*c*O per L cell culture.
The preparation of the two-subunit C*c*O was more detailed. *P. denitrificans* membranes (~ 20 mg membrane protein / mL) were solubilised using ~ 3 % (w/v) LM in 20 mM Tris-Cl, 100 mM NaCl, 1 mM EDTA, pH 8, 0.25 mg/mL pefabloc, 0.02 mg/mL avidin at 4°C for 12 min. The solubilisate was mixed 2:3 with strep-tagged Fv fragments 7E2 (*E. coli* periplasm in 100 mM Tris-Cl, 1 mM EDTA, 500 mM sucrose, pH 8) at 4°C for 12 min resulting in a final concentration of ~ 2 % (w/v) LM after dilution and ultracentrifuged 1 h at 100000 g (70Ti rotor, 60000 rpm, 4°C). The equilibration buffer of streptavidin column was 20 mM Tris-Cl, 100 mM NaCl, 1 mM EDTA, pH 8, 0.05 % LM at 4°C, the protein sample was bound and then the buffer was exchanged to 50 mM KP_i, pH 8, 1 mM EDTA, pH 5, 0.05 % LM at 4°C. The elution agent was 5 mM lipoic acid at a low pH at 4°C (100 mM KP_i,1 mM EDTA, pH 6). The pH of the eluate was increased to pH 7.2 by titration of 1 M K_2HPO_4 to the sample. 1.5 % (v/v) LDAO was added resulting in the removal of SU III and IV and solution was incubated on ice for 30 min. After dilution of the sample with 40 mL H_2O containing 0.08 % LDAO, C*c*O was loaded onto a Q sepharose for buffer exchange using 10 mM Tris-Cl, 20 mM NaCl, pH 8, 0.08 % LDAO, 4°C. The elution buffer was 10 mM Tris-Cl, 600 mM NaCl, pH 8, 0.08 % LDAO at 4°C. The detergent was exchanged to UM (for crystallisation) or LM (for functional experiments). The eluted C*c*O was concentrated to 200 µM at 4°C using a Centriprep, 50 kDa.

2.8.2 Production of the Fv fragment 7E2

Fv fragments 7E2 were expressed in *E. coli* cells after the induction using IPTG (Kleymann *et al.*, 1995). 4 x 200 mL LB medium were inoculated each with 50 µL cryo-stock culture of the *E. coli* strain JM 83 carrying the plasmid pASK68 (Amp^r). Cells were incubated shaking at 30°C o.n.. 12 x 2 L LB-medium was inoculated each using 50 mL *E. coli* culture and grown to an OD_{550nm} of 0.5. Induction was started by addition of 0.5 mM IPTG. Cells were harvested by centrifugation (10000 g, JLA-8000 rotor, 6500 rpm, 4°C) and periplasm was prepared by an osmotic schock. Cells were resuspended in 200 mL buffer (35 mM KP_i, 500 mM sucrose, 1 mM EDTA, pH 8, 4°C (chloride-free) or in standard buffer 100 mM Tris-Cl, 1 mM EDTA, 500 mM sucrose, pH 8, 4°C) and incubated on ice for 30 min. Cells were centrifuged two times (GSA rotor, 12000 rpm, 30 min, 4°C) and 30 mL-aliquots of the supernatant (periplasm) were stored at -20°C.

2.8.3 Activity assays

2.8.3.1 Cytochrome *c* oxidation assay

Cyt *c* (horse heart, Sigma) was dissolved to a high concentration (4 - 8 mM) in 200 µL 30 mM KP_i, pH 7 and an excess of dithionite was used for reduction. Excess dithionite was removed from reduced cyt *c* by gel filtration at 4°C (PD10 column). The concentration of the resulting reduced cyt *c* solution was determined by difference absorption spectroscopy ($\varepsilon_{redox550nm}$ = 18.7 $M^{-1}cm^{-1}$) and adjusted to 40 µM in the reaction buffer (in 30 mM KP_i, pH 7, + 0.05 % LM). To 1 mL reaction buffer 100 pM C*c*O (final concentration) were added and the decrease of the absorption at λ = 550 nm was recorded at RT for 3 mins.

2.8.3.2 Oxygen determination using an oxygen electrode

5 pmol of C*c*O in a volume of 20 µL was mixed with 980 µL of 30 mM KP_i, pH 7.5, 0.1 % (w/v) LM, 1 mg/mL asolectin, 3 mM ascorbate, 0.6 mM TMPD) and placed in the chamber of the Pt-Ag/AgCl based Clark-Type oxygen electrode temperatured at 10°C. After recording the baseline for 5 mins, the reaction was started by addition of 40 µM oxidised cyt *c*. The reaction was followed by the decrease of the dioxygen concentration for 15 min.

2.8.4 Preparative *suicide inactivation* and repurification

Suicide inactivation was induced by addition of excess reduced cyt *c* to the two-subunit C*c*O. The enzyme became inactive during multiple turnovers. The two-subunit C*c*O mixed with oxidised cyt *c* was used as the positive control.

Positive control: The mixture of **oxidised** cyt *c* and 2 SU-wt rec C*c*O in 30 mM KP_i, pH 7.3, 0.08 % UM was incubated at 4°C for 3 h and for repurification anion exchange chromatography of *active* (positive control) 2 SU-wt rec C*c*O sample was performed using Q sepharose. 2 SU-wt rec C*c*O was further purified by gel filtration using a TSK 3000 column (10 mM Tris-Cl, 20 mM NaCl, pH 7.3, 0.08 % UM).

Suicide inactivation: The mixture of **reduced** cyt *c* and 2 SU-wt rec C*c*O in 30 mM KP_i, pH 7.5, 3 mM ascorbate, 0.6 mM TMPD and 0.08 % UM was incubated at 4°C for 3 h. The enzyme was further purified in the same way as the *active* 2 SU-wt rec C*c*O.

2.8.5 Proton pumping experiments

2.8.5.1 Preparation of proteoliposomes

Proteoliposomes were prepared using the cholate dialysis method (Darley-Usmar, 1987). Asolectin and cholate were prepared as described (Pfitzner *et al.*, 2000). Anion exchange chromatography was used for reduction of the detergent concentration of purified C*c*O. The Q sepharose column was equilibrated with 10 mM HEPES, 50 mM KCl, pH 7.3, 0.015 % LM in the cold room and then C*c*O was loaded onto the column. The protein sample was washed using equilibration buffer and eluted with 10 mM HEPES, 500 mM KCl, pH 7.3, 0.015 % LM. C*c*O was concentrated to 200 μM using a Centriprep (50 kDa) at 4°C.
Purified asolectin (40 mg/mL) and 2 % recrystallised cholate were dissolved in 100 mM HEPES, pH 7.3 and sonified at 4°C (Branson Sonifier II 250, 10 x 30 s, 50 % duty cycle) until the solution became clear indicating dissolved/solubilised lipid. The solution was centrifuged at 5000 g at 4°C for 15 min to remove aggregates. C*c*O was added to the supernantant in a final concentration of 4 μM. The proteoliposomes were dialysed against 100 mM HEPES, pH 7.3 (V x 200) for 4 - 12 h, against 10 mM HEPES, pH 7.3, 50 mM KCl, 50 mM sucrose (V x 200) for 2 x 12 h and against "buffer-free" 50 μM HEPES, pH 7.3, 55 mM KCl, 55 mM sucrose (V x 500) for 2 x 12 h.

2.8.5.2 Respiration control of proteoliposomes

The C*c*O activity (chapter 2.8.3.1 in absence of LM) was recorded using the proteoliposomes instead of solubilised C*c*O. 5 μL proteoliposome suspension were added to 1 mL 40 μM reduced cyt *c* in 30 mM KP_i, pH 7 without or in presence of 5 μM valinomycin and 10 μM CCCP.
Valinomycin is a K^+ ionophor and CCCP is an H^+ uncoupler. The ratio of the slopes of both traces provides the Respiration Control Ratio (rcr). Uncoupled proteoliposomes show an increased activity compared to coupled proteoliposomes which show an rcr up to 8 - 9.

2.8.5.3 Stopped flow apparatus

Phenolred is a pH indicator used for proton pumping experiments. pH changes were recorded at λ = 555.4 nm (isosbestic point of cyt *c*). Both syringes were filled with 2 mL unbuffered solutions of proteoliposomes or reduced cyt *c* (in the last dialysis buffer); both pHs were adjusted to 7.30. In the experiment 400 nM C*c*O incorporated into liposomes plus 10 μM valinomycin and 60 μM

phenolred at pH 7.30 were mixed in the ratio (v/v) 1:1 with the 40 μM reduced cyt *c* at pH 7.30 and the change of the absorption was recorded at λ = 555.4 nm for 2 s. Then 0.4 μM CCCP was added to the same C*c*O sample and again mixed 1:1 with the 40 μM reduced cyt *c* solution and the kinetic was recorded for 2 s.

2.8.6 Spectroscopic measurements

2.8.6.1 UV-vis spectroscopy

The concentration of C*c*O was detrmined using UV-vis spectroscopy ($\varepsilon_{ox425nm}$ = 158 mM^{-1} cm^{-1}). Redox difference absorption spectra were recorded using air/ferricyanide oxidised and dithionite reduced C*c*O samples ($\varepsilon_{redox606-630nm}$ = 25.7 mM^{-1} cm^{-1}). Some of the isolated variant C*c*Os were found to be partly reduced after isolation. These variants were oxidised with ferricyanide at 4°C o.n. and applied to gel filtration chromatography (PD10, 10 mM KP_i, 1 mM EDTA, pH 8).

Difference absorption spectra of C*c*O in the $\mathbf{P_H/F^{\bullet}_H}$ state and $\mathbf{F_H}$ state intermediates (*minus* the **O** state) were recorded after addition of equimolar, low or excess amounts of H_2O_2 (ε_{240nm} = 40 M^{-1} cm^{-1}). 10 μM pulsed and air oxidised C*c*O samples in 50 mM KP_i, pH 9, 0.05 % LM for the $\mathbf{P_H}$ state or 50 mM Mes-OH, pH 6, 0.05 % LM for the $\mathbf{F^{\bullet}_H}$ state were mixed with H_2O_2 in a molar ratio of 1: 2 or 1:5 and incubated for 3 min.

For formation of the $\mathbf{F_H}$ state 10 μM of pulsed and air oxidised C*c*O in 50 mM KP_i, pH 9, 0.05 % LM were mixed with H_2O_2 in a molar ratio of 1:500 and incubated for 3 min.

The $\mathbf{P_{CO}}$ state was induced by short bubbling of CO through 10 μM C*c*O in 50 mM KP_i, pH 9, 0.05 % LM aerobically.

Difference absorption spectra of the $\mathbf{P_{10}}$ state intermediate were recorded after shifting the pH from 8 to 10. 10 μM of pulsed and air oxidised C*c*O samples in 10 mM KP_i, pH 8, 0.05 % LM were mixed with 100 mM glycine-OH, pH 10 and incubated for 30 min.

pH shifts were induced by addition of 100 mM Mes-OH, pH 6 or 100 mM K_2HPO_4.

2.8.6.2 EPR spectroscopy

EPR spectra of the $\mathbf{P_H/F^{\bullet}_H}$ state and $\mathbf{F_H}$ state intermediates were recorded after induction of the intermediates using H_2O_2 in molar ratios. 200 μM of pulsed and air oxidised C*c*O samples in 50 mM KP_i, pH 9, 0.05 % LM ($\mathbf{P_H}$ state) or 50 mM Mes-OH, pH 6, 0.05 % LM ($\mathbf{F^{\bullet}_H}$ state) were mixed with H_2O_2 in a molar ratio of 1:1. For formation of the **F** state C*c*O in 50 mM KP_i, pH 9, 0.05 % LM was mixed with H_2O_2 in a ratio of 1:500. EPR spectra of the $\mathbf{P_{10}}$ state intermediate were recorded

after pH 10 buffer incubation. 200 μM of pulsed and air oxidised C*c*O samples in 10 mM KP_i, pH 8, 0.05 % LM were mixed with 100 mM glycine-OH, pH 10.

2.8.7 Matrix assisted laser induced desorption/ionisation mass spectrometry

SDS-PAGE separated polypeptides were Coomassie-stained and the bands were excised in 1 mm^2 pieces, placed into Eppendorf tubes and incubated two times with 100 mM $(NH_4)_2CO_3$, 50 % acetonitrile at 37°C for 45 min. The gel pieces were dried in 100 μL acetonitrile and soaked with 20 mg/mL trypsin at 37°C o.n.. The supernatant (1. extraction) and the acetonitrile extracts (2. extraction) were mixed for analysis. Peptides were dissolved in 5 μL of 70 % acetonitrile and 0.1 % trifluoric acid. MALDI-TOF/TOF spectra of *active* and *suicide inactivated* C*c*O were recorded and the calibration was performed using trypsin autoproteolysis peptides (Peptide calibration standard, Bruker). The masses of the monoisotopic peaks were searched on the Mascot peptide fingerprint data base (Mascot).

3 RESULTS

3.1 Differences of native and homologously produced wild type cytochrome *c* oxidases from *P. denitrificans*

In order to study the function and structure of C*c*O in detail, sufficient amounts of the protein have to be produced. The structures and functional properties of native wild type C*c*O and homologously produced variants of C*c*O (mutated C*c*Os) were determined in previous experiments, however, the results have never been compared to a homologously produced recombinant wild type C*c*O. The first aims of this work then were 1) the purification of the native wild type C*c*O obtained using the *P. denitrificans strain* ATCC 13543 (wt ATCC C*c*O) and 2) the production and purification of the homologously produced recombinant wild type C*c*O (wt rec C*c*O) using the *P. denitrificans* AO1 deletion strain (kindly provided by Prof. Ludwig, JWG University of Frankfurt). Both wild type C*c*Os had to be characterised and compared in their biochemical properties, because their production processes were different.

The wt ATCC C*c*O was purified from n-dodecyl-β-D-maltopyranoside (β-LM)-solubilised native membranes by affinity chromatography using the Fv fragment 7E2.

For cloning of the wt rec C*c*O, the gene of subunit Iβ was removed from the plasmid pUP6 using restriction enzymes and the resulting fragment cloned into the expression vector pUP39 (Figure 2.7-1). The expression plasmid pUP39-wt-*cta*DIIβ was transferred from *E. coli* DH5α cells into the *P. denitrificans* AO1 deletion strain by conjugation. In this expression system an overexpressed wt rec C*c*O was produced which does not contain an affinity tag and wt rec C*c*O has also been purified from β-LM-solubilised membranes by affinity chromatography using the Fv fragment 7E2.

The solubilisation of membranes using the detergent β-LM extracts the four-subunit C*c*O. However, further purification of the enzyme with N-N-dimethyldodecylamine-N-oxide (LDAO) reduces this to the two-subunit C*c*O, which is comprised of the *core subunits* I and II. In order to differentiate these different C*c*Os it is important to characterise the β-LM-purified four-subunit C*c*Os (4 SU-wt C*c*O) and the LDAO treated two-subunit C*c*Os (2 SU-wt C*c*O).

In this chapter, the structural and functional characterisation of homologously produced recombinant wild type C*c*O (4 SU-wt rec C*c*O), the native wild type C*c*O (4 SU-wt ATCC C*c*O) and their two-subunit forms (2 SU-wt rec C*c*O and 2 SU-wt ATCC C*c*O) is presented.

3.1.1 Purification of differently produced wild type cytochrome *c* oxidases

In order to determine the purity and the subunit composition of the differently produced wt C*c*Os, SDS-PAGE analyses were performed after their purification. The purification of the 4 SU-wt ATCC C*c*O yielded roughly 0.5 mg C*c*O per liter cell culture and the purification of the 4 SU-wt rec C*c*O gave a yield of roughly 1.0 – 1.5 mg C*c*O per litre cell culture (data not shown), indicating the successful overproduction of the 4 SU-wt rec C*c*O.

SDS-PAGE analysis is a qualitative method used to analyse the efficiency of protein purification, and to provide information about the ratio of the produced subunits of the C*c*Os. The subunit composition of the 4 SU-wt ATCC C*c*O and the 4 SU-wt rec C*c*O as well as for the 2 SU-wt ATCC C*c*O were obtained using this method. To compare the subunit composition of the 4 SU-forms, especially the presence and the amount of subunit III, an SDS-PAGE gel was run until the migration of subunits II and III was sufficient to separate both efficiently and then the gel was silver-stained. In order to check the lack of subunit III in the 2 SU-wt ATCC C*c*O a standard SDS-PAGE gel of the 4 SU- and 2 SU-wt ATCC C*c*O was run and then this gel was Coomassie-stained.

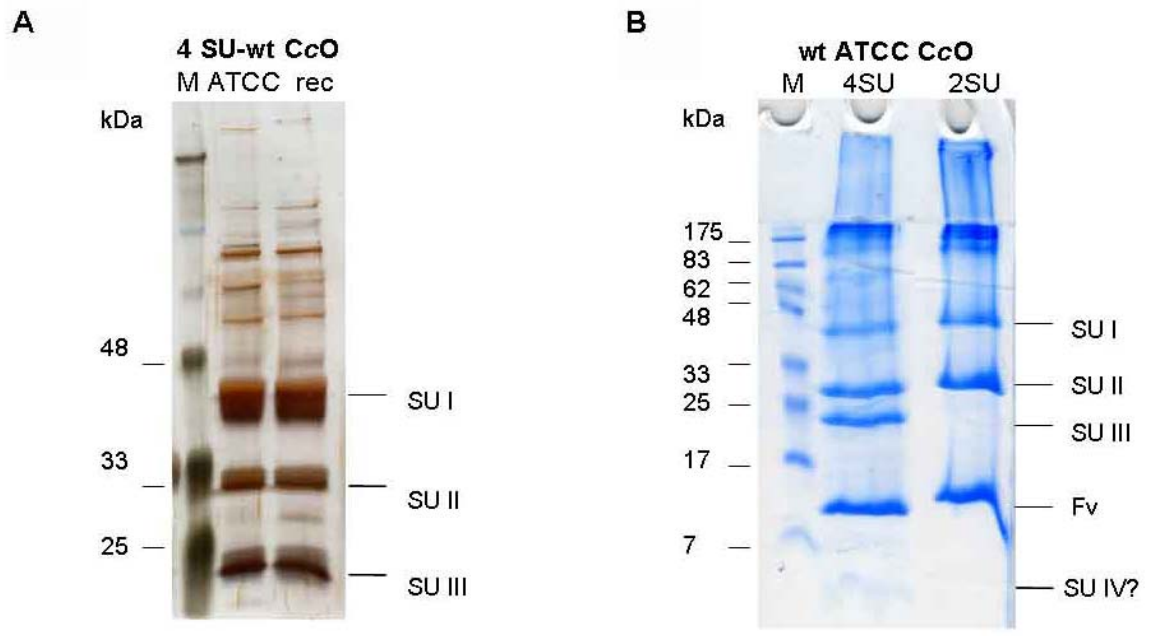

Figure 3.1-1 12 % SDS-PAGE gels of 4 SU-wt ATCC C*c*O, 2 SU-wt ATCC C*c*O and 4 SU-wt rec C*c*O. (A) Silver-stained 4 SU-wt ATCC C*c*O and 4 SU-wt rec C*c*O. (B) Coomassie-stained 4 SU-wt ATCC C*c*O and 2 SU-wt ATCC C*c*O. Marker (M)

The silver-stained SDS-PAGE gel shows bands of the subunits from the purified 4 SU-wt ATCC C*c*O and the 4 SU-wt rec C*c*O (Figure 3.1-1 A) and displays for both versions of wt C*c*Os three (SU I – III) of the four subunits. The single bands of the subunits show the same appearance and the same relative intensity for both the 4 SU-wt ATCC C*c*O and 4 SU-wt rec C*c*O, which suggests identical protein composition for both types of C*c*Os. Some protein impurities, which possess higher molecular masses, are observed in addition to subunits of wt C*c*Os in the SDS-PAGE gel.
The purification protocol for the 2 SU-wt ATCC C*c*O includes additional chromatographic steps for the removal of subunits III and IV. In Figure 3.1-1 B the Coomassie-stained 2 SU-wt ATCC C*c*O lacks the band of subunit III, while the bound Fv fragment is detected in both 4 SU-wt ATCC C*c*O and in 2 SU-wt ATCC C*c*O. Subunit IV of 4 SU-wt ATCC C*c*O is hardly observed in this SDS-PAGE gel, because of the small signal and the lack of stainable amino acids in subunit IV. The same result was obtained for the 2 SU-wt rec C*c*O (data not shown).
In summary, from SDS-PAGE gels the ratio of subunits appears not to differ between native 4 SU-wt ATCC C*c*O and the recombinant overexpressed and overproduced 4 SU-wt rec C*c*O, and the 2 SU-wt ATCC C*c*O has been identified by the lack of subunit III. The determination of the subunit composition alone is not able to identify functional differences, however activity assays might provide information about the functional differences in the native and recombinant enzymes.

3.1.2 Activity assays

In order to obtain information about the functional quality of the purified wt C*c*Os enzymatic activity assays have been employed using different substrates of C*c*O. The measured turnover activity of C*c*O provides the proof for its functional integrity and its catalytic ability to reduce dioxygen to water. In C*c*O activity assays, the concentration decrease of two substrates, reduced cyt *c* and dioxygen, was followed as a function of time using a spectrophotometer or an oxygen electrode. Cyt *c* oxidation was followed by recording the decrease of the absorption at λ = 550 nm (the extinction coefficient for cyt *c* oxidation is $\varepsilon_{redox550nm}$ = 18.7 mM^{-1} cm^{-1}) and the consumption of dioxygen was determined using the Clark-type oxygen electrode. The activity of *P. denitrificans* C*c*O is mainly expressed in electrons per second and reveals a general turnover of 600 electrons per second at RT (Witt *et al.*, 1998). However, the enzymatic activity of C*c*O depends strongly on the buffer conditions used. Thus, distinct parameters such as pH; ionic strength; detergents; lipids and dioxygen supplementation result in different turnover numbers.

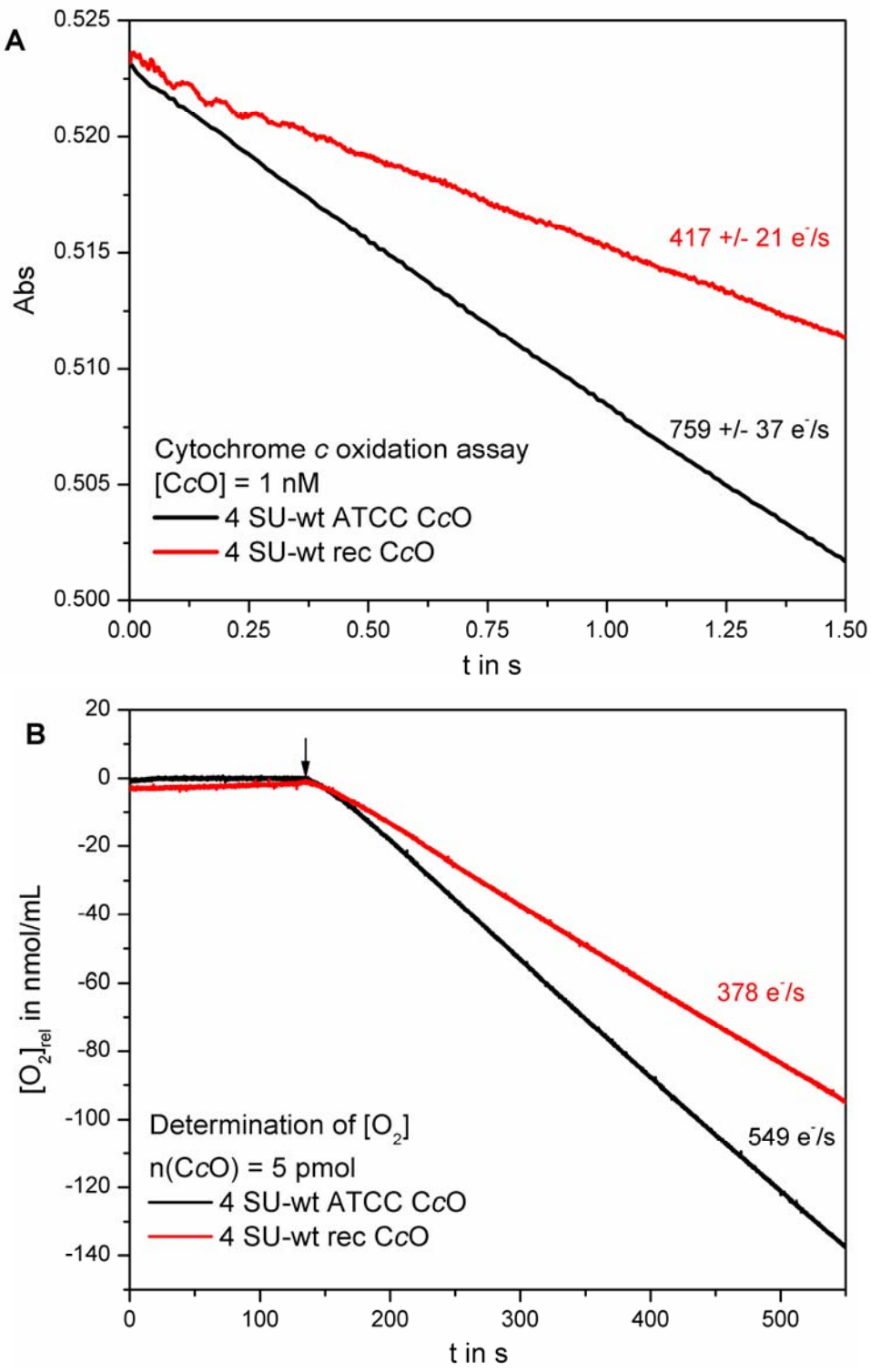

Figure 3.1-2 Cyt *c* oxidation activity and dioxygen consumption activity of 4 SU-wt ATCC C*c*O (black) and 4 SU-wt rec C*c*O (red). (A) Stopped flow experiment monitoring cyt *c* oxidation. Final 30 μM reduced cyt *c* in 30 mM KP_i, pH 7, 0.05 % LM were mixed with a final concentration of 1 nM C*c*O at RT. (B) Consumption of dioxygen recorded using an oxygen electrode. 5 pmol C*c*O, 0.6 mM TMPD, 3 mM ascorbate in 1 mL 30 mM KP_i, pH 7.3, 0.1 % LM, 1 mg/mL asolectin were mixed at 10°C. The arrow indicates the addition of cyt *c* to the final concentration of 40 μM.

Cyt *c* oxidation and dioxygen consumption assays confirm activity for the 4 SU-wt ATCC C*c*O and for the 4 SU-wt rec C*c*O, however the latter showed a decreased turnover number in both assays (see Figure 3.1-2 A and B). The activity of the 4 SU-wt rec C*c*O (red curve) showed a turnover of 417 +/- 21 e^-/s in the cyt *c* oxidation assay, but the 4 SU-wt ATCC C*c*O (black curve) performs the cyt *c* oxidation with an increased activity of 759 +/- 37 e^-/s (Figure 3.1-2 A). In another experimental setup, the dioxygen consumption assay, the 4 SU-wt rec C*c*O (red curve) displays a turnover activity of only 378 e^-/s and the 4 SU-wt ATCC C*c*O (black curve) presents a higher turnover number of 549 e^-/s (Figure 3.1-2 B). Both activity assays show that 4 SU-wt rec *CcO* displays roughly 60 % of the 4 SU-wt ATCC C*c*O activity. The enzymatic activity of the recombinantly produced protein is severly reduced compared to the native form and this result provides the first indication that the 4 SU-wt rec C*c*O shows an impaired function. The reason for the decreased activity might lie in incorrectly assembled recombinant C*c*Os or the decreased insertion of redox-active metals into 4 SU-wt rec C*c*O. However, protein concentrations of the 4 SU-wt ATCC C*c*O and the 4 SU-wt rec C*c*O both were equally determined by the haem absorption in the Soret region (ε_{425nm} = 158 mM^{-1} cm^{-1}), which should have led to comparable amounts of fully active protein in the activity assays. Additionally, the ratio of λ = 280 nm to λ = 425 nm (bulk protein : haem *a*) was determined for both wt C*c*Os and showed identical results (data not shown), indicating the accurate ratio of bulk protein to the prosthetic group haem *a*. The protein environment of prosthetic groups is important for the redox potential of their metal centres and thus for the functional properties of the whole enzyme. The recombinantly produced 4 SU-wt rec C*c*O might show non-functional insertion of the prosthetic groups as the cause for its reduced functionality, because the SDS-PAGE analysis has demonstrated the presence of all proteinous *core subunits*.

3.1.3 UV-vis spectroscopy – reduced *minus* oxidised difference absorption spectra

To investigate whether the haem A prosthetic groups, which are chromophores, have been correctly inserted, the haem groups were characterised by (UV)-vis spectroscopy. The absorbance gives information about the protein environment of the haem groups and thus provides hints for the accurate insertion of these particular groups into subunit I of C*c*O. C*c*O is a green coloured protein and as a haem-containing cytochrome it shows distinct maxima, which are characterised by the type of the bound haem groups. The absorption spectrum of C*c*O is dominated by the haem groups, because the Cu-centres or the other bound metal ions hardly contribute to the spectral properties. The absorption spectra from λ = 380 to 650 nm of the air-oxidised and the dithionite-reduced wt C*c*Os were recorded using a spectrophotometer. The

spectra of the 4 SU-wt ATCC C*c*O and the 4 SU-wt rec C*c*O are similar in the Soret- and α-region (Figure 3.1-3). However, there are shifts in the Soret maximum of the oxidised samples.

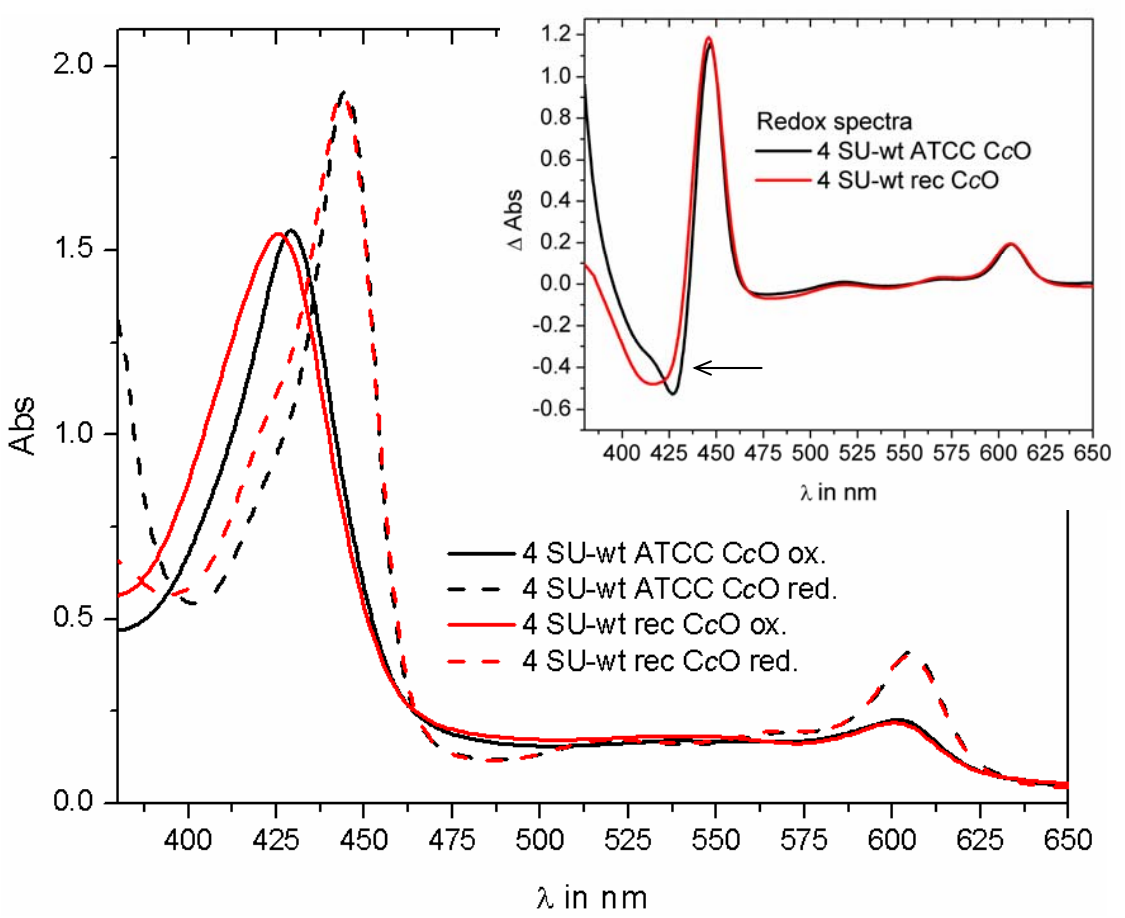

Figure 3.1-3 Absorption spectra of differently produced wt C*c*Os from λ = 380 to 650 nm. Each C*c*O spectrum is normalised to a concentration of 10 μM ($\varepsilon_{redox606-630nm}$ = 25.7 $mM^{-1}cm^{-1}$). 4 SU-wt ATCC C*c*O is shown in black, 4 SU-wt rec C*c*O in red. Spectra show the air-oxidised (ox.) samples (—) or the dithionite-reduced (red.) samples (- - -). The inset shows the reduced *minus* oxidised difference absorption spectra; the arrow indicates the Soret minimum of 4 SU-wt ATCC C*c*O.

The Soret maximum of the 4 SU-wt rec C*c*O (Figure 3.1-3, red straight line) is blue shifted against the 4 SU-wt ATCC C*c*O (Figure 3.1-3, black straight line) from λ = 427 nm to 425 nm indicating differences in the environment of haem *a*. The minimum of the Soret region in the reduced *minus* oxidised difference absorption (redox) spectrum (Figure 3.1-3 inset) shows that the 4 SU-wt ATCC C*c*O contains two distinct absorption fractions in this area (see black arrow). These two individual absorptions are smeared into one broad minimum in the redox difference absorption spectrum of the 4 SU-wt rec C*c*O. Accordingly, spectra of the 2 SU-forms of the wt C*c*Os showed similar results as for the respective 4 SU-wt C*c*Os (data not shown).

In summary, the redox spectra of the two differently produced wt C*c*Os provide indications for their functional inhomogeneity. The 4 SU-wt rec C*c*O might have changes in the H-bond network

around the haem A groups and thus the role of the haem groups, especially in the controlled electron transfer, may be impaired by shifts of their reduction potential.

3.1.4 Total X-ray reflection fluorescence – metal analysis

In order to analyse, next to the haem A groups, the role of the other redox-active metals, the Cu_A centre and Cu_B centre, the metal content of the 4 SU-wt ATCC C*c*O and the 4 SU-wt rec C*c*O was determined by TXRF. C*c*O is a metalloprotein and it binds several metal ions such as the iron ions of the haem groups, copper ions, magnesium/manganese ions and calcium ions. However, the haem groups dominate the visible absorption properties of the enzyme (chapter 3.1.3). TXRF measurements were performed (Claudia Rittmeyer, JWG University of Frankfurt) in order to determine the copper content, because either the two functional Cu_A ions or the functional Cu_B ion might be lost in the recombinantly produced 4 SU-wt rec C*c*O. Special copper chaperones might not have inserted these Cu ions successfully, resulting in mis-assembled inactive C*c*O. In addition to Fe and Cu, TXRF can also detect other important metals and elements such as S and Zn. The resulting values of the TXRF data are normalised to the sulphur (S) concentration of the wt C*c*Os using the information that one C*c*O + Fv frament contains 68 S (Table 3.1-1 A). The bar diagram of Figure 3.1-4 shows the TXRF results (Table 3.1-1 B) of the wt C*c*O samples, the 4 SU-wt ATCC C*c*O is shown in grey bars and the 4 SU-wt rec C*c*O in red bars.

Table 3.1-1 (A) Sulphur content of wt C*c*O plus Fv fragment 7E2.

C*c*O	**SU I**	**SU II**	**SU III**	**SU IV**	**Fv**
Cys	4	4	2	0	4
Met	30	8	10	2	4

= 68 S/C*c*O-Fv

Table 3.1-2 (B) TXRF data of 4 SU-wt ATCC C*c*O and 4 SU-rec C*c*O normalised to 68 S.

	4 SU-wt ATCC C*c*O	**4 SU-wt rec C*c*O**
C*c*O	1 +/- 0.02	1 +/- 0.02
S	68.0	68.0
Fe	2.3 +/- 0.1	2.1 +/- 0.1
Cu	2.9 +/- 0.0	3.0 +/- 0.1
Zn	0.6 +/- 0.0	2.3 +/- 0.1

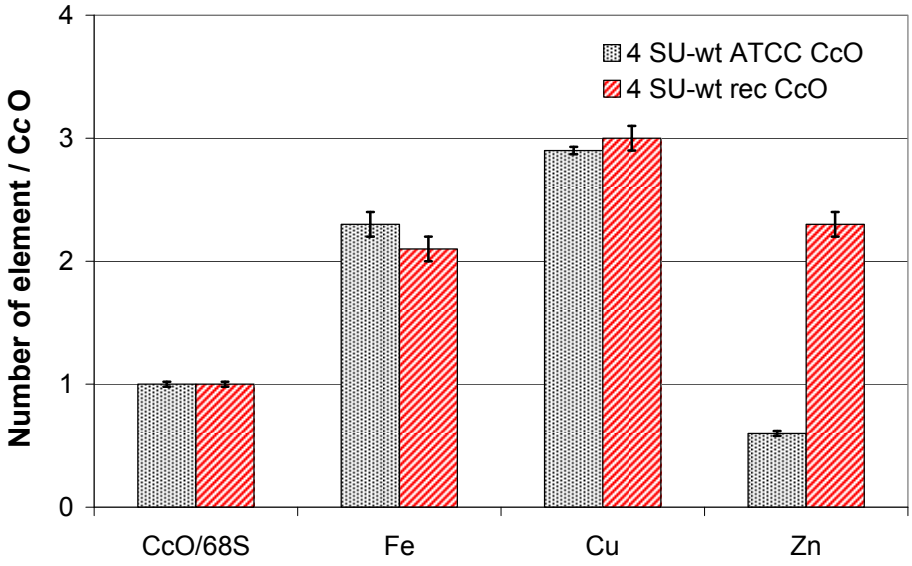

Figure 3.1-4 TXRF element analysis of 4 SU-wt ATCC C*c*O (black) and 4 SU-wt rec C*c*O (red) buffered in 50 mM Tris-Ac, pH 8, 0.05 % LM. Data are normalised to the sulphur signal.

The iron and copper contents do not show any deviations between the two differently produced wt C*c*Os. In Type A *aa*$_3$-C*c*Os the dinuclear Cu_A centre and the Cu_B centre provide in sum three copper ions and the two haem groups provide two iron ions (Fe*a* and Fea_3), and thus the copper to iron ratio of wt C*c*O is 3 Cu : 2 Fe. Both the 4 SU-wt rec C*c*O and the 4 SU-wt ATCC C*c*O show this accurate Cu : Fe ratio (Figure 3.1-4). Accordingly, there is no loss of the redox-active Cu_A or Cu_B centre in the 4 SU-wt rec C*c*O, which might have been the reason for its decreased activity.

An unexpected result was found for the Zn content. Zn^{2+} is an inhibitor of C*c*O and the standard purification buffer contains EDTA, which should remove inhibiting Zn^{2+} ions (and complex free Ca^{2+} or Mn^{2+} as well). The Zn concentration of the 4 SU-wt rec C*c*O is almost four-fold compared to the 4 SU-wt ATCC C*c*O indicating that Zn^{2+} is tightly bound by the recombinant protein (Figure 3.1-4). The bound inhibiting Zn^{2+} of the 4 SU-wt rec C*c*O might provide an explanation for the reduced activity of this enzyme.

In summary, the metal composition of both wt C*c*Os been determined: the ratio of copper to iron was 3 Cu : 2 Fe; the Zn^{2+} concentration of the 4 SU-wt rec C*c*O is very high. The increased concentration of bound inhibiting Zn^{2+} might inhibit the activity of the 4 SU-wt rec C*c*O.

3.1.5 H_2O_2-induced model intermediates

3.1.5.1 UV-vis spectroscopy

In order to analyse the general ability of the wt C*c*Os to form artificial intermediates, UV-vis and EPR spectroscopic experiments were perfomed using the 4 SU- and 2 SU-wt ATCC C*c*O and the 4 SU-wt rec C*c*O. The successful induction of H_2O_2-induced intermediates in a high yield provides indications for the functional integrity of the wt C*c*Os.

Injecting electrons into the wt C*c*O induces shifts in the Soret and α region as seen in the fully reduced (four-electron reduced) *minus* oxidised difference absorption spectrum (see Figure 1.3-1). The formation of H_2O_2-induced intermediates is an effective method for spectroscopic studies on these intermediate states of wt C*c*O (two- and three-electron reduced states), because peroxide provides dioxygen, 2 e^- and 2 H^+. Difference absorption spectra (*minus* the **O** state, ground state) reveal maxima characteristic of the particular intermediate (Figure 3.1-5). All wt C*c*O samples show H_2O_2-induced $\mathbf{P_H}$ state formation at pH 9 after addition of stoichiometric (1:1 to 1:5) amounts of H_2O_2 resulting in a 610 nm maximum ($\varepsilon_{610\text{-}635nm}$ = 11 $mM^{-1}cm^{-1}$ (Wikström and Morgan, 1992)) in the $\mathbf{P_H}$ state (*minus* the **O** state) difference absorption spectrum. However, the yield of $\mathbf{P_H}$ state formed by the 4 SU-wt rec C*c*O (Figure 3.1-5 A, red line) is decreased from ~ 40 % to ~ 15 % compared to 4 SU- and 2 SU-wt ATCC C*c*O (Figure 3.1-5 A, black and dark blue line).

The experiment results in a different difference absorption spectrum, if it is performed at pH 6. The same amount of H_2O_2 (1:1 to 1:5) creates the $\mathbf{F^{\bullet}_H}$ state having a maximum at 575 nm in the difference absorption spectrum (*minus* the **O** state) using the 4 SU-wt C*c*Os at pH 6 with a similar yield of ~ 40 % for the 4 SU-wt ATCC C*c*O (Figure 3.1-5 A, ε_{575nm} = 5.3 $mM^{-1}cm^{-1}$ (Wikström and Morgan, 1992), grey line) and only ~ 15 % for the 4 SU-wt rec C*c*O (Figure 3.1-5 A, magenta line).

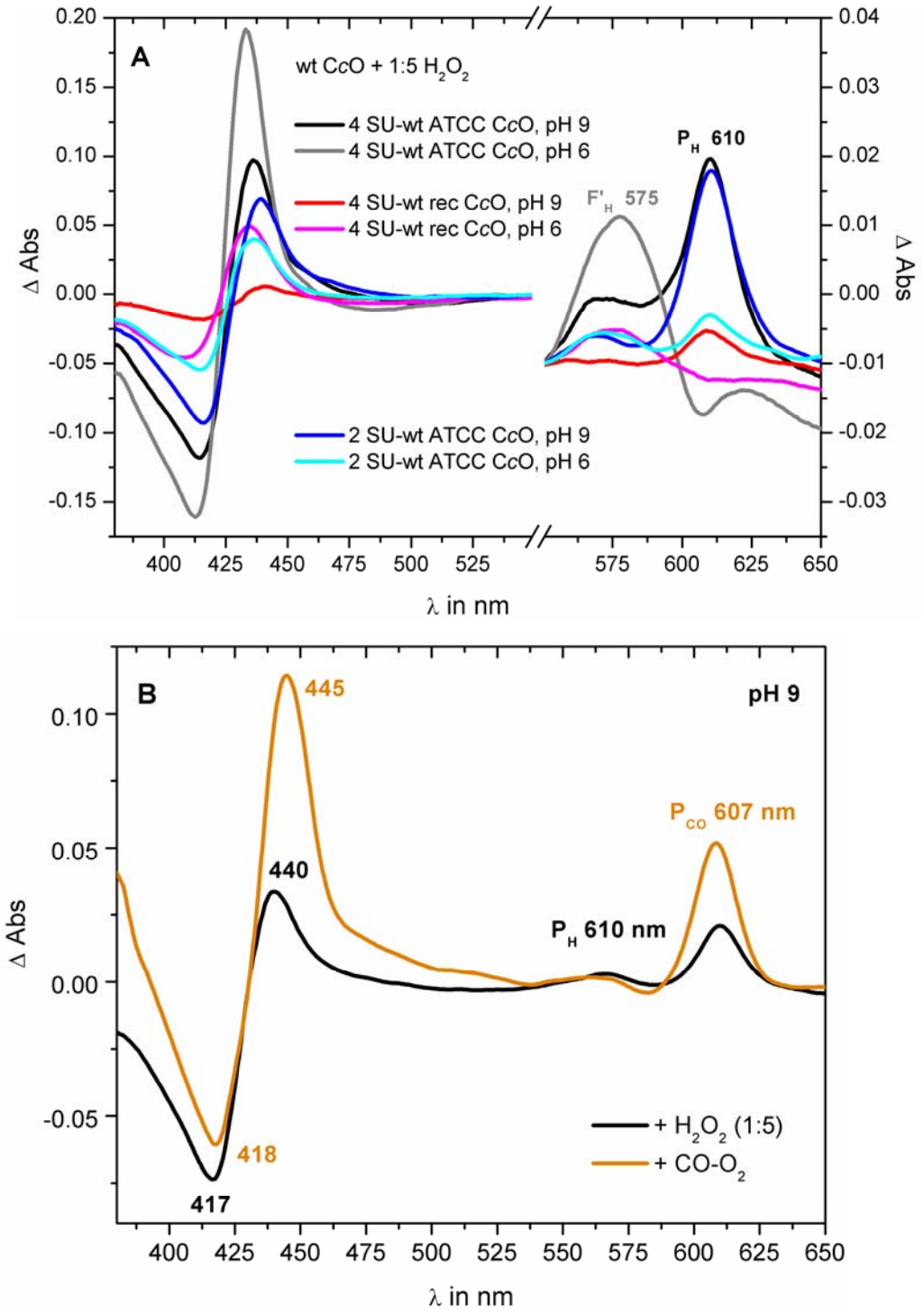

Figure 3.1-5 Difference absorption spectra of the intermediates from differently produced wt C*c*Os (*minus* the O state) in the P_H/P_{CO} states and the $F^{\bullet}_H$ state. (A) Pulsed and air oxidised C*c*O in 50 mM KP_i, pH 9, 0.05 % LM (P_H state) or 50 mM Mes-OH, pH 6, 0.05 % LM ($F^{\bullet}_H$ state) were mixed with H_2O_2 in a molar ratio of 1:5. (B) 4 SU-wt ATCC C*c*O in 50 mM KP_i, 0.05 % LM at pH 9 were mixed with a molar ratio of 1:5 H_2O_2 (black line) or treated with CO-O_2 (orange line). The spectra are normalised to 10 µM C*c*O. 2 SU-wt rec C*c*O was not determined.

The 2 SU-wt ATCC C*c*O (Figure 3.1-5 A, light blue line) does not generate the same 575 nm maximum as the 4 SU-wt ATCC C*c*O. Moreover, the 2 SU-wt ATCC C*c*O shows a yield of only ~ 15 % of the $\mathbf{F^{\bullet}_H}$ state next to an additional extra $\mathbf{P_H}$ state having a 610 nm maximum at pH 6. The 2 SU-wt ATCC C*c*O seems to have a blocked proton transfer pathway, because the $\mathbf{P_H}$ state can typically be formed at high pH only. The Soret region of all wt C*c*Os shows for each intermediate qualitatively the same spectrum, first the minima at λ = ~ 415 nm and then the maxima at λ = ~ 438 nm.
The 2 SU-wt rec C*c*O was not characterised by these type of experiments, because it was preferentially used for crystallisation trials.

The $\mathbf{O} \rightarrow \mathbf{P_H}$ state transition is induced by addition of H_2O_2 (= O_2 + 2 e^- + 2 H^+) to the wt C*c*O at pH 9, however the two electrons can also be provided by CO at high pH (CO + 2 OH^- → 2 e^- + CO_2 + H_2O). A similar **P** species, the so called $\mathbf{P_{CO}}$ state, is derived at high pH by short bubbling of CO through an O_2-saturated 4 SU-wt ATCC C*c*O solution, but the 610 nm maximum is blue shifted to 607 nm (Figure 3.1-5 B, orange line). The Soret region of both **P** species ($\mathbf{P_H}$ and $\mathbf{P_{CO}}$ state) is red shifted compared to the oxidised spectrum, however, these shifts deviate from each other significantly.
The Soret shift in the $\mathbf{P_{CO}}$ state difference absorption spectrum is red shifted as compared to the $\mathbf{P_H}$ state (Figure 3.1-5 B). In these difference absorption spectra the Soret region of the $\mathbf{P_H}$ state has a minimum at 417 nm and a maximum at 440 nm, whereas the $\mathbf{P_{CO}}$ state has a minimum at 418 nm and a maximum at 445 nm. The yield of $\mathbf{P_{CO}}$ state is increased to a value of ~ 80 % compared to the H_2O_2-induced $\mathbf{P_H}$ state having a yield of 40 %.

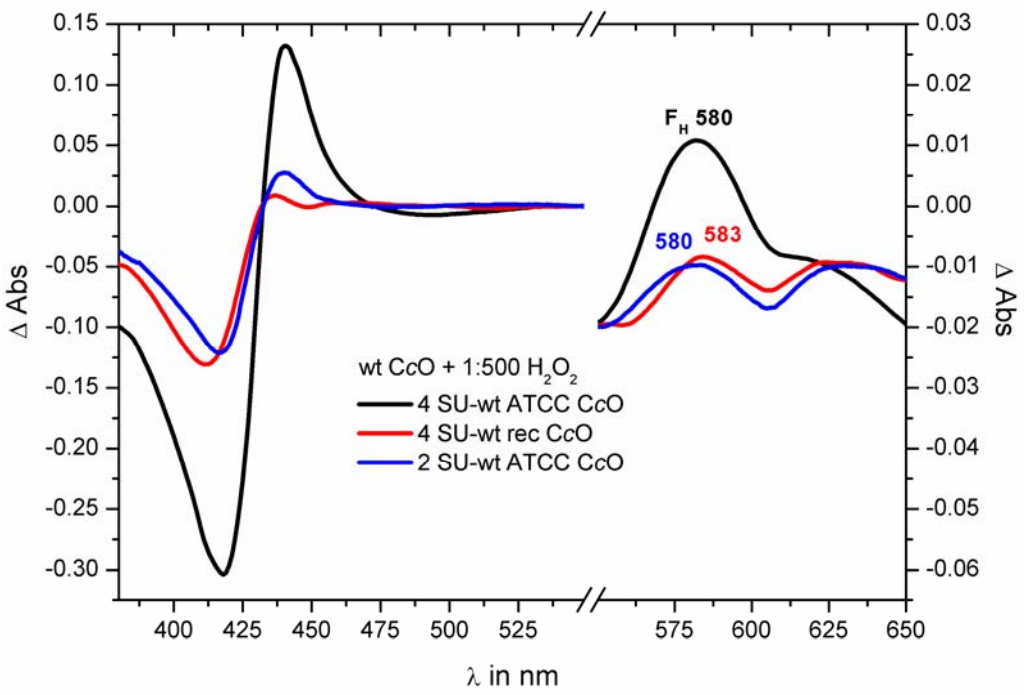

Figure 3.1-6 Difference absorption spectra of differently produced wt C*c*Os (*minus* the O state) in the F state. 10 µM of pulsed and air oxidised C*c*O in 50 mM KP_i, pH 9, 0.05 % LM were mixed with H_2O_2 in a molar ratio of 1:500. 2 SU-wt rec C*c*O was not determined.

Wt C*c*O reacts with an excess of H_2O_2 (in the range of 1:500) to form the $\mathbf{F_H}$ state resulting in a broad 580 nm maximum in the difference absorption spectrum (*minus* the **O** state) (ε_{580nm} = 5.3 $mM^{-1}cm^{-1}$ (Wikström and Morgan, 1992), Figure 3.1-6, black line). The yield of $\mathbf{F_H}$ state is highest using the 4 SU-wt ATCC C*c*O exhibiting a value of ~ 65 %. The 4 SU-wt rec C*c*O displays a different reactivity towards excess H_2O_2 (Figure 3.1-6, red line) and additionally displays a red shift of the maximum from λ = 580 nm to 583 nm and a blue shift in the Soret region. The 2 SU-wt ATCC C*c*O already demonstrated low yield forming the $\mathbf{F^{\bullet}_H}$ state, and the yield of the $\mathbf{F_H}$ state is also low, because of the required protonation step within C*c*O during the transition from the **P** state to $\mathbf{F^{\bullet}/F}$ states (Figure 3.1-6, blue line).

In summary, the native 4 SU-wt ATCC C*c*O is most usable for the induction of H_2O_2-induced intermediates. For the native C*c*O the yield of the $\mathbf{P_H}$ and $\mathbf{F^{\bullet}_H}$ state lies around 40 %. The 2 SU-wt ATCC C*c*O displays a different reactivity against H_2O_2 at pH 6 indicating a lower accessibility for protons. 4 SU-wt rec C*c*O shows, in addition to the previously determined low turnover activity (chapter 3.1.2), also a different reactivity towards H_2O_2. The CO-induced $\mathbf{P_{CO}}$ state using the native 4 SU-wt ATCC C*c*O is slightly different compared to the $\mathbf{P_H}$ state showing absorption shifts

in the difference absorption spectrum and an increased yield from 40 % to 80 %. The induced $\mathbf{F_H}$ state shows a yield of 65 % using the native 4 SU-wt ATCC C*c*O, but shows lower yields when the native 2 SU-wt ATCC C*c*O or the recombinantly produced 4 SU-wt rec C*c*O is employed for induction of this state.

3.1.5.2 EPR spectroscopy

In order to analyse the tyrosyl 167 radical signal during the $\mathbf{P_H}$ and $\mathbf{F^{\bullet}_H}$ states EPR spectroscopy was used to determine the yield of the EPR active signal. C*c*O reacts with H_2O_2 to form the $\mathbf{P_H}$ state or the electronically equal $\mathbf{F^{\bullet}_H}$ state at high or low pH, respectively. Four electrons are required for the dioxygen bond splitting, but the metals of the binuclear centre provide only three electrons. The fourth electron originates from a amino acid residue and Y167 was determined to provide this fourth electron in the $\mathbf{P_H}$ or $\mathbf{F^{\bullet}_H}$ states. The organic radical signal of the 4 SU-wt ATCC C*c*O was recorded by EPR spectroscopy in the $\mathbf{F^{\bullet}_H}$ state at pH 6 (Figure 3.1-7, **O** state black line, $\mathbf{F^{\bullet}_H}$ state red line) and the intensity of this radical signal compared to the intensity of the Cu_A signal reflects the yield of this organic radical. The 2 SU-wt ATCC C*c*O is able to reach the same yield of this organic radical as observed in its EPR spectrum (data not shown), but the 4 SU-wt rec C*c*O (blue line) shows decreased radical formation compared to the native 4 SU-/2 SU-wt ATCC C*c*Os and these ratios are similar to the yields of the intermediates as determined by UV-vis spectroscopy (chapter 3.1.5.1).

In general, the transition metal ions of the haem a_3-Cu_B binuclear centre are strongly coupled to each other and so there are only weak or no obtainable EPR resonances, and thus the binuclear centre is almost EPR silent. The EPR spectra in the region of the high-spin haem a_3 ($g \approx 6$) were compared between the 4 SU- and 2 SU-wt ATCC C*c*O (data not shown). The already small intensity of the high-spin haem a_3 in relation to the signal of low-spin haem *a* or the Cu_A signal ($g \approx 2$) is decreased in the 2 SU-wt ATCC C*c*O, which indicates a stronger coupling of the binuclear centre, if C*c*O lacks subunit III (data not shown).

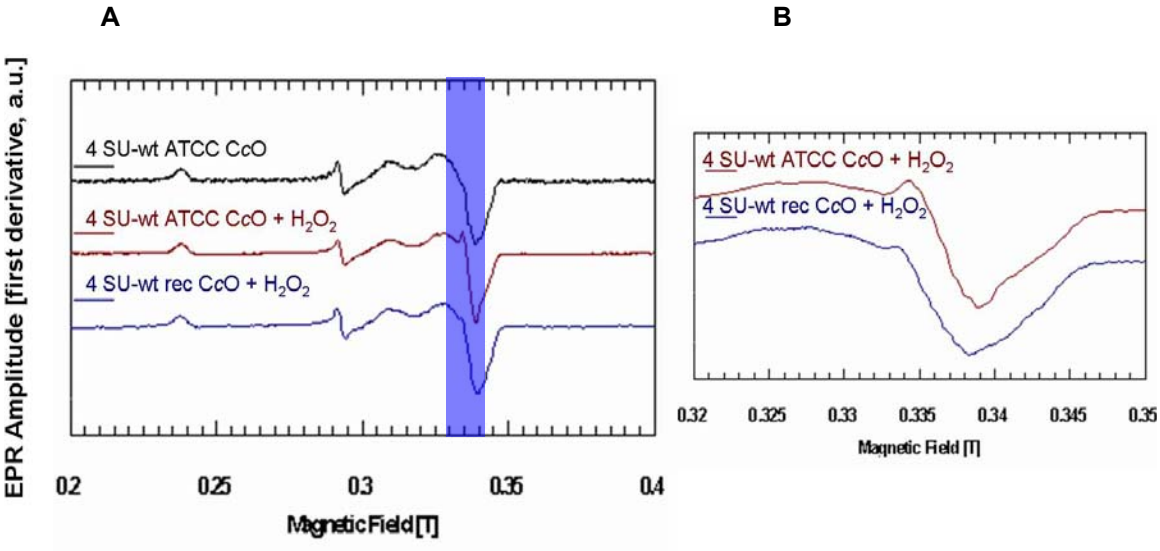

Figure 3.1-7 EPR spectra of the 4 SU-wt ATCC C*c*O and 4 SU-wt rec C*c*O. 200 µM oxidised C*c*O in 50 mM Mes-OH, pH 6, 0.05 % LM (F$^{\bullet}$ state) and 200 µM H_2O_2 were mixed at 4°C (molar ratio 1:1). The samples were transferred immediately to a suprasil quartz EPR tube, frozen in liquid nitrogen and X-Band continuous-wave EPR spectra were recorded. (A) at 10 K. (B) difference spectra (*minus* the O **state) at 20 K.**

The EPR spectrum of the CO-O_2 generated $\mathbf{P_{CO}}$ state in 4 SU- wt ATCC C*c*O at pH 9 has thus far revealed little or no induced amino-acid radical species (data not shown), although this $\mathbf{P_{CO}}$ state has a maximum at 607 nm in the (UV)-vis difference absorption spectrum (Figure 3.1-5). In fact, the data suggest that the $\mathbf{P_H}$ and $\mathbf{P_{CO}}$ states of 4 SU-wt ATCC C*c*O may not be identical, especially in terms of EPR analysis.

In summary, the native 4 SU-wt ATCC C*c*O shows the highest yield of the tyrosyl 167 radical signal during the $\mathbf{F^{\bullet}_H}$ state and the 2 SU-wt ATCC C*c*O displays a similar yield of the organic radical, indicating that the formation of the tyrosyl 167 radical might not be connected with the yield of the $\mathbf{F^{\bullet}_H}$ state as determined by UV-vis spectroscopy. The 4 SU-wt rec C*c*O displays very weak radical signals during the $\mathbf{F^{\bullet}_H}$ state. The CO-induced $\mathbf{P_{CO}}$ state shows no radical signal such as the $\mathbf{P_H}$ state, which is, next to the absorption differences, another indication for the difference between these two intermediate states. The binuclear centre of the 2 SU-wt ATCC C*c*O seems to be more tightly coupled compared with the 4 SU-form of C*c*O, because the resonance at the g-value around 6 is decreased in the 2 SU-form of C*c*O.

3.2 Determination of *suicide inactivation* in the absence of subunit III

To understand the importance of subunit III of wt C*c*O, the function of the 2 SU-wt C*c*O was investigated by determination of the catalytic activity. The standard purification protocol of wt C*c*O includes the usage of the rather mild (in the case of C*c*O) detergent β-LM for solubilisation, resulting in the 4 SU-wt C*c*O. However, treatment of the 4 SU-wt C*c*O with the rather harsh detergent LDAO results in the 2 SU-wt C*c*O, which lacks subunit III and IV. The 2 SU-wt C*c*O was shown as a functionally active enzyme, because all redox-active metal centres are located in subunits I and II. Turnover experiments have been performed to determine the catalytic properties of the 2 SU-wt C*c*O and the analysis of the consumption of dioxygen in an activity assay revealed the importance of subunit III. 4 SU-wt C*c*O reduces the substrate dioxygen to form two water molecules (1 $O_2 \rightarrow 2\ H_2O$) and the removal of one O_2 molecule indicates one single turnover. The decrease of the dioxygen concentration therefore gives directly the number of turnovers per C*c*O, if the protein concentration is known.
Whereas the 4 SU-wt C*c*O was able to run more than 3 x 10^6 continuous turnovers, the 2 SU-wt C*c*O became inactive (dies) after roughly 30,000 turnovers. Is was proposed that SU III provides the structural stability for the binuclear site by long-distance stabilisation of the binuclear centre during the dioxygen reduction chemistry. Finally, this continuous inactivation of the 2 SU-wt C*c*O during catalytic turnover has been termed *suicide inactivation*.

3.2.1 Analytical experiment of *suicide inactivation*

In order to reproduce the previously published phenomenon of *suicide inactivation* during catalytic turnover the 2 SU-wt rec C*c*O was subjected to an activity assay using the Clark-Type oxygen electrode and compared to the 4 SU-wt rec C*c*O (in this case the recombinant protein was used, because the 2 SU-wt rec C*c*O was predominantly used for cystallisation trials after *suicide inactivation*). The s*uicide inactivation* is induced by a constant catalytic turnover of 2 SU-wt rec C*c*O. Thus, isolated 2 SU-wt rec C*c*O is known to be extremely stable e.g. it does not aggregate when stored at 4°C, but *suicide inactivation* starts, when 2 SU-wt C*c*O is employed in an activity assay.

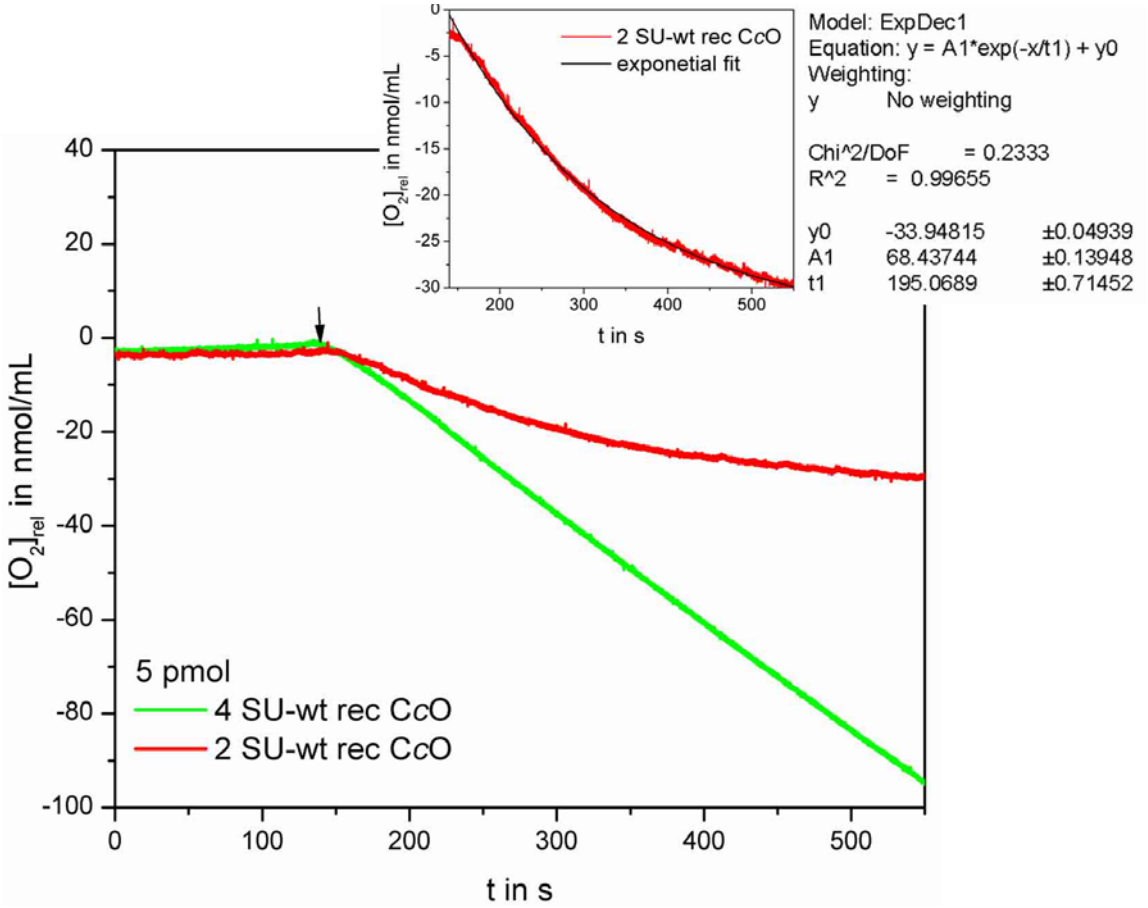

Figure 3.2-1 Measurement of the *suicide inactivation* of the 2 SU-wt rec C*c*O compared with the 4 SU-wt rec C*c*O using an oxygen electrode (5 pmol of 4 SU- and 2 SU-wt rec C*c*O, 3 mM ascorbate, 0.6 mM TMPD, 0.1 % LM in 1 mL 30 mM KP_i, pH 7.5). The inset shows the data of an exponential fit of the 2 SU-wt rec C*c*O. The arrow indicates the addition of 40 µM cyt *c*.

The 4 SU- and 2 SU-wt rec C*c*O (Figure 3.2-1) react differently in the analytical activity experiment and the two samples do not show comparable turnover behaviours. The 4 SU-wt rec C*c*O (green curve) displays a continuous constant turnover yielding a straight line in the activity assay. In contrast, the lifetime of 2 SU-wt rec C*c*O (red curve) decreases during turnover activity and the kinetics show an exponential decrease of the dioxygen concentration (Figure 3.2-1 inset, exponential fit of the 2 SU-wt rec C*c*O kinetics).

Again, this effect of 2 SU-wt C*c*O lacking SU III during turnover is termed the *suicide inactivation* (Bratton *et al.*, 1999b) and *inactivated* 2 SU-C*c*O was proposed to exhibit a structural change. This structural change might cause the loss of Cu_B or other structural defects (Bratton *et al.*, 1999a). The loss of activity might also be induced by ROS such as hydroxyl radicals, and these may cause formation of an interhelical cross-link between two helices.

3.2.2 Preparative experiment of *suicide inactivation*

In order to define the reason for *suicide inactivation*, the proposed structural change within wt C*c*O should be proven by MALDI and by the determination of the structure of *suicide inactivated* 2 SU-wt rec C*c*O. The large scale production of the 2 SU-wt rec C*c*O has provided the opportunity for a preparative *suicide inactivation* experiment and Table 3.2-1 shows the reaction scheme for the preparative *suicide inactivation* experiment and for the positive control, active protein.

Table 3.2-1 Experimental conditions for the large scale 2 SU-wt rec C*c*O *suicide inactivation* and for the *active* positive control.

	Total amount	**Cyt *c***	**Reduction system**	**O_2 supply**
Suicide inactivation	10 mg	reduced	Ascorbate and TMPD	yes
Active (positive control)	5 mg	oxidised	no	yes

The 2 SU-wt rec C*c*O reacted with reduced cyt *c* and a reduction system composed of ascorbate and TMPD in an open (oxygen providing) setup to induce *suicide inactivation*. This setup ensured the conditions for a continuous turnover. The mixture was incubated until no catalytic activity was measured of the *suicide inactivated* 2 SU-wt rec C*c*O (data not shown). The positive control was also mixed with cyt *c*, in this case oxidised one, however reducing agents were not added to the reaction mixture.

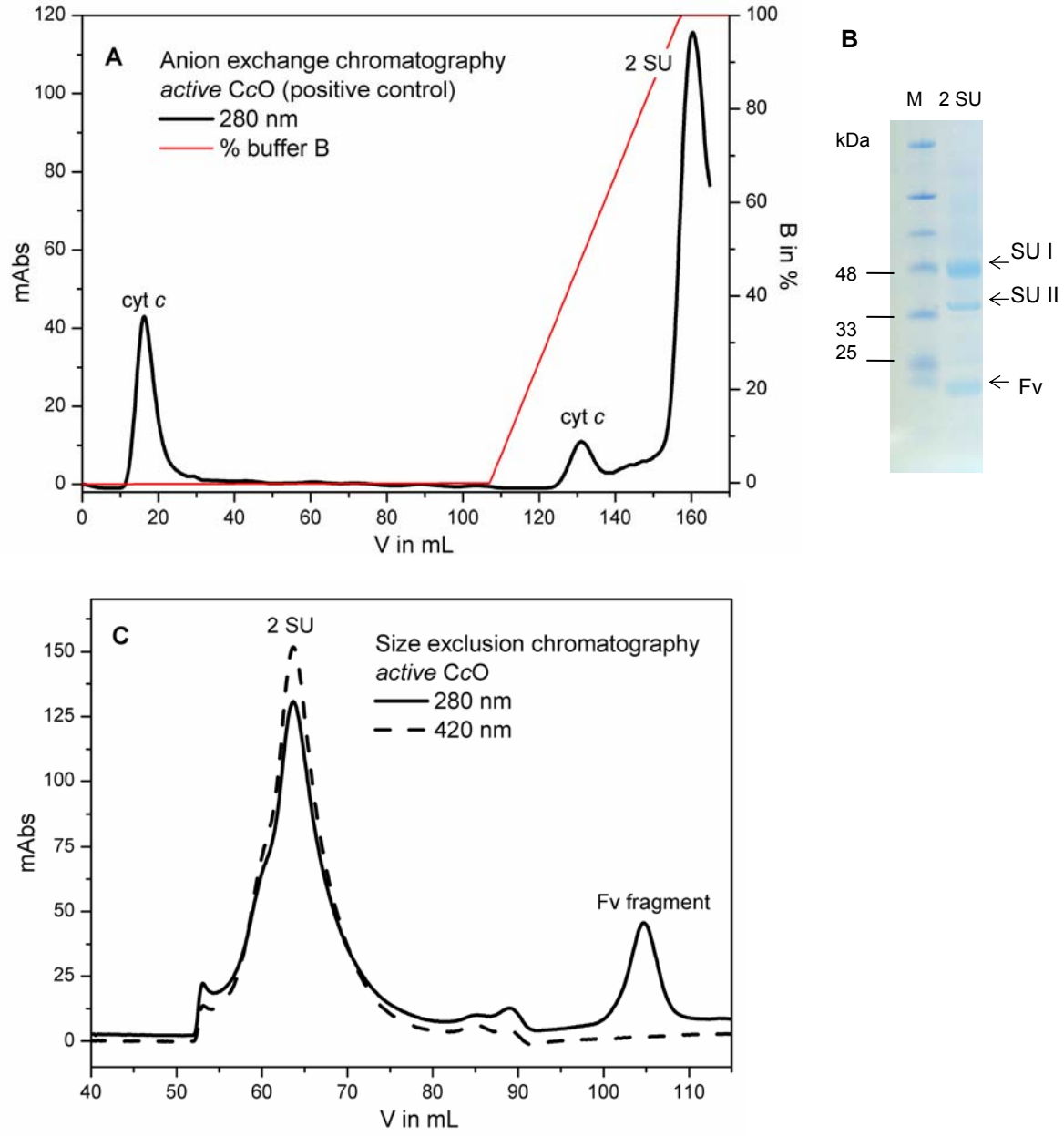

Figure 3.2-2 Repurification of the *active* 2 SU-wt rec C*c*O (positive control) for crystallisation. (A) Anion exchange chromatography: elution profile of the mixture of oxidised cyt *c* and 2 SU-wt rec C*c*O in 30 mM KP_i, pH 7.3, 0.08 % UM using Q sepharose. (B) 12 % SDS-PAGE gel of *active* 2 SU-wt rec C*c*O (2 SU). (C) Size exclusion chromatography of the pooled 2 SU-wt rec C*c*O fractions after addition of excess Fv fragment: gel filtration elution profile of 2 SU-wt rec C*c*O using TSK 3000. Buffer B contained 600 mM NaCl.

Both 2 SU-wt rec C*c*Os were repurified for crystallisation trials. Cationic impurities such as cyt *c* and salts were separated using anion exchange chromatography. The anion exchange chromatography elution profiles and SDS-PAGE analysis of *active* and *suicide inactivated* 2 SU-wt rec C*c*Os show first the separation from cyt *c* in the flowthrough and secondly (bound) cyt *c* at

the starting NaCl gradient at roughly 200 mM NaCl (Figure 3.2-2 A and Figure 3.2-3 A). The SDS-PAGE analysis of repurified *active* 2 SU-wt rec C*c*O, which was eluted at 600 mM NaCl, shows pure SU I and II of 2 SU-wt rec C*c*O and the bound Fv fragment (Figure 3.2-2 B).

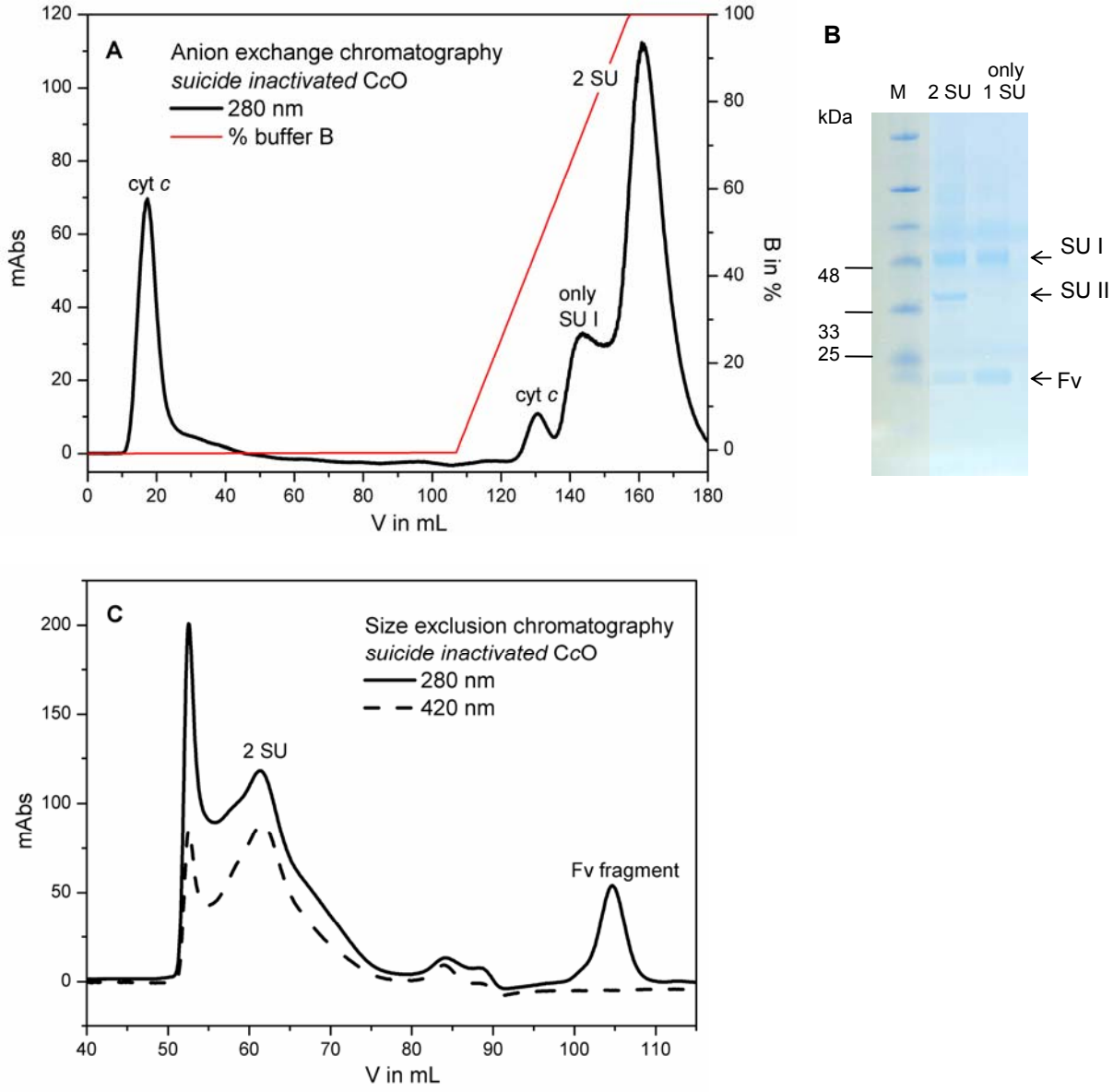

Figure 3.2-3 Repurification of the *suicide inactivated* 2 SU-wt rec C*c*O for crystallisation. (A) Anion exchange chromatography: elution profile of the mixture of cyt *c*, TMPD, ascorbate and 2 SU-wt rec C*c*O in 30 mM KP_i, pH 7.3, 0.08 % UM using Q sepharose. (B) 12 % SDS-PAGE gel of *suicide inactivated* 2 SU-wt rec C*c*O (2 SU) and the peak eluting at lower salt concentration (only SU I). (C) Size exclusion chromatography of the pooled 2 SU-wt rec C*c*O fractions after addition of excess Fv fragment: gel filtration elution profile of 2 SU-wt rec C*c*O using TSK 3000. Buffer B contained 600 mM NaCl.

The elution profile from the Q sepharose column of the *suicide inactivated* 2 SU-wt rec C*c*O shows an additional peak at an NaCl concentration of roughly 350 mM. According to SDS-PAGE analysis this shoulder is a 1 SU-wt rec C*c*O (only SU I) plus Fv fragment (Figure 3.2-3 B). Finally, the samples were analysed by gel filtration before the MALDI experiments and the crystallisation trials. Figure 3.2-2 C and Figure 3.2-3 C display size exclusion elution profiles of the pooled ion exchange fractions from the *active* and *suicide inactivated* 2 SU-wt rec C*c*Os. The *active* 2 SU-wt rec C*c*O chromatogram of gel filtration shows a typical elution profile for 2 SU-wt rec C*c*Os. First, the 2 SU-wt rec C*c*O maximum appears at an elution volume of ≈ 60 mL exhibiting absorption at λ = 280 nm and 420 nm. In contrast, the previously added excess Fv fragment (for crystallisation) elutes around 105 mL displaying only absorption at λ = 280 nm. Both 2 SU-wt rec C*c*Os have the same elution profile. However, the *suicide inactivated* sample shows an extra peak in void volume indicating aggregated protein.

In summary, the *suicide inactivated* 2 SU-wt rec C*c*O had been produced in a large scale together with a positive control, which still represents an active enzyme. Both protein forms were repurified for further experiments and *suicide inactivated* 2 SU-wt rec C*c*O shows a high tendency for aggregation as determined by gel filtration.

3.2.3 Identification of the recombinant two-subunit cytochrome *c* oxidase

In order to detect an interhelical cross-link in *suicide inactivated* 2 SU-wt rec C*c*O, the peak composition of mass spectra of subunits I and II of *suicide inactivated* and *active* 2 SU-wt rec C*c*O were compared. However, no differences in either sample were obtained in the mass spectra, indicating that there is no induced chemical link between peptides in *suicide inactivated* 2 SU-wt rec C*c*O. Finally, the MALDI-TOF/TOF experiment was performed using the *active* and *suicide inactivated* 2 SU-wt rec C*c*Os in order to identify both proteins before starting the crystallisation trials. Trypsin digested proteins deliver distinct peptides with different masses. Based on the known cleavage site of trypsin, the peptides can be identified using the peptide fingerprint/Mascot program. The mass spectra of *active* and *suicide inactivated* 2 SU-wt rec C*c*Os were recorded and analysed (Tobias Beckhaus, JWG University of Frankfurt). Both samples showed identical mass spectra, and thus only the spectra of *active* 2 SU-wt rec C*c*O subunit I and II are shown in Figure 3.2-4 (the spectra of *suicide inactivated* 2 SU-wt rec C*c*O subunit I and II are not shown).

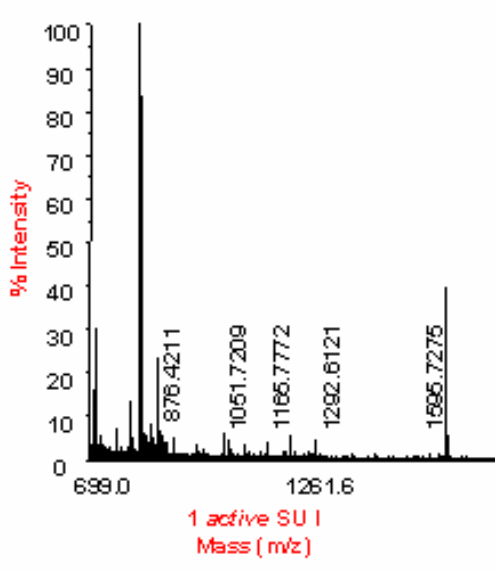

Figure 3.2-4 (A)

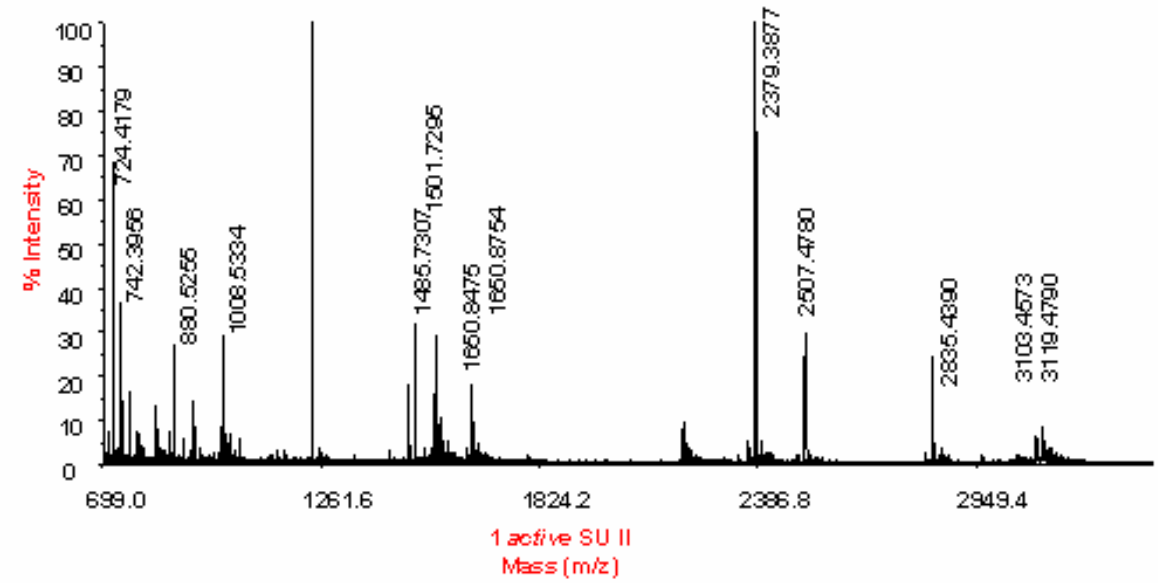

Figure 3.2-4 (B)

Figure 3.2-4 Mass spectra of the *active* 2 SU-wt rec C*c*O. (A) Subunit I. (B) Subunit II. The mass spectra of the *suicide inactivated* 2 SU-wt rec C*c*O subunit I and II were identical to the *active* 2 SU-wt rec C*c*O (data not shown).

Several peaks were detected in the mass spectrum of trypsin digested SU I (Figure 3.2-4 A) and SU I was identified having a Probability Based Mowse Score of 24 (scores greater than 67 are significant ($p < 0.05$)). Six peptides have matched out of 34 mass values and Figure 3.2-5 shows the identification of several peptides of SU I (red labelled peptides). However, there is no identification of any peptide from a transmembrane α-helix (TMH) of the hydrophobic core domain of SU I (TMHMM predicted TMHs bold).

SU I

MADAAVHGHGDHHDTRGFFTRWFMSTNHKDI**GILYLFTAGIVGLISVCFTVYM**RMELQHPGV
QYMCLEGARLIADASAECTPNGHLWNV**MITYHGVLMMFFVVIPALFGGFG**NYFMPLHIGAPD
MAFPRLNN**LSYWMYVCGVALGVASLLAPGGN**DQMGSGVGWVLYPPLSTTEAGYSMD**LAIFA**
VHVSGASSILGAINIITTFLNMRAPGMTLFKVPLF**AWSVFITAWLILLSLPVLAGAIT**MLLMDR
NFGTQFFDPAGGGDPVLYQHILWFFG**HPEVYIIILPGFGIISHVISTFA**KKPIF**GYLPMVLAMAA**
IGILGFVVWAHHMYTAGMSLTQQA**YFMLATMTIAVPTGIKVFSWIAT**MWGGSIEFKTPMLW
AFGFLFLFTVGGVTGVVLSQAPLDRVYHDTYYV**VAHFHYVMSLGAVFGIFAGVYY**WIGKMSG
RQY**PEWAGQLHFWMMFIGSNLIFFPQ**HFLGRQGMPRRYIDYPVEFAYWNNISSI**GAYISFASF**
LFFIGIVFYTLFAGKRVNVPNYWNEHADTLEWTLPSPPPEHTFETLPKREDWDRAHAH

SU II

MMAIATKRRGVAA**VMSLGVATMTAVPALAQDVLGDL**PVIGKPVNGGMNFQPASSPLAHDGQ
WDLH**FVLYIITAVTIFVCLLLLICIVR**FNRRANPVPARFTHNTPIE**VIWTLVPVLILVAIGAFSLP**
ILFRSQEMPNDPDLVIKAIGHGWYWSYEYPNDGVAFDALMLEKEALADAGYSEDEYLLATDNP
VVVPVGKKVLVQVTATDVIHAWTIPAFAVKQDAVPGRIAGLWFSVDGEGVYFGQCSELCGINH
AYMPIVVK AVSQEKYEAWLAGAKEEFAADASDYLPASPVKLASAE

Figure 3.2-5 Identified peptides derived from subunit I and II of the *active* 2 SU-wt rec C*c*O (identified peptides are shown in red, overlaps in magenta, underlined means identification of an additional methionine-oxidised peptide, TMHMM predicted TMHs are bold, SU II = subunit II precursor sequence).

On the other hand, more peaks were detected in the mass spectrum using trypsin digested SU II (Figure 3.2-4 B) and SU II is identified having a Probability Based Mowse Score of 91. Eleven peptides were matched out of 49 mass values. Many soluble peptides of SU II were identified (Figure 3.2-5, red labelled peptides), however no peptide from the TMHs was identified. In summary, both subunits of *active* 2 SU-wt rec C*c*O and of *suicide inactivated* 2 SU-wt rec C*c*O were analysed using MALDI-TOF/TOF for further experiments such as crystallisation trials.

3.3 Crystallisation of the recombinantly produced two-subunit cytochrome *c* oxidase

In order to determine the structure of *suicide inactivated* and *active* (positive control) C*c*Os, the 2 SU-wt rec C*c*Os were both subjected to crystallisation trials by vapour diffusion. The structure of the recombinant 2 SU-wt rec C*c*O was also compared to the determined structure of the native 2 SU-wt ATCC C*c*O. The positive control of the *suicide inactivation* experiment, representing the standard 2 SU-form of a wt C*c*O, was crystallised and the structure determined at 2.25 Å resolution, however, the *suicide inactivated* 2 SU-wt rec C*c*O could not be crystallised.

3.3.1 Crystallisation trials

2 SU-wt ATCC C*c*O was co-crystallised with the specifically binding Fv fragment as described (Ostermeier *et al.*, 1997). In order to crystallise the *active* or *suicide inactivated* 2 SU-wt rec C*c*O after identification by MALDI, crystallisation trials were performed using the same conditions as used by Ostermeier *et al*.

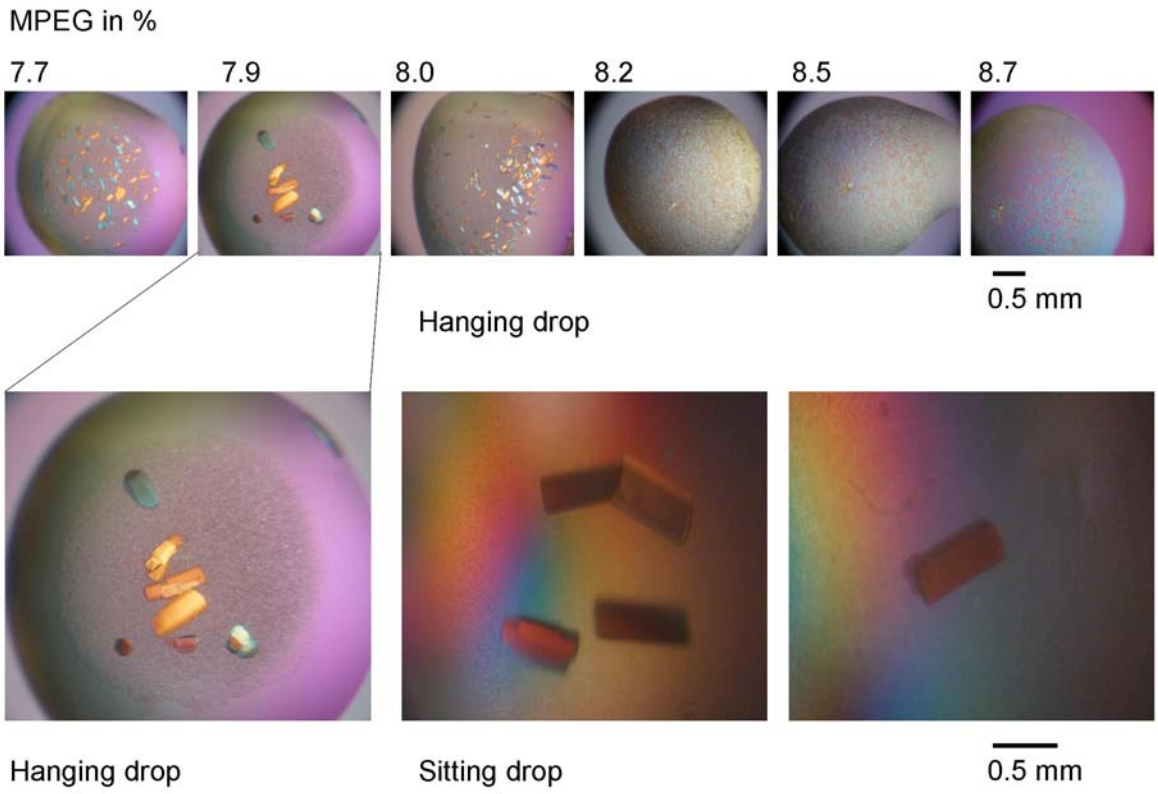

Figure 3.3-1 Protein crystals of the *active* 2 SU-wt rec C*c*O at pH 5.5 and at various concentrations of MPEG.

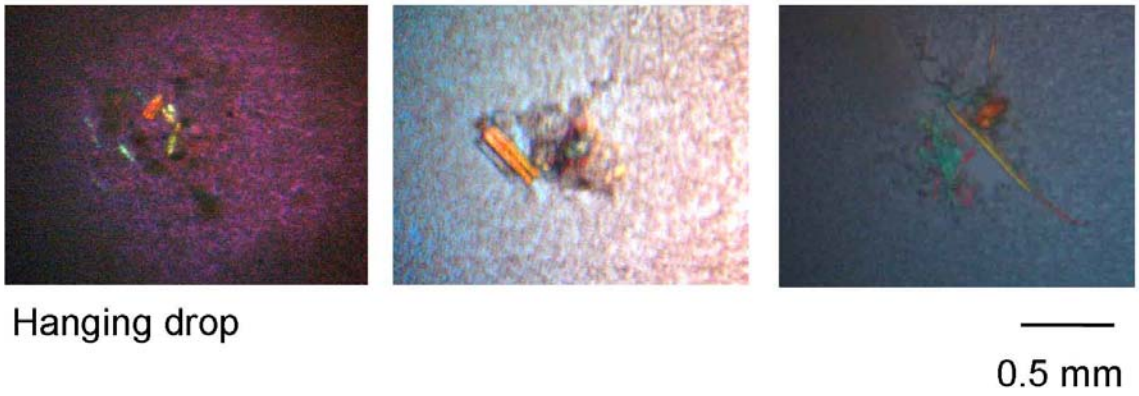

Figure 3.3-2 Protein crystals of the *suicide inactivated* 2 SU-wt rec C*c*O at pH 5.5 and at various concentrations of MPEG.

The *active* 2 SU-wt rec C*c*O crystallised in various conditions successfully. Figure 3.3-1 shows protein crystals obtained by the hanging drop method at pH 5.5 at various concentrations of MPEG. Crystal development occurs in a typical bell-shaped Gaussian distribution as a function of the MPEG concentration. The *active* 2 SU-wt rec C*c*O forms many small crystals at low MPEG concentrations; on the other hand, it forms large crystals in conditions with slightly higher MPEG concentration. The further increase of the MPEG concentration leads to a decreased crystallisation performance, but increased precipitation of aggregates. The optimal conditions gave crystals of 500 µm using the sitting drop technique. In parallel to *active* 2 SU-wt rec C*c*O, the *suicide inactivated* 2 SU-wt rec C*c*O should behave in same manner and crystallise in similar conditions, if there occurred no structural change leading to the *inactivated* form. All trials to cystallise *suicide inactivated* 2 SU-wt rec C*c*O have only shown precipitated protein. The a*ctive* 2 SU-wt C*c*O crystallised for example in the presence of 7.9 % MPEG at pH 5.5, however *suicide inactivated* 2 SU-wt rec C*c*O formed no crystals under these conditions. Only “crystal-like” aggregates and needles embedded in precipitate (Figure 3.3-2) have been observed. Data collection of *suicide inactivated* protein crystals has not been possible due to the low quality of these “crystals”.

In summary, the importance of subunit III for the structural and functional integrity of C*c*O was investigated using 2 SU-wt rec C*c*O. If C*c*O contains only subunit I and II, it loses its functional integrity during turnover activity. This s*uicide inactivation* might be caused by a structural change regarding the area around the binuclear site. Crystallisation trials with *suicide inactivated* 2 SU-wt rec C*c*O have been ineffective using standard crystallisation conditions indicating a severe structural instability and the tendency of *suicide inactivated* 2 SU-wt rec C*c*O to aggregate. However, crystals of *active* 2 SU-wt rec C*c*O were obtained in these conditions.

3.3.2 Crystal structure of the two-subunit recombinant wild type cytochrome *c* oxidase

The structure determination of a protein provides deeper insights into its possible modes of function. High-resolution structures allow the assignment of catalytically active amino acids, prosthetic groups or functional water molecules. The quality of *active* 2 SU-wt rec C*c*O crystals and the usage of cryo-conditions have allowed improvement of the resolution from 2.7 Å (Ostermeier et al., 1997) to 2.25 Å. The recombinant 2 SU-wt rec C*c*O was determined to have the identical structure as the native 2 SU-wt ATCC C*c*O taking into account the different resolutions of both structures (data not shown). The improved resolution of the 2 SU-wt rec C*c*O allows the assignment of rigid, fixed water molecules within the structure of wt C*c*O.

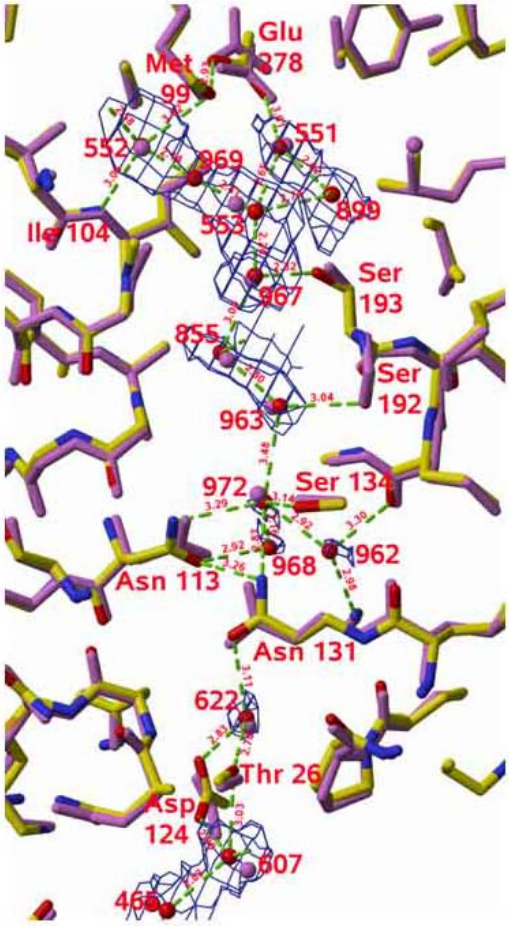

Figure 3.3-3 D-pathway structure of the 2 SU-wt rec C*c*O. H-bonds between H_2O molecules are represented in dashed green lines (length in Å). The electron density of H_2O molecules is shown in blue wire-frame representation at a contour level of 0.2 σ (magenta: structure of variant N131D, Dürr *et al.*, submitted). Figure provided by Dr. Jürgen Köpke.

The D-pathway of wt C*c*O contains several fixed water molecules acting as a proton wire and water networks have been found in the D-pathway of wt C*c*O (Dr. Jürgen Köpke). First, electron

densities representing H_2O molecules are located at the entrance of the D-pathway below the triad of N131-N113-N199 (residue N199 not shown). Above this triad the water chain continues to residue E278, the end of the D-pathway.

E278 is proposed as a branching point for substrate and pumped protons and it might function as a flexible switch and gating point for proton distribution either to the binuclear site or to the pumping site.

In summary, the structure of *active* 2 SU-wt rec C*c*O was determined at 2.25 Å resolution and shows the identical structure compared with the native 2 SU-wt ATCC C*c*O having a resulution of 2.7 Å.

3.3.3 Electron density between haem Fea_3 and Cu_B during the O state

In order to fit the observed electron density between the metal ions of the binuclear site ($Fe^{+III}a_3$-x-x-Cu^{+II}_B) during the **O** state, various model molecules were used for fitting. The electron density observed between the two metal ions of the binuclear centre is an interesting feature of the high-resolution structure, because the current model of the catalytic cycle proposes two independent O species, an OH^- ion and a H_2O molecule, bound by the metal ions of the binuclear site. Several chemically possible species have been modelled into this density: a single H_2O, a peroxy-bridge (O^--O^-) or a dioxygen (O=O), two independent O species (e.g. 2 H_2O or 1 H_2O + 1 OH^-), a CO_3^{2-} or a Cl^- (Dr. Jürgen Köpke). The results show that there is a high probability that not an OH^- and a H_2O, but a peroxide ion (O^--O^-) is bound by the binuclear centre during the **O** state (data not shown).

In summary, several possible molecules were modelled into the observed electron density between the metal ions of the binuclear site. However, only the peroxy-bridge and the fitted Cl^- provide a good fit for this unknown species (Dr. Jürgen Köpke). Regarding the catalytic function of C*c*O, the reduction of O=O, only an oxygen species in the binuclear centre during the **O** state is functionally reasonable. Finally, the most logical bound species is an O^--O^-, because 1) its modelling gives no peak in the difference map, and 2) its two negative charges are best for the charge compensation of the binuclear site, because the haem a_3-Fe^{3+} and the Cu_B^{2+} are both positively charged. The overall charge of the binuclear site can be calculated as following: the porphyrin ring provides a charge of – 2, the two metals of + 5 and the peroxy-bridge provides – 2 resulting in a sum of charge of ΣQ = + 1.

3.4 Functional studies using native cytochrome *c* oxidase

In order to define the mechanism of wt CcO in further detail, experiments were performed using spectroscopic methods such as UV-vis spectroscopy, EPR spectroscopy and FTIR spectroscopy. The results presented in chapter 3.1 show that 4 SU-wt ATCC C*c*O represents the most native und functional wt C*c*O. Therefore, all following functional studies have been performed using this form of wt C*c*O to obtain the most natural reaction of the enzyme towards the particular treatment during the respective experiment.

3.4.1 Identification of an oxygen species in the binuclear site during the O **state**

To obtain more information about the nature of the bound species between the metal ions of the binuclear site ($Fe^{+III}a_3$-x-x-Cu^{+II}_B) during the **O** state, dioxygen pulse experiments were performed and recorded using FTIR spectroscopy.

In general, wt C*c*O is isolated resting in the air-oxidised **O** state. For dioxygen pulsing, a reducing agent, for example dithionite, is used in stoichiometric amounts sufficient for the anaerobisation of the solution and one single turnover of wt C*c*O. The dioxygen pulse is performed by mixing the sample with an air (O_2) containing buffer. The oxygen pulsing effect can be investigated using FTIR spectroscopy and this spectroscopic method was employed in order to find evidence for a bound peroxy-bridge during the **O** state. Functional pulsing experiments using the isotopes $^{16}O_2$ or $^{18}O_2$ can provide the answer if wt C*c*O binds an O species during the **O** state, and Figure 3.4-1 shows the absolute FTIR spectra of pulsed $^{16}O_2$-4 SU-wt ATCC C*c*O and $^{18}O_2$-4 SU-wt ATCC C*c*O.

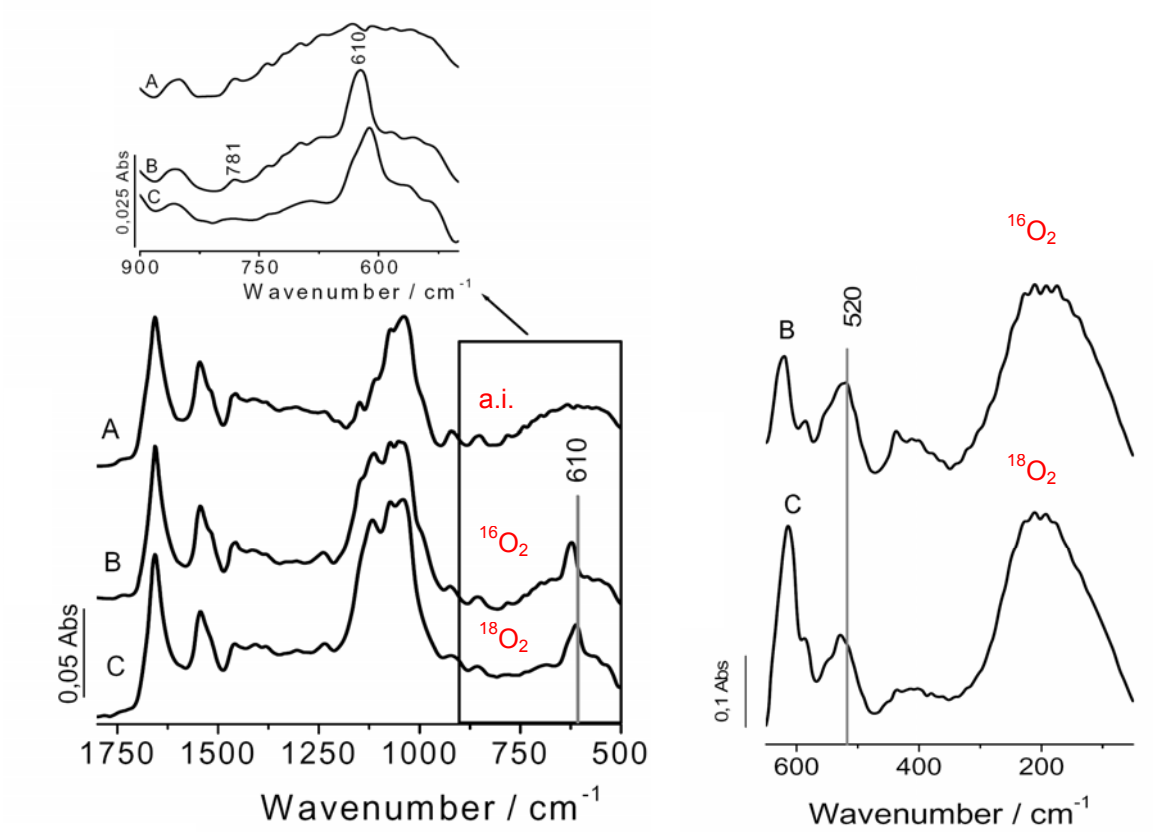

Part 1 Part 2

Figure 3.4-1 FTIR spectra of the 4 SU-wt ATCC C*c*O during the O state. Part 1 shows the absorbance from 1750 to 500 cm^{-1} and Part 2 from 650 to 50 cm^{-1}. Spectrum A: as isolated (a.i.), spectrum B: pulsed with $^{16}O_2$ and spectrum C: pulsed with $^{18}O_2$. ν(Fe-O) = 781 cm^{-1}, ν(Fe-O) = 520 cm^{-1} and ν(dithionite/sulfate) = 610 cm^{-1}. Spectra were recorded by Prof. Petra Hellwig, University of Strasbourg.

The 4 SU-wt ATCC C*c*O "as isolated" (a.i.) displays typical FTIR absorbances (Figure 3.4-1, spectrum A). Different modes of vibration occur, such as vibrations originating from the atoms of the functional groups of amino acids, H-bonds or metal-ligand vibrations. Similar maxima are observed after the pulsing procedure, however, there are differences using $^{16}O_2$- or $^{18}O_2$-containing buffers (spectra B and C). The oxygen sensitive bands of the Fe-O vibration are at wavenumber 781 cm^{-1} and around 520 cm^{-1}. The absorption of the added dithionite and after its reactants are also observable in spectra B and C having a maximum at the wavenumber around 610 cm^{-1}.

In summary, the pulsed 4 SU-wt ATCC C*c*Os with $^{16}O_2$ or $^{18}O_2$ have displayed shifts in the vibration modes between Fe and ^{16}O and ^{18}O (Fe-$^{16/18}O$ vibration) providing evidence that an O species binds the Fea_3 in the binuclear site after the dioxygen pulse. The resulting Fea_3-O bond during the **O** state excludes a bound Cl^-, which also gives a good fit for the electron density in the binuclear site (chapter 3.3.3), and these findings rather suggest an oxygen species bound by the

metal ion of the binuclear site. A peroxy-bridge even provides the best charge compensation for the positively charged binuclear site ($Fe^{+III}a_3$-O^--O^--Cu^{+II}_B).

3.4.2 Reversibility of P → F state transition

3.4.2.1 UV-vis spectroscopy

To gain further information regarding the properties of the intermediates formed during the natural catalytic cycle, H_2O_2-induced intermediates were studied and newly discovered intermediate states were characterised by spectroscopic methods. The specific aim of these experiments was to assess the reversibility of the H_2O_2-induced **P** → **F** state transition, although this transition is generally assumed to be irreversible. The H_2O_2-induced $\mathbf{P_H/F^{\bullet}_H}$ and $\mathbf{F_H}$ states have already been introduced in chapter 3.1. The excess H_2O_2 of the $\mathbf{F_H}$ state can be removed by catalase treatment of 4 SU-wt ATCC C*c*O and the effects of this treatment were studied by UV-vis and EPR spectroscopy. 12 μM pulsed, reoxidised and chloride-free purified 4 SU-wt ATCC C*c*O was reacted (< 60 s) with equivalents of H_2O_2 (stoichiometric range of ratio 1:1 to 1:5) at pH 9 to form the $\mathbf{P_H}$ state. The maximum in the difference absorption spectrum (*minus* the **O** state) is observed at 610 nm (Figure 3.4-2, black line).

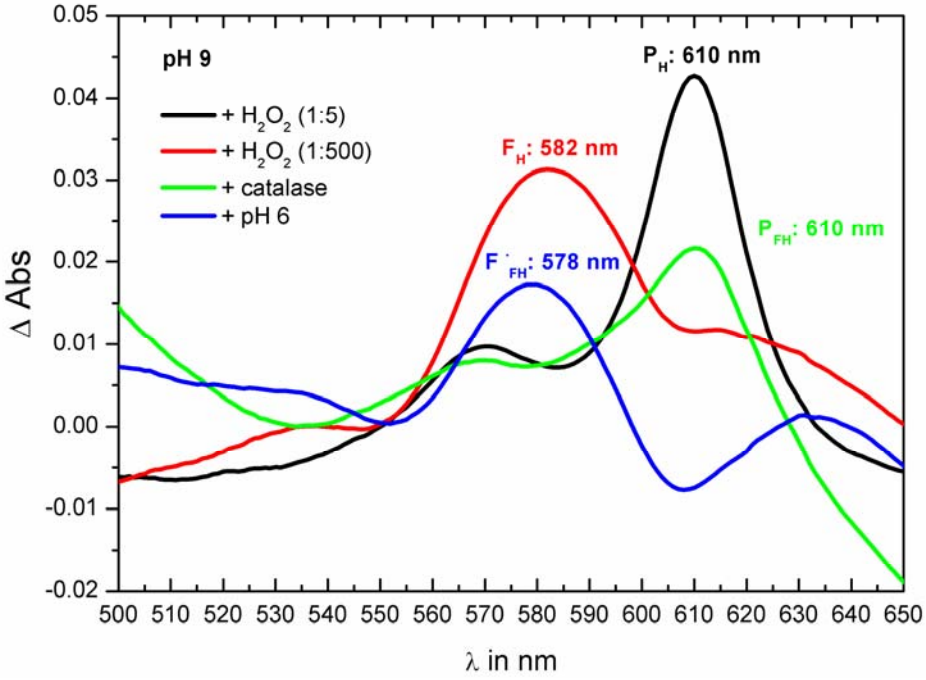

Figure 3.4-2 Difference absorption spectra (*minus* the O state) obtained from intermediates of the 4 SU-wt ATCC C*c*O at high pH. 12 μM solubilised 4 SU-wt ATCC C*c*O in 50 mM KP_i, pH 9, 0.05 % LM were successively mixed with H_2O_2 in a molar ratio of 1:5 (black line), with 1:500 H_2O_2 (red line), with 80 units catalase (green line) and with a final concentration of 100 mM Mes-OH, pH 5.4 (blue line).

After addition of an excess of H_2O_2 (1:500) to the 4 SU-wt ATCC C*c*O in the $\mathbf{P_H}$ state the 610 nm

peak shifts to 582 nm (Figure 3.4-2, red line) indicative of the $\mathbf{F_H}$ state formation. Compared to the $\mathbf{P_H}$ state, the $\mathbf{F_H}$ state has an additional electron within the binuclear centre, which can be provided by a second H_2O_2 molecule exclusively. When catalase is used to remove the excess of H_2O_2 this 582 nm maximum disappears and a **P**-like species, opposite to the direction of the natural catalytic cycle, again occurs at 610 nm (Figure 3.4-2, green line). The reaction describes the reversibility of the $\mathbf{P_H} \leftrightarrow \mathbf{F_H}$ transition by performing an artificial $\mathbf{F_H} \rightarrow \mathbf{P_H}$ backwards transition by removing the excess H_2O_2 of the $\mathbf{F_H}$ state. When the pH of the same sample is now lowered to pH 6 the spectrum reveals the typical $\mathbf{P_H} \rightarrow \mathbf{F^{\bullet}_H}$ conversion with a maximum at 578 nm (Figure 3.4-2, blue line).

In order to specify the effect of a possibly generated membrane potential of the $\mathbf{P_H} \rightarrow \mathbf{F_H}$ transition, the same experiment was performed using the 4 SU-wt ATCC C*c*O reconstituted into proteoliposomes. The difference absorption spectra (*minus* the **O** state) from these experiments are shown in Figure 3.4-3. The internal pH of the vesicles was pH 7.3, whereas that of the bulk medium pH 9. With low amounts of H_2O_2, the $\mathbf{P_H}$ state is again formed with a maximum at 610 nm (Figure 3.4-3, black line).

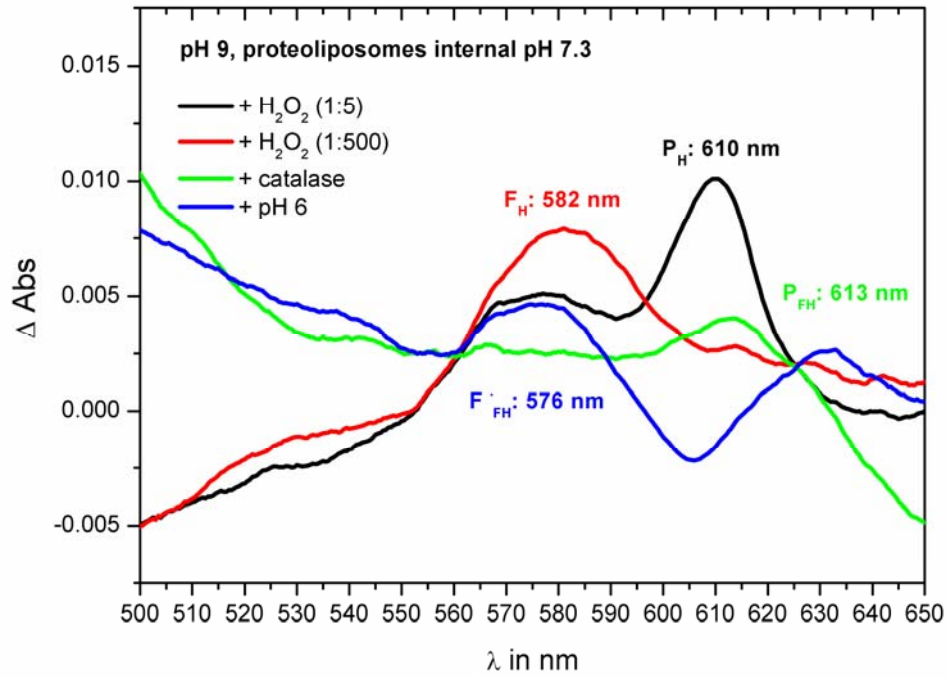

Figure 3.4-3 Difference absorption spectra (*minus* the O state) obtained from intermediates of 4 SU-wt ATCC C*c*O proteoliposomes at high pH. 9 µM reconstituted 4 SU-wt ATCC C*c*O in 50 mM KP_i, pH 9 were successively mixed with H_2O_2 in a molar ratio of 1:5 (black line), with 1:500 H_2O_2 (red line), with 80 units catalase (green line) and with 100 mM Mes-OH, pH 5.4 (blue line).

However, this $\mathbf{P_H}$ state has a significant proportion of the $\mathbf{F^{\bullet}_H}$ state probably due to the less alkaline medium inside the proteoliposomes. The $\mathbf{F_H}$ state is again obtained after adding excess H_2O_2 and it shows a 582 nm maximum (Figure 3.4-3, red line). When the H_2O_2 of the bulk

medium of the reconstituted 4 SU-wt ATCC C*c*O is removed by adding catalase the **P**-like state is generated with a maximum at 613 nm (Figure 3.4-3, green line). This catalase induced **P** state is convertible to the $\mathbf{F^{\bullet}_H}$ state by lowering the pH to 6 and then it exhibits a maximum at 576 nm (Figure 3.4-3, blue line).

The catalase induced **P**-like state was reproducibly obtained in several experiments with solubilised and reconstituted 4 SU-wt ATCC C*c*O. However, the location of the maximum differed slightly from experiment to experiment. The induced maxima lay between λ = 610 and 613 nm, the majority of the catalase induced $\mathbf{P_H}$ states have shown a maximum around 612 nm (data not shown).

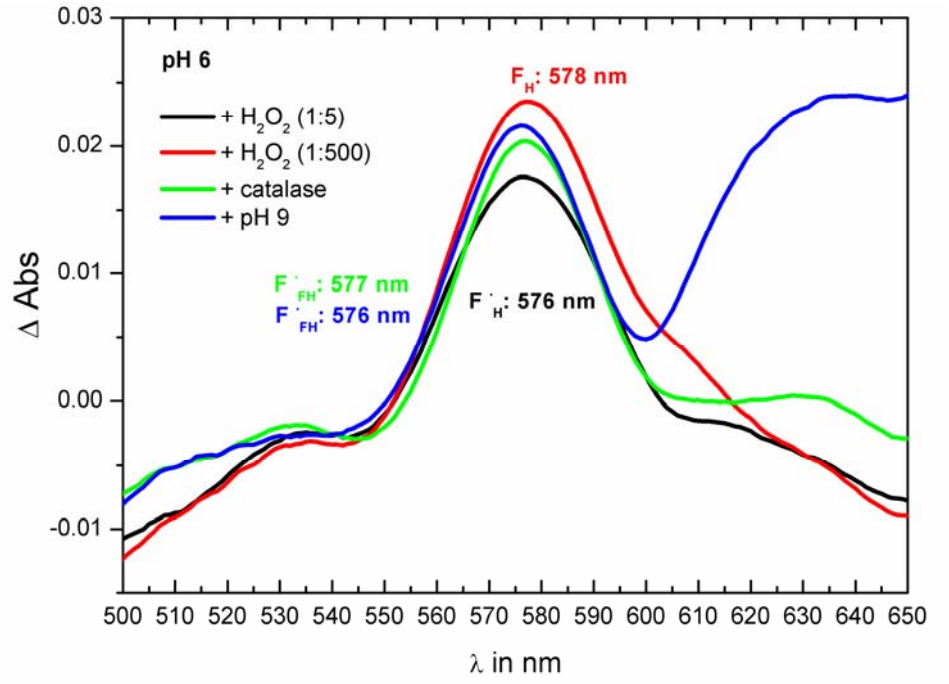

Figure 3.4-4 Difference absorption spectra (*minus* the O state) obtained from intermediates of the 4 SU-wt ATCC C*c*O at low pH. 12 µM solubilised 4 SU-wt ATCC C*c*O in 50 mM Mes-OH, pH 6, 0.05 % LM were successively mixed with H_2O_2 in amolar ratio of 1:5 (black line), with 1:500 H_2O_2 (red line), with 80 units catalase (green line) and with 100 mM K_2HPO_4 (blue line).

A series of experiments using solubilised 4 SU-wt ATCC C*c*O was also performed at pH 6 (Figure 3.4-4). As expected, the reaction of the 4 SU-wt ATCC C*c*O with low amounts of H_2O_2 (range 1:1 to 1:5) at pH 6 results in formation of the $\mathbf{F^{\bullet}_H}$ state having a maximum in the difference absorption spectrum (*minus* the **O** state) at 576 nm (Figure 3.4-4, black line). An excess of H_2O_2 to form the $\mathbf{F_H}$ state shifts this peak slightly to 578 nm (Figure 3.4-4, red line). Again addition of catalase to remove excess H_2O_2 results in a peak at 578 nm (Figure 3.4-4, green line), however increasing the pH to 9 shows no $\mathbf{F^{\bullet}_H} \rightarrow \mathbf{P_H}$ state conversion (Figure 3.4-4, blue line) as expected, because the $\mathbf{P_H} \rightarrow \mathbf{F^{\bullet}_H}$ transition is irreversible.

To differentiate these $\mathbf{F_H} \rightarrow \mathbf{P_H}$ and $\mathbf{F_H} \rightarrow \mathbf{F^{\bullet}_H}$ induced **P** and $\mathbf{F^{\bullet}}$ species we have named these catalase-induced intermediates $\mathbf{P_{FH}}$ and $\mathbf{F^{\bullet}_{FH}}$, respectively, to indicate their formation from the **F** state by $\underline{H_2O_2}$ removal (Figure 3.4-2 to Figure 3.4-4).

In summary, spectroscopic studies using the 4 SU-wt ATCC C*c*O have demonstrated the induction of the new $\mathbf{P_{FH}}$ and $\mathbf{F^{\bullet}_{FH}}$ states. Low and excess amounts of H_2O_2 induce the $\mathbf{P_H/F^{\bullet}_H}$ and $\mathbf{F_H}$ states, respectively, and catalase-treatment of the $\mathbf{F_H}$ state leads to the apparent reverse, opposite to the natural catalytic cycle, transition of $\mathbf{F_H} \rightarrow \mathbf{P_H/F^{\bullet}_H}$ states. This catalase-induced states are presented here as $\mathbf{P_{FH}/F^{\bullet}_{FH}}$ states.

3.4.2.2 EPR spectroscopy

In order to find out whether the tyrosyl 167 radical of the $\mathbf{P_H/F^{\bullet}_H}$ states is also present in the catalase-induced $\mathbf{P_{FH}/F^{\bullet}_{FH}}$ states, EPR studies of the 4 SU-wt ATCC C*c*O were performed to identify and characterise these radical species. Figure 3.4-5 A and Figure 3.4-5 C show the EPR signals observed when mixing C*c*O in the **O** state (magenta lines) with equimolar amounts of H_2O_2 (1:1) at pH 9 for the $\mathbf{P_H}$ state and at pH 6 for the $\mathbf{F^{\bullet}_H}$ state, respectively (black lines). In addition to the EPR signals from the dinuclear Cu_A centre and the low-spin haem *a*, an additional narrow EPR signal is observed at g ~ 2 after the addition of H_2O_2. This organic radical signal was well described previously in the literature, and is attributed to the tyrosyl radical situated at residue Y167 (Budiman *et al.*, 2004). This radical species vanishes in both cases after excess H_2O_2 (1:500) is added (Figure 3.4-5 A and Figure 3.4-5 C, red lines). Thus, the disappearance of this signal is clearly associated with the $\mathbf{P_H/F^{\bullet}_H} \rightarrow \mathbf{F_H}$ state transition. Upon catalase treatment to form the $\mathbf{P_{FH}}$ or $\mathbf{F^{\bullet}_{FH}}$ states a narrow EPR-active signal is reactivated without adding other chemicals. Upon closer inspection this EPR signal is identical, in terms of overall line width and partially resolved hyperfine structure (Figure 3.4-5 B, black and green line), with the signal observed in both the $\mathbf{P_H}$ (data not shown) and $\mathbf{F^{\bullet}_H}$ states. The only difference is an apparent increase in signal intensity relative to the Cu_A EPR signal. In contrast to the UV-vis spectroscopic experiments, pH shift experiments, either from pH 6 to pH 9 or vice versa, do not alter the yield of this narrow radical signal dramatically, but rather only induce very slight pH-dependent differences of the Cu_A signal (Figure 3.4-5 A, blue line).

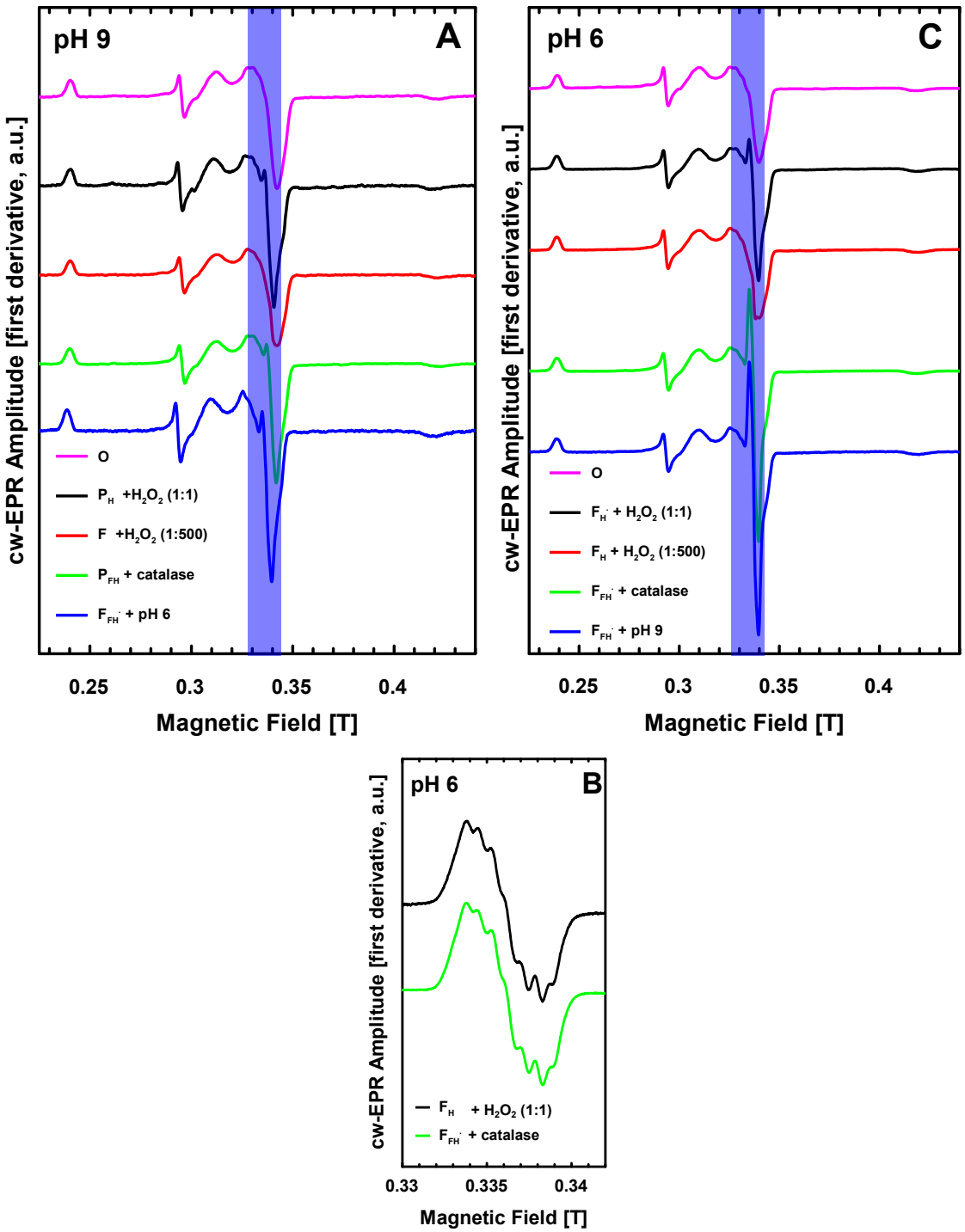

Figure 3.4-5 EPR spectra of the 4 SU-wt ATCC C*c*O at high pH (A) and at low pH (C): the O state (magenta spectra), the P_H (A) / $F^{\bullet}_H$ (C) state (black lines), the F_H state (red lines), the P_{FH} (A) / $F^{\bullet}_{FH}$ (C) state (green lines), the $F^{\bullet}_{FH}$ state (blue lines). Experimental conditions: Microwave frequency, 9.43 GHz; microwave power, 2 mW; field modulation frequency, 100 kHz; field modulation amplitude, 1.0 mT peak to peak; T = 20 K. Experimental conditions for the g ~ 2 region (B) were the same as above except for microwave power, 20 mW and modulation amplitude, 0.4 mT peak to peak.

3.4.2.3 Anaerobic experiments

In order to test whether the reversibility of the $\mathbf{P_H} \rightarrow \mathbf{F_H}$ state transition of C*c*O depends on the concentration of dioxygen, an anaerobic $\mathbf{F_H}$ state was treated with catalase.

Ruitenberg *et al.* used a reliable method for **E** state production in 2001 (after Witt and Chan, 1987). Hence, in his method the $\mathbf{F_H}$ state is made anaerobic using glucose and glucose oxidase. After adding catalase, CO is bubbled through the sample of this anaerobic $^{\text{anaerobic}}\mathbf{F_H}$ state. CO provides two electrons and produces the **E** state ($^{\text{anaerobic}}\mathbf{F_H}$ state + 2 e^- → **E** state) as shown in Figure 3.4-6.

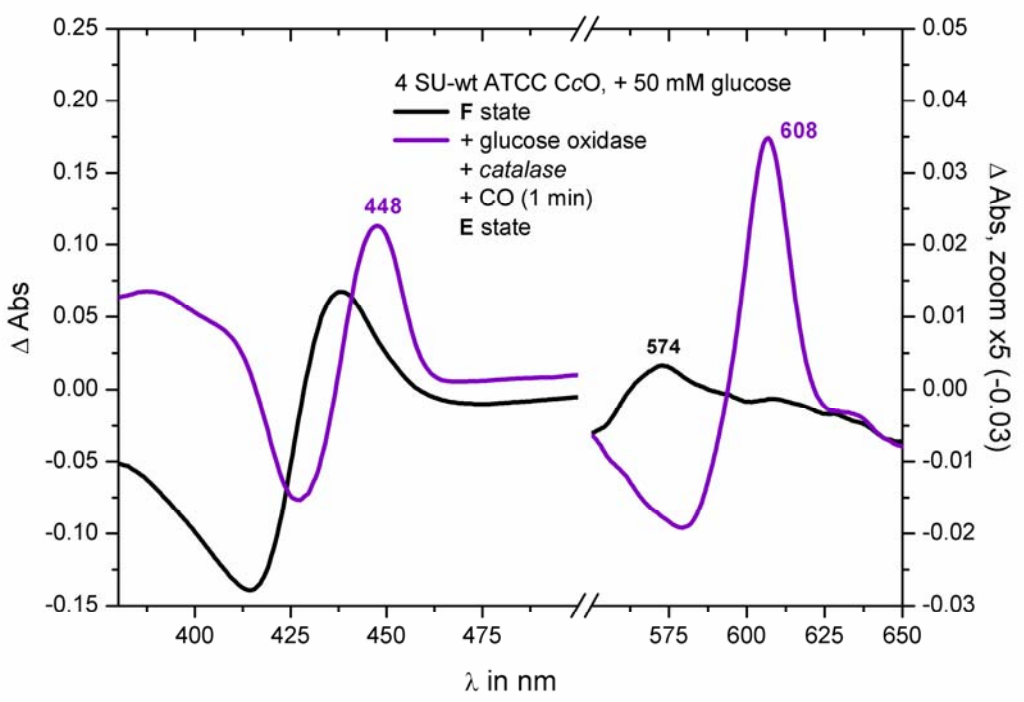

Figure 3.4-6 Difference absorption spectra of the F_H **state and the** E **state (*minus* the** O **state) of 4 SU-wt ATCC C*c*O (after Ruitenberg *et al.*, 2001). 10 µM 4 SU-wt ATCC C*c*O in 25 mM HEPES, pH 7.4, 0.05 % LM, 50 mM glucose (+ Argon) were mixed with H_2O_2 in a molar ratio of 1: 500. Glucose oxidase, 80 units catalase and CO were mixed to the sample.**

Catalase was added to C*c*O in the H_2O_2-induced $\mathbf{F_H}$ state. However, as shown in the current work, a catalase treatment of the $\mathbf{F_H}$ state leads to the $\mathbf{P_{FH}}$ state at high pH! Thus, he would have induced the $\mathbf{P_{FH}} \rightarrow$ **O** state transition after addition of CO and the mixed valence CO-bound form after reaction with further CO, but not would have formed the **E** state. Obviously the under anaerobic conditions the $\mathbf{F_H}$ state is stable ($^{\text{anaerobic}}\mathbf{F_H}$ state) in the presence of catalase and addition of CO induces the $^{\text{anaerobic}}\mathbf{F_H} \rightarrow$ **E** state transition. Thus, the $^{\text{aerobic}}\mathbf{F_H}$ state reacts to the $\mathbf{P_{FH}}$ state after addition of calalase, but the $^{\text{anaerobic}}\mathbf{F_H}$ state remains an $\mathbf{F_H}$ state. However, the sequence of these events occurring after removal of dioxygen, but before addition of calalase, has not been verified so far.

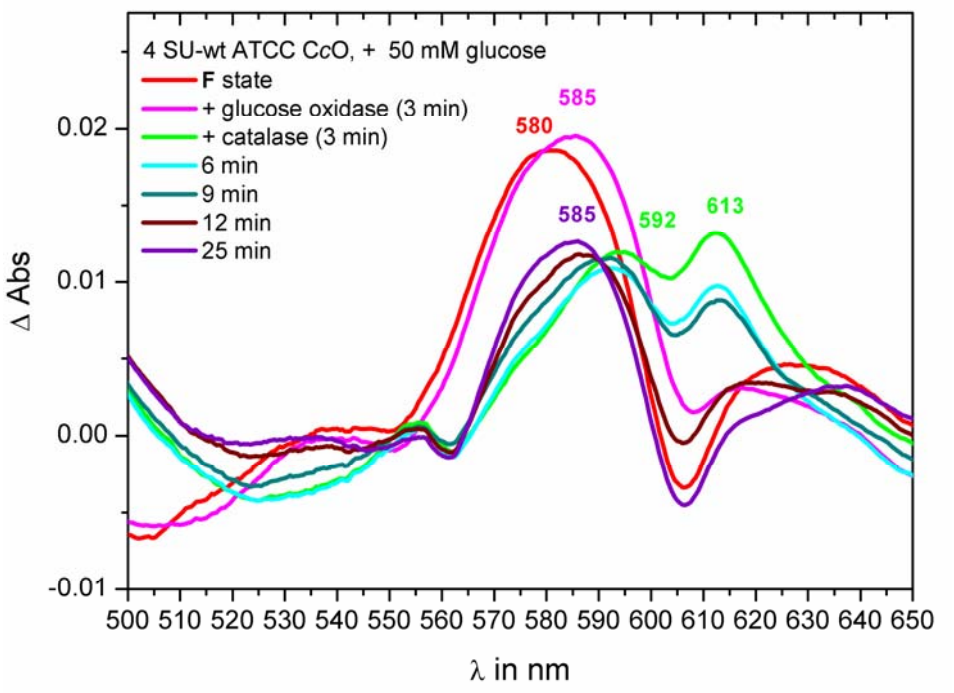

Figure 3.4-7 Difference absorption spectra of the stable ^{anaerobic}F state (*minus* the O state) of 4 SU-wt ATCC C*c*O. 9 µM 4 SU-wt ATCC C*c*O in 50 mM KP_i, pH 9, 0.05 % LM, 50 mM glucose (+ Argon) were mixed with H_2O_2 in a molar ratio of 1: 500. Glucose oxidase and 80 units catalase were mixed to the sample.

Here, the $^{aerobic}\mathbf{F_H}$ state, which exhibits a maximum at 580 nm in the difference absorption spectrum (*minus* the **O** state) (Figure 3.4-7, red line), is converted into an $^{anaerobic}\mathbf{F_H}$ state having a maximum at 585 nm (Figure 3.4-7, magenta line) after addition of glucose oxidase. The catalase treatment of the $^{anaerobic}\mathbf{F_H}$ state has not induced a stable $\mathbf{P_{FH}}$ state at pH 9, but it has induced a stable ^{anaerobic}**F** state after roughly 10 minutes again having the 585 nm maximum (Figure 3.4-7, violet line). However, the catalase treated $^{anaerobic}\mathbf{F_H}$ state of 4 SU-wt ATCC C*c*O has still reacted first into the $\mathbf{P_{FH}}$ state having a maximum at 613 nm (Figure 3.4-7, green line) and then, via a mixed species at 592 nm (possibly the mixed valenced **R** state, light blue line), has again formed the ^{anaerobic}**F** state having a maximum at 585 nm (Figure 3.4-7, violet line). The reaction back to the ^{anaerobic}**F** state has taken a few minutes, but the disappearance of the $\mathbf{P_{FH}}$ species was complete in less than 10 minutes and the enzyme may have passed through the mixed valence **R** state having a maximum at roughly 590 nm.

In summary, the $\mathbf{P_H} \rightarrow \mathbf{F_H}$ state transition is reversible in the presence of catalase and dioxygen, however, the $\mathbf{F_H} \rightarrow \mathbf{P_{FH}}$ state transition was found out to be blocked under anaerobic conditions.

3.4.2.4 Alternative forms of wild type cytochrome *c* oxidase

To find out whether the reversibility of $\mathbf{P_H} \rightarrow \mathbf{F_H}$ state transition is also observed using other types of wt C*c*Os, the 4 SU-wt rec C*c*O and even the 2 SU-wt ATCC C*c*O were employed for the catalase experiment. The native 4 SU-wt ATCC C*c*O has given higher yields of H_2O_2-induced intermediates than the recombinant homologously produced 4 SU-wt rec C*c*O as described in chapter 3.1. However, the $\mathbf{F_H} \rightarrow \mathbf{P_H}$ transition occurring after addition of catalase is also observed using 4 SU-wt rec C*c*O (Figure 3.4-8 A) or using 2 SU-wt ATCC C*c*O (Figure 3.4-8 B).

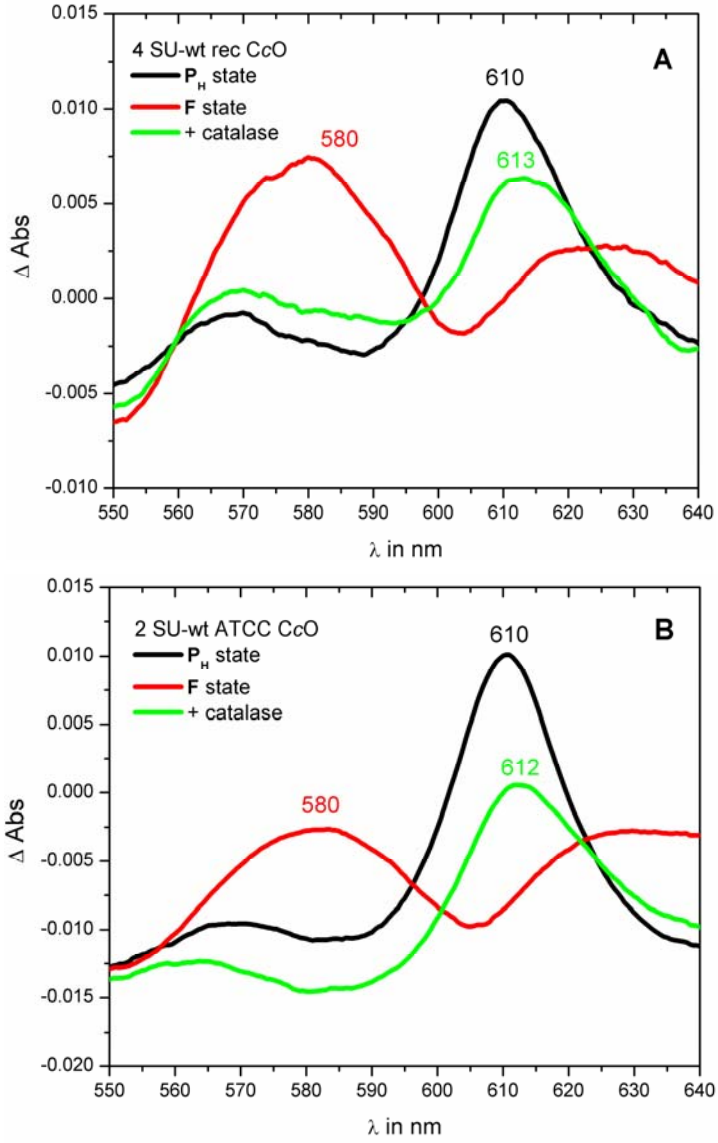

Figure 3.4-8 Difference absorption spectra (*minus* the O state) from intermediates of alternative wt C*c*Os (A) Spectra obtained from the 4 SU-wt rec C*c*O at high pH. 10 µM 4 SU-wt rec C*c*O in 50 mM KP_i, pH 9, 0.05 % LM were successively mixed with H_2O_2 in a molar ratio of 1:5 (black line), with 1:500 H_2O_2 (red line), with 80 units catalase (green line). (B) Spectra obtained from 2 SU-wt ATCC C*c*O at high pH. 10 µM 2 SU-wt ATCC C*c*O in 50 mM KP_i, pH 9, 0.05 % LM were successively mixed with H_2O_2 in a molar ratio of 1:5 (black line), with 1:500 H_2O_2 (red line), with 80 units catalase (green line).

The 4 SU-wt rec C*c*O has also displayed the standard $\mathbf{P_H}$ state after adding low amounts of H_2O_2 at pH 9. The typical maximum around 610 nm in the difference absorption spectrum (*minus* the **O** state) (Figure 3.4-8 A, black line) was obtained. The $\mathbf{F_H}$ state was induced having a 580 nm maximum after adding excess H_2O_2 to the same sample (Figure 3.4-8 A, red line). Consequently, after addition of catalase the $\mathbf{P_{FH}}$ state was formed exhibiting a red shifted $\mathbf{P_{FH}}$ state maximum at 613 nm (Figure 3.4-8 A, green line).

The native 2 SU-wt ATCC C*c*O showed the same reactivity against H_2O_2 as the 4 SU-wt ATCC C*c*O at pH 9. The $\mathbf{P_H}$ state was induced after addition of low amounts of H_2O_2 (Figure 3.4-8 B, black line) and the $\mathbf{F_H}$ state having a broad 580 nm maximum was formed after mixing excess H_2O_2 to the 2 SU-form (Figure 3.4-8 B, red line). Thus, the $\mathbf{F_H} \rightarrow \mathbf{P_{FH}}$ transition was the same as in the 4 SU-form after addition of catalase (Figure 3.4-8 B, green line). However, this $\mathbf{P_{FH}}$ state is slightly red shifted exhibiting a maximum at 612 nm in the difference absorption spectrum (*minus* the **O** state).

In summary, the $\mathbf{P_H} \rightarrow \mathbf{F_H}$ conversions also occur in other types of wt C*c*Os such as the recombinantly produced wt C*c*O and the 2 SU-form of native wt C*c*O.

3.4.3 The O → P_{10} state transition in the absence of reduction equivalents

Artificially induced intermediates play an important role in understanding the mechanism of C*c*O. In the context of discovering new ways of intermediate induction we have established the formation of a novel $\mathbf{P_{10}}$ state. Next to other previously induced $\mathbf{P_H}$, $\mathbf{P_R}$ and $\mathbf{P_{CO}}$ states and the catalase-induced $\mathbf{P_{FH}}$ state of this work, the $\mathbf{P_{10}}$ state might be a genuine **P** state, representing an oxoferryl intermediate.

3.4.3.1 UV-vis spectroscopy

To characterise the properties of wt C*c*O further, the pH of C*c*O in the **O** state was shifted from pH 8 to 10 and the 4 SU-wt ATCC C*c*O at pH 10 was studied by UV-vis and EPR spectroscopy. The alkaline shift led, without addition of reduction equivalents, to an apparent **O** → **P** state transition as determined by difference absorption spectroscopy. This **P**-like state was formed from the **O** state simply by shifting the pH from pH 8 to 10. A 612 nm maximum in the difference absorption spectrum (*minus* the **O** state) was observed and this newly discovered **P** state was named the $\mathbf{P_{10}}$ state.

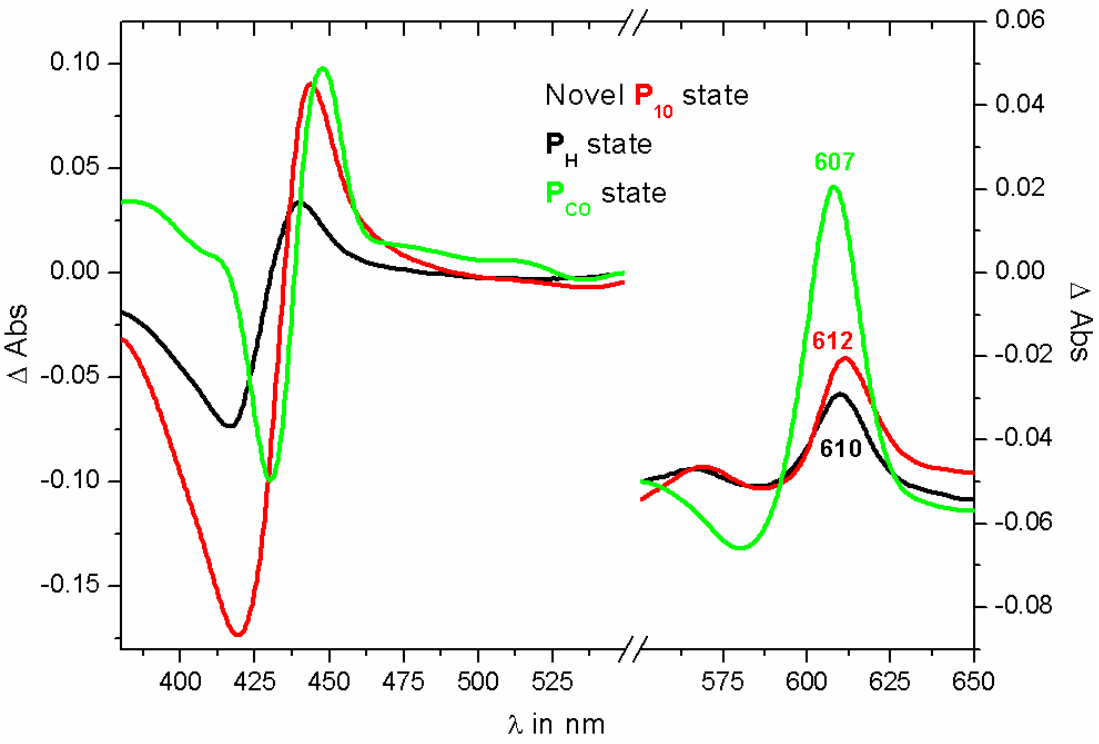

Figure 3.4-9 Difference absorption spectra of the P_{10}, P_H and P_{CO} states (*minus* the O state) of 4 SU-wt ATCC C*c*O. 10 µM of pulsed and air oxidised 4 SU-wt ATCC C*c*O samples in 10 mM KP_i, pH 8, 0.05 % LM were mixed with 100 mM glycine-OH, pH 10, 0.05 % LM for the P_{10} state, with 50 mM KP_i, pH 9, 0.05 % LM and H_2O_2 in a molar ratio 1:5 for the P_H state and with 50 mM KP_i, pH 9, 0.05 % LM and CO for the P_{CO} state.

Figure 3.4-9 compares the visible difference absorption spectrum of this $\mathbf{P_{10}}$ state with the $\mathbf{P_H}$ and $\mathbf{P_{CO}}$ state. It was not known at the time whether the $\mathbf{P_{10}}$ state contains an oxoferryl intermediate and whether it hosts an amino acid radical at Y167 similar to the H_2O_2-induced $\mathbf{P_H}$ and the catalase-induced $\mathbf{P_{FH}}$ state.

Thus, further characterisation of this novel $\mathbf{P_{10}}$ state was performed using spectroscopic methods. First, the time dependence of formation of the $\mathbf{P_{10}}$ state was determined by recording the change of the absorptions from λ = 360 nm to 800 nm after the pH 10 shift.

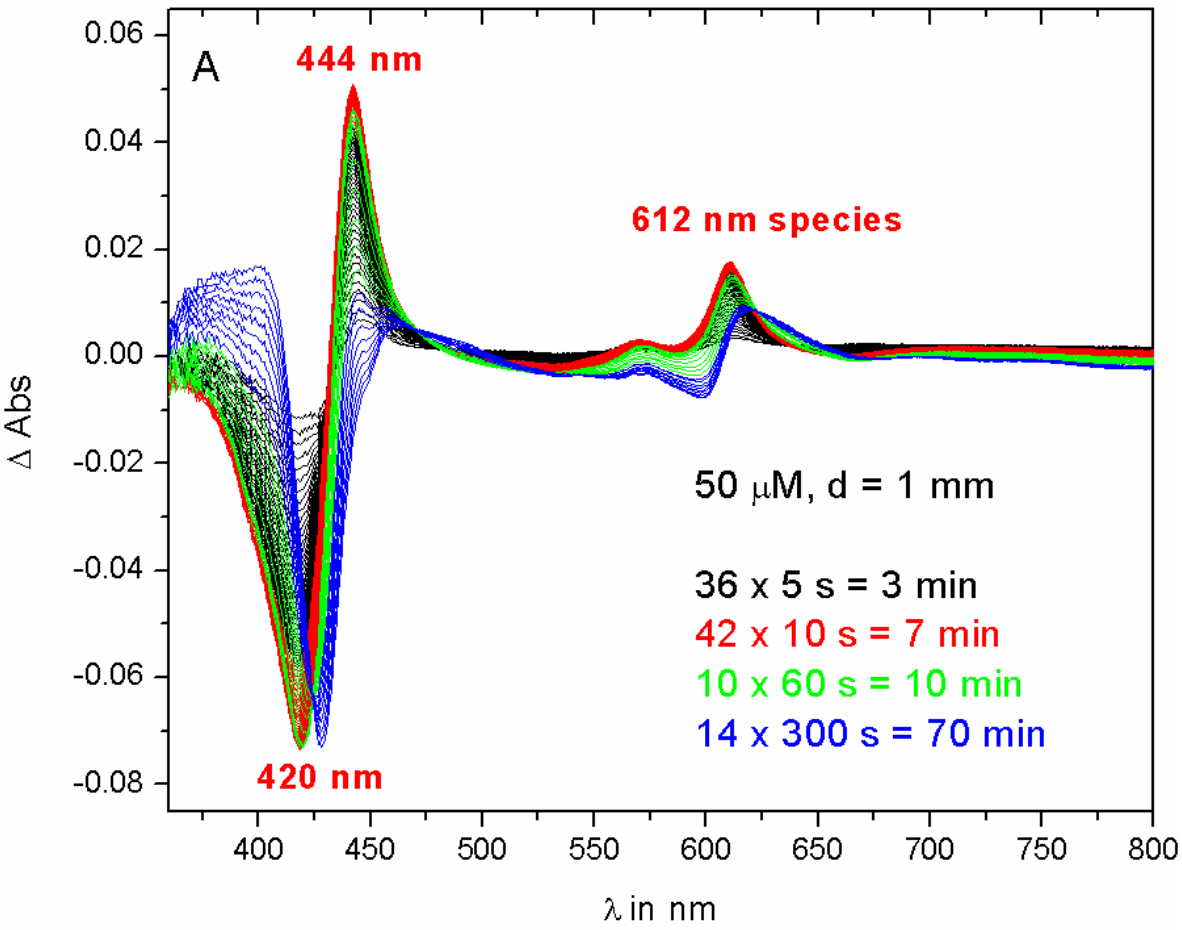

Figure 3.4-10 Time dependence of P_{10} state formation (A). 50 μM 4 SU-wt ATCC C*c*O in 10 mM KP_i, pH 8, 0.05 % LM was mixed with 100 mM glycine-OH, pH 10, 0.05 % LM. Difference absorption spectra (*minus* the O state) were recorded at time intervals (Δt) as shown. (B) and (C) enlargements, next page.

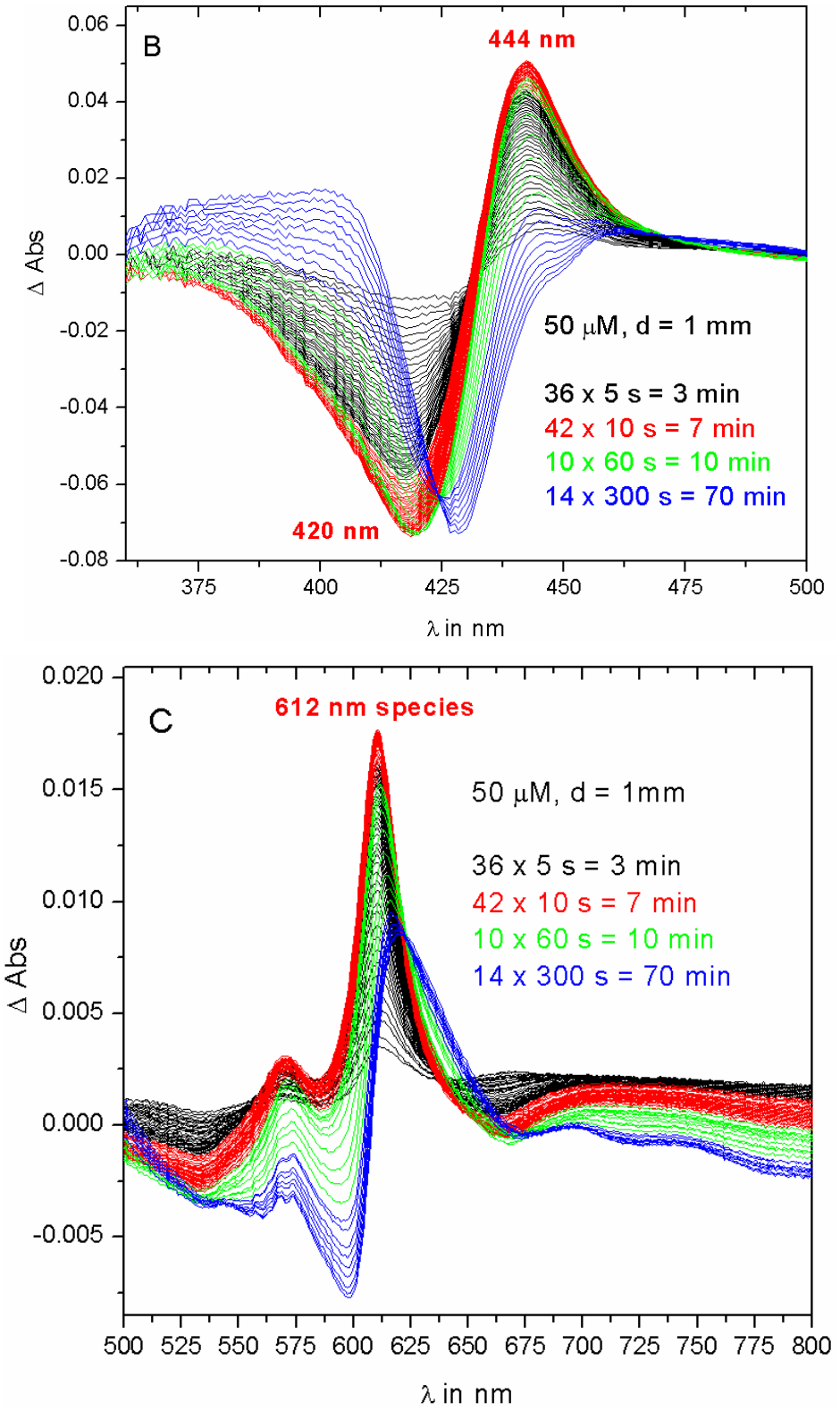

Figure 3.4-10 Time dependence of P_{10} state formation (B) and (C). 50 μM 4 SU-wt ATCC C*c*O in 10 mM KP_i, pH 8, 0.05 % LM was mixed with 100 mM glycine-OH, pH 10, 0.05 % LM. Difference absorption spectra (*minus* the O state) were recorded at time intervals (Δt) as shown. (B) and (C) show enlargements of (A), previous page.

Figure 3.4-10 displays the difference absorption spectra (*minus* the **O** state) of 50 μM C*c*O at pH 10 during different time intervals (36 times 5 s in black, 42 times 10 s in red, 10 times 60 s in green and 14 times 300 s in blue). The black and red traces show formation of the $\mathbf{P_{10}}$ state, while the green and blue traces represent the decay of the $\mathbf{P_{10}}$ state and the formation of a new species, which is red shifted compared to the maximum of the $\mathbf{P_{10}}$ state.

According to these experimental data, the formation of the $\mathbf{P_{10}}$ state is rather slow compared to the $\mathbf{P_H}$ state formation. 50 μM of 4 SU-wt ATCC C*c*O require 300 s at pH 10 to form the $\mathbf{P_{10}}$ state completely and 10 μM of 4 SU-wt ATCC C*c*O require 800 s to reach the $\mathbf{P_{10}}$ state completely (Figure 3.4-11, not the OD of the 612 nm species is shown, but the product of the concentration and the pathlength of the cuvette).

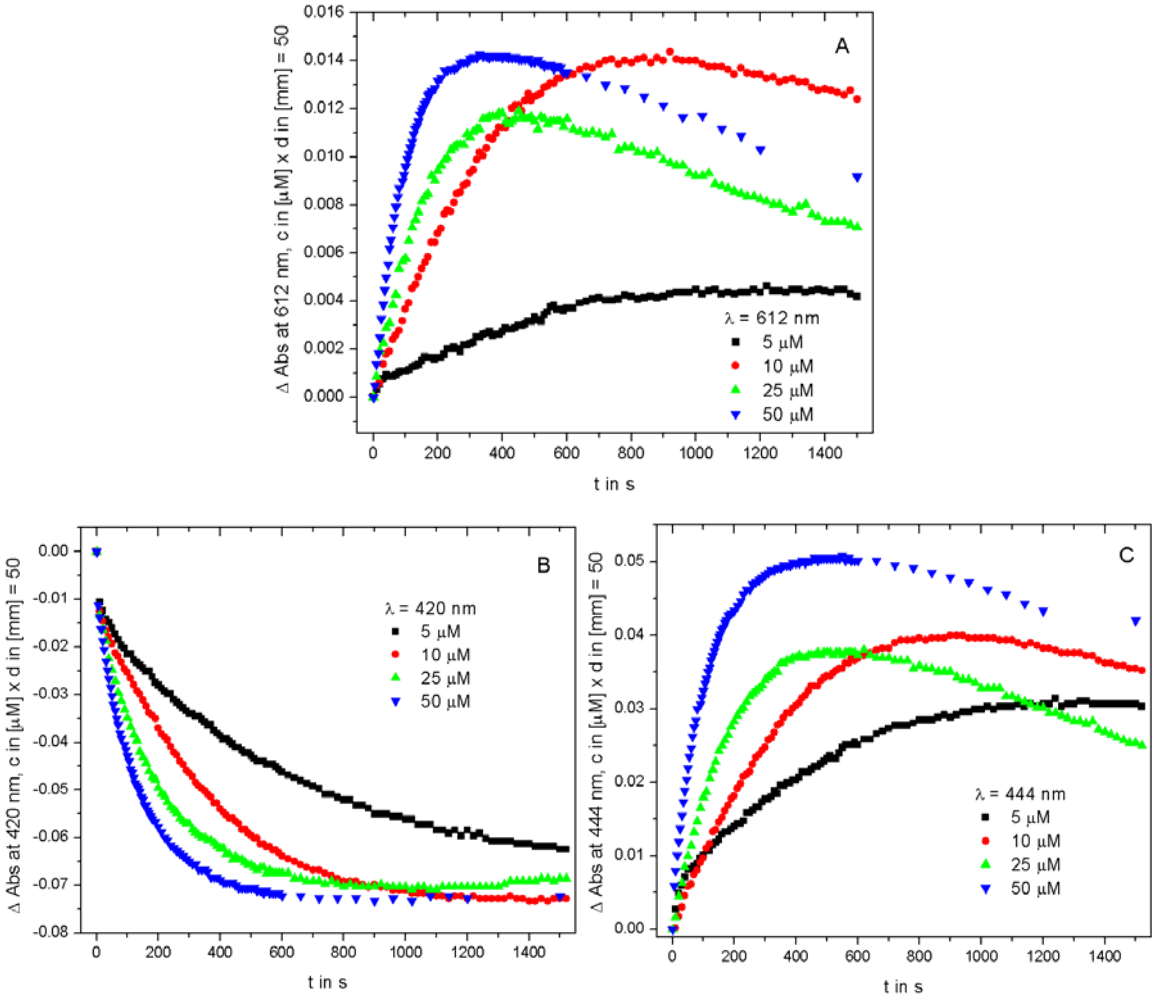

Figure 3.4-11 Kinetics of the P_{10} state formation in dependence of the concentration of C*c*O. (A) at λ = 612 nm (B) 419 nm and (C) 444 nm.

The speed of formation and stability of the **P_{10}** state depend on the concentration of C*c*O. The time dependence of the absorption changes at λ = 612 nm, 420 nm and 444 nm of 5 μM, 10 μM, 25 μM and 50 μM C*c*O was analysed. As is seen, the **P_{10}** state is formed more rapidly at higher concentrations of C*c*O. In addition, the **P_{10}** state decays faster at high C*c*O concentrations, while the formation of this state is still observable at the lower concentrations of C*c*O.

A logarithmic plot using the time dependence of the 612 nm species formation did not show a straight line, indicating that the apparent **O** → **P_{10}** state transition is not a monomolecular reaction (Figure 3.4-12).

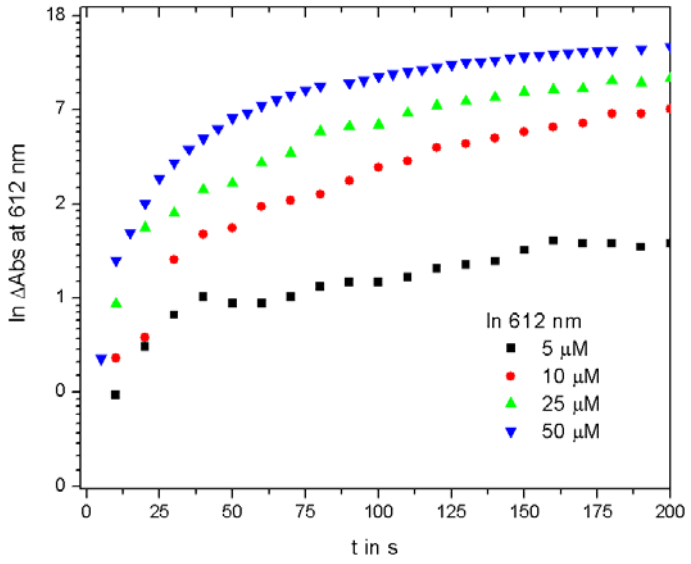

Figure 3.4-12 Logarithmic plot of the data points at λ = 612 nm from 0 – 200 s. The plot indicates that the time dependence of P_{10} state formation does not follow first order kinetics.

The initial rates of the **O** → **P_{10}** state transition depend on the concentration of C*c*O and Figure 3.4-13 shows the exponentially increasing initial rates with increasing concentrations of 4 SU-wt ATCC C*c*O.

The velocity of the reaction was also shown to be dependent on the pH of the alkaline buffer solutions. Low alkaline pH values such as pH 8.5 are sufficient to start a slow formation of the **P_{10}** state, however the velocity exponentially increases at higher pH values up to 10 (Figure 3.4-14).

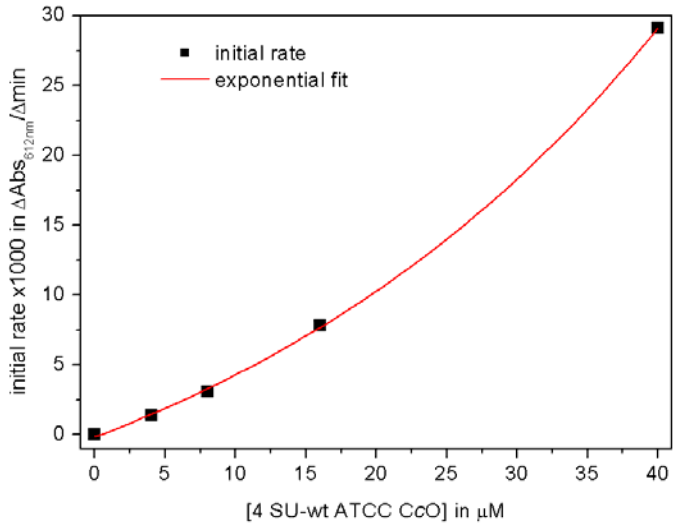

Figure 3.4-13 Initial rate of P_{10} state formation as a function of [4 SU-wt ATCC C*c*O]. 4-40 μM 4 SU-wt ATCC C*c*O in 10 mM KP_i, pH 8, 0.05 % LM were mixed with 100 mM glycine-OH, pH 10, 0.05 % LM. The increase in absorbance at λ = 612 nm was recorded.

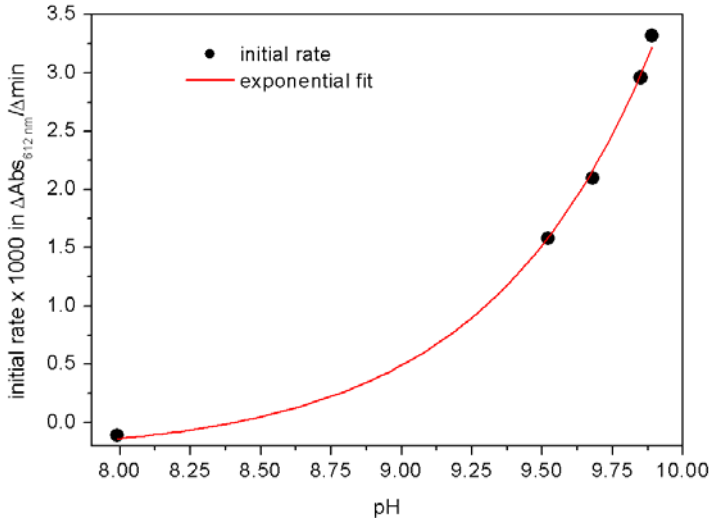

Figure 3.4-14 Initial rate of P_{10} state formation as a function of pH value. 5 μM 4 SU-wt ATCC C*c*O in 10 mM KP_i, pH 8, 0.05 % LM were mixed with 0-100 mM glycine-OH, pH 10, 0.05 % LM. The increase in absorbance at λ = 612 nm was recorded.

It is known from other proteins that incubation at a pH value of pH 10 destroys or impairs their enzymatic activity. In order to determine the stability of the 4 SU-wt ATCC C*c*O at pH 10 the protein was incubated in 100 mM KP_i, pH 8 or in 100 mM glycine-OH, pH 10 for 2 hours. Both samples were tested in two cyt *c* oxidation activity assays, at pH 8 (30 mM KP_i, pH 8) and at pH 10 (30 mM glycine-OH, pH 10). The results showed no difference in the activities between the control incubated at pH 8 and the sample incubated at pH 10 - in either assay (data not shown).

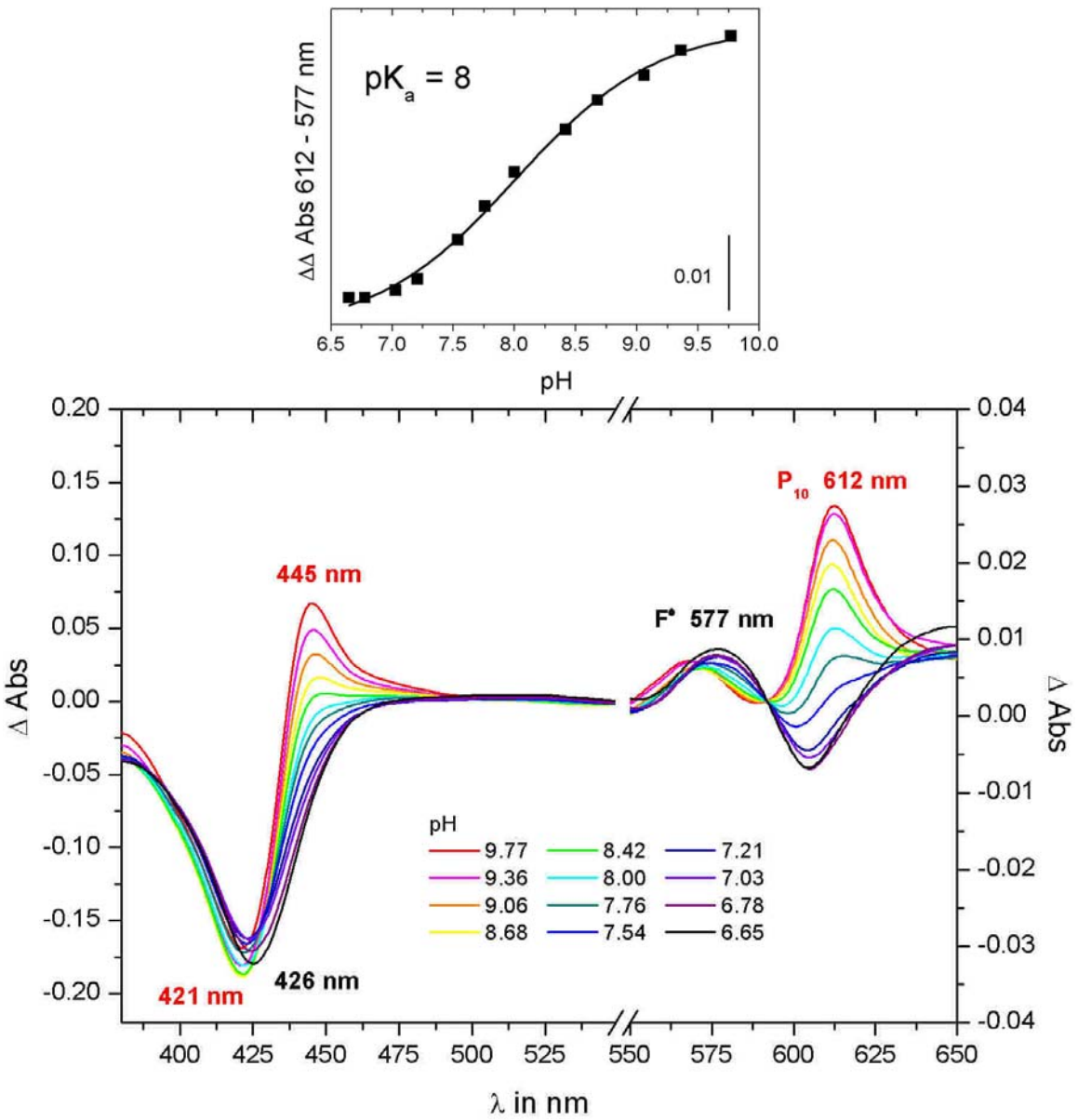

Figure 3.4-15 Difference absorption spectra (*minus* the O state) of the transition of the P_{10} state to the $F^{\bullet}$ state of 4 SU-wt ATCC C*c*O. 10 µM 4 SU-wt ATCC C*c*O in 10 mM KP_i, pH 8, 0.05 % LM was mixed with 100 mM glycine-OH, pH 10, 0.05 % LM and incubated for 20 min. Then the P_{10} state was titrated with 0 – 150 mM Mes-OH, pH 6 and each spectrum recorded 3 min after mixing. The pH was measured using a pH electrode. The isosbestic point of the $P_{10} \rightarrow F^{\bullet}$ transition occurs at λ = 592 nm. The inset shows the fit of the pK_a value calculation.

In order to confirm that the **P_{10}** state is a real **P** state it was tested whether the **P_{10}** state forms the **$F^{\bullet}$** at low pH values as expected for the standard **P** state, when the pH value is shifted to pH < 7 (as described in chapter 3.1.5). The **P_{10}** state was titrated using different amounts of pH 6 buffer and single spectra of stable intermediates resulting from the acid titration of the **P_{10}** state to the

electronically equal $\mathbf{F}^{\bullet}$ state were recorded (the error of dilution was corrected, Figure 3.4-15). The 612 nm maximum of the $\mathbf{P_{10}}$ state in the difference absorption spectrum (*minus* the **O** state) decreased during acidification. In contrast, the maximum at 577 nm increased below pH 8 with decreasing pH values. The isosbestic point of the $\mathbf{P_{10}}$ state → $\mathbf{F}^{\bullet}$ state transition was determined to be at the wavelength of λ = 592 nm, and the pK_a value of this transition is roughly 8 as calculated using the Poisson-Boltzmann equation (see inset Figure 3.4-15).

In summary, the novel $\mathbf{P_{10}}$ state shows a maximum at λ = 612 nm in the difference absorption spectra. This state resembles standard **P** states such as the $\mathbf{P_{CO}}$, $\mathbf{P_H}$ and $\mathbf{P_R}$ state. However, the $\mathbf{P_{10}}$ state evolves from the **O** state without addition of any reduction equivalents. Simply, the alkaline shift from pH 8 to 10 induces $\mathbf{P_{10}}$ state formation. The $\mathbf{P_{10}}$ → $\mathbf{F}^{\bullet}$ state transition by lowering the pH value to pH 6 displays an isosbestic point at λ = 592 nm and a pK_a value of 8. The incubation of the 4 SU-wt ATCC C*c*O at pH 10 for two hours does not reduce the catalytic activity of the protein compared to the control.

3.4.3.2 EPR spectroscopy

To characterise the $\mathbf{P_{10}}$ state further, EPR spectroscopic studies were performed to look for potential radical species in the 4 SU-wt ATCC C*c*O at pH 10. In Figure 3.4-16 the EPR spectrum of the $\mathbf{P_{10}}$ state induced by 100 mM glycine-OH, pH 10 (red line), is compared with the H_2O_2-induced $\mathbf{P_H}$ state (black line). In addition to the EPR signals from the dinuclear Cu_A centre and the low-spin haem *a* of the **O** state (magenta line), an additional narrow EPR signal was observed at g ~ 2 after addition of 1:1 H_2O_2 for the $\mathbf{P_H}$ state or after treatment with 100 mM pH 10 buffer for the $\mathbf{P_{10}}$ state. This organic radical signal of the $\mathbf{P_{10}}$ state was assigned to the tyrosyl Y167 radical such as that in the $\mathbf{P_H}$ state. This EPR signal is identical, in terms of overall line width and the partially resolved hyperfine structure, with the signal observed in both the $\mathbf{P_H}$ state and the $\mathbf{P_{10}}$ state (data not shown). The only difference is a shift of the signal intensity relative to the Cu_A-EPR signal in the $\mathbf{P_{10}}$ state, and in terms of EPR spectroscopic properties the data demonstrate the identity of the $\mathbf{P_H}$ and $\mathbf{P_{10}}$ states of the 4 SU-wt ATCC C*c*O.

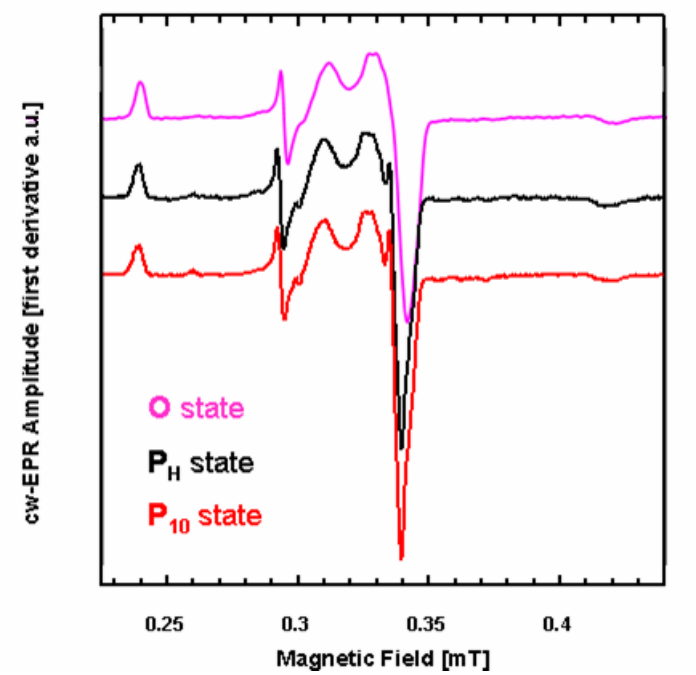

Figure 3.4-16 EPR spectra of the P_H and P_{10} states of 4 SU-wt ATCC C*c*O. 200 µM oxidised C*c*O (magenta) in 50 mM KP_i, pH 9, 0.05 % LM and H_2O_2 was mixed in a molar ratio of 1:1 at 4°C (P_H state, black). 200 µM oxidised C*c*O in 10 mM KP_i, pH 8, 0.05 % LM was mixed with 100 mM glycine-OH, pH 10, 0.05 % LM (P_{10} state, red). The sample was transferred immediately to a suprasil quartz EPR tube, frozen in liquid nitrogen and X-Band continuous-wave EPR spectra were recorded at 10 K.

3.4.3.3 Induction of the P_{10} state in variants

Variant W272F

For further characterisation of the **P_{10}** state, the pH 10 reaction of the variant W272F was investigated by UV-vis spectroscopy, because variant W272F is inactive and not able to form the tyrosyl Y167 radical.

Y167 is not part of the binuclear site, but it is H-bonded to residue W272, which is next to the binuclear centre and thus part of the binuclear site. The absorption behaviour of 4 SU-wt rec C*c*O and variant W272F during pH 10 treatment is depicted in Figure 3.4-17. Both show characteristic absorption differences after induction of the **P_{10}** state. The 4 SU-wt rec C*c*O forms a **P_{10}** state having a maximum at 612 nm in the difference absorption spectrum (*minus* the **O** state) (Figure 3.4-17, black line) and addition of a pH 6 buffer to the 4 SU-wt rec C*c*O sample induces the **$F^{\bullet}$** state having a maximum at 578 nm (Figure 3.4-17, grey line).

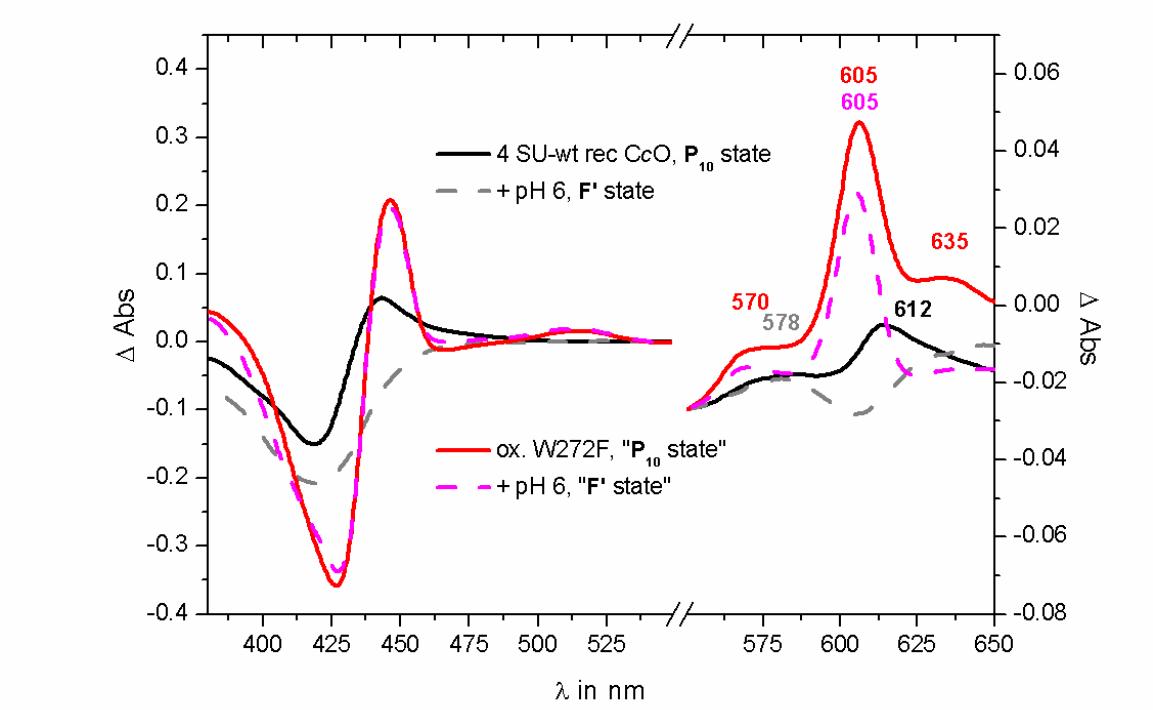

Figure 3.4-17 Difference absorption spectra (*minus* the O state) of the P_{10} and $F^{\bullet}$ state from 4 SU-wt rec C*c*O and the variant W272F. 10 µM 4 SU-wt rec C*c*O in 10 mM KP_i, pH 8, 0.05 % LM was mixed with 100 mM glycine-OH, pH 10, 0.05 % LM and incubated for 20 min (—). Then the P_{10} state was mixed with 150 mM Mes-OH, pH 6 and the spectrum recorded after 3 min (- - -). Variant W272F was oxidised with ferricyanide and subjected to gel filtration to remove ferri/ferrocyanide.

However, variant W272F exhibited a 605 nm maximum and extra maxima at roughly 570 nm and 635 nm instead of a single 612 nm maximum at pH 10, indicating the reduction of the low-spin haem *a* and a probable reduction of Cu_B (Figure 3.4-17, red line). Shifting the pH from 10 to 6 for variant W272F did not result in $\mathbf{F}^{\bullet}$ state formation (Figure 3.4-17, magenta line). The pH 10-induced 605 nm maximum was not changed by the shift to pH 6, indicating a redox state which is independent of the protonation state within the protein. The extra maximum ~ 635 nm of the "$\mathbf{P_{10}}$ state" of variant W272F is pH-dependent, because at pH 6 the extra maximum has vanished in the difference absorption spectrum.

In summary, the variant W272F, which is not able to form any stable radical, shows reduction of the low-spin haem *a* and possible reduction of Cu_B at pH 10 instead of $\mathbf{P_{10}}$ state formation as determined by UV-vis spectroscopy.

Variants of the D/K-pathway and the variant Y167F

In order to determine the role of the proton pathways of wt C*c*O in $\mathbf{P_{10}}$ state development, the effect of alkaline pH on variants of the D/K-pathway and variant Y167F was studied by difference absorption spectroscopy. The 4 SU-wt rec C*c*O and D/K-pathway variants and variant Y167F were pulsed with dithionite and reoxidised prior to the induction of the $\mathbf{P_{10}}$ state. Figure 3.4-18 shows the difference absorption spectra (*minus* the **O** state) at pH 10 of the 4 SU-wt rec C*c*O compared to the D/K-pathway variants and variant Y167F. The 4 SU-wt rec C*c*O forms the $\mathbf{P_{10}}$ state having a maximum at 612 nm in the difference absorption spectrum and then forms the $\mathbf{F^{\bullet}}$ state upon decreasing the pH from 10 to 6 (Figure 3.4-18, black lines).

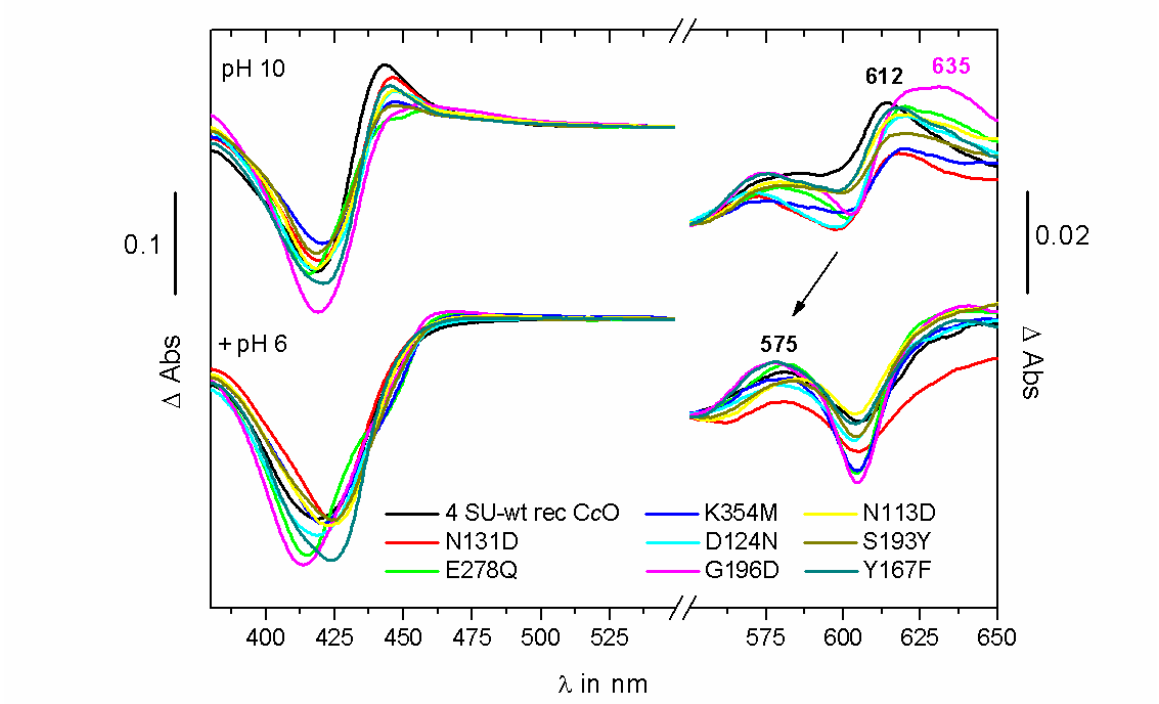

Figure 3.4-18 Difference absorption spectra of the P_{10} and $F^{\bullet}$ state (*minus* the O state) of 4 SU-wt rec C*c*O and the variants N131D, E278Q, K354M, D124N, G196D, N113D, S193Y and Y167F. 10 μM pulsed and air-oxidised 4 SU-wt rec C*c*O in 10 mM KP_i, pH 8, 0.05 % LM was mixed with 100 mM glycine-OH, pH 10, 0.05 % LM and incubated for 20 min. Then the solution containing the P_{10} state was mixed with 150 mM Mes-OH, pH 6 and the spectrum recorded after 3 min. Variants E278Q and K354M were partly reduced after the pulsing procedure.

All D/K-pathway variants and variant Y167F form a $\mathbf{P_{10}}$-like state having a maximum at 612 nm in the difference spectra (*minus* the **O** state) (Figure 3.4-18). However, additional shoulders appear in the range of λ ~ 635 nm resulting in broad maxima of mixed species. Thus, the 612 nm maximum of the D/K-pathway variants and variant Y167F is red shifted compared to the maximum of the 4 SU-wt rec C*c*O. The induced $\mathbf{F^{\bullet}}$ states of D/K-pathway variants and variant Y167F have similar absorption spectra as the spectrum from the 4 SU-wt rec C*c*O. In summary,

D/K-pathway mutations and variation of residue Y167 to Y167F do not influence formation of the **P_{10}** state.

3.4.4 Detection of dioxygen production in H_2O_2-induced intermediates

To obtain further insights into the properties of the binuclear centre, the 4 SU-wt ATCC C*c*O reaction cycle was investigated under the artificial conditions of excess H_2O_2 using a Clark-type oxygen electrode.

In general, the soluble protein cytochrome *c* peroxidase (C*c*P) and catalases are known to decompose H_2O_2. The catalytic activity of catalase results in the disproportion of two H_2O_2 to form two H_2O and O_2 ($2\ H_2O_2 \rightarrow 2\ H_2O + O_2$). The development of O_2 can be followed using an oxygen electrode. C*c*P catalyses the decomposition of H_2O_2 to H_2O and the electron donor of this redox reactions are two reduced molecules of cyt *c*. Accordingly, the peroxidase cycle of wt C*c*O has been well described and discussed (Orii, 1982), which leads to the assumption that wt C*c*O is also able to reduce H_2O_2 instead of O_2.

It will be shown here that wt C*c*O in the presence of excess H_2O_2 releases O_2 and thus may perform a catalase-like turnover; however, side products such as superoxide or hydroxyl radicals might be produced as precursors of these O_2 molecules.

3.4.4.1 Stoichiometric production of dioxygen – the catalase-like mechanism

In order to investigate the catalase-type mechanism of C*c*O excess amounts of H_2O_2 were added to the protein sample and the reaction was followed using an oxygen electrode. Mixing excess amounts of H_2O_2 (1:10 to 1:500) to C*c*O induces the **F_H** state resulting in a stable broad 580 nm maximum in the difference absorption spectrum (*minus* the **O** state). The induction of this state has not been recorded previously using an oxygen electrode.

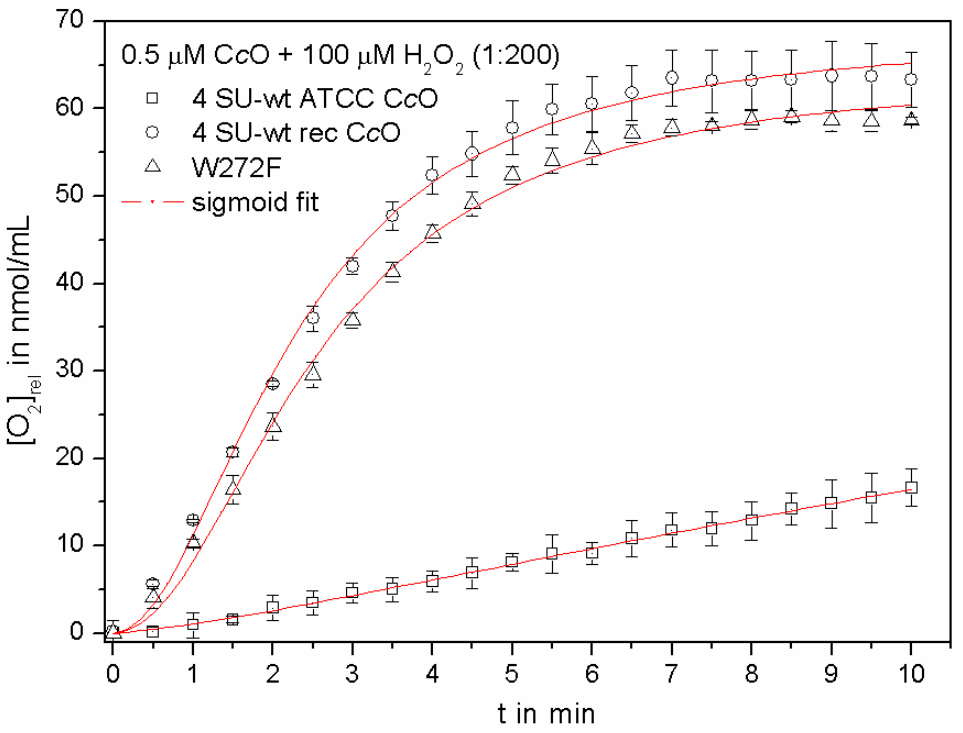

Figure 3.4-19 Dioxygen production by different wt C*c*Os after F_H state induction. Time dependence of production of dioxygen by 4 SU-wt ATCC C*c*O (squares), 4 SU-wt rec C*c*O (circles) and variant W272F (triangles). 0.5 µM C*c*O was mixed with 100 µM H_2O_2 at a molar ratio of 1:200 (= 100 nmol H_2O_2). (The measured values for O_2 production should show 50 % of the used amount of H_2O_2, however they show 60 – 65 %)

Incubation of $\mathbf{F_H}$ states by excess H_2O_2 (1:200) in 4 SU-wt ATCC C*c*O (Figure 3.4-19, squares), 4 SU-wt rec C*c*O (circles) and in variant W272F (triangles) was accompanied by O_2 formation and the O_2 concentration increases continuously after H_2O_2 addition as determined with an oxygen electrode. This result shows that the O_2 release under $\mathbf{F_H}$ inducing conditions is a property of the recombinantly produced 4 SU-wt rec C*c*O and the variant W272F. The 4 SU-wt ATCC C*c*O also shows O_2 production, however, the speed of release of O_2 is decreased. Each curve was analysed using a sigmoidal fit. These traces represent, first, the initial formation of the $\mathbf{F_H}$ state, which is then followed by O_2 production. The 4 SU-wt rec C*c*O and inactive variant W272F produced dioxygen faster than 4 SU-wt ATCC C*c*O indicating the extra function of the recombinantly produced 4 SU-wt rec C*c*O and variant W272F.

The determined O_2 production was not influenced by the addition of ferricyanide, but was inhibited at low pH (pH 6) and by azide (data not shown).

Theoretically, C*c*O cleaves the O^--O^- bond of H_2O_2 and the next one-electron input from an H_2O_2 to C*c*O leads to $\mathbf{F_H}$ state formation and to the production of one superoxide $^{\bullet}O_2^-$ molecule (reaction for the one-electron donation: $H_2O_2 \rightarrow 1\ e^- + 2\ H^+ + {}^{\bullet}O_2^-$).

In summary, wt C*c*O is able to convert H_2O_2 molecules to H_2O and O_2, similar to catalase ($2\ H_2O_2 \rightarrow 2\ H_2O + O_2$). The production of O_2 after H_2O_2 treatment seems to be a side reaction of the binuclear centre, which is not influenced by ferricyanide as an electron acceptor. This O_2-producing side reaction is more advanced in the inactive variant W272F, which provides evidence that only the presence of the prosthetic groups, mainly the haem a_3 group, is necessary for the H_2O_2 decomposition.

3.4.4.2 Determination of the Michaelis-Menten constant and the turnover number

In order to determine the Michaelis-Menten constant and the turnover number of the catalase-like catalytic cycle of wt C*c*O, the time dependence of the O_2 formation was recorded using different types of C*c*Os including 4 SU-wt rec C*c*O, the bovine C*c*O and the *cbb*$_3$-C*c*O from *Pseudomonas stutzeri.* Table 3.4-1 shows the kinetic data of H_2O_2 decomposition by the different C*c*Os.

Table 3.4-1 K_M values and rate constants of H_2O_2 decomposition by different types of wt C*c*Os.

C*c*O	K_M [μM]	k_2 [O_2/min]
4 SU-wt ATCC *aa*$_3$-C*c*O *P. denitrificans*	225 +/- 45	3.5 +/- 0.3
4 SU-wt rec *aa*$_3$-C*c*O *P. denitrificans*	143 +/- 13	37.6 +/- 1.2
cbb$_3$-C*c*O *P. stutzeri*	2923 +/- 146	20.6 +/- 0.4
aa$_3$-C*c*O bovine	3372	10.5

The K_M and k_2 values of 4 SU-wt ATCC C*c*O, 4 SU-wt rec C*c*O, *cbb*$_3$-C*c*O from *P. stutzeri* and bovine C*c*O were determined. The K_M values of the *P. denitrificans* enzymes lie in the micromolar range, whereas *P. stutzeri* and bovine enzymes have a value in the milimolar range. The 4 SU-wt rec C*c*O shows the highest turnover rate, producing 37.6 +/- 1.2 O_2/min. The 4 SU-wt ATCC C*c*O is less O_2-leaky, producing only 3.5 +/- 0.3 O_2/min. The *P. stutzeri* and bovine enzymes have lower affinities for H_2O_2 (K_M ~ mM), but they have similar turnover rates of roughly 10 - 20 O_2/min.

3.4.4.3 Qualitative assay using other haem-copper oxidases

In order to determine the ability of other wt C*c*Os to form O_2 from H_2O_2, a qualitative commercial H_2O_2-decomposition assay was performed using different types of oxidases such as the bovine C*c*O or the *ba*$_3$ quinol oxidase from *P. denitrificans*. All of these C*c*Os are cytochromes which contain a haem a_3 group (or a b_3 group) and a Cu_B ion in subunit I forming the binuclear centre. Haem containing cytochromes catalyse the decomposition of H_2O_2 because of the complexed

redox-active Fe ion. Several types of oxidases were investigated in order to find out how wide spread the O_2 production after H_2O_2 treatment of high-spin haem-containing enzymes is (Figure 3.4-20). The control reaction in the H_2O_2 decomposition assay was performed using catalase because catalases are optimised enzymes for the decomposition of H_2O_2 to O_2 and H_2O. All tested C*c*Os showed a catalase-like activity. However, the 4 SU-wt rec C*c*O and the variant W272F, which were purified using an Fv fragment, displayed the highest reaction rates.

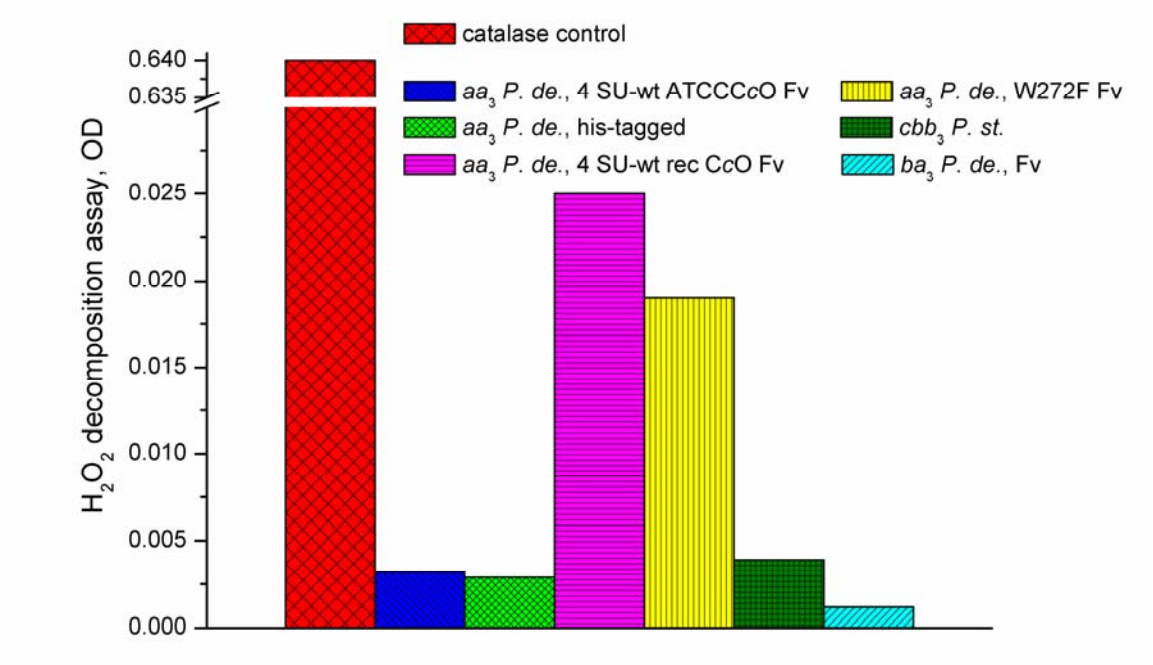

Figure 3.4-20 H_2O_2 decomposition activity of different C*c*Os. H_2O_2 decomposition was measured using the Sigma catalase activity kit (modified assay). *P.de. = P. denitrificans* (4 SU-C*c*Os), *P. st =: P. stutzeri.*

The 4 SU-wt rec-his C*c*O from *P. denitrificans* (kindly provided by Prof. Bernd Ludwig, JWG University of Frankfurt), which was purified via a polyhistidyl tag, showed a low O_2 leakiness, similar to that of the 4 SU-wt ATCC C*c*O, the *cbb*$_3$-C*c*O from *P. stutzeri* and the *ba*$_3$ quinol oxidase from *P. denitrificans*.

In summary, the catalase-like activity of oxidases is a common side reaction. Recombinantly produced wt C*c*Os, which were purified using Fv fragments, display increased O_2 production compared with the native C*c*Os.

3.5 Determination of the electron pathway from Y167 to the binuclear site

After characterising the functional mechanism of formation of different intermediates of C*c*O, in the following chapter, the importance of key amino acid residues for these reactions is investigated. In order to identify the electron pathway from Y167 to the binuclear site, a mutagenesis study was performed to determine the participating amino acids. Low amounts of H_2O_2 induce the $\mathbf{P_H/F^{\bullet}_H}$ states, representing a two-electron reduced intermediate of wt C*c*O, as already described in chapter 3.1. The $\mathbf{P_H/F^{\bullet}_H}$ intermediate state is an oxoferryl state and the dioxygen bond is already cleaved, four electrons are required. Previous work has shown that the haem a_3-Fe ion of the $\mathbf{P_H/F^{\bullet}_H}$ state has an oxidation number +IV, forming the $Fe^{IV}=O^{2-}$ oxoferryl intermediate, Cu^{II}_B is oxidised and Y167 hosts a stable amino acid radical. However, Y167 is not directly part of the binuclear site and the missing electron for dioxygen reduction has to be transferred along a distinct electron pathway.

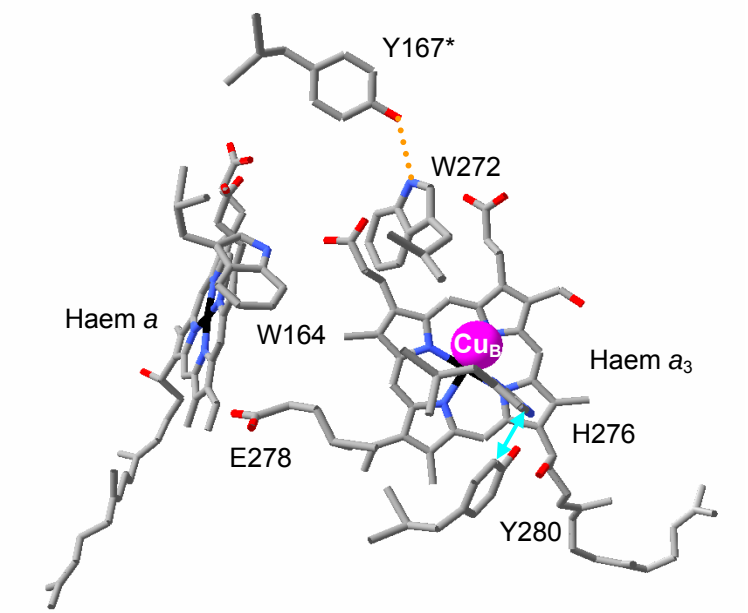

Figure 3.5-1 Section of the binuclear centre of CcO (the Y280-H276 link is indicated as a light blue double arrow, pdb-file: 1ar1, Ostermeier *et al*., 1997).

Therefore, in tracing the electron pathway of the H_2O_2-induced formation of the $\mathbf{P_H/F^{\bullet}_H}$ state, W272 is proposed to be the primary electron donor, because it is part of the binuclear site and it provides an H-bond to Y167 (Figure 3.5-1, orange). The missing electron of the resulting W272 cation/neutral radical is thought to be replenished by Y167. Finally, Y167 hosts a stable radical in

the $\mathbf{P_H/F^{\bullet}_H}$ states, however, Y280 (Figure 3.5-1) is suggested to host the radical in the natural cycle, because the variant Y167F is catalytically highly active.

3.5.1 Variants of W272

To characterise the primary electron donor of the fourth electron several W272 variants (Table 3.5-1) were produced. The variant W272F was designed in order to disrupt the proposed electron transfer pathway, because a phenylalanine residue (F) is not able to stabilise a single electron. Indeed, the F-variant does not function as a stable host for a radical.

Table 3.5-1 Variant C*c*Os of the binuclear centre. All variant enzymes have mutations nearby the binuclear site of C*c*O. The purpose of the variant production and the turnover activity of the variants are shown compared with the 4 SU-wt rec C*c*O.

C*c*O	Purpose of variant production	Turnover in % wt rec
4 SU-wt rec C*c*O	-	100
W272F	Loss of function, no Y167 radical via W272F	< 1
W272Y	Y167* radical via W272Y*	< 1
W272H	Y167* radical via W272H*	< 1
W272F/Y167F	Loss of function, no Y167 radical	< 1
W272Y/Y167F	Gain of function, stable W272Y* radical	< 1
W272H/Y167F	Gain of function, stable W272H* radical	< 1

On the other hand, it is known that tyrosines (Y) and histidines (H) stabilise radicals through mesomerisation and delocalisation of the aromatic π electron system (Lassmann *et al.*, 1999; Lassmann *et al.*, 2000; Biglino *et al.*, 2006). The electron pathway from Y167 to the binuclear site was assumed to work in the variants W272Y and W272H and the organic radical signal was expected at Y167*.

Based on the variant Y167F (Budiman *et al.*, 2004), which does not show the tyrosyl Y167 radical signal, double mutations including residues W272Y or W272H were considered to potentially host the stable amino acid radical at W272Y* or W272H*. Thus, the variants W27F; W272Y and W272H; and the double variants Y167F/W272F; Y167F/W272Y and Y167F/W272H were produced and the turnover of all variants was determined and compared with that of the 4 SU-wt rec C*c*O (Table 3.5-1).

Including the variant W272F, none of the variants having a W272 mutation, show turnover. All W272 variants are inactive, “dead”, enzymes. Even the variants W272Y and W272H are inactive,

although is was speculated that these variants are partially active. Accordingly, all double variants W272F/Y167F, W272Y/Y167F and W272H/Y167F are also enzymatically inactive.

3.5.1.1 UV-vis spectroscopy

In order to determine the ability of the inactive W272 variants to form $\mathbf{P_H/F^{\bullet}_H}$ states these variants were studied by UV-vis spectroscopy. The difference absorption spectra (*minus* the **O** state) show the results of attempts to demonstrate $\mathbf{P_H}$ and $\mathbf{F^{\bullet}_H}$ state formation of the variants W272F, W272Y, W272H, W272F/Y167F, W272Y/Y167F, W272H/Y167F compared with the 4 SU-wt rec C*c*O (Figure 3.5-2) and with the variant Y167F (Budiman *et al*., 2004). The results of the experiments at pH 9 are depicted in Figure 3.5-2 and those at pH 6 are shown in Figure 3.5-3, respectively.

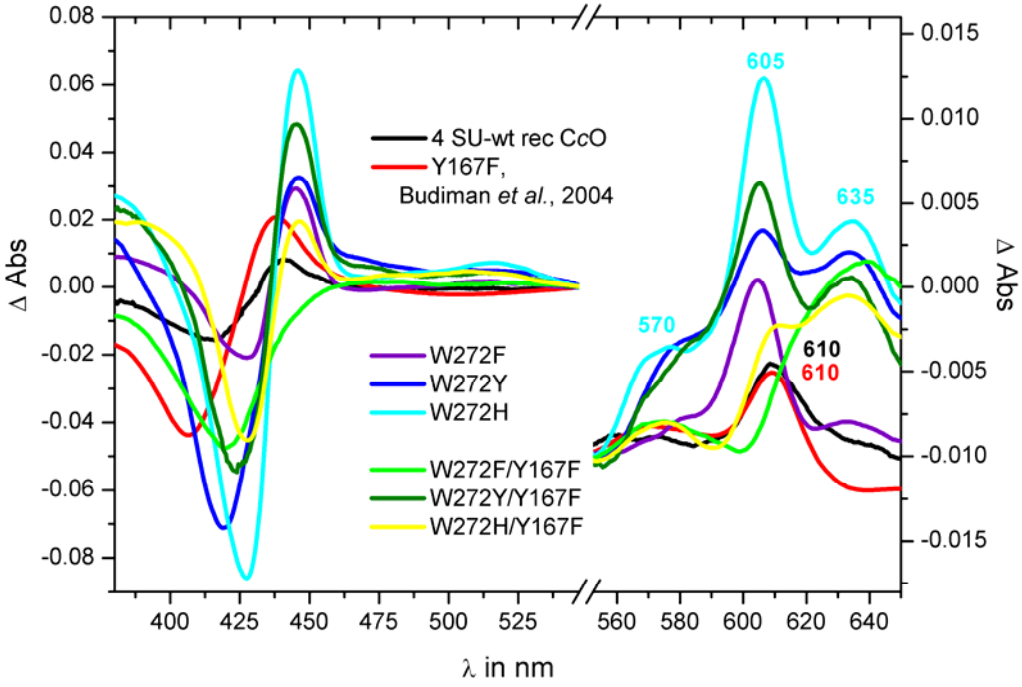

Figure 3.5-2 Difference absorption spectra (*minus* the O state) of P_H states of the variants W272F, W272Y, W272H, W272F/Y167F, W272Y/Y167F, W272H/Y167F compared with the 4 SU-wt rec C*c*O and the variant Y167F (Budiman *et al*., 2004). 10 µM oxidised C*c*O in 50 mM KP_i, pH 9, 0.05 % LM were mixed with H_2O_2 in a molar ratio of 1:2.

The 4 SU-wt rec C*c*O forms the $\mathbf{P_H}$ state after H_2O_2 treatment at a molar ratio of 1:2 at pH 9, having a 610 nm species in the difference absorption spectrum (*minus* the **O** state) (Figure 3.5-2, black line) as already introduced in chapter 3.1. In addition, the variant Y167F was also able to generate a standard $\mathbf{P_H}$ state as determined by UV-vis spectroscopy (Budiman *et al.*, 2004, red line). However, the W272 variants have extra maxima at λ = 570 nm and at λ = 635 nm after 1:2-molar H_2O_2 treatment at pH 9. The maximum at 610 nm of the 4 SU-wt rec C*c*O and variant

Y167F were not observed with the W272 variants. The maximum is shifted to λ = 605 nm, which is indicative of reduction of the low-spin haem *a*. The Soret regions of all W272 type variants were different from the absorbances of the 4 SU-wt rec C*c*O and the variant Y167F. The Soret minima and maxima were both red shifted as compared to the wild type signal. The Soret maximum of the W272 type variants is shifted to 445 nm, indicating again low-spin haem *a* reduction. The formation of the 605 nm maximum (and of the 445 nm maximum) using W272 variants was more obvious when the experiment was performed at pH 6 (Figure 3.5-3).

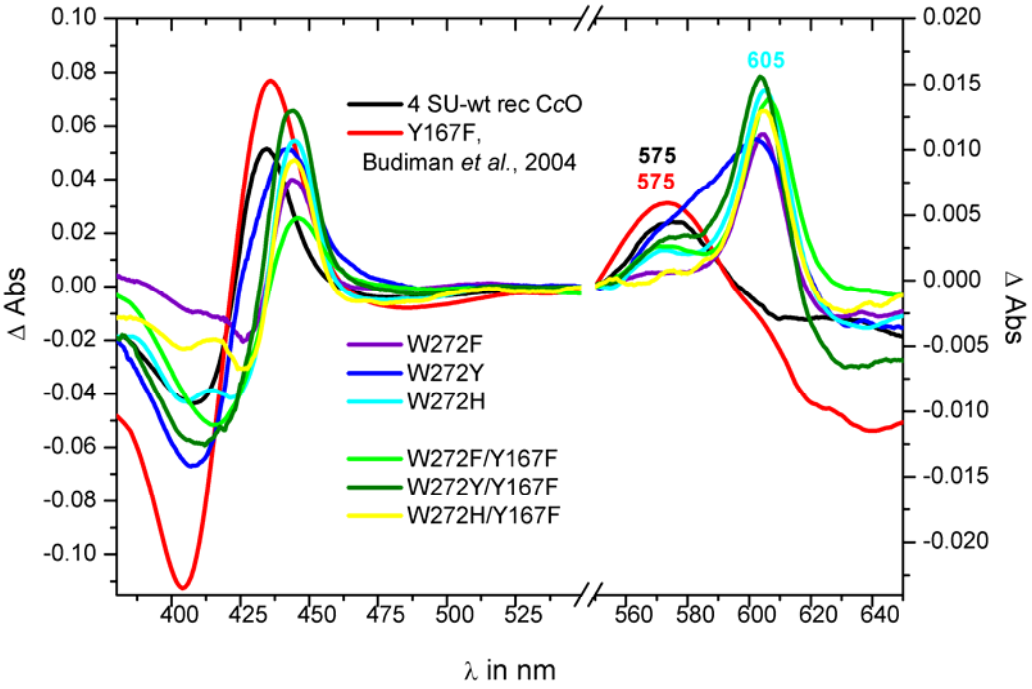

Figure 3.5-3 Difference absorption spectra (*minus* the O state) of $F^{\bullet}_{H}$ states of the variants W272F, W272Y, W272H, W272F/Y167F, W272Y/Y167F, W272H/Y167F compared with the 4 SU wt rec C*c*O and the variant Y167F (Budiman *et al*., 2004). 10 µM oxidised C*c*O in 50 mM Mes-OH, pH 6, 0.05 % LM were mixed with H_2O_2 in a molar ratio of 1:2.

The W272 variants do not show $\mathbf{F^{\bullet}_{H}}$ state generation as indicated by the absence of a 575 nm maximum (Figure 3.5-3). Instead, they exhibit the same 605 nm maximum as at pH 9, but without having the extra maximum at 635 nm. The Soret region of all W272 variants at pH 6 is different from the 4 SU-wt rec C*c*O and the variant Y167F. The Soret minima and maxima are again red shifted. The Soret maximum appears at λ = 445 nm, suggesting low-spin haem *a* reduction. However, variant W272Y (Figure 3.5-3, dark blue line) shows a smeared maximum between 570 and 605 nm at pH 6, which indicates mixed species.

In summary, all W272 variants are inactive and do not form $\mathbf{P_H}$ or $\mathbf{F^{\bullet}_{H}}$ states. Instead of $\mathbf{P_H}$ or $\mathbf{F^{\bullet}_{H}}$ state formation the electrons from H_2O_2 are re-distributed to form reduced low-spin haem *a* with a maximum at 605 nm in the difference absorption spectrum (*minus* the **O** state) indicating the importance for a conserved tryptophan residue at position 272.

3.5.1.2 EPR spectroscopy

To confirm the inability of the W272 variants to form the H_2O_2-induced $\mathbf{F^{\bullet}_H}$ state, the W272 variants were investigated using EPR spectroscopy. The 4 SU-wt rec CcO hosts a tyrosyl Y167 radical in the $\mathbf{F^{\bullet}_H}$ intermediate as described in this work previously (compare chapter 3.1.5.1). In addition, this EPR signal is not detectable in the variant Y167F (Budiman et al., 2004), indicating the importance of Y167 as a stable host for an organic radial.

The tyrosyl 167 radical of the "$\mathbf{F^{\bullet}_H}$ state" was not inducable in all W272 variants mixing the sample 1:1-molar with H_2O_2 at pH 6 (data not shown). According to the results of the results of the UV-vis spectroscopic measurements, the W272 variants do not show a tyrosyl radical at residue Y167 and thus the electron pathway of the 4^{th} electron is blocked.

3.5.2 Comparison of the variant W272F with the variant W164F

In order to investigate the importance of the tryptophan residues near the binuclear site, two tryptophan variants, W272F and W164F, were produced and charcterised by UV-vis and EPR spectroscopy. Trytophan (W) residues are very large, aromatic and buried in the hydrophobic core of a membrane protein. They are important for the structural integrity of the protein, because their large hydrohobic indol ring cannot be replaced by another aromatic amino acid of a similar size. In the case of C*c*O, it makes sense to compare two nearby W → F variants. Therefore, variant W164F was produced for comparison with variant W272F (Figure 3.5-1). W164F has a residual enzymatic activity of 20 % compared with the 4 SU-wt rec C*c*O (Table 3.5-2) and W272F has already been described as an inactive enzyme in Table 3.5-1 of this work.

Table 3.5-2 Variant C*c*Os close to the binuclear centre. Both variant enzymes have mutations near the active site of C*c*O. The purpose of variant production and variant turnover activity is shown compared with 4 SU-wt rec C*c*O.

C*c*O	Purpose of variant production	Turnover in % wt rec
4 SU-wt rec C*c*O	-	100
W272F	Loss of function, no Y167 radical via W272F	< 1
W164F	Comparison to the W272F variant	20

Both W residues of the variants are located between the haem A groups, suggesting their similar structural importance.

According to the proposed structural significance, the variant W272F and W164F enzymes have both been subjected to crystallisation attempts in the 2 SU-C*c*O forms in order to determine their structure.

However, the crystallisation trials did not result in crystals, because of the loss of protein stability during the purification of the 2 SU-form of these variants (data not shown). The LDAO treatment led to protein aggregation of the 2 SU-W272F and 2 SU-W164F variants. This result confirms the structural importance of W residues within the hydrophobic core of subunit I and provides indications for a stabilising effect of subunit III.

The 4 SU-forms of variant W272 and W164F were very stable, UV-vis absorption and EPR spectroscopic experiments could be performed.

3.5.2.1 UV-vis spectroscopy

Variants W272F and W164F were further characterised by UV-vis spectroscopy. The behaviour of both variants against low amounts of H_2O_2 (1:1 to 1:5) is depicted in Figure 3.5-4 and Figure 3.5-5. Both variants performed the same reactions after induction of the $\mathbf{P_H}$ and $\mathbf{F^{\bullet}_H}$ states.

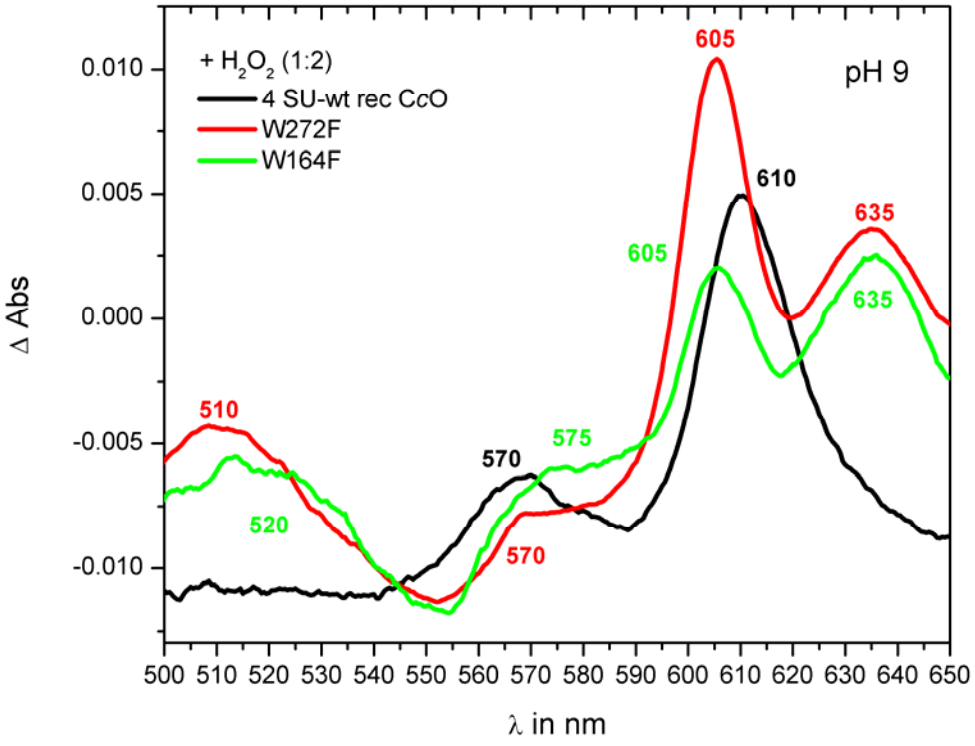

Figure 3.5-4 The P_H state of the variants W272F and W164F. Difference absorption spectra (*minus* the O state) of the intermediates of the variant C*c*Os are compared with the 4 SU-wt rec C*c*O. 10 µM oxidised C*c*O in 50 mM KP_i, pH 9, 0.05 % LM was mixed with H_2O_2 in a molar ratio of 1:2.

Again, the 4 SU-wt rec C*c*O has formed the **P_H** state having an maximum at 610 nm in the difference absorption spectrum (*minus* the **O** state) after molar H_2O_2 addition (1:2) at pH 9 as previously desribed in this work (Figure 3.5-4). In addition, the maximum at 570 nm is seen which also indicates **P_H** state formation. However, both variants, W272F and W164F, exhibited a 605 nm maximum at pH 9 instead of the 610 nm maximum of the **P_H** state; and extra maxima at roughly 510 nm and 635 nm and a shoulder around 570 nm. The 605 nm maximum indicates that the electrons from H_2O_2 are shifted to form reduced low-spin haem *a*. The extra maxima are pH dependent, because only the 605 nm maximum was also detected at pH 6 (Figure 3.5-5). The **$F^{\bullet}_H$** state of 4 SU-wt rec C*c*O was formed at pH 6 showing a maximum at 575 nm after H_2O_2 treatment. However, the maxima of W272F and of W164F at pH 6 were seen at 605 nm compared with the maximum at 575 nm in the spectrum of the 4 SU-wt rec C*c*O.

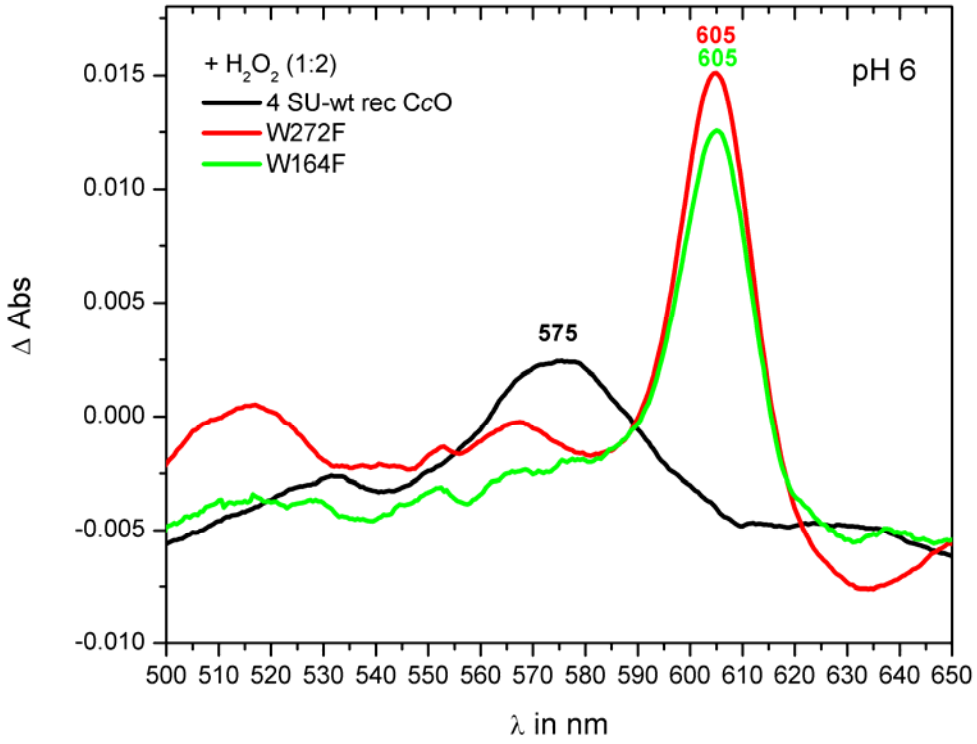

Figure 3.5-5 The $F^{\bullet}_H$ state of the variants W272F and W164F. Difference absorption spectra (*minus* the O state) of the intermediates of the variant C*c*Os are compared with the 4 SU-wt rec C*c*O. 10 µM oxidised C*c*O in 50 mM Mes-OH, pH 6, 0.05 % LM was mixed with H_2O_2 in a molar ratio of 1:2.

Both variants were also compared in their ability to form the **F_H** state in the presence of excess H_2O_2 (1:500, Figure 3.5-6). Variant W164F was still able to form an **F_H** state, showing a maximum at 580 nm, but on the other hand, the inactive variant W272F does not show formation of the **F_H** state, exhibiting a maximum at 567 nm instead of the 583 nm maximum of the **F_H** state from 4 SU-wt rec C*c*O in the differerence absorption spectrum (*minus* the **O** state).

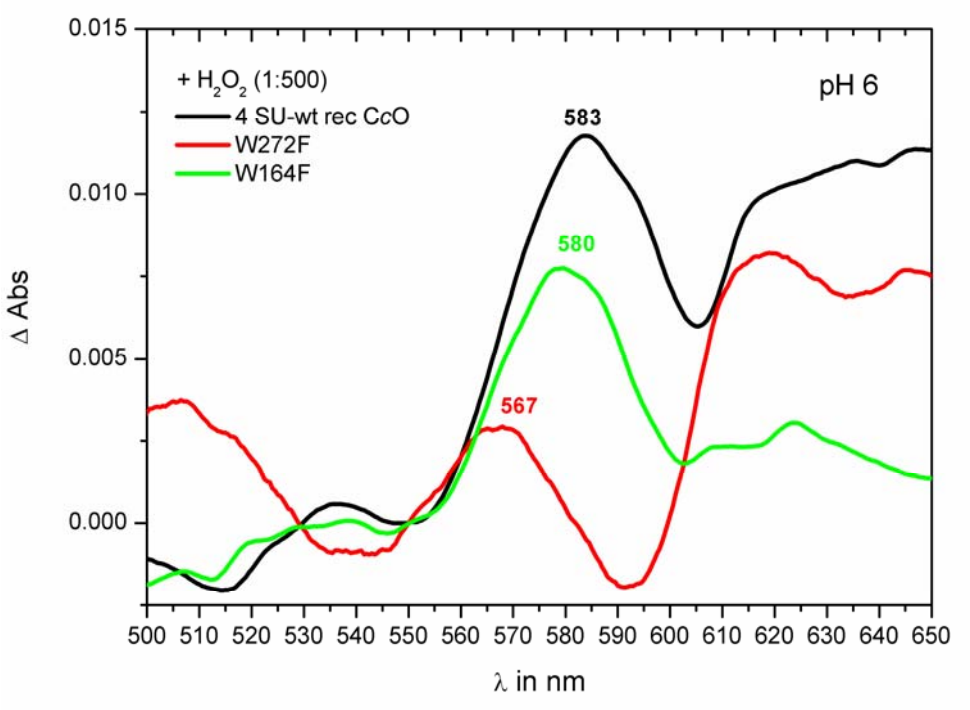

Figure 3.5-6 The F_H state of the variants W272F and W164F. Difference absorption spectra (*minus* the O state) of the intermediates of the variant C*c*Os are compared with the 4 SU-wt rec C*c*O. 10 µM oxidised C*c*O in 50 mM Mes-OH, pH 6, 0.05 % LM was mixed with H_2O_2 in a molar ratio of 1:500.

In summary, Y167 is not directly part of the binuclear site of C*c*O and for the identification of the primary electron donor of the $\mathbf{P_H/F^{\bullet}_H}$ formation two tryptophans, W272 and W164, which are located nearby the binuclear site, were investigated by mutagenesis. Evidence is provided by activity assays and by UV-vis spectroscopy that W272 may be a fast electron donor for the O_2 molecule. Both tryptophan residues play important roles for the stability of the whole enzyme and possibly for the redox potentials of the prosthetic groups, because electrons of H_2O_2 reduce haem *a* in the "$\mathbf{P_H/F^{\bullet}_H}$" states of variants W272F and W164F.

3.5.2.2 EPR spectroscopy

In order to show the importance of W272F for the formation of the tyrosyl Y167 radical in the $\mathbf{F^{\bullet}_H}$ state, variant W272F was compared with variant W164F using EPR spectroscopy. The variant W164F has hosted a radical at Y167 during the $\mathbf{F^{\bullet}_H}$ intermediate, but the variant W272 not.

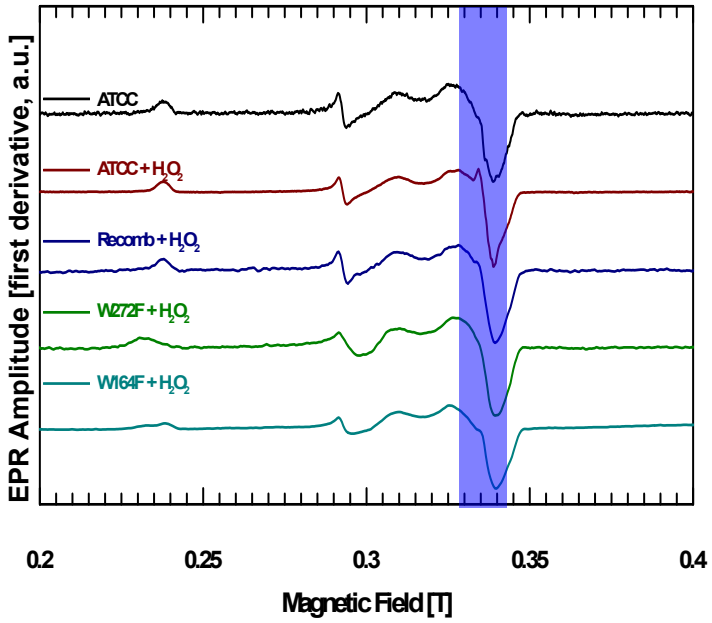

Figure 3.5-7 (A)

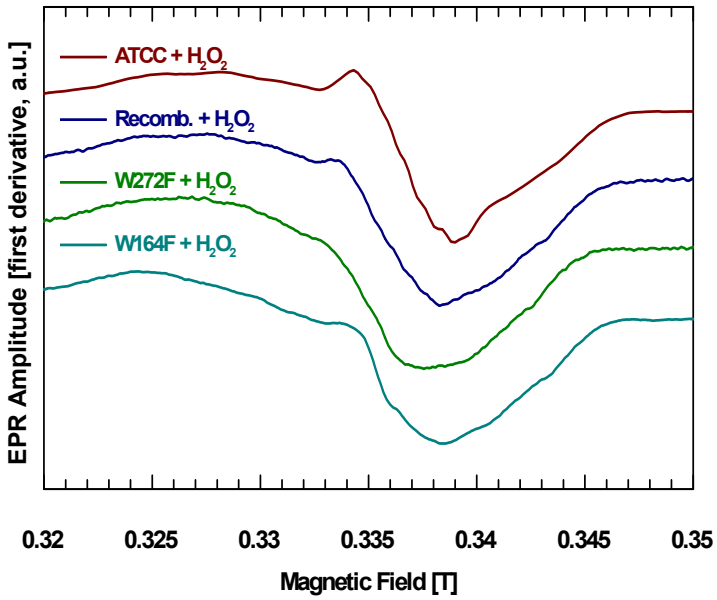

Figure 3.5-7 (B)

Figure 3.5-7 EPR spectra of the 4 SU-wt ATCC C*c*O, 4 SU-wt rec C*c*O (Recomb.) and of the variant enzymes W272F and W164F. 200 µM oxidised C*c*O in 50 mM KP_i, pH 9, 0.05 % LM ($F^{\bullet}_H$ state) and H_2O_2 were mixed at 4°C (molar ratio 1:1). The sample was transferred immediately to a suprasil quartz EPR tube, frozen in liquid nitrogen and X-Band continuous-wave EPR spectra were recorded. (A) at 10 K. (B) difference spectra (*minus* the O state) at 20 K.

Figure 3.5-7 shows the induced tyrosyl Y167 radical signal of the $\mathbf{F^{\bullet}_H}$ state of the 4 SU-wt ATCC C*c*O and the 4 SU-wt rec C*c*O at both 10 K and 20 K. However, the inactive variant W272F did not display this organic radical signal. Compared to the 4 SU-wt rec C*c*O, variant W164F formed a recognisable radical signal after 1:1-molar H_2O_2 treatment at pH 6.

In summary, W164F displays a residual enzymatic activity of 20 % compared with 4 SU-wt rec C*c*O. The redox potentials of the metal centres of the variants W272F and W164F may be shifted, resulting in reduction of the low-spin haem *a* instead of $\mathbf{P_H/F^{\bullet}_H}$ state formation. However, W164F is able to form the tyrosyl Y167 radical in the $\mathbf{F^{\bullet}_H}$ state as determined by EPR spectroscopy.

3.6 Proton pumping by D-pathway variants of cytochrome *c* oxidase

In order to analyse the proton pumping activity of D-pathway variants, proton pumping experiments were performed using both D-pathway variants and the 4 SU-wt rec C*c*O reconstituted into liposomes.

Proton pumping is a crucial function of the redox-driven C*c*O. While the solubilised C*c*O should also be able to pump protons, this cannot be determined in the absence of membranes. However, reconstitution of wt C*c*O into liposomes provides a "natural-like" bilayer environment allowing the conditions for the generation of a membrane potential. The wt C*c*O creates an electrochemical proton gradient during turnover, which is proposed to be based on a fixed stoichiometry of 1 H^+/e^-. Thus, for each electron input and substrate proton uptake one proton is supposed to be pumped across the membrane bilayer. Table 3.6-1 and Figure 3.6-1 show the produced and investigated D-pathway variants, which were employed for this experiment.

Table 3.6-1 D-pathway variant C*c*Os for proton pumping experiments. The recombinantly produced variant C*c*Os are listed in comparison with the 4 SU-wt rec C*c*O. (P. denitrificans* cells kindly provided by Prof. Bernd Ludwig, JWG University of Frankfurt)**

C*c*O	Plasmid	Strain
4 SU-wt rec C*c*O	pUP39	AO1
N131D	pUP39	AO1
D124N	pUP39	AO1
D30N	pUP39	AO1
H28A	pUP39	AO1
N113D*	pUP39	AO1
G196D	pUP39	AO1
S193Y	pUP39	AO1
H28A/N131D	pUP39	AO1
D124N/D30N	pUP39	AO1

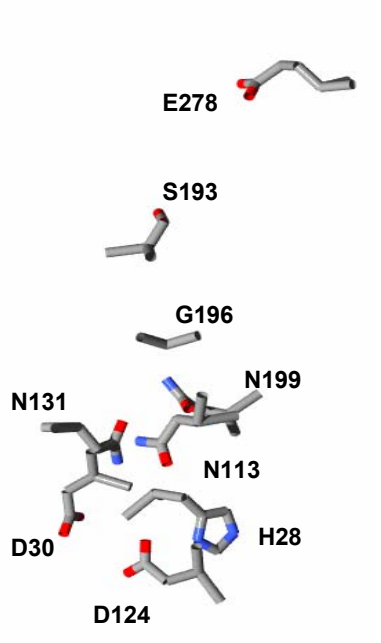

Figure 3.6-1 Selected residues of the D-pathway. The residues H28 and D30 form a cluster with the residue D124. The triad of three asparagines (N113, N131 and N199) is shown. G196 and S193 lead protons to E278 (pdb-file 1ar1, Ostermeier *et al*., 1997).

Residues H28 and D30 at the entrance of the D-pathway had been proposed to participate in the proton pumping. These two and several other D-pathway variants were compared with the 4 SU-wt rec C*c*O and the experiment included the well studied variants N131D and D124N as control variants. In addition, the properties of the variants G196D; S193Y; N113D; and the double variants N131D/H28A and D30N/D124N were investigated.

Redox difference absorption spectra of the 4 SU-wt rec C*c*O and the variant C*c*Os showed only slight differences in the α-peak region (Figure 3.6-2) indicating proper insertion of the haem A groups in all cases.

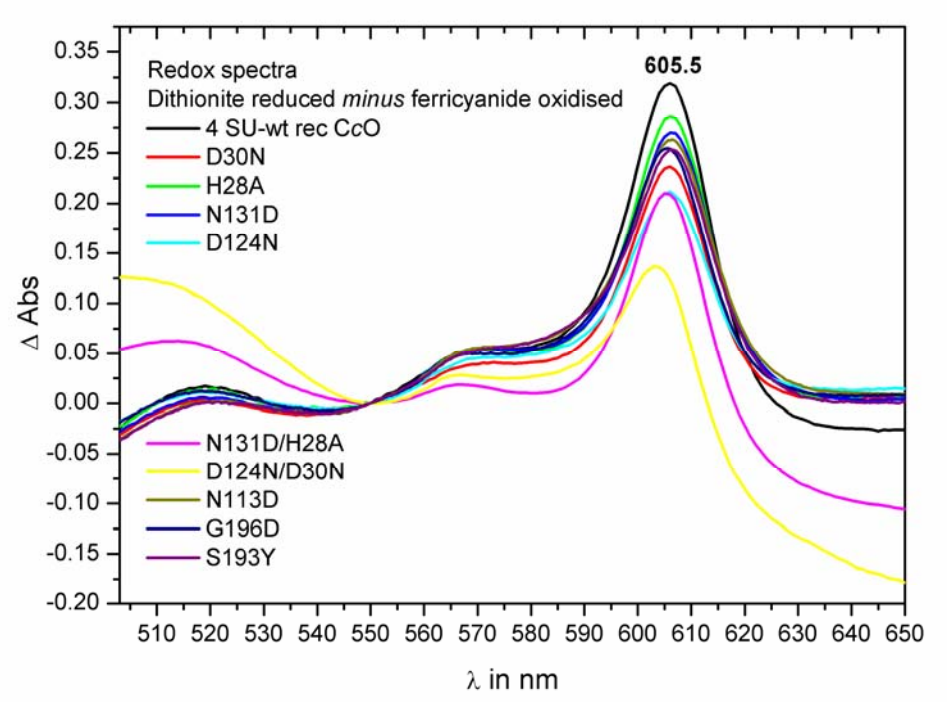

Figure 3.6-2 Reduced *minus* oxidised difference absorption spectra of 10 μM 4 SU-wt rec C*c*O and of the variants D30N; H28A; N131D; D124N; N131D; N131D/H28A; D124N/D30N; N113D; G196D and S193Y.

Important functional properties of the 4 SU-wt rec C*c*O and the variant C*c*Os are listed in Table 3.6-2:

1) the cyt *c* turnover activities of the solubilised C*c*Os;

2) the respiration control ratio (rcr) of the reconstituted enzymes into liposomes; and

3) the proton pumping activity across the liposome bilayer formulated in pumped H^+/e^-.

The rcr value is a measure of the tightness of the particular C*c*O-proteoliposomes. C*c*O pumps protons across the membrane, inhibiting its own activity due to the resulting membrane potential. Addition of the proton uncoupler CCCP and the K^+ ionophor valinomycin leads to an uncoupled system without a membrane potential generation or a pH-gradient. Therefore, in this case the activity of C*c*O-proteoliposomes is not inhibited and the turnover number is increased. The ratio

of the slopes of the initial rates (uncoupled/coupled) of these two measurements is termed the "respiration control" ratio of the respective C*c*O-proteoliposome.

Table 3.6-2 Enzymatic turnover and proton pumping activity of solubilised C*c*O variants compared with the 4 SU-wt rec C*c*O (cyt *c* oxidation assay) and the respiratory control ratio (rcr) values of C*c*Os reconstituted into proteoliposomes (rcr = uncoupled/coupled liposomes cyt *c* oxidation activity). In addition the number of pumped protons per electron is shown.

C*c*O	Turnover in % (solubilised C*c*Os)	Rcr values of the proteoliposomes	Pumped H^+/e^- ratio
4 SU-wt rec C*c*O	100	5.1	1.0
N131D	100	2.7	0.0
D124N	5	1.2	0.0
D30N	100	3.2	1.0
H28A	100	4.6	1.0
N113D	63	3.8	0.0
G196D	3	1.8	0.0
S193Y	45	2.8	0.5
N199D (Pfitzner, 2000)	82	n.d.	0.0
N131D/H28A	100	3.9	0.0
D30N/D124N	5	1.1	0.0

Quantitative proton pumping measurements were performed using the pH indicator phenol red. Phenol red is a pH dependent dye and the pH change in the bulk solution caused by the active C*c*O-proteoliposomes was monitored by the absorbance changes at λ = 555.4 nm at substrate-limited conditions in an unbuffered activity experiment. Coupled and uncoupled C*c*O-proteoliposomes were compared by recording the different kinetics for two seconds using a stopped flow apparatus. The difference of the pH decrease in the bulk solution caused by the pumped protons ($4\ H^+_{\ i} \rightarrow 4\ H^+_o$) is compared to the pH increase caused by the "removed" chemical protons ($4\ H^+ + O_2 \rightarrow 2\ H_2O$).

The rcr value determined for the 4 SU-wt rec C*c*O-proteoliposomes was roughly 5, and the pump ratio was 1 H^+/e^-. In agreement with previous data (see chapter 1.2), variant N131D shows 100 % turnover, a lower rcr value and does not pump protons. In addition, the variant D124N also does not pump protons and shows only 5 % residual activity and a very low rcr value of around 1.2. Variants H28A and D30N both possess 100 % turnover, an rcr value above 3 and displayed a total proton pumping activity with a ratio of pumped H^+/e^- = 1. N131D/H28A and D30N/D124N are the double variants of H28A or D30N together with the classical D-pathway mutations N131D or D124N. However, they did not show suppression of the proton pumping deficiency (by charge compensation), having the same effect such as the dominant classical mutation. Variant G204D of *R. sphaeroides* was reported to exhibit low turnover activity and a decoupled proton pumping

phenotype, and this was confirmed using the homologous *P. denitrificans* variant G196D (Table 3.6-2).

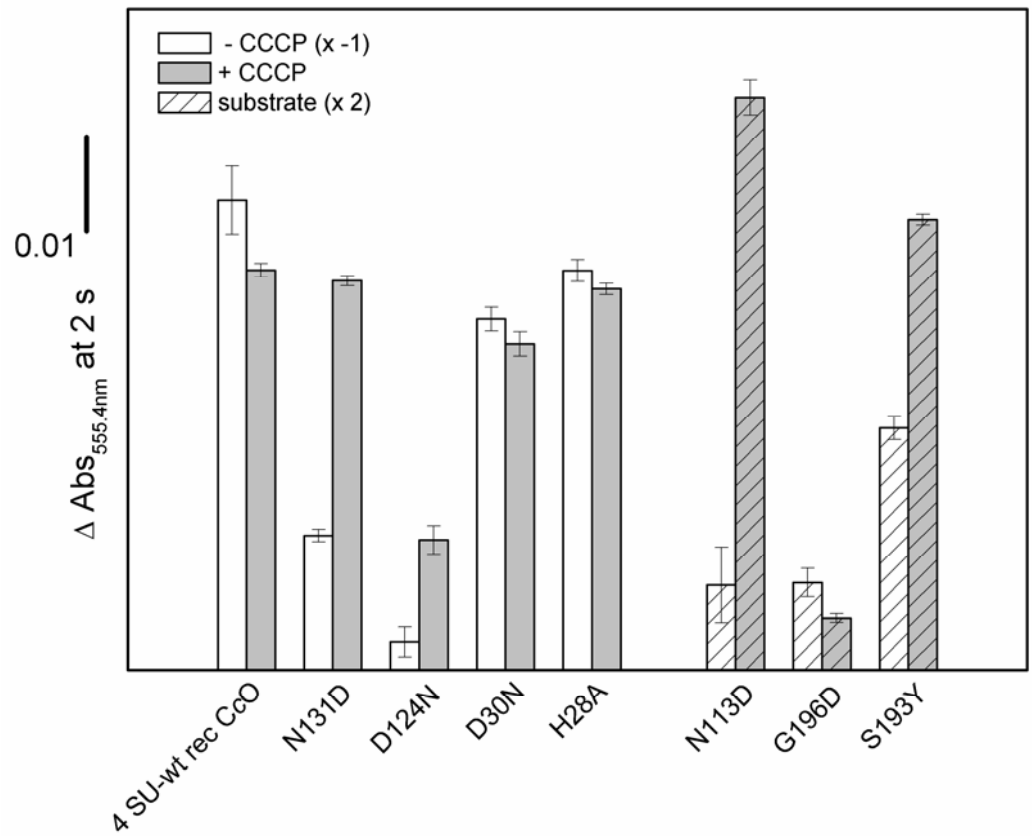

Figure 3.6-3 Summary of the proton pumping experiments. The bars represent the $\Delta Abs_{555.4nm}$ at 2 s. White bars represent proton pumping activity, whereas grey bars show loss of chemical protons in decoupled vesicles demonstrating the dioxygen reduction activity. Bare bars represent 20 μM cyt *c* measurements. Dashed bars represent 40 μM cyt *c* measurements. All measurements were performed using substrate-limited conditions (for details see appendix 6.4).

S193Y is a D-pathway variant, which we expected to show a deficient proton pumping, because upon modelling the structure of S193Y the large Y displaces some water molecules within the water chain of the D-pathway. However, this variant still possesses 45 % turnover activity and has a proton pumping stoichiometry of $H^+/e^- = 0.5$.

N113 is the third asparagine residue of a triad-arrangement of asparagines within the D-pathway (N131, N199 and N113). However, the inability of variant N113D to pump protons has not been demonstrated so far. The experiments have shown that variant N113D also has a relatively high turnover number of 63 % as with variants N131D and N199D and, in addition, the proton pumping activity is absent in this variant. Thus, all three variants, N131D, N199D and N113D, show normal cyt *c* oxidation activity, but their proton pumping is absent, enzymatic turnover and proton pumping are decoupled.

The bar diagram of Figure 3.6-3 summarises the end point data (at 2 s) of all kinetics of the stopped flow proton pumping experiments. Therefore, H28A and D30N do pump protons in

contrast to the expectations from the results of the pK_a value determination by electrostatic calculations (Olkhova *et al.*, 2004). Variants N113D and G196D have lost their capacity to pump protons, because of the additional negative charge within the D-pathway, and variant S193Y is still rougly 50 % active in both turnover and proton pumping activity.

4 DISCUSSION

4.1 Comparison of the differently produced wild type cytochrome *c* oxidases

4.1.1 Cloning, overexpression and purification of the recombinantly produced wild type cytochrome *c* oxidase

In this work, we have produced two different wt C*c*Os, the native 4 SU-wt ATCC C*c*O and the recombinant homologously produced 4 SU-wt rec C*c*O. The native 4 SU-wt ATCC C*c*O was purified using the Fv fragment 7E2 and this enzyme might be the most natural wt C*c*O, because the native *P. denitrificans* cells (ATCC 13543) are not genetically manipulated and they regulate the production of the required amount of wt C*c*O.
The cloning of 4 SU-wt rec C*c*O has led to a protein, which is homologously overproduced in the *P. denitrificans* AO1 deletion strain. The plasmid-encoded gene for subunit Iβ, *cta*DIIβ, is under the control of the constitutive *cta*C2 promoter. However, the presence of excess plasmids leads to overexpression of 4 SU-wt rec C*c*O. Therefore, the overproduction of the 4 SU-wt rec C*c*O is likely and indeed, the purification of the recombinant C*c*O resulted in in two to three times higher yields of purified protein compared with the 4 SU-wt ATCC C*c*O.

Use of the engineered recombinant wt C*c*O has not only resulted in the improvement of the yield, but also in the dysfunction of the overproduced 4 SU-wt rec C*c*O as reflected in the decreased enzymatic activity. The overexpression system may fail to assemble subunits and to correctly insert all prosthetic groups into the bulk protein of the 4 SU-wt rec C*c*O and thus, overexpression may overburden the machinery of metalloprotein biosynthesis or the membranes of the *P. denitrificans* AO1 deletion strain might not provide sufficient amounts of special fatty acids for distinct lipids.
The structures of both types of wt C*c*Os were determined for homologously produced 4 SU-wt rec C*c*O at 2.25 Å resolution and for the native 4 SU-wt ATCC C*c*O at 2.7 Å resolution showing no structural differences. However, it may be that only the pool of wt C*c*Os having the correct (or at least the same) structure cystallise and impurities such as mis-assembled 4 SU-wt rec C*c*Os or aggregates are found in the solution or precipitate.
In order to avoid these problems in future projects the mutagenesis of the genomic DNA by homologous recombination might be the best method to produce a recombinant (mutated) 4 SU-wt rec C*c*O exhibiting higher quality.

4.1.2 Biochemical analysis

In the case of C*c*O from *P. denitrificans*, an Fv fragment had been developed for use in purification by affinity chromatography and for crystallisation trials. This antibody fragment strategy allows for the purification of folded and assembled C*c*Os because it binds C*c*O at the interface between SU I and SU II. However, the Fv fragment also shows a high affinity to subunit I alone (see SDS-PAGE gel of Figure 3.2-3 B) and the Fv fragment-based purification may have resulted in an inhomogenous protein sample, because partly assembled C*c*Os can be co-purified.
SDS-PAGE analysis of wt C*c*Os provides the first indications for the purity of the protein sample and secondly it provides information about the composition of the subunits from the protein complex. The subunit composition, the intensity and the molecular mass of the single subunit bands, of both 4 SU-wt C*c*Os does not differ in SDS-PAGE analysis (Figure 3.1-1). The distribution of the subunits is typical for our Fv-fragment based purified C*c*Os showing three of four subunits and the bound Fv fragment. In spite of the similar molecular masses of subunit III compared with the subunit II, the subunit III runs further into the SDS-PAGE gel. Presumably, this effect is due to the extreme hydrophobicity of subunit III resulting in a higher SDS-binding and thus in faster migration of the hydrophobic bundle through the gel.
The 2 SU-wt ATCC C*c*O, comprising only subunits I and II, represents a functionally active form of C*c*O. It contains all redox-active transition metals and proton pathways providing functionality. SU III and IV are successfully removed by LDAO treatment of the 4 SU-wt ATCC C*c*O as indicated by the absence of these subunits in the Coomassie-stained SDS-PAGE gel (Figure 3.1-1 B).
The functional comparison of the 4 SU-wt ATCC C*c*O with the 4 SU-wt rec C*c*O was performed using activity assays. The 4 SU-wt ATCC C*c*O displays the standard activity in activity assays (~ 600 e^-/s), whereas the 4 SU-wt rec C*c*O shows a decreased turnover number (~ 400 e^-/s). We conclude that the integrity of the protein complex of the 4 SU-wt rec C*c*O might be impaired, because it shows only ~ 60 % of the native activity in cyt *c* oxidation and dioxygen reduction (Figure 3.1-2). To explain the decreased turnover activity, we suppose that the recombinant wt C*c*O might be only partly produced showing missing subunits, incorrect metal incorporation or a different lipid composition. 1 SU-C*c*O is not distinguishable from 4 SU-C*c*O using UV-vis spectroscopy, because the overall absorbance of C*c*O is dominated by the low-spin haem *a*. However, applying anion chromatography provides no indication for single subunits eluting earlier upon employing high salt gradients.

4.1.3 Reduced *minus* oxidised difference absorption spectra

Difference absorption spectroscopy is the standard method to characterise cytochromes. Cytochrome *a* absorbs light in the Soret- and in the α-region. Oxidised 4 SU-wt ATCC C*c*O and 4 SU-wt rec C*c*O show these typical absorbances (Keilin, 1925) at λ = 425 nm and 604 nm (Figure 3.1-3). However, the 4 SU-wt rec C*c*O has a blue shifted Soret maximum from λ = 427 nm to 425 nm and this blue shift is rather typical for the slow form of C*c*O. The redox difference absorption spectra of the 4 SU-wt ATCC C*c*O and 4 SU-wt rec C*c*O are similar in the distribution of their minima and maxima, however, the 4 SU-wt rec C*c*O has a broad single minimum in the Soret region, whereas the 4 SU-wt ATCC C*c*O has two contributions to this minimum. In general, changes of the electronic environment of the haem A groups are accompanied by shifts of maxima in the visible absorption spectrum and thus by redox potential shifts of these prosthetic groups. One single H-bond change is enough to shift the redox potential of a bound prosthetic group (Ostafin *et al.*, 2006) and minimal structural deviations may induce functional defects. The 4 SU-wt rec C*c*O might show shifts in the redox potentials of its prosthetic groups and the determination of the redox potentials may provide answers for the impaired function of this protein and explain the spectral differences.

4.1.4 Metal analysis

C*c*O contains haem A groups and non-haem metals such as the redox-active copper ions and redox-inactive metal ions. The assembly process of C*c*O is very complicated as previously determined by genetic methods. There are several synthases involved, for example the haem A synthase and chaperones or assembly factors such as Cox11 (Carr and Winge, 2003; Khalimonchuk *et al.*, 2007), all of which are essential factors for the synthesis of C*c*O. The chaperone Cox11 helps to integrate Cu_B into subunit I and we suggested that the overproduction of subunit I from recombinantly produced C*c*O might impair the Cu_B-metalisation by Cox11. TXRF measurements were performed in order to determine the metal composition of the 4 SU-wt rec C*c*O and identify the copper content. The results demonstrate that there is no difference in the content of redox-active metals of the 4 SU-wt rec C*c*O compared with the 4 SU-wt ATCC C*c*O. The determined ratio of copper to iron is 3 Cu : 2 Fe and thus Cu_B is not missing in the aa_3-4 SU-wt rec C*c*O (Figure 3.1-4), as it had been assumed. The Zn^{2+} content is unexpectedly high in the 4 SU-wt rec C*c*O, although EDTA-containing buffers were used for the purification. Zn^{2+} is a commonly known inhibitor of C*c*O, binding special motifs comprised of aspartic acids and histidines (Aagaard and Brzezinski, 2001; Ädelroth and Brzezinski, 2004) and high Zn^{2+} concentrations in 4 SU-wt rec C*c*O preparations may explain its impaired catalytic activity.

Specific interactions between lipids and membrane proteins have been observed in recent high-resolution crystal structures (Iwata *et al.*, 1995; Tsukihara *et al.*, 1996; Kyoko Shinzawa-Itoh *et al.*, 2007; Qin *et al.*, 2007) and individual conserved lipid binding sites in the membrane-spanning region have been revealed. Protein bound lipids also play important roles that are crucial for the assembly, the maintenance of structure and the activity of C*c*O. It was shown that the addition of lipids to detergent-purified C*c*O leads to an increase of the turnover activity by 40 % (Robinson *et al.*, 1990). Moreover, the total removal of CL from bovine C*c*O leads to a loss of turnover activity and the subsequent reintroduction of CL to C*c*O yields an active enzyme. This experiment indicates that CL may represent a structural and functional lipid for the active form of C*c*O, even in bacterial C*c*O. However, the structures of the C*c*O from *P. denitrificans* (1qle) and from *R. sphaeroides* (1m56) revealed no CL or PG molecules, the C*c*O from *P. denitrificans* shows only two resolved PC molecules in addition to bound detergent molecules and the C*c*O of *R. sphaeroides* displays only six assigned PE molecules. However, these structural results are not comparable; because each structure of C*c*O resulted from different purification protocols and crystallisation conditions. Indeed, 13 complete lipid molecules are resolved in bovine C*c*O including 2 CL, 1 PC, 3 PE, 4 PG and 3 TGL (Shinzawa-Itoh *et al.*, 2007) and most of these lipids are located at the interfaces of subunits of the 13 SU-bovine C*c*O. CL is proposed to be essential for the activity of even bacterial C*c*O. Recently, an MS-analysis of lipids from crystallised bovine C*c*O was performed in order to identify the alkyl chains and the position of the unsaturated bonds. Evidence was found for conserved binding sites for physiologically important lipids, especially distinct fatty acid chains. PG with vaccenate (*cis*-Δ^{11}-octadecenoate) was found in bovine C*c*O and in *P. denitrificans* C*c*O indicating that vaccenate is conserved in spite of the abundance of oleate (*cis*-Δ^{9}-octadecenoate). The analysis of bovine C*c*O indicates that the protein moiety selects *cis*-vaccenate near the O_2 transfer pathway against *trans*-vaccenate and the results suggest that vaccenate plays a critical role in O_2 transfer.

The overproduction of the 4 SU-wt rec C*c*O in the AO1 deletion strain using plasmid-encoded subunit I may lead to a deficiency of *cis*-Δ^{11}-octadecenoate in the membrane of this strain and only the abundant *cis*-Δ^{9}-octadecenoate is incorporated into the 4 SU-wt rec C*c*O leading to a less active enzyme.

4.1.5 Induction of H_2O_2-induced model intermediates

All wt C*c*Os show the $\mathbf{P_H}$ state formation at pH 9 after addition of H_2O_2 in low amounts (molar ratio of 1:1 to 1:5) resulting in a 610 nm maximum in the difference absorption spectrum (*minus* the **O** state, Figure 3.1-5 A and Jünemann *et al.*, 2000). However, the same experiment at pH 6 shows formation of the $\mathbf{F^{\bullet}_H}$ state having a maximum at 575 nm in the difference absorption spectrum (*minus* the **O** state). The 4 SU-wt rec C*c*O exhibits severely impaired reactivity towards H_2O_2

showing a decreased yield of the $\mathbf{P_H}$ and $\mathbf{F^{\bullet}_H}$ states of 15 % instead of 40 % compared with the 4 SU-wt ATCC C*c*O as determined by UV-vis spectroscopy.

The 2 SU-wt ATCC C*c*O shows the same formation of the $\mathbf{P_H}$ state as the 4 SU-wt ATCC C*c*O, however, the formation of the $\mathbf{F^{\bullet}_H}$ state is decreased due to preferential $\mathbf{P_H}$ state formation, although the pH is below 7. This result indicates that the proton accessibility of the 2 SU-wt ATCC C*c*O via the proton pathways is disrupted and protonation steps fail within the binuclear site. The surface of subunit I, which is not occupied by subunits III and IV in 2 SU-wt ATCC C*c*O, is located nearby the D-pathway. The D-pathway of 2 SU-wt ATCC C*c*O might be disrupted, because of the missing subunits and thus the $\mathbf{F^{\bullet}_H}$ state of 2 SU-wt ATCC C*c*O at pH 6 contains portions of the electronically equal $\mathbf{P_H}$ state.

The 4 SU-wt ATCC C*c*O reacts with an excess of H_2O_2 (molar ratio of 1:500) to form the $\mathbf{F_H}$ state resulting in a broad 580 nm maximum in the difference absorption spectrum (*minus* the **O** state, Figure 3.1-6) and the 4 SU-wt rec C*c*O displays a different reactivity towards excess H_2O_2 having a yield of only 15 % instead of 65 % confirming its decreased turnover activity. In summary, all functional properties of recombinantly produced wt C*c*O are impaired as determined by activity assays and UV-vis spectroscopy of H_2O_2-induced intermediates. This result is even demonstrated in the inability of forming the tyrosyl 167 radical during the $\mathbf{F^{\bullet}_H}$ state (Figure 3.1-7) as studied by EPR spectroscopy.

4.2 Importance of subunit III and *suicide inactivation* of the two-subunit cytochrome *c* oxidase

The 2 SU-wt ATCC C*c*O lacks subunit III and IV, however, all functionally necessary redox-active metals are located in subunit I and II and EPR spectra of the high-spin haem a_3 (g ~ 6) suggest a stronger coupling of the binuclear centre in 2 SU-wt ATCC C*c*O (data not shown) implying a structural change in the absence of subunit III. The lack of the hydrophobic subunit III may induce minimal structural changes within the binuclear site, probably resulting in different spatial orientations of the EPR active/silent species. It was suggested that the loss of subunit III leads to a less rigid binuclear site, which is more flexible and therefore more fragile.

The seven membrane-spanning helices of subunit III form a V-shaped cleft (bundles of five helices against two helices) binding lipids and providing structural integrity and stability during catalytic turnovers. The loss of subunit III does not influence non-active (as isolated) 2 SU-wt C*c*O, because isolated 2 SU-forms of wt C*c*O are extremly stable when stored at 4°C. However, *suicide inactivation* is initiated as soon as the 2 SU-wt C*c*O starts multiple turnover activity (Figure 3.2-1). *Suicide inactivation* (Bratton *et al.*, 1999b; Mills and Hosler, 2005) leads to an inactivation of the whole population of 2 SU-wt rec C*c*O during turnover. Recently it was demonstrated by mutagenesis studies of conserved lipid binding sites that not the presence of subunit III alone, but

also the presence of lipids prevents *suicide inactivation*. Thus, the 4 SU-C*c*O variants R218A (R provides fixation of a lipid head group) and W51A-F80A (van der Waals contacts to the fatty acid alkyl chain) are proposed to mimic the loss of subunit III (Varanasi *et al.*, 2006). Even in case of these 4 SU-variants s*uicide inactivation* occurs although subunit III is completely retained. *Suicide inactivation* may originate from a structural instability of the binuclear centre in the absence of the stabilising conserved lipids, because *suicide inactivated* 2 SU-wt rec C*c*O shows a high tendency to dissociate into individual subunits and to show aggregation of free subunits. This is demonstrated in elution profiles of anion exchange chromatography and gel filtration (Figure 3.2-3) of *suicide inactivated* 2 SU-wt rec C*c*O. In theory, structural changes such as interhelical cross-links induced by reactive oxygen species might have been the reason for s*uicide inactivation*. Subunit I and subunit II of the *active* and s*uicide inactivated* 2 SU-wt rec C*c*O were studied using MALDI-TOF/TOF and analysed at the Mascot data bank (Figure 3.2-4). The mass spectra of the peptides from SU I of *suicide inactivated* 2 SU-wt rec C*c*O were inconclusive concerning identification of any structural change compared with *active* 2 SU-wt rec C*c*O. However, subunit I and subunit II of both proteins were used in crysallisation trials.
However, there has not been any success in the crystallisation of *suicide inactivated* 2 SU-wt rec C*c*O. Many crystallisation trials yielded with amorphous aggregates of denatured protein and we assume that the structural change induced by *suicide inactivation* is very severe and leads to an structurally unstable protein (Figure 3.3-2) The protein sample might have been too inhomogeneous with a high tendency to aggregate, which has resulted in precipitates in the crystallisation trials.

4.3 Functional studies – peroxide bound intermediates

4.3.1 The peroxide bound O state

Most structures of C*c*O represent the enzyme in its oxidised state (Tsukihara *et al.*, 1996; Ostermeier *et al.*, 1997; Qin *et al.*, 2006). In all of these structures electron density is present between the metal ions a_3-Fe^{3+} and Cu_B^{2+} of the binuclear site. There have been attempts to determine the bound species which gives rise to this electron density and the first structures at a high resolution provided a good fit for a complexed Cl^- or a bound O^--O^-. The *active* 2 SU-wt rec C*c*O at 2.25 Å resolution also shows this electron density between the metals of the binuclear site and the modelling of different species, for example independent O species such as two H_2O molecules or a CO_3^{2-}, demonstrates that here also an O^--O^- molecule can be accomodated. A Cl^- also fits nicely into the free space of the electron density in the binuclear site, but FTIR studies

exclude a Cl^- during the pulsed **O** state (Figure 3.4-1). The isotope effect of $^{16/18}O_2$ certainly provides evidence for the presence of a Fe-oxygen species in the binuclear site during **O** state as determined by FTIR spectroscopy and an oxygen species may make good sense regarding the catalytic function of O_2 reduction.

Evidence has been already provided for the absence of a peroxide species at the haem a_3-Fe during the **P** state as determined by Raman spectroscopy (Proshlyakov *et al.*, 1996b; Ogura and Kitagawa, 2004), C*c*O is generally not believed to contain a peroxide during catalysis and it has been argued that C*c*O does not produce reactive oxygen species like complexes I and III of the respiratory chain (Lenaz *et al.*, 2006; Cape *et al.*, 2007). However, the electron density in the binuclear site during the **O** state is well fitted by two closely spaced O species, consistent with an O–O structure. Additionally, an O^--O^- may have a catalytic function rather than Cl^-, which does not participate in dioxygenic redox chemistry. Moreover, the two negative charges of an O^--O^- can efficiently neutralise the excess of positive charge placed on the oxidised metal centres (a_3-Fe^{3+} and Cu_B^{2+}, Figure 4-1).

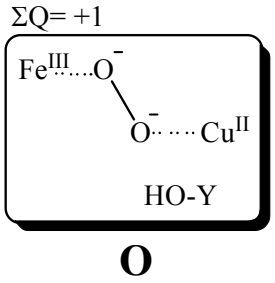

Figure 4-1 Model of the peroxide bound O **state. Peroxide is complexed between the oxidised metal centres Haem(-II)Fe(+III)-O^--O^--Cu(+II)$_B$. Y280 is presented as part of the binuclear site. The net charge of the binuclear site is in sum ΣQ = +1.**

Several groups have constructed protein-free, complex chemical models that mimic the binuclear centre. There are recent C*c*O model molecules representing new structural and functional analogues of its binuclear site (Collman *et al.*, 2003; del Rio *et al.*, 2005; Liu *et al.*, 2005; Collman *et al.*, 2007b). Molecules of this type are Fe/Cu[NMePr]$^+$-derivates, [(F_8TPP)Fe^{III}-(O_2^{2-})-Cu^{II}(TMPA)](ClO_4) or [($L^{N4\text{-}OH}$)Cu^I/Fe^{II}(TMPIm)]. These complexes possess groups that mimic the haem a_3, Cu_B and the covalently linked Y280-H276 structure. Using these molecules, haem^{III}-peroxo-Cu^{II} and haem^{III}-superoxo/Cu^I species have been observed. These binuclear site models seem to simulate the events occurring between the two metal ions and suggest the possible reactions within C*c*O.

One of the model molecules mentioned above is also able to react to an oxygenated form. This oxygenated molecule reacts via a haem^{III}-superoxo/Cu^I species to an oxoferryl-cupric-tyrosyl radical mimicking an intermediate exhibiting an EPR active radical nearby the artificial binuclear

centre. Thus, this species is a model for the natural **P** state intermediate (Collman *et al.*, 2007a). In general it is observed both for model compounds as well as for C*c*O that such haem a_3-Fe(III/II) or Cu_B(II/I) metal centres can independently bind or complex several different dioxygen/peroxide species.

4.3.2 Reversibility of P → F state transition – the peroxide bound F_H state

In Figure 4-2 a new model for the H_2O_2-induced intermediate structures of C*c*O is presented. The $\mathbf{P_H}$ and $\mathbf{F^{\bullet}_H}$ states are both depicted as already well-known from the literature. C*c*O forms the $\mathbf{F_H}$ state in the presence of an excess of H_2O_2, which was commonly thought to be an oxoferryl state plus a complexed water molecule bound to Cu_B.

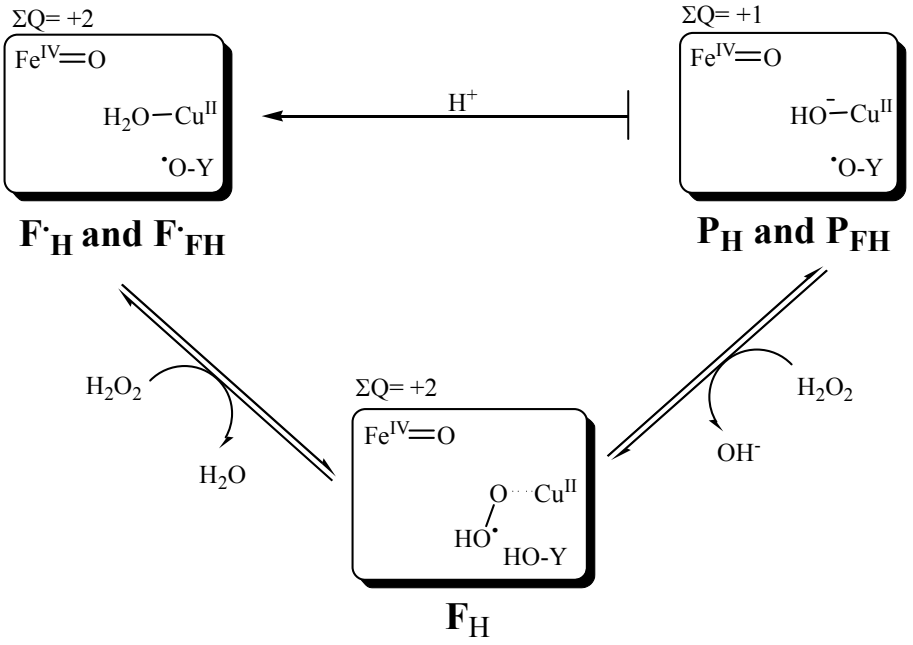

Figure 4-2 Model of the $F^{\bullet}_H/P_H$ state → the F_H state → the $F^{\bullet}_{FH}/P_{FH}$ state transitions. C*c*O complexes a neutral protonated superoxide at Cu_B in the F_H state reversibly (Cu(II)-$^{\bullet}O_2H$). Simply by adding catalase excess superoxide/peroxide is removed and C*c*O reforms the $F^{\bullet}_{FH}/P_{FH}$ states.

However, the $\mathbf{P_H/F^{\bullet}_H}$ → $\mathbf{F_H}$ state reaction is reversible simply by reducing the H_2O_2 concentration using catalase (chapter 3.4.2). Several groups have identified superoxide anions ($^{\bullet}O_2^-$) in the **F** state by trapping methods although in amounts far below expected (Ksenzenko M. Yu., 1992; Fabian and Palmer, 1995), thus we propose that the H_2O_2-induced $\mathbf{F_H}$ state is actually an oxoferryl state with a stable, poorly exchangeable superoxide anion bound to Cu_B (Cu_B-$^{\bullet}O_2^-$ or

Cu_B-$^{\bullet}O_2H$). This may explain the potential of a second H_2O_2 molecule to reduce the Y167 radical in the $\mathbf{P_H/F^{\bullet}_H}$ state via a one-electron donation to form the $\mathbf{F_H}$ state.

The apparent $\mathbf{F_H} \rightarrow \mathbf{P_{FH}/F^{\bullet}_{FH}}$ transition includes the reformation of a radical species. The partially resolved hyperfine structure, such as that seen in Figure 3.4-5 B, can be used to assign such tyrosyl radical signals (MacMillan *et al.*, 1999; Budiman *et al.*, 2004; Svistunenko *et al.*, 2004) and Figure 3.4-5 B clearly reveals that the radical species is the same in both the $\mathbf{F^{\bullet}_H}$ and $\mathbf{F^{\bullet}_{FH}}$ states (and also the $\mathbf{P_H}$ and $\mathbf{P_{FH}}$ states, data not shown). Thus this signal indicates that the tyrosyl radical is located on Y167. This electron can then be regained by the superoxide (Cu_B-$^{\bullet}O_2^-$) in the $\mathbf{F_H}$ state of C*c*O with formation of a $\mathbf{P_{FH}}$ or $\mathbf{F^{\bullet}_{FH}}$ state during catalase treatment. The first $^{\bullet}O_2^-$ can then leave Cu_B as a diffusible O_2^{2-}, HO_2^- or as a H_2O_2 molecule.

However, the overall question is whether this $\mathbf{F_H} \rightarrow \mathbf{P_{FH}/F^{\bullet}_{FH}}$ reaction is a "one-electron backwards" or a "three-electron forwards via **O** state" reaction.

As shown in Figure 3.4-6, when an $^{\mathbf{anaerobic}}\mathbf{F_H}$ state, formed by addition of glucose and glucose oxidase, is treated with CO and catalase no **P** state is formed but rather an **E** state ($^{\mathbf{anaerob}}\mathbf{F_H}$ + catalase + CO $\rightarrow \mathbf{E_{CO}}$) (Ruitenberg *et al.*, 2000b). Thus, the stability of an $^{\mathbf{anaerobic}}\mathbf{F}$ state in the presence of catalase (Figure 3.4-7) would explain the need for a "three-electron forward" ($^{\mathbf{aerob}}\mathbf{F_H}$ + catalase $\rightarrow \mathbf{P_{FH}/F^{\bullet}_{FH}}$) reaction, because in "Ruitenberg's approach" no third molecule of H_2O_2 is available for the $\mathbf{F} \rightarrow \mathbf{O}$ decay and further reaction is excluded due to the lack of O_2. In fact, we propose that the $\mathbf{P_{FH}}$ and $\mathbf{F^{\bullet}_{FH}}$ states are formed from the $\mathbf{F_H}$ state passing an **O** state via a three-electron reaction with a putative H_2O_2- and O_2- dependent system at H_2O_2-limited conditions.

However, if this reaction were indeed a "three-electron forward" reaction then it would be expected that one superoxide should be released per electron. Thus far, although such superoxide production was demonstrated for C*c*O, such high amounts have yet to be observed. Then again two superoxide (2 $^{\bullet}O_2^-$) molecules disproportionate to O_2^{2-} and $\mathbf{O_2}$, restricting their observation! However, in this work $\mathbf{O_2}$ production upon $\mathbf{F_H}$ state formation at pH 9 was shown using a Clark-Type oxygen electrode. Several haem-copper oxidases display this effect. The catalase-like mechanism of oxidases reveals the peroxidase activity of C*c*O as described in the literature (Orii, 1982). The K_M value of 4 SU-wt ATCC C*c*O for H_2O_2 is 225 μM +/- 45 μM (Table 3.4-1), which is in good agreement with published data (K_M = 180 μM for the bovine C*c*O). Superoxide dismutase (SOD) does not disturb the dioxygen production of C*c*O during peroxide treatment and this indicates that SOD does not influence the cycling of C*c*O's calalase-like mechanism. Accordingly, superoxide molecules might be retained intra-molecularly within C*c*O and thus Cu_B may provide a protein-internal storage for $^{\bullet}O_2^-$ and O_2^{2-}.

Moreover, evidence has been presented for superoxide production even during the natural catalytic cycle of C*c*O (Fridovich and Handler, 1961).

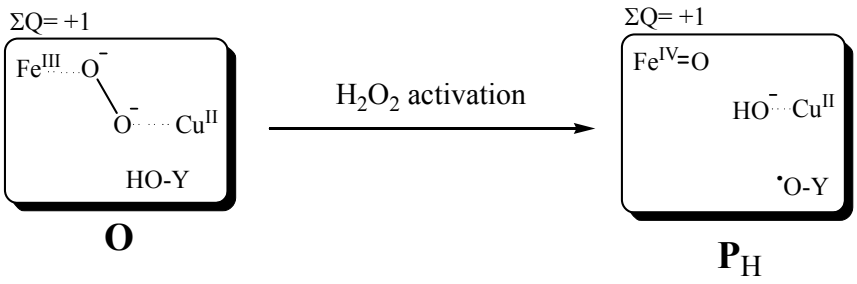

Figure 4-3 Model for the formation of the P_H state from the peroxide bound O state.

If the $\mathbf{F_H}$ state does contain a superoxide attached in the binuclear site, then it is likely that the **O** state, which is formed by addition of one electron and one proton to the $\mathbf{F_H}$ state, contains a bound peroxide species. Indeed, a peroxide bridging the haem a_3-Fe and the Cu_B is the best fit for the electron densities in the X-ray structure of the **O** state in beef heart C*c*O, in *R. sphaeroides* C*c*O and in *P. denitrificans* C*c*O. The peroxide bound in the **O** state might be unreactive and requires a second H_2O_2, or a dioxygen plus two electrons plus two activating protons for formation of the $\mathbf{P_H}$ state (Figure 4-3).

It would be important to know whether the $\mathbf{O} \rightarrow \mathbf{P_H}$ step is dioxygen dependent and, while the $^{anaerob}\mathbf{F_H}$ state is quite simple to create using glucose and glucose oxidase, the anaerobic $\mathbf{O} \rightarrow \mathbf{P_H}$ state transitions have so far proved difficult to study. First, the monooxygenase glucose oxidase produces H_2O_2 (glucose + H_2O → lactone + H_2O_2), which induces the $\mathbf{P_H}$ state by itself (data not shown). Furthermore, a vacuum line reinforces, on the one hand, the H_2O_2 decomposition of the H_2O_2 reagent solution by shifting the equilibrium (2 H_2O_2 → 2 H_2O + O_2), thus the H_2O_2 stock solution would contain a decreased H_2O_2 concentration. On the other hand, anaerobisation via evacuation and nitrogenation may not induce anaerobic but only microaerobic conditions.

It is well-known that the $\mathbf{P} \rightarrow \mathbf{F}$ state transition in the natural cycle is accompanied by the generation of a membrane potential (Wikström, 1989). Thus, the reversion of the $\mathbf{P_H} \rightarrow \mathbf{F_H}$ state transition would appear different in solubilised C*c*O and C*c*O reconstituted into proteoliposomes. The results of this work show that the H_2O_2/catalase-induced $\mathbf{P_{FH}}$/$\mathbf{F^{\bullet}_{FH}}$ and $\mathbf{F_H}$ state transitions are not hindered energetically and/or kinetically. A possibility to explain the reversibility might be the uncoupling of the binuclear centre during this artificial H_2O_2 treatment and that the energy-requiring gating mechanisms of the proton pump steps are uncoupled from the redox reactions at the haem a_3-Cu_B centre in this case. Experiments to verify this using C*c*O reconstituted into proteoliposomes were performed. Figure 3.4-3 shows the ability of the reconstituted C*c*O into proteoliposomes to perform the same reactions as the solubilised C*c*O. Obviously the generated membrane potential, built from one $\mathbf{P} \rightarrow \mathbf{F}$ state transition, is negligibly small. The effect of any non-catalytically produced membrane potential (the membrane potential can also drive the $\mathbf{F} \rightarrow \mathbf{P}$

state transition) does not seem to be crucial, especially if the system is buffered. Thus, the single forwards or backwards transition steps are not energetically hindered in both the solubilised and the reconstituted C*c*O.

The results presented here suggest a new interpretation for the function of the covalently linked Y280-H276 Cu_B ligand. The structures of many proteins involving H_2O_2 in their catalytic mechanisms such as catalases or galactose oxidase have also revealed covalently linked amino acid residues near their active sites. These covalent bonds are deliberately induced within the protein by additional H_2O_2 reactions. The H_2O_2-linked amino acids provide stable conditions for further reactions with H_2O_2 within the enzyme. Here we propose that H_2O_2 or O_2^{2-} is indeed an intermediate molecule in the natural C*c*O cycle, and that the enzyme thus uses the covalently linked Y280-H276-Cu_B structure for structural stabilisation of H_2O_2 species and to support the metal centres during dioxygen reduction reactions. Regarding the formation of this cross-link, this covalent bond is more likely induced into C*c*O by the first electron inputs via Cu_A and the first O_2 reduction chemistry in contrast to co-translational enzymatically catalysed formation.

In summary, the reversibility of the $\mathbf{P_H} \rightarrow \mathbf{F_H}$ state transition turned out to result from a forward reaction, which implies an intrinsically bound superoxide/peroxide during the $\mathbf{F_H}$ and **O** states in the presence of catalase. The lack of H_2O_2 in the bulk solution demands for reduction equivalents stored within C*c*O.

4.3.3 The novel P_{10} state – evidence for the peroxide bound O state

The induction of the $\mathbf{P_{10}}$ state in the absence of reduction equivalents supports the idea of a bound peroxide during the **O** state (Figure 3.4-9), because the transition of the $\mathbf{O} \rightarrow \mathbf{P_{10}}$ state is induced simply by increasing pH from 8 to 10. The pH 10 species shows a maximum at 612 nm in the difference absorption spectrum (*minus* the **O** state) and possesses the additional tyrosyl 167 radical species (Figure 3.4-16). The potential of the $\mathbf{P_{10}} \rightarrow \mathbf{F^{\bullet}}$ state transition (612 nm → 575 nm) indicates a functional importance for this putative **P**-like state (Figure 3.4-15). The transition of the $\mathbf{P_{10}} \rightarrow \mathbf{F^{\bullet}}$ state has an isosbestic point at λ = 592 nm, which fits quite well to the standard transition of the $\mathbf{P_H} \rightarrow \mathbf{F^{\bullet}_H}$ state. However, the "pK_a" of this transition is rather high having a value of pK_a = 8.

The formation of the $\mathbf{P_{10}}$ state is kinetically very slow suggesting a kinetically hindered reaction, which may have a lower activation energy, if the pH is increased (Figure 3.4-14). On the other hand, the fully formed $\mathbf{P_{10}}$ state is stable for around 20 min when the experiment is performed in the range of 10 μM C*c*O. It is observed that $\mathbf{P_{10}}$ state evolution shows similarities to $\mathbf{P_H}$ state formation (Figure 3.4-13). Thus, the rate of formation depends on the C*c*O concentration, which also happens in the reaction with H_2O_2. This effect may originate in intermolecular interactions of C*c*Os accompanied by an inter-protein electron exchange.

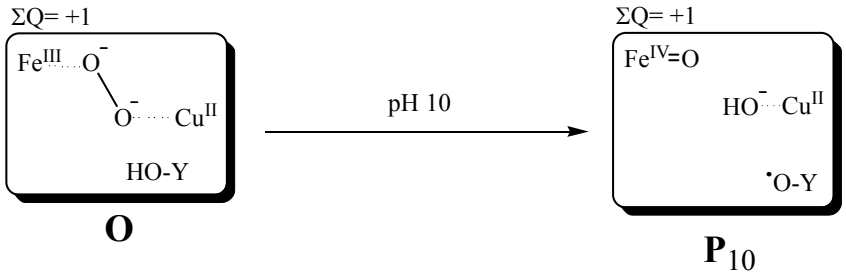

Figure 4-4 Model for the formation of the P_{10} **state from the peroxide bound** O **state.**

In this context, it is expected that the variant W272F would show the same phenotype in $\mathbf{P_{10}}$ state formation as in formation of the $\mathbf{P_H}$ state, because it is not able to form an oxoferryl state by cleaving the dioxygen bond. Indeed, in a pH shift experiment from pH 8 to 10, the variant W272F did not form a $\mathbf{P_{10}}$ state, but distributed electrons to its redox-active metal centres (Figure 3.4-17) and a maximum at 605 nm indicative for haem *a* reduction and a maximum at 635 nm for putative Cu_B reduction were obtained from the difference absorption spectrum (*minus* the **O** state). Several variants of the D/K-pathway and variant Y167F were also investigated with respect to $\mathbf{P_{10}}$ formation in order to determine the importance of functional proton and electron pathways (Figure 3.4-18). However, all variants tested (D124N, N131D, E278Q, K354M, G196D, N113D, S193Y and Y167F) showed distorted spectra, but full $\mathbf{P_{10}}$ state formation and the maxima at 612 nm were slightly red shifted and accompanied by a certain proportion of the maximum at 635 nm. Nonetheless, the transition of $\mathbf{P_{10}} \rightarrow \mathbf{F^{\bullet}}$ state has been observed in all variants.

In summary, C*c*O may contain a bound peroxide in the **O** state and reacts to a $\mathbf{P_{10}}$ state upon shifting the pH from 8 to 10. Both intrinsic electrons of this bound peroxide are used for the O^{-}-O^{-} bond splitting followed by the formation of a putative oxoferryl intermediate in the $\mathbf{P_{10}}$ state accompanied by the recorded tyrosyl 167 radical (Figure 4-4).

4.3.4 New model of the native catalytic cycle – introduction of the peroxide bound O, E, R, P and F states

The results presented here provide experimental evidence for a peroxide bound in the **O** state. A new model for catalytic cycle of C*c*O was designed (Figure 4-5) including a bound peroxide during the **O** state to stabilise the charge within the binuclear centre, resulting in a net charge of $\Sigma Q = +1$.

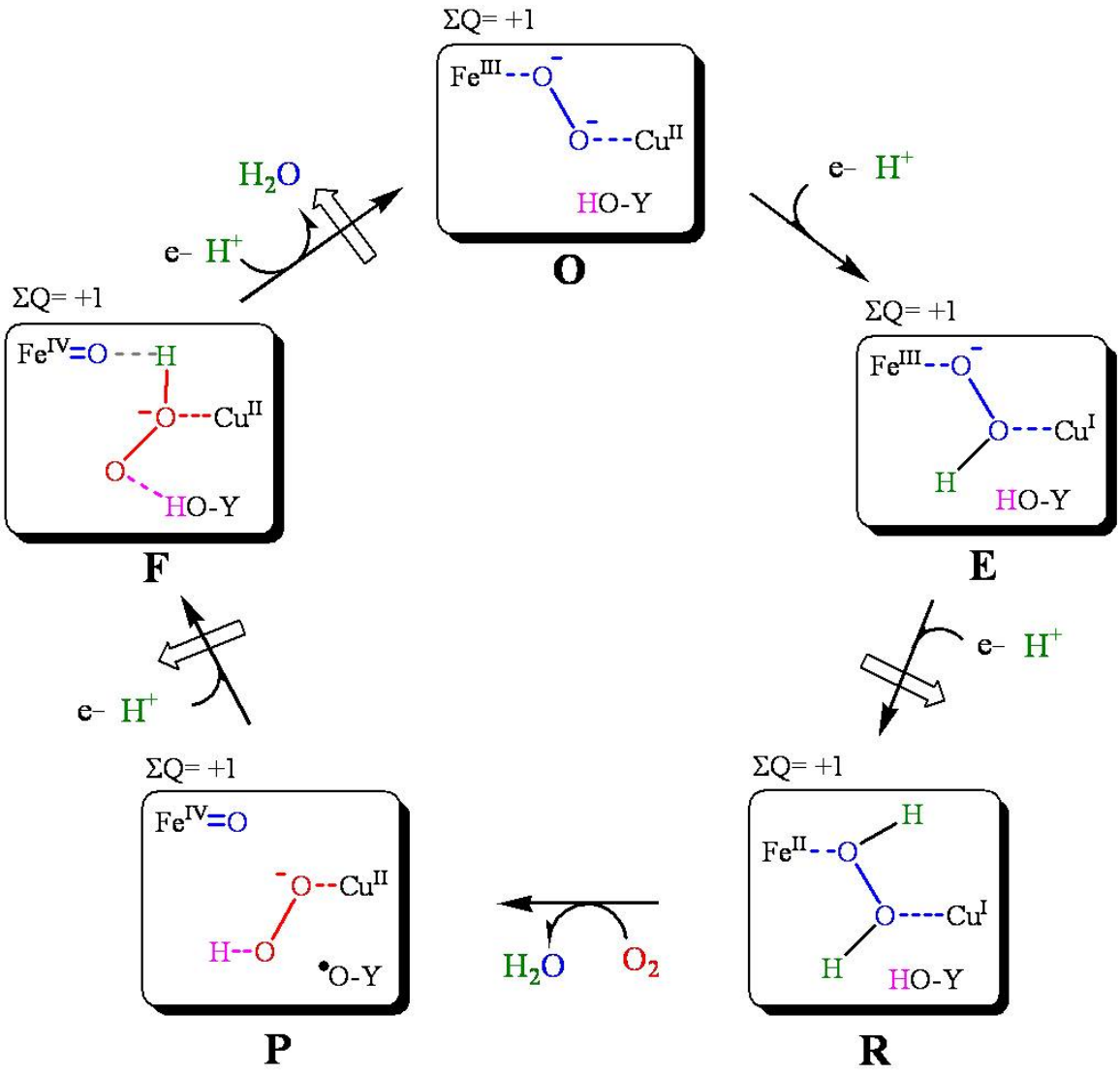

Figure 4-5 New model for the natural catalytic cycle of C*c*O. The boxes represent redox and protonation states of the intermediates in the haem a_3-Cu_B binuclear centre plus Y280. Intermediates are represented below the boxes as O, E, R, P **and** F **states. The** O **state shows a peroxide ion complexed between the two oxidised metal centres. The** P **state contains an oxoferryl intermediate plus a protonated peroxide ion at Cu_B in the presence of the Y280* radical. The** F **state reforms Y280 having a delocalised negative charge between Cu_B and Y280. The overall net charge of the centres for each state is ΣQ = + 1. The model includes proton pumping by electrostatic repulsion. Black arrows indicate e^- and H^+ uptake or the formation of water; empty arrows represent the pumping steps.**

According to recent publications, each electron input into C*c*O is followed by an uptake of two protons. Thus, the first chemical proton neutralises one negative charge of the bound peroxide, whereas the electron reduces the high-potential Cu_B forming the **E** state (Fe(III)-O^--OH-$Cu(I)_B$); and another proton is pumped across the membrane. First, the pumped proton is stored at a pumping site and then secondly pumped via an exit channel after the energy conversion from redox energy to conformational change. This pumping site for pumped protons may be located at

the haem a_3 propionates or at a cluster comprised of the haem a_3 propionates and other negatively charged amino acids (Michel 1998, Michel 1999, Wikström and Verkhovsky, 2007).

The intrinsically bound peroxide (Figure 4-5, blue) accepts the first two incoming protons and the first two electrons reduce the metal centres. Thus, the overall charge of the binuclear centre is constantly at +1 and the *mixed-valence* **R** state state is formed accompanied by a complexed H_2O_2 (Fe(II)-HO-OH-Cu(I)$_B$). C*c*O can now act as a peroxidase using its haem a_3 group for the HO-OH splitting. The resulting **P** state may be formed independently from the Cu_B chemistry having an oxoferryl intermediate (Fe(IV)=O^{2-}). Fe(II) of the **R** state provides two electrons for this reaction and when H_2O leaves the binuclear centre the reduced Cu(I)$_B$ centre can accept a new O_2 molecule (Figure 4-5, red). O_2 is reduced to an O_2^{2-} species in a concerted electron donation of Cu(I)$_B$ and Y280 in the natural cycle and the generated **P** state contains a protonated peroxide ion complexed at Cu_B (Fe(IV)=O^{2-} HOO^--Cu(II)$_B$). The negative charge at the protonated peroxide in the **P** state cannot be stabilised by the neutral Y280 radical and this electronic arrangement of charges during the **P** state provides the absorption properties required for the absorbance at λ = 610 nm. A further electron/proton input leads to the **F** state showing a reduced and protonated Y280. The now neutral Y280 can be deprotonated, forming a tyrosinate anion and thus protonate the peroxide anion, and intramolecular protolysis delocalises the negative charge within the binuclear site and mesomerisation leads to an absorbance at 580 nm in the **F** state. The **O** state is induced via further electron and proton input resulting in an Fe(III)-OH^- species, which is protonated to release an H_2O molecule and electronic and spatial rearrangement of the peroxide species then leads back to the ground state.

There are several arguments against the peroxide bound **O** state. One argument is that the **O** state would react to a **P** state directly, if having two electrons intrinsically.

However, a counter-argument might be that the complexed peroxide may have to be activated either by a second H_2O_2 molecule (providing H^+ to the binuclear centre) or by the shift of the equilibrium at very high pH. Thus, the a_3Fe^{+3}-O^--O^--$Cu^{+2}{}_B$ structure seems to be very stable electrostatically and does not further react without external activation.

The two metals of the binuclear site of oxidised 2 SU-wt rec C*c*O display a distance of a_3Fe–Cu_B = 4.59 Å comparable to oxidised C*c*O from *R. sphaeroides* (1m56) having a distance of 4.82 Å while oxidised bovine C*c*O (1v54) shows a distance between Fe-a_3 and Cu_B of 4.99 Å. However, the reduced bovine C*c*O (1v55) shows a longer distance of 5.13 Å. The loss of the putative bound peroxide in the fully reduced C*c*O may result in higher flexibility of the metal centres (Haem^{2-}-a_3-Fe^{2+} and $Cu^{1+}{}_B$), because the negatively charged species has left the centre and thus the binuclear site is empty in this state.

There is still the possibility that the continuous turnover of C*c*O excludes peroxide molecules. After peroxide splitting in the **P** state, no additional O_2 may bind to the Cu_B and then the binuclear site would be peroxide-free during this state. This state may result in an energy-rich **O** state

(maybe the *fast* form or **O~** state (Wikström and Verkhovsky, 2002)) and then the formation of the **R** state in C*c*O may induce the new binding of an O_2 molecule at Fe(II). According to this reacton, the catalytic cycle runs further on such as previously proposed (during **P** state an OH^- is bound at Cu_B).

Another question is, why other groups do not see a peroxide bound in the **R** state? Most groups reduce C*c*O forming a four-electron reduced (fully reduced) enzyme and there is no opportunity to observe a peroxide species in this approach since even all O_2 molecules of the bulk solution are reduced to water by reducing agents such as dithionite. All bound peroxides are also reduced to water and therefore, pulsing reduced C*c*O with O_2 forms the well described **A** state (Fe(II)-O_2) comparable to oxygenated haemoglobin.

In summary, the structure of 2 SU-wt rec C*c*O; the reversibility of the **P** → **F** state transition and the formation of the $\mathbf{P_{10}}$ state suggest a complexed O^--O^- during the **O** state instead of a bound H_2O molecule and a bound OH^- ion. Whether the $\mathbf{P_{10}}$ state contains in fact an oxoferryl intermediate (Fe(IV)=O^{2-}) has still to be proven by Raman and MCD spectroscopy or by other available methods such as calometric approaches.

4.4 The electron pathway from Y167 to the binuclear site

It was proposed that residue Y167 is not the direct donor of the "missing" electron that is required for the reductive cleavage of the dioxygen bond in C*c*O but that the radical species may be formed in a secondary process in the steady state of the reaction with H_2O_2. Thus, the original donor of the "missing" electron is still a point of debate.

The origin of the radical that can be observed in the reaction of C*c*O with H_2O_2 was previously assigned to Y167, however it was also demonstrated that this residue is not essential for the function of the enzyme, because the variant Y167F is still able to form an oxoferryl state and maintains a relatively high turnover rate while retaining full proton pumping activity (Budiman *et al.*, 2004).

Two configurations of the **P** state in rapid electronic equilibrium were observed in pre-steady state reaction kinetics of C*c*O from *P. denitrificans* (Wiertz *et al.*, 2004). One species was assigned to a tryptophan cation radical while for the second species a tyrosine radical could not be ruled out. The authors postulated that W272 or W164 might be the source of this radical. In addition, the possible involvement of a tryptophan residue in dioxygen bond cleavage was discussed (Svistunenko *et al.*, 2004). They suggested that a tryptophan residue might form an intermediate radical state between the original donor of the electron which is supposed to be the cross-linked Y280 and the observed tyrosyl radical at residue 167. At variance, it was discussed on the basis of quantum chemical calculations that the actual donor of the missing electron might be W272 (Siegbahn and Blomberg, 2004).

The experiments performed here using W272 variants have revealed two important pieces of information. 1) The mutation of W272 drastically affects the catalytic function of C*c*O and 2) the W272 variants completely lose the ability to form the $\mathbf{P_H/F^{\bullet}_H}$ and $\mathbf{F_H}$ states in the reaction with H_2O_2, indicating that also in the catalytic cycle the cleavage of the O_2 bond might not be possible (Table 3.5-1 and Figure 3.5-2 and Figure 3.5-3).

Furthermore, no EPR signal from a radical species was observed using W272 variants (data not shown) and from this we conclude that W272 plays an important role in the formation of the radical species at Y167 and also possibly in the catalytic mechanism of the enzyme itself. W272 is located in subunit I of C*c*O at a distance of 8.5 Å from the haem Fea_3 iron and 5 Å from Cu_B and is also directly H-bonded to Y167. A close relationship between these two residues and the possibility of electron transfer between them seems to be obvious.

As no other radical EPR signal was observed in W272 variants, one may speculate if this tryptophan really is the original donor of the “missing” electron required for dioxygen bond cleavage. However, the involvement of another amino acid residue, for example Y280, cannot be excluded because the lifetime of this radical species either be very short or EPR silent. In this case, W272 could form an intermediate radical state between the original electron donor and Y167, and in variant W272F this pathway is demonstrated to be blocked.

Another reason why the radical at Y167 may not be formed in variant W272F could be due to its close position to the binuclear center. This may affect the structural integrity and functionality of the binuclear site and the reaction with H_2O_2 may be impaired, as indicated by the change of the spectral properties of variant W272F in the $\mathbf{P_H/F^{\bullet}_H}$ states.

Variant W164F lacks a large tryptophan residue nearby the binuclear site between the haem A groups; however, an EPR-signal from Y167 is still observed (Figure 3.5-7), although this residue is also located close to the binuclear site. The turnover rate of W164F is relatively high, having 20 – 40 % of wild type activity (Table 3.5-2). But, in the reaction with H_2O_2 no $\mathbf{P_H/F^{\bullet}_H}$ is observed in variant W164F as determined by UV-vis spectroscopy (Figure 3.5-4 and Figure 3.5-5), but rather an $\mathbf{F_H}$ state at low pH (Figure 3.5-6). The variants W272F and W164F display 605 nm and 635 nm maxima instead of the standard maximum of the $\mathbf{P_H}$ state at 610 nm in the difference absorption spectrum (*minus* the **O** state). Presumably, the O–O bond is not broken and this result indicates the reformation of electron arrangements due to redox potential shifts and the distribution of the excess of two electrons of the H_2O_2. Regarding typical absorption properties of the reduced haem *a* absorbances, the maximum at 605 nm clearly indicates that electrons are distributed to haem *a*. Moreover, singly reduced $Cu(I)_B$ shows an absorbance band shift of its charge-transfer complex from λ = 665 nm (haem a_3-Fe^{III} – Cu^{II}_B) to λ = 635 nm (haem a_3-Fe^{III} – Cu^{I}_B) (Belevich *et al*., 2007). However, the absorption coefficient of the $Cu(I)_B$-charge transfer complex is very small (Mitchell *et al.*, 1991), which may exclude reduced $Cu(I)_B$ as the origin of

the enlarged 635 nm maximum in this state. Additionally, the maxima at λ = 635 nm from W272F and W164F vanish at low pH. But in spite of all these similarities in the UV-vis difference absorption spectra, a radical at residue Y167 can still be detected in variant W164F by EPR spectroscopy, but not in variant W272F and this observation supports the proposal of the special importance of residue W272 for the formation of the radical at Y167.

The scenario that W272 is the original donor of the missing electron which is the replenished by a nearby tyrosine residue, either Y167 or the cross-linked Y280, also provides a likely explanation why in the $\mathbf{P_H}$ state, created with H_2O_2, a radical is located at Y167 is observed whereas not in **P** states created by other means: H_2O_2 carries two H atoms into the binuclear site; for the reductive cleavage of the O=O double bond, therefore, no extra protons are required for the formation of an oxoferryl state, whereas in the native cycle a proton is required. The hydroxyl group of Y280 can deliver a proton plus an electron, whereas Y167 appears to be too far away for a proton delivery to the binuclear site. Therefore it is feasible that in the native cycle Y280 is the secondary donor of the missing electron whereas upon treatment with H_2O_2 it also can be Y167.

The proposal that W272 is the primary donor of the missing electron also makes sense with respect to the conservation of this residue. W272 appears to be absolutely conserved within the superfamily of haem-copper containing terminal oxidases. Whereas, Y280, commonly believed to be the donor of the missing electron at present, is also highly conserved in the most distant members of this superfamily, the *cbb*$_3$-Type C*c*Os, because this tyrosine used for the His-Tyr cross-link is provided by a neighbouring α-helix in *cbb*$_3$-Type C*c*Os (Rauhamaki *et al.*, 2006).

In order to replace the function of residue W272, other radical stabilising residues (Lassmann *et al.*, 1999; Lassmann *et al.*, 2000; Biglino *et al.*, 2006) at the same position, here W272Y or W272H, were produced by site-directed mutagenesis (Table 3.5-1). The importance of a tryptophan residue at position 272 is clear since no other residue can suppress the phenotype of the missing W272.

On the one hand, the structural instability of W272F showed up in trials to prepare the 2 SU-form of W272F, which resulted in protein aggregations during LDAO treatment. On the other hand, another proposed functional importance of W272 was recently revealed by time-dependent EPR analysis.

In those experiments it was observed that after the **F** state a neutral tryptophan radical (W*) is formed (Wiertz *et al.*, 2007) and the **F** state is reduced by the assigned W272, relaxing back to the **O** state, whereas the ε1-N-proton of W272 is suggested to leave the binuclear site to be pumped. The missing electron of W272* is then replenished by cyt *c*. Again, the four-electron reduced (fully reduced) C*c*O reacting with O_2 does not reveal the stabilised Y167 radical in the $\mathbf{P_R}$ state such as in the H_2O_2-induced $\mathbf{P_H}$ state, but rather a tryptophan radical after the **F** state. W272 is suggested as the natural electron donor to the oxoferryl intermediate **F** state forming the

suggested intermediate $\mathbf{F_{W^*}}$ state. This result seems to be unexpected, but it further confirms the functional importance of W272.

In summary, the stabilised radical is hosted at Y167 during $\mathbf{P_H/F^{\bullet}_H}$ states in reactions with low molar equivalents of H_2O_2. This electron pathway from Y167 to O_2 may be facilitated via its H-bonded W272. In addition, several tryptophans of the bovine C*c*O can be easily oxidised, when the binuclear centre reacts with H_2O_2 (Lemma *et al.*, 2007) and generally, tryptophans play important roles for the catalytic function of C*c*O. Residue W272 especially displays two independently proposed functions:
1) W272 provides the 4th electron for dioxygen reduction in the $\mathbf{P_H/F^{\bullet}_H}$ states
2) W272 reduces the oxoferryl intermediate of the **F** state resulting in formation of the $\mathbf{F_{W^*}}$ state.

4.5 Functional studies on the D-pathway

C*c*O is a redox-driven proton pump and solubilised C*c*O reconstituted into liposomes pumps protons across the membrane bilayer generating an electrochemical proton gradient. Each electron input from reduced cyt *c* (from the bulk solution) and the uptake of protons, chemical and pumped protons (from the interior of the vesicles), build up this membrane potential (see review Ferguson-Miller and Babcock, 1996). Pumping experiments using pH indicators have allowed to determine the pump stoichiometry in pumped protons per electron input (H^+/e^-). Thus, *aa*$_3$-C*c*O from *P. denitrificans* displays a ratio of one pumped proton per single electron input (Table 3.6-2). Polar residues within the hydrophobic core of subunit I have been mutated in order to reveal the mode of this proton translocation and the residues D124 and N131 were identified having functional importance for proton uptake and pumping, respectively (Table 3.6-2). Variant D124N has lost much of its catalytic activity, because its cyt *c* oxidation and proton pumping activities are almost abolished; these results were recently confirmed using ATR-FTIR spectroscopy (Gorbikova *et al.*, 2007a; Gorbikova *et al.*, 2007b). On the other hand, the variants N131D, N113D (this work) and N199D (Pfitzner *et al.*, 2000) show full or high cyt *c* oxidation activity, but do not pump protons across the membrane bilayer. The introduction of a negative (N → D) charge seems to disturb the electrostatical coupling of the D-pathway, resulting in pK_a shifts of amino acids and disruption of H-bonds of water molecules.
Thus, variant N131D shows in the electron density map a disturbed and distorted coordination of water molecules as identified by comparison with the electron density map of the 2 SU-wt rec C*c*O of this work (Dürr *et al.*, submitted). The result may explain the deficiency in proton pumping of variant N131D (Fetter *et al.*, 1995a; Pfitzner *et al.*, 1998), because the distorted water network may have a direct influence on residue E278. E278 is a proposed branching point for protons: chemical protons are gated to the binuclear site, whereas pumped protons are gated to a putative

pumping site. It is proposed for the natural catalytic cycle that the mobility of E278 is the basis for a mechanical gating mechanism of protons, which is driven by the redox energy and the electrostatics of C*c*O. E278 may move its side chain to provide protons first to the binuclear side and then, after dihedral angle spinning, to deliver protons to the exit pathway maybe via the haem a_3 propionates. Recently, the moving of the side chain of E278 has also been calculated in MD simulations (Tuukkanen *et al.*, 2007).

Again, the structure of N131D (Dürr *et al.*, submitted) provides indications that the redox energy of dioxygen reduction might be coupled to electrostatic and H-bond networks and thus might switch E278 into different conformations in order to pump protons across the membrane.

Residue N131 forms together with residues N113 and N199 a special three-asparagine motif, a asparagine-triad. To understand the nature of the pumping deficiency of variants N131D, N113D (this work) and N119D (Pfitzner *et al.*, 2000) the structure of the 2 SU-wt rec wt C*c*O has been analysed with attention to the properties of the D-pathway. It is proposed that the D-pathway facilitates the transfer of all pumped protons. The uncharged asparagines N131, N113 and N199 of the asparagine-triad might block the proton transfer in the wild type D-pathway. Water molecules are located at the entrance of the D-pathway below the N131-N113-N199 asparagine-triad. Above this triad the water chain continues to residue E278, the end of the D-pathway. A not known redox-coupled mechanism may then induce a structural change at the asparagine-triad and thus may re-structure the water network for an effective proton transfer. The water chain connecting the entrance of the D-pathway with E278 might be distorted in N131D, N113D and N199D due to the introduced negative (protonatable) charge. To determine the meaning of the asparagine-triad in detail, further mutagenesis studies have to be performed. The production of double variants in these positions or the substitution of the asparagines to serines might provide evidence for a regulated proton blocking mechanism at the N131-N113-N199 asparagine-triad.

Wt C*c*O seems such electrostatically coupled (Johansson, 2007) that one single, additional negative charge in the D-pathway may decouple the energy-consuming pumping step from energy-providing redox chemistry. This putative charge effect was demonstrated in variant N131**D** (Pfitzner *et al.*, 1998), N113**D** (this work), N199**D** (Pfitzner *et al.*, 1998; Han *et al.*, 2006); G196**D** (this work and (Han *et al.*, 2005)) and more recently in S189**D** (Namslauer *et al.*, 2007). However, these aspatic residues might be protonated and thus may not change the electrostatics, and the phenotypes of these variants may also be caused by a structural change.

As recently published, the combination of a redox-coupled conformational change of D51 (bovine numbering, a homolougous residue to D51 does not exist in C*c*O from *P. denitrificans*) located near the intermembrane surface and the existence of an H-bond network connecting D51 to the matrix surface suggests in bovine C*c*O that the proton-pumping process is mediated at D51. Mutation analyses resulted in support of the proposal that D51 plays a critical role in the proton

pumping process (Yoshikawa *et al.*, 2006). However, these results have not been accepted in this field.

In an additional publication it was reported that a redox-dependent module of H503/D91 (bovine numbering) controls both dioxygen reduction and proton pumping. In the reduced state, a water molecule is fixed by H-bonds between H503 and D91 of the D-pathway. Thus, D91/H503 cooperatively traps protons on the fixed water molecule. Upon oxidation, the H503 imidazole ring rotates by 180 degrees to break the H-bond to the protonated water and releases the proton to D91. On reduction, D91 donates the proton to the dioxygen reduction site through the D-pathway (Muramoto *et al.*, 2007). Overall, the results presented here demonstrate the influence of charged or polar amino acids for proton transfer in the D-pathway.

Contiuum electrostatic calculations suggested the participation of residue H28 and D30 in proton pumping because their pK_a values were strongly dependent on the dielectric constant within the C*c*O (Olkhova *et al.*, 2005b). However, proton pumping experiments of variants H28A and D30N revealed that they display full activity in both dioxygen reduction and proton pumping (Table 3.6-2) and this biochemical data suggest that these residues do not play a role in proton pumping. These pumping experiments were performed using 4 SU-variants, in contrast to the contiuum electrostatic calculations. In these calculations, the structure of 2 SU- wt ATCC C*c*O (pdb-file 1ar1) was used for simulations, but residues H28 and D30 are located near subunit III. Thus, subunit III may influence the pK_a values of H28 and D30 instead of the bulk water used in these calculations.

In summary, additionally introduced negative charges in the D-pathway may impair the efficiency of C*c*O's proton pumping. The wt C*c*O seems to be very strongly electrostatically coupled and the protein might so connect the energy-providing redox chemistry to the energy-consuming proton pumping steps.

4.6 Conclusions and outlook

The recombinant homologously 4 SU-wt rec C*c*O was compared with the native 4 SU-wt ATCC C*c*O. The results show different properties of 4 SU-wt rec C*c*O, for example in enzymatic activity or in the redox difference absorption spectrum. TXRF measurements showed in both wt C*c*Os the same ratio of the redox-active Fe and Cu (2 Fe : 3 Cu) indicating full complement of the functional metals. The origin of its decreased activity remains elusive and further studies have to be performed such as analyses of different growth conditions, potentially followed by lipid analyses, or finally the establishment of a new expression system (see chapter 4.1).

The importance of subunit III for the structural and functional integrity of C*c*O was demonstrated using the 2 SU-wt rec C*c*O. Mass spectra have not shown a putative (Mills and Hosler, 2005)

covalent bond in *suicide inactivated* 2 SU-wt rec C*c*O (see chapter 3.2). However, the *suicide inactivated* protein shows high instability and denaturates in crystallisation trials. This result indicates that the structural change after inactivation is severe and not only the structure of the active site may be changed, but also the structure of the *suicide inactivated* bulk protein, missing subunit III. Indications are provided, that not subunit III itself, but specifically bound lipids may stabilise the whole protein complex (Varanasi *et al.*, 2006). Accordingly, crystals of the control (*active* 2 SU-wt rec C*c*O) have been obtained under same crystallisation conditions as for *suicide inactivated* 2 SU-wt rec C*c*O (see chapter 4.2).

The identification of the stabilising effect of subunit III can possibly be determined by employment of other spectroscopic methods. The integrity of the binuclear site in dependence of lipids might be observable using FTIR, ATR, MCD or Raman spectroscopy.

Functional studies using the 4 SU-wt ATCC C*c*O have demonstrated a bound peroxide (O^{-}-O^{-}) intermediate during the catalytic cycle (see chapter 4.3). H_2O_2-induced reactions have provided further insights into the overall mechanism of C*c*O as determined by spectroscopic methods. Catalase treatment of the $\mathbf{F_H}$ state leads, contrary to the natural direction of the catalytic cycle, to the apparent transition of the $\mathbf{F_H} \rightarrow \mathbf{P_H/F^{\bullet}_H}$ states, which is accompanied by reappearance of an EPR signal from the $Y167^{\bullet}$ radical. We conclude from these results that the $\mathbf{F_H}$ state hosts a superoxide (or peroxide) adduct at Cu_B in the binuclear site. This proposal is supported by the structures of several C*c*Os in the **O** state (Tsukihara *et al.*, 1996; Ostermeier *et al.*, 1997; Qin *et al.*, 2006) and by the possible charge compensation provided by a peroxide in the binuclear site (Fe^{3+}-O^{-}-O^{-}-$Cu^{2+}{}_B$).

Another support for this proposal provides the novel $\mathbf{P_{10}}$ state having a maximum at λ = 612 nm in the difference absorption spectrum (*minus* the **O** state). It confirms the idea of a peroxide bound in the **O** state. Simply, the alkaline shift from pH 8 to 10 induces $\mathbf{P_{10}}$ state formation. The electrons from the putative bound O^{-}-O^{-} in the **O** state may be used to form the "oxoferryl" state in $\mathbf{P_{10}}$ state. Using EPR spectroscopy it was shown that Y167 hosts a radical species in the $\mathbf{P_{10}}$ state such as in the $\mathbf{P_H}$ state, however, this result does not prove an oxoferryl state. To adress the question whether the $\mathbf{P_{10}}$ state contains an oxoferryl intermediate, other spectroscopic methods have to be employed. For further experiments, MCD and Raman spectroscopy are reliable methods to identify oxoferryl intermediates (Fe^{IV}=O^{2-}).

Finally, the functional and structural information from all these experimental data was used for the analysis of C*c*O's catalytic mechanism. Based on these results a new model for the natural catalytic cycle is proposed (see chapter 4.3.4).

The putative role of peroxide in the catalytic cycle of C*c*O during different intermediate states is demonstrated in this work. This proposal has to be confirmed by other experiments using different methods. A bound peroxide in the **O** state should be removable by pulsing C*c*O with an inhibitor such as CO or CN^{-}. An exact "counting" of the electrons necessary for the first complete catalytic

cycle might also provide evidence for the bound peroxide species during the **O** state (Mochizuki *et al.*, 1999). This might be performed by titration of NADH/NADPH, dithionite or other reduction agents to oxidised C*c*O. A peroxide molecule bound between the haem-a_3-Fe and Cu_B (Fe^{3+}-O^{-}-O^{-}-Cu^{2+}_B) has already been shown in several model molecules of the binuclear site (del Rio *et al.*, 2005). The next exiting step would be the confirmation of this structure in the binuclear site of C*c*O in the **O** state.

5 References

1. Aagaard A, Brzezinski P (2001) Zinc ions inhibit oxidation of cytochrome *c* oxidase by oxygen. *FEBS Lett.* **494**:157-160.
2. Aagaard A, Namslauer A, Brzezinski P (2002) Inhibition of proton transfer in cytochrome *c* oxidase by zinc ions: delayed proton uptake during oxygen reduction. *Biochimica et Biophysica Acta (BBA) - Bioenergetics* **1555**:133-139.
3. Ädelroth P, Brzezinski P (2004) Surface-mediated proton-transfer reactions in membrane-bound proteins. *Biochimica et Biophysica Acta (BBA) - Bioenergetics* **1655**:102-115.
4. Ädelroth P, Ek MS, Mitchell DM, Gennis RB, Brzezinski P (1997) Glutamate 286 in cytochrome *aa*(3) from *Rhodobacter sphaeroides* is involved in proton uptake during the reaction of the fully-reduced enzyme with dioxygen. *Biochemistry* **36**:13824-13829.
5. Ädelroth P, Gennis RB, Brzezinski P (1998) Role of the Pathway through K(I-362) in Proton Transfer in Cytochrome *c* Oxidase from *R. sphaeroides*. *Biochemistry* **37**:2470-2476.
6. Babcock GT, Wikström M (1992) Oxygen Activation and the Conservation of Energy in Cell Respiration. *Nature* **356**:301-309.
7. Balaban RS, Nemoto S, Finkel T (2005) Mitochondria, Oxidants, and Aging. *Cell* **120**:483-495.
8. Belevich I, Bloch DA, Belevich N, Wikström M, Verkhovsky MI (2007) Exploring the proton pump mechanism of cytochrome *c* oxidase in real time. *Proc. Natl. Acad. Sci. U. S. A.* **104**:2685-2690.
9. Belevich I, Verkhovsky MI, Wikström M (2006) Proton-coupled electron transfer drives the proton pump of cytochrome *c* oxidase. *Nature* **440**:829-832.
10. Bickar D, Bonaventura J, Bonaventura C (1982) Cytochrome *c* Oxidase Binding of Hydrogen-Peroxide. *Biochemistry* **21**:2661-2666.
11. Biglino D, Schmidt PP, Reijerse EJ, Lubitz W (2006) PELDOR study on the tyrosyl radicals in the R2 protein of mouse ribonucleotide reductase. *Physical Chemistry Chemical Physics* **8**:58-62.
12. Bloch D, Belevich I, Jasaitis A, Ribacka C, Puustinen A, Verkhovsky MI, Wikström M (2004) The catalytic cycle of cytochrome *c* oxidase is not the sum of its two halves. *Proc. Natl. Acad. Sci. U. S. A.* **101**:529-533.
13. Bränden G, Pawate AS, Gennis RB, Brzezinski P (2006) Controlled uncoupling and recoupling of proton pumping in cytochrome *c* oxidase. *Proc. Natl. Acad. Sci. U. S. A.* **103**:317-322.
14. Bränden M, Sigurdson H, Namslauer A, Gennis RB, Ädelroth P, Brzezinski P (2001) On the role of the K-proton transfer pathway in cytochrome *c* oxidase. *Proc. Natl. Acad. Sci. U. S. A.* **98**:5013-5018.
15. Bratton MR, Pressler MA, Hosler JP (1999) Suicide inactivation of cytochrome c oxidase: Catalytic turnover in the absence of subunit III alters the active site. *Biochemistry* **38**:16236-16245.
16. Brittain T, Little RH, Greenwood C, Watmough NJ (1996) The reaction of *Escherichia coli* cytochrome *bo* with H_20_2: Evidence for the formation of an oxyferryl species by two distinct routes. *FEBS Lett.* **399**:21-25.
17. Brown S, Moody AJ, Mitchell R, Rich PR (1993) Binuclear centre structure of terminal protonmotive oxidases. *FEBS Lett.* **316**:216-223.
18. Brzezinski P, Ädelroth P (2006) Design principles of proton-pumping haem-copper oxidases. *Current Opinion in Structural Biology Membranes / Engineering and design* **16**:465-472.
19. Brzezinski P, Ädelroth P (1998) Proton-controlled electron transfer in cytochrome *c* oxidase: Functional role of the pathways through Glu 286 and Lys 362. *Acta Physiol. Scand.* **163**:7-16.
20. Brzezinski P, Larsson G (2003) Redox-driven proton pumping by heme-copper oxidases. *Biochimica et Biophysica Acta (BBA) - Bioenergetics* **1605**:1-13.
21. Budiman K, Kannt A, Lyubenova S, Richter O-MH, Ludwig B, Michel H, MacMillan F (2004) Tyrosine 167: The Origin of the Radical Species Observed in the Reaction of Cytochrome *c* Oxidase with Hydrogen Peroxide in *Paracoccus denitrificans*. *Biochemistry* **43**:11709-11716.
22. Buse G, Soulimane T, Dewor M, Meyer HE, Bluggel M (1999) Evidence for a copper-coordinated histidine-tyrosine cross-link in the active site of cytochrome oxidase. *Protein Sci.* **8**:985-990.
23. Busenlehner LS, Salomonsson L, Brzezinski P, Armstrong RN (2006) Mapping protein dynamics in catalytic intermediates of the redox-driven proton pump cytochrome *c* oxidase. *Proc. Natl. Acad. Sci. U. S. A.* **103**:15398-15403.
24. Calhoun MW, Lemieux LJ, Garcia-Horsman JA, Thomas JW, Alben JO, Gennis RB (1995) The highly conserved methionine of subunit I of the heme-copper oxidases is not at the heme-copper

dinuclear center: Mutagenesis of M110 in subunit I of cytochrome bo_3-type ubiquinol oxidase from *Escherichia coli*. *FEBS Lett.* **368**:523-525.

25. Calhoun MW, Thomas JW, Gennis RB (1994) The Cytochrome-Oxidase Superfamily of Redox-Driven Proton Pumps. *Trends Biochem. Sci.* **19**:325-330.
26. Calhoun MW, Thomas JW, Hill JJ, Hosler JP, Shapleigh JP, Tecklenburg MMJ, Fergusonmiller S, Babcock GT, Alben JO, Gennis RB (1993) Identity of the Axial Ligand of the High-Spin Heme in Cytochrome-Oxidase - Spectroscopic Characterization of Mutants in the *Bo*-Type Oxidase of *Escherichia-Coli* and the Aa_3-Type Oxidase of *Rhodobacter-Sphaeroides*. *Biochemistry* **32**:10905-10911.
27. Cape JL, Bowman MK, Kramer DM (2007) A semiquinone intermediate generated at the Q(o) site of the cytochrome *bc*(1) complex: Importance for the Q-cycle and superoxide production. *Proc. Natl. Acad. Sci. U. S. A.* **104**:7887-7892.
28. Carr HS, Winge DR (2003) Assembly of cytochrome *c* oxidase within the mitochondrion. *Accounts of Chemical Research* **36**:309-316.
29. Castresana J, Saraste M (1995) Evolution of Energetic Metabolism - the Respiration-Early Hypothesis. *Trends Biochem. Sci.* **20**:443-448.
30. Chance B, Saronio C, Leigh JS (1975) Functional Intermediates in Reaction of Cytochrome-Oxidase with Oxygen. *Proc. Natl. Acad. Sci. U. S. A.* **72**:1635-1640.
31. Chance B, Saronio C, Leigh JS (1975) Functional Intermediates in Reaction of Membrane-Bound Cytochrome-Oxidase with Oxygen. *J. Biol. Chem.* **250**:9226-9237.
32. Chelikani P, Fita I, Loewen PC (2004) Diversity of structures and properties among catalases. *Cellular and Molecular Life Sciences (CMLS)* **V61**:192-208.
33. Chepuri V, Lemieux L, Au DCT, Gennis RB (1990) The Sequence of the *Cyo* Operon Indicates Substantial Structural Similarities between the Cytochrome-*O* Ubiquinol Oxidase of *Escherichia-Coli* and the *Aa*3-Type Family of Cytochrome-*C* Oxidases. *J. Biol. Chem.* **265**:11185-11192.
34. Chepuri V, Lemieux L, Hill J, Alben JO, Gennis RB (1990) Recent Studies of the Cytochrome-*O* Terminal Oxidase Complex of *Escherichia-Coli*. *Biochimica et Biophysica Acta (BBA)* **1018**:124-127.
35. Collman JP, Decreau RA, Yan Y, Yoon J, Solomon EI (2007) Intramolecular Single-Turnover Reaction in a Cytochrome *c* Oxidase Model Bearing a Tyr244 Mimic. *J. Am. Chem. Soc.* **129**:5794-5795.
36. Collman JP, Devaraj NK, Decreau RA, Yang Y, Yan Y-L, Ebina W, Eberspacher TA, Chidsey CED (2007) A Cytochrome *c* Oxidase Model Catalyzes Oxygen to Water Reduction Under Rate-Limiting Electron Flux. *Science* **315**:1565-1568.
37. Collman JP, Kaplun M, Sunderland CJ, Boulatov R (2004) Electrocatalytic Reduction of ROOH by Iron Porphyrins. *J. Am. Chem. Soc.* **126**:11166-11167.
38. Collman JP, Sunderland CJ, Berg KE, Vance MA, Solomon EI (2003) Spectroscopic Evidence for a Heme-Superoxide/Cu(I) Intermediate in a Functional Model of Cytochrome *c* Oxidase. *J. Am. Chem. Soc.* **125**:6648-6649.
39. Conroy CW, Tyma P, Daum PH, Erman JE (1978) Oxidation-Reduction Potential Measurements of Cytochrome-*C* Peroxidase and pH Dependent Spectral Transitions in Ferrous Enzyme. *Biochimica et Biophysica Acta (BBA)* **537**:62-69.
40. Degier JWL, Lübben M, Reijnders WNM, Tipker CA, Slotboom DJ, Vanspanning RJM, Stouthamer AH, Vanderoost J (1994) The Terminal Oxidases of *Paracoccus Denitrificans*. *Mol. Microbiol.* **13**:183-196.
41. del Rio D, Sarangi R, Chufan EE, Karlin KD, Hedman B, Hodgson KO, Solomon EI (2005) Geometric and Electronic Structure of the Heme-Peroxo-Copper Complex $[(F_8TPP)Fe^{III}\text{-}(O_2^{2-})\text{-}Cu^{II}(TMPA)](ClO_4)$. *J. Am. Chem. Soc.* **127**:11969-11978.
42. delRio D, Galindo A (2003) DFT Analysis of Bis(ethylene) Complexes of Molybdenum and Tungsten: Substitution Reactions and Bond Dissociation Energies. *Organometallics* **22**:3117-3123.
43. Embden G, Zimmermann M (1927) Über die Bedeutung der Adenylsäure für die Muskelfunktion. *Zeitschrift der physiologischen Chemie* **127**:137-140.
44. Erman JE, Vitello LB (2002) Yeast cytochrome *c* peroxidase: mechanistic studies via protein engineering. *Biochimica et Biophysica Acta (BBA) - Protein Structure and Molecular Enzymology* **1597**:193-220.
45. Fabian M, Palmer P (1995) The Interaction of Cytochrome *c* Oxidase with Hydrogen Peroxide: The Relationship of Compounds P and F. *Biochemistry* **34**:13802-13810.
46. Fabian M, Skultety L, Jancura D, Palmer G (2004) Implications of ligand binding studies for the catalytic mechanism of cytochrome *c* oxidase. *Biochimica et Biophysica Acta (BBA) - Bioenergetics* **1655**:298-305.
47. Fabian M, Wong WW, Gennis RB, Palmer G (1999) Mass spectrometric determination of dioxygen bond splitting in the "peroxy" intermediate of cytochrome *c* oxidase. *Proc. Natl. Acad. Sci. U. S. A.* **96**:13114-13117.

48. Faxén K, Salomonsson L, Ädelroth P, Brzezinski P (2006) Inhibition of proton pumping by zinc ions during specific reaction steps in cytochrome *c* oxidase. *Biochimica et Biophysica Acta (BBA) - Bioenergetics* **1757**:388-394.
49. Ferguson-Miller S, Babcock GT (1996) Heme/Copper Terminal Oxidases. *Chemical Reviews* **96**:2889-2908.
50. Fetter JR, Qian J, Shapleigh J, Thomas JW, Garcia-Horsman A, Schmidt E, Hosler J, Babcock GT, Gennis RB, Ferguson-Miller S (1995) Possible Proton Relay Pathways in Cytochrome-C-Oxidase. *Proc. Natl. Acad. Sci. U. S. A.* **92**:1604-1608.
51. Finzel BC, Poulos TL, Kraut J (1984) Crystal-Structure of Yeast Cytochrome-*C* Peroxidase Refined at 1.7 Å Resolution. *J. Biol. Chem.* **259**:3027-3036.
52. Forte E, Scandurra FM, Richter OMH, D'Itri E, Sarti P, Brunori M, Ludwig B, Giuffre A (2004) Proton uptake upon anaerobic reduction of the *Paracoccus denitrificans* cytochrome *c* oxidase: A kinetic investigation of the K354M and D124N mutants. *Biochemistry* **43**:2957-2963.
53. Fridovich I, Handler P (1961) Detection of Free Radicals Generated During Enzymic Oxidations by Initiation of Sulfite Oxidation. *J. Biol. Chem.* **236**:1836-&.
54. Garcia-Horsman JA, Barquera B, Rumbley J, Ma JX, Gennis RB (1994) The Superfamily of Heme-Copper Respiratory Oxidases. *J. Bacteriol.* **176**:5587-5600.
55. Gennis RB (1998) Protein structure - Cytochrome *c* oxidase: One enzyme, two mechanisms? *Science* **280**:1712-1713.
56. Gennis RB (1998) PROTEIN STRUCTURE: Cytochrome *c* Oxidase: One Enzyme, Two Mechanisms? *Science* **280**:1712-1713.
57. Gennis RB (1992) Site-Directed Mutagenesis Studies on Subunit-I of the Aa_3-Type Cytochrome-*C*-Oxidase of *Rhodobacter-Sphaeroides* - a Brief Review of Progress to Date. *Biochimica Et Biophysica Acta (BBA)* **1101**:184-187.
58. Gerhus E, Steinrucke P, Ludwig B (1990) *Paracoccus denitrificans* cytochrome *c*1 gene replacement mutants. *J. Bacteriol.* **172**:2392-2400.
59. Goodin DB, McRee DE (1993) The Asp-His-Fe Triad of Cytochrome-C Peroxidase Controls the Reduction Potential, Electronic-Structure, and Coupling of the Tryptophan Free-Radical to the Heme. *Biochemistry* **32**:3313-3324.
60. Gorbikova EA, Belevich NP, Wikström M, Verkhovsky MI (2007) Protolytic reactions on reduction of cytochrome *c* oxidase studied by ATR-FTIR spectroscopy. *Biochemistry* **46**:4177-4183.
61. Gorbikova EA, Belevich NP, Wikström M, Verkhovsky MI (2007) Time-resolved ATR-FTIR spectroscopy of the oxygen reaction in the D124N mutant of cytochrome *C* oxidase from *Paracoccus denitrificans*. *Biochemistry* **46**:13141-13148.
62. Haldar D, Freeman K, Work TS (1966) Biogenesis of Mitochondria. *Nature* **211**:9-12.
63. Haltia T, Finel M, Harms N, Nakari T, Raitio M, Wikstrom M, Saraste M (1989) Deletion of the Gene for Subunit-III Leads to Defective Assembly of Bacterial Cytochrome-Oxidase. *The EMBO Journal* **8**:3571-3579.
64. Haltia T, Puustinen A, Finel M (1988) The *Paracoccus denitrificans* cytochrome aa_3 has a third subunit. *Eur J Biochem.* **15**:543-546.
65. Haltia T, Saraste M, Wikström M (1991) Subunit III of cytochrome *c* oxidase is not involved in proton translocation: a site-directed mutagenesis study. *The EMBO Journal* **10**:2015-2021.
66. Han D, Morgan JE, Gennis RB (2005) G204D, a mutation that blocks the proton-conducting D-channel of the *aa*(3)-type cytochrome *c* oxidase from *Rhodobacter sphaeroides*. *Biochemistry* **44**:12767-12774.
67. Han D, Namslauer A, Pawate A, Morgan JE, Nagy S, Vakkasoglu AS, Brzezinski P, Gennis RB (2006) Replacing Asn207 by aspartate at the neck of the D channel in the *aa*(3)-type cytochrome *c* oxidase from *Rhodobacter sphaeroides* results in decoupling the proton pump. *Biochemistry* **45**:14064-14074.
68. Harman D (1956) Aging - a Theory Based on Free-Radical and Radiation-Chemistry. *Journals of Gerontology* **11**:298-300.
69. Harrenga A, Michel H (1999) The cytochrome *c* oxidase from *Paracoccus denitrificans* does not change the metal center ligation upon reduction. *J. Biol. Chem.* **274**:33296-33299.
70. Hatefi Y (1985) The Mitochondrial Electron Transport and Oxidative Phosphorylation System. *Annu. Rev. Biochem.* **54**:1015-1069.
71. Hellwig P, Behr J, Ostermeier C, Richter OMH, Pfitzner U, Odenwald A, Ludwig B, Michel H, Mantele W (1998) Involvement of glutamic acid 278 in the redox reaction of the cytochrome *c* oxidase from *Paracoccus denitrificans* investigated by FTIR spectroscopy. *Biochemistry* **37**:7390-7399.
72. Hellwig P, Grzybek S, Behr J, Ludwig B, Michel H, Mantele W (1999) Electrochemical and Ultraviolet/Visible/Infrared Spectroscopic Analysis of Heme *a* and a_3 Redox Reactions in the

Cytochrome *c* Oxidase from Paracoccus denitrificans: Separation of Heme *a* and a_3 Contributions and Assignment of Vibrational Modes. *Biochemistry* **38**:1685-1694.

73. Hiner ANP, Raven EL, Thorneley RNF, Garcia-Canovas F, Rodriguez-Lopez JN (2002) Mechanisms of compound I formation in heme peroxidases. *J. Inorg. Biochem.* **91**:27-34.
74. Hofacker I, Schulten K (1998) Oxygen and proton pathways in cytochrome *c* oxidase. *Proteins-Structure Function and Genetics* **30**:100-107.
75. Hosler JP (2004) The influence of subunit III of cytochrome *c* oxidase on the D pathway, the proton exit pathway and mechanism-based inactivation in subunit I. *Biochimica et Biophysica Acta (BBA) - Bioenergetics* **1655**:332-339.
76. Hosler JP, Ferguson-Miller S, Calhoun MW, Thomas JW, Hill J, Lemieux L, Ma JX, Georgiou C, Fetter J, Shapleigh J, Tecklenburg MMJ, Babcock GT, Gennis RB (1993) Insight into the Active-Site Structure and Function of Cytochrome-Oxidase by Analysis of Site-Directed Mutants of Bacterial Cytochrome-aa_3 and Cytochrome-*bo*. *J. Bioenerg. Biomembr.* **25**:121-136.
77. Hosler JP, Shapleigh JP, Mitchell DH, Kim Y, Pressler MA, Georgiou C, Babcock GT, Alben JO, FergusonMiller S, Gennis RB (1996) Polar residues in helix VIII of subunit I of cytochrome *c* oxidase influence the activity and the structure of the active site. *Biochemistry* **35**:10776-10783.
78. Ito N, Phillips SEV, Stevens C, Ogel ZB, McPherson MJ, Keen JN, Yadav KDS, Knowles PF (1991) Novel thioether bond revealed by a 1.7 Å crystal structure of galactose oxidase. *Nature* **350**:87-90.
79. Iwaki M, Puustinen A, Wikström M, Rich PR (2003) ATR-FTIR Spectroscopy of the P_M and F Intermediates of Bovine and *Paracoccus denitrificans* Cytochrome *c* Oxidase. *Biochemistry* **42**:8809-8817.
80. Iwata S, Ostermeier C, Ludwig B, Michel H (1995) Structure at 2.8 Å resolution of cytochrome *c* oxidase from *Paracoccus denitrificans*. *Nature* **376**:660-669.
81. Johansson M. P., Kaila V. R. I., L. L. (2007) Charge parameterization of the metal centers in cytochrome *c* oxidase, p NA.
82. John P, Whatley FR (1975) *Paracoccus denitrificans* and the evolutionary origin of the mitochondrion. *Nature* **254**:495-498.
83. Jones P, Dunford HB (2005) The mechanism of Compound I formation revisited. *J. Inorg. Biochem.* **99**:2292-2298.
84. Jünemann S, Heathcote P, Rich PR (2000) The reactions of hydrogen peroxide with bovine cytochrome *c* oxidase. *Biochimica et Biophysica Acta (BBA) - Bioenergetics* **1456**:56-66.
85. Jünemann S, Meunier B, Gennis RB, Rich PR (1997) Effects of mutation of the conserved lysine-362 in cytochrome *c* oxidase from *Rhodobacter sphaeroides*. *Biochemistry* **36**:14456-14464.
86. Kalckar HM (1944) SPECTROSCOPIC MICRODETERMINATION OF MUSCLE ADENYLIC ACID. *Science* 131-132.
87. Karpefors M, Adelroth P, Brzezinski P (2000) The onset of the deuterium isotope effect in cytochrome *c* oxidase. *Biochemistry* **39**:5045-5050.
88. Keilin D (1925) On Cytochrome, a Respiratory Pigment, Common to Animals, Yeast, and Higher Plants. *Proceedings of the Royal Society of London. Series B, Containing Papers of a Biological Character* **98**:312-339
89. Khalimonchuk O, Bird A, Winge DR (2007) Evidence for a pro-oxidant intermediate in the assembly of cytochrome oxidase. *J. Biol. Chem.* **282**:17442-17449.
90. Kim YC, Wikström M, Hummer G (2007) Kinetic models of redox-coupled proton pumping. *Proc. Natl. Acad. Sci. U. S. A.* **104**:2169-2174.
91. Kirichenko AV, Pfitzner U, Ludwig B, Soares CM, Vygodina TV, Konstantinov AA (2005) Cytochrome *c* oxidase as a calcium binding protein. Studies on the role of a conserved aspartate in helices XI-XII cytoplasmic loop in cation binding. *Biochemistry* **44**:12391-12401.
92. Kleymann G, Ostermeier C, Ludwig B, Skerra A, Michel H (1995) Engineered Fv Fragments as a Tool for the One-Step Purification of Integral Multisubunit Membrane-Protein Complexes. *Bio-Technology* **13**:155-160.
93. Kohler RE (1973) The background to Otto Warburg's conception of the Atmungsferment. *J. Hist. Biol.* **6**:171-192.
94. Konstantinov AA, Siletsky S, Mitchell D, Kaulen A, Gennis RB (1997) The roles of the two proton input channels in cytochrome *c* oxidase from *Rhodobacter sphaeroides* probed by the effects of site-directed mutations on time-resolved electrogenic intraprotein proton transfer. *Proc. Natl. Acad. Sci. U. S. A.* **94**:9085-9090.
95. Ksenzenko M. Yu. VTV, Berka V., Ruuge E.K. and Konstantinov A. A. (1992) Cytochrome oxidase-catalysed superoxide generation from hydrogen peroxide. *FEBS Lett.* **297**:63-66.
96. Lancaster CRD (2003) The role of electrostatics in proton-conducting membrane protein complexes. *FEBS Lett.* **545**:52-60.

97. Lassmann G, Eriksson LA, Himo F, Lendzian F, Lubitz W (1999) Electronic structure of a transient histidine radical in liquid aqueous solution: EPR continuous-flow studies and density functional calculations. *Journal of Physical Chemistry A* **103**:1283-1290.
98. Lassmann G, Eriksson LA, Lendzian F, Lubitz W (2000) Structure of a transient neutral histidine radical in solution: EPR continuous-flow studies in a Ti^{3+}/EDTA-Fenton system and density functional calculations. *Journal of Physical Chemistry A* **104**:9144-9152.
99. Lee A, Kirichenko A, Vygodina T, Siletsky SA, Das TK, Rousseau DL, Gennis R, Konstantinov AA (2002) Ca^{2+}-binding site in *Rhodobacter sphaeroides* cytochrome *c* oxidase. *Biochemistry* **41**:8886-8898.
100. Lee HM, Das TK, Rousseau DL, Mills D, Ferguson-Miller S, Gennis RB (2000) Mutations in the putative H-channel in the cytochrome *c* oxidase from *Rhodobacter sphaeroides* show that this channel is not important for proton conduction but reveal modulation of the properties of heme *a*. *Biochemistry* **39**:2989-2996.
101. Lemieux LJ, Calhoun MW, Thomas JW, Ingledew WJ, Gennis RB (1992) Determination of the Ligands of the Low-Spin Heme of the Cytochrome-*O* Ubiquinol Oxidase Complex Using Site-Directed Mutagenesis. *J. Biol. Chem.* **267**:2105-2113.
102. Lemma G, Weintraub, Carroll, Musatov, Robinson (2007) Tryptophan 334 oxidation in bovine cytochrome *c* oxidase subunit I involves free radical migration. *FEBS Lett.* **581**:437-442.
103. Lenaz G, Fato R, Genova ML, Bergamini C, Bianchi C, Biondi A (2006) Mitochondrial Complex I: Structural and functional aspects. *Biochimica et Biophysica Acta (BBA) - Bioenergetics* **1757**:1406-1420.
104. Liu JG, Naruta Y, Tani F (2005) A Functional Model of the Cytochrome *c* Oxidase Active Site: Unique Conversion of a Heme- peroxo-Cu^{II} Intermediate into Heme- superoxo/Cu^{I}. *Angewandte Chemie, English Edition* **44**:1836-1840.
105. Lohmann K (1929) Über die Phosphatfraktion im Muskel. *Naturwissenschaften* **17**:
106. Ludwig B, Schatz G (1980) A two-subunit cytochrome *c* oxidase (cytochrome aa_3) from *Paracoccus dentrificans*. *Proc. Natl. Acad. Sci. U. S. A.* **77**:196-200.
107. MacMillan F, Budiman K, Angerer H, Michel H (2006) The role of tryptophan 272 in the *Paracoccus denitrificans* cytochrome *c* oxidase. *FEBS Lett.* **580**:1345-1349.
108. MacMillan F, Kannt A, Behr J, Prisner T, Michel H (1999) Direct Evidence for a Tyrosine Radical in the Reaction of Cytochrome *c* Oxidase with Hydrogen Peroxide. *Biochemistry* **38**:9179-9184.
109. Marantz Y, Nachliel E, Aagaard A, Brzezinski P, Gutman M (1998) The proton collecting function of the inner surface of cytochrome c oxidase from Rhodobacter sphaeroides. *Proc. Natl. Acad. Sci. U. S. A.* **95**:8590-8595.
110. Margulis L (1970) Origin of Eukaryote Cells. *Yale University Press, New Haven*
111. Martin W (1999) A briefly argued case that mitochondria and plastids are descendants of endosymbionts, but that the nuclear compartment is not. *Proceedings of the Royal Society B: Biological Sciences* **266**:1387-1387.
112. McCord JM, Fridovic I (1969) Superoxide Dismutase - an Enzymic Function for Erythrocuprein. *Fed. Proc.* **28**:346-&.
113. McCord JM, Fridovic I (1969) Utility of Superoxide Dismutase in Studying Free Radical Reactions 2. Radicals Generated by Interaction of Sulfite, Dimethyl Sulfoxide, and Oxygen. *J. Biol. Chem.* **244**:6056-6063.
114. Meyerhof O, Kiessling W (1933) *Biochemische Zeitschrift* **264**:
115. Michel H (1999) Bioenergetics: Proton pumping by cytochrome *c* oxidase. *Nature* **402**:602-603.
116. Michel H (1999) Cytochrome *c* oxidase: Catalytic cycle and mechanisms of proton pumping - A discussion. *Biochemistry* **38**:15129-15140.
117. Michel H (1998) The mechanism of proton pumping by cytochrome *c* oxidase. *Proc. Natl. Acad. Sci. U. S. A.* **95**:12819-12824.
118. Michel H, Behr J, Harrenga A, Kannt A (1998) CYTOCHROME *C* OXIDASE: Structure and Spectroscopy. *Annu. Rev. Biophys. Biomol. Struct.* **27**:329-356.
119. Mills DA, Hosler JP (2005) Slow proton transfer through the pathways for pumped protons in cytochrome *c* oxidase induces suicide inactivation of the enzyme. *Biochemistry* **44**:4656-4666.
120. Minagawa J, Mogi T, Gennis RB, Anraku Y (1992) Identification of Heme and Copper Ligands in Subunit-I of the Cytochrome-*Bo* Complex in *Escherichia Coli*. *J. Biol. Chem.* **267**:2096-2104.
121. Mitchell DM, Fetter JR, Mills DA, Ädelroth P, Pressler MA, Kim Y, Aasa R, Brzezinski P, Malmstrom BG, Alben JO, Babcock GT, Ferguson-Miller S, Gennis RB (1996) Site-Directed Mutagenesis of Residues Lining a Putative Proton Transfer Pathway in Cytochrome *c* Oxidase from *Rhodobacter sphaeroides*. *Biochemistry* **35**:13089-13093.
122. Mitchell P, Moyle J (1967) Chemiosmotic Hypothesis of Oxidative Phosphorylation. *Nature* **213**:137-139.

123. Mitchell R, Mitchell P, Rich PR (1991) The assignment of the 655 nm spectral band of *cytochrome oxidase*. *FEBS Lett.* **280**:321-324.
124. Mitchell R, Rich PR (1994) Proton uptake by cytochrome *c* oxidase on reduction and on ligand binding. *Biochimica et Biophysica Acta (BBA) - Bioenergetics* **1186**:19-26.
125. Mochizuki M, Aoyama H, Shinzawa-Itoh K, Usui T, Tsukihara T, and, Shinya Y (1999) Quantitative Reevaluation of the Redox Active Sites of Crystlline Bovine Heart Cytochrome *c* Oxidase. *J. Biol. Chem.* **274**:33403-33411.
126. Moody AJ, Brandt U, Rich PR (1991) Single electron reduction of `slow' and `fast' cytochrome *c* oxidase. *FEBS Lett.* **293**:101-105.
127. Morgan JE, Verkhovsky MI, Wikström M (1996) Observation and Assignment of Peroxy and Ferryl Intermediates in the Reduction of Dioxygen to Water by Cytochrome *c* Oxidase. *Biochemistry* **35**:12235-12240.
128. Moser CC, Page CC, Dutton PL (2006) Darwin at the molecular scale: selection and variance in electron tunnelling proteins including cytochrome *c* oxidase. *Philosophical Transactions of the Royal Society B: Biological Sciences* **361**:1295-1305.
129. Muramoto K, Hirata K, Shinzawa-Itoh K, Yoko-O S, Yamashita E, Aoyama H, Tsukihara T, Yoshikawa S (2007) A histidine residue acting as a controlling site for dioxygen reduction and proton pumping by cytochrome *c* oxidase. *Proc. Natl. Acad. Sci. U. S. A.* **104**:7881-7886.
130. Namslauer A, Aagaard A, Katsonouri A, Brzezinski P (2003) Intramolecular proton-transfer reactions in a membrane-bound proton pump: The effect of pH on the peroxy to ferryl transition in cytochrome *c* oxidase. *Biochemistry* **42**:1488-1498.
131. Namslauer A, Brzezinski P (2004) Structural elements involved in electron-coupled proton transfer in cytochrome *c* oxidase. *FEBS Lett.* **567**:103-110.
132. Namslauer A, Lepp H, Branden M, Jasaitis A, Verkhovsky MI, Brzezinski P (2007) Plasticity of proton pathway structure and water coordination in cytochrome *c* oxidase. *J. Biol. Chem.* **282**:15148-15158.
133. Namslauer A, Pawatet AS, Gennis R, Brzezinski P (2003) Redox-coupled proton translocation in biological systems: Proton shuttling in cytochrome *c* oxidase. *Proc. Natl. Acad. Sci. U. S. A.* **100**:15543-15547.
134. Nicholls P, Chanady GA (1981) Interactions of Cytochrome-aa_3 with Oxygen and Carbon-Monoxide - the Role of the 607-nm Complex. *Biochimica Et Biophysica Acta (BBA)* **634**:256-265.
135. Nyquist RM, Heitbrink D, Bolwien C, Gennis RB, Heberle J (2003) Direct observation of protonation reactions during the catalytic cycle of cytochrome *c* oxidase. *Proc. Natl. Acad. Sci. U. S. A.* **100**:8715-8720.
136. Ogura T, Kitagawa T (2004) Resonance Raman characterization of the P intermediate in the reaction of bovine cytochrome *c* oxidase. *Biochimica et Biophysica Acta (BBA) - Bioenergetics* **1655**:290-297.
137. Olkhova E, Helms V, Michel H (2005) Titration behavior of residues at the entrance of the D-pathway of cytochrome *c* oxidase from *Paracoccus denitrificans* investigated by continuum electrostatic calculations. *Biophys. J.* **89**:2324-2331.
138. Olkhova E, Hutter MC, Lill MA, Helms V, Michel H (2004) Dynamic water networks in cytochrome *c* oxidase from *Paracoccus denitrificans* investigated by molecular dynamics simulations. *Biophys. J.* **86**:1873-1889.
139. Orii Y (1982) The Cytochrome-*C* Peroxidase-Activity of Cytochrome-Oxidase. *J. Biol. Chem.* **257**:9246-9248.
140. Ostefin AE, Popova JA, Payne CK, Mizukami H, Norris Jr. JR (2006) Temperature dependent UV-vis spectral changes in hydrogen- and deuterium-bonded photosynthetic reaction centers of *Rhodobacter sphaeroides*. *Photosynthetica* **44**:433-438.
141. Ostermeier C, Harrenga A, Ermler U, Michel H (1997) Structure at 2.7 Å resolution of the *Paracoccus denitrificans* two-subunit cytochrome *c* oxidase complexed with an antibody Fv fragment. *Proc. Natl. Acad. Sci. U. S. A.* **94**:10547-10553.
142. Panskus G, Steinrücke P, Ludwig B (1988) Subunit-II of the *Paracoccus-Denitrificans* Cytochrome-*C*-Oxidase - Expression Studies of Its Cloned Gene in *E. Coli*. *Ann. N. Y. Acad. Sci.* **550**:308-313.
143. Papa S, Capitanio N, Glaser P, Villani G (1994) The proton pump of heme-copper oxidases. *Cell Biol. Int.* **18**:345-356.
144. Pasteur L (1860) Memoire sur la fermentation de alcoolique. *Compt. Rend. Acad. Sci. (Paris)* **48**:1149-1152.
145. Pawate AS, Morgan J, Namslauer A, Mills D, Brzezinski P, Ferguson-Miller S, Gennis RB (2002) A mutation in subunit I of cytochrome oxidase from *Rhodobacter sphaeroides* results in an increase in steady-state activity but completely eliminates proton pumping. *Biochemistry* **41**:13417-13423.
146. Pereira MM, Santana M, Teixeira M (2001) A novel scenario for the evolution of haem-copper oxygen reductases. *Biochimica et Biophysica Acta (BBA) - Bioenergetics* **1505**:185-208.

147. Pfitzner U, Hoffmeier K, Harrenga A, Kannt A, Michel H, Bamberg E, Richter OMH, Ludwig B (2000) Tracing the D-Pathway in Reconstituted Site-Directed Mutants of Cytochrome *c* Oxidase from *Paracoccus denitrificans*. *Biochemistry* **39**:6756-6762.
148. Pfitzner U, Kirichenko A, Konstantinov AA, Mertens M, Wittershagen A, Kolbesen BO, Steffens GCM, Harrenga A, Michel H, Ludwig B (1999) Mutations in the Ca^{2+} binding site of the *Paracoccus denitrificans* cytochrome *c* oxidase. *FEBS Lett.* **456**:365-369.
149. Pfitzner U, Odenwald A, Ostermann T, Weingard L, Ludwig B, Richter O-MH (1998) Cytochrome *c* Oxidase (Heme aa_3) from *Paracoccus denitrificans*: Analysis of Mutations in Putative Proton Channels of Subunit I. *J. Bioenerg. Biomembr.* **30**:89-97.
150. Pinakoulaki E, Pfitzner U, Ludwig B, Varotsis C (2002) The role of the cross-link His-Tyr in the functional properties of the binuclear center in cytochrome *c* oxidase. *J. Biol. Chem.* **277**:13563-13568.
151. Proshlyakov DA, Ogura T, Shinzawa-Itoh K, Yoshikawa S, Kitagawa T (1996) Microcirculating System for Simultaneous Determination of Raman and Absorption Spectra of Enzymatic Reaction Intermediates and Its Application to the Reaction of Cytochrome *c* Oxidase with Hydrogen Peroxide. *Biochemistry* **35**:76-82.
152. Proshlyakov DA, Ogura T, Shinzawa-Itoh K, Yoshikawa S, Kitagawa T (1996) Resonance Raman/Absorption Characterization of the Oxo Intermediates of Cytochrome *c* Oxidase Generated in Its Reaction with Hydrogen Peroxide: pH and H_2O_2 Concentration Dependence. *Biochemistry* **35**:8580-8586.
153. Puustinen A, Wikström M (1999) Proton exit from the heme-copper oxidase of *Escherichia coli*. *Proc. Natl. Acad. Sci. U. S. A.* **96**:35-37.
154. Qian J, Shi WJ, Pressler M, Hoganson C, Mills D, Babcock GT, Ferguson-Miller S (1997) Aspartate-407 in *Rhodobacter sphaeroides* cytochrome *c* oxidase is not required for proton pumping or manganese binding. *Biochemistry* **36**:2539-2543.
155. Qin L, Hiser C, Mulichak A, Garavito RM, Ferguson-Miller S (2006) Identification of conserved lipid/detergent-binding sites in a high-resolution structure of the membrane protein cytochrome *c* oxidase. *Proc. Natl. Acad. Sci. U. S. A.* **103**:16117-16122.
156. Qin L, Sharpe MA, Garavito RM, Ferguson-Miller S (2007) Conserved lipid-binding sites in membrane proteins: a focus on cytochrome *c* oxidase. *Curr. Opin. Struct. Biol.* **17**:444-450.
157. Raitio M, Pispa JM, Metso T, Saraste M (1990) Are there isoenzymes of cytochrome *c* oxidase in *Paracoccus denitrificans*? *FEBS Lett.* **261**:431-435.
158. Rauhamaki V, Baumann M, Soliymani R, Puustinen A, Wikström M (2006) Identification of a histidine-tyrosine cross-link in the active site of the *cbb*(3)-type cytochrome *c* oxidase from *Rhodobacter sphaeroides*. *Proc. Natl. Acad. Sci. U. S. A.* **103**:16135-16140.
159. Ribacka C, Verkhovsky MI, Belevich I, Bloch DA, Puustinen A, Wikström M (2005) An elementary reaction step of the proton pump is revealed by mutation of tryptophan-164 to phenylalanine in cytochrome *c* oxidase from *Paracoccus denitrificans*. *Biochemistry* **44**:16502-16512.
160. Rich PR, Rigby SEJ, Heathcote P (2002) Radicals associated with the catalytic intermediates of bovine cytochrome *c* oxidase. *Biochimica et Biophysica Acta (BBA) - Bioenergetics* **1554**:137-146.
161. Richter OMH, Ludwig B. (2003) Cytochrome *c* oxidase - structure, function, and physiology of a redox-driven molecular machine, in *Reviews of Physiology, Biochemistry and Pharmacology*, pp 47-74.
162. Rigby SEJ, Jünemann S, Rich PR, Heathcote P (2000) Reaction of Bovine Cytochrome *c* Oxidase with Hydrogen Peroxide Produces a Tryptophan Cation Radical and a Porphyrin Cation Radical. *Biochemistry* **39**:5921-5928.
163. Riistama S, Puustinen A, Verkhovsky MI, Morgan JE, Wikstrom M (2000) Binding of O_2 and its reduction are both retarded by replacement of valine 279 by isoleucine in cytochrome *c* oxidase from *Paracoccus denitrificans*. *Biochemistry* **39**:6365-6372.
164. Robinson NC, Zborowski J, Talbert L (1990) Cardiolipin-depleted bovine heart cytochrome c oxidase: binding stoichiometry and affinity for cardiolipin derivatives. *Biochemistry* **29**:8962-8969.
165. Ruitenberg M, Kannt A, Bamberg E, Fendler K, Michel H (2002) Reduction of cytochrome *c* oxidase by a second electron leads to proton translocation. *Nature* **417**:99-102.
166. Ruitenberg M, Kannt A, Bamberg E, Ludwig B, Michel H, Fendler K (2000) Single-electron reduction of the oxidized state is coupled to proton uptake via the K pathway in *Paracoccus denitrificans* cytochrome *c* oxidase. *Proc. Natl. Acad. Sci. U. S. A.* **97**:4632-4636.
167. Salomonsson L, Faxen K, Ädelroth P, Brzezinski P (2005) The timing of proton migration in membrane constituted cytochrome *c* oxidase. *Proc. Natl. Acad. Sci. U. S. A.* **102**:17624-17629.
168. Sambrook J, Russell DW (2001) *Molecular Cloning: A Laboratory Manual* Vol. 2, third edition ed., Cold Spring Harbor Laboratory Press.
169. Saraste M (1999) Oxidative phosphorylation at the fin de siecle. *Science* **283**:1488-1493.

170. Saraste M, Holm L, Lemieux L, Lubben M, Vanderoost J (1991) The Happy Family of Cytochrome Oxidases. *Biochem. Soc. Trans.* **19**:608-612.
171. Satterlee JD, Erman JE (1981) Proton Nuclear Magnetic-Resonance Characterization of the Oxidized Intermediates of Cytochrome-*C* Peroxidase. *J. Biol. Chem.* **256**:1091-1093.
172. Schägger H (2002) Respiratory chain supercomplexes of mitochondria and bacteria. *Biochimica et Biophysica Acta (BBA) - Bioenergetics* **1555**:154-159.
173. Schmidt B, McCracken J, Ferguson-Miller S (2003) A discrete water exit pathway in the membrane protein cytochrome *c* oxidase. *Proc. Natl. Acad. Sci. U. S. A.* **100**:15539-15542.
174. Scholes P, Mitchell P (1970) Respiration-driven proton translocation in *Micrococcus denitrificans*. *J. Bioenerg. Biomembr.* **1**:309-323.
175. Shapleigh JP, Hosler JP, Tecklenburg MMJ, Kim YY, Babcock GT, Gennis RB, Fergusonmiller S (1992) Definition of the Catalytic Site of Cytochrome-*C*-Oxidase - Specific Ligands of Heme-*a* and the Heme-a_3-Cu_B Center. *Proc. Natl. Acad. Sci. U. S. A.* **89**:4786-4790.
176. Shinzawa-Itoh K, Aoyama H, Muramoto K, Terada H, Kurauchi T, Tadehara Y, Yamasaki A, Sugimura T, Kurono S, Tsujimoto K, Mizushima T, Yamashita E, Tsukihara T, and, Yoshikawa S (2007) Structures and physiological roles of 13 integral lipids of bovine heart cytochrome *c* oxidase. *The EMBO Journal* **26**:1713–1725.
177. Siegbahn PEM, Blomberg MRA (2004) Important roles of tyrosines in Photosystem II and cytochrome oxidase. *Biochimica et Biophysica Acta (BBA) - Bioenergetics* **1655**:45-50.
178. Siletsky SA, Han D, Brand S, Morgan JE, Fabian M, Geren L, Millett F, Durham B, Konstantinov AA, Gennis RB (2006) Single-electron photoreduction of the P_M intermediate of cytochrome *c* oxidase. *Biochimica et Biophysica Acta (BBA) - Bioenergetics* **1757**:1122-1132.
179. Siv GEA, Olof K, Björn C, Charles GK (2003) On the origin of mitochondria: a genomics perspective. *Philosophical Transactions of the Royal Society B: Biological Sciences* **358**:165-179.
180. Smirnova IA, Ädelroth P, Gennis RB, Brzezinski P (1999) Aspartate-132 in cytochrome *c* oxidase from *Rhodobacter sphaeroides* is involved in a two-step proton transfer during oxo-ferryl formation. *Biochemistry* **38**:6826-6833.
181. Steinrücke P, Gerhus E, Jetzek M, Turba A, Ludwig B (1991) The Cytochrome *c* Reductase Oxidase Respiratory Pathway of *Paracoccus Denitrificans* - Genetic and Functional-Studies. *J. Bioenerg. Biomembr.* **23**:227-239.
182. Steinrücke P, Gerhus E, Ludwig B (1991) *Paracoccus-Denitrificans* Mutants Deleted in the Gene for Subunit-II of Cytochrome-*C*-Oxidase Also Lack Subunit-I. *J. Biol. Chem.* **266**:7676-7681.
183. Svistunenko DA (2005) Reaction of haem containing proteins and enzymes with hydroperoxides: The radical view. *Biochimica et Biophysica Acta (BBA) - Bioenergetics* **1707**:127-155.
184. Svistunenko DA, Wilson MT, Cooper CE (2004) Tryptophan or tyrosine? On the nature of the amino acid radical formed following hydrogen peroxide treatment of cytochrome *c* oxidase. *Biochimica Et Biophysica Acta (BBA) - Bioenergetics* **1655**:372-380.
185. Tan M-L, Balabin I, Onuchic JN (2004) Dynamics of Electron Transfer Pathways in Cytochrome *c* Oxidase. *Biophys. J.* **86**:1813-1819.
186. Thomas JW, Lemieux LJ, Alben JO, Gennis RB (1993) Site-Directed Mutagenesis of Highly Conserved Residues in Helix VIII of Subunit-I of the Cytochrome-*bo* Ubiquinol Oxidase from *Escherichia Coli* - an Amphipathic Transmembrane Helix That May Be Important in Conveying Protons to the Binuclear Center. *Biochemistry* **32**:11173-11180.
187. Thomas JW, Puustinen A, Alben JO, Gennis RB, Wikström M (1993) Substitution of asparagine for aspartate-135 in subunit I of the cytochrome *bo* ubiquinol oxidase of *Escherichia coli* eliminates proton-pumping activity. *Biochemistry* **32**:10934-10928.
188. Tsaprailis G, English A (2003) Different pathways of radical translocation in yeast cytochrome *c* peroxidase and its W191F mutant on reaction with H_2O_2 suggest an antioxidant role. *Journal of Biological Inorganic Chemistry* **8**:248-255.
189. Tsukihara T, Aoyama H, Yamashita E, Tomizaki T, Yamaguchi H, Shinzawa-Itoh K, Nakashima R, Yaono R, Yoshikawa S (1996) The Whole Structure of the 13-Subunit Oxidized Cytochrome *c* Oxidase at 2.8 Å. *Science* **272**:1136-1144.
190. Tsukihara T, Shimokata K, Katayama Y, Shimada H, Muramoto K, Aoyama H, Mochizuki M, Shinzawa-Itoh K, Yamashita E, Yao M, Ishimura Y, Yoshikawa S (2003) The low-spin heme of cytochrome c oxidase as the driving element of the proton-pumping process. **100**:15304-15309.
191. Tuukkanen A, Kaila VRI, Laakkonen L, Hummer G, Wikström M (2007) Dynamics of the glutamic acid 242 side chain in cytochrome *c* oxidase. *Biochimica et Biophysica Acta (BBA) - Bioenergetics* **1767**:1102-1106.
192. Vanderoost J, Deboer APN, Degier JWL, Zumft WG, Stouthamer AH, Vanspanning RJM (1994) The Heme-Copper Oxidase Family Consists of 3 Distinct Types of Terminal Oxidases and Is Related to Nitric-Oxide Reductase. *FEMS Microbiol. Lett.* **121**:1-9.

193. Varanasi L, Mills D, Murphree A, Gray J, Purser C, Baker R, Hosler J (2006) Altering conserved lipid binding sites in cytochrome *c* oxidase of *Rhodobacter sphaeroides* perturbs the interaction between subunits I and III and promotes suicide inactivation of the enzyme. *Biochemistry* **45**:14896-14907.
194. Verkhovsky MI, Belevich I, Bloch DA, Wikström M (2006) Elementary steps of proton translocation in the catalytic cycle of cytochrome oxidase. *Biochimica et Biophysica Acta (BBA) - Bioenergetics* **1757**:401-407.
195. Verkhovsky MI, Jasaitis A, Verkhovskaya ML, Morgan JE, Wikström M (1999) Proton translocation by cytochrome *c* oxidase. *Nature* **400**:480-483.
196. Verkhovsky MI, Morgan JE, Wikström M (1996) Redox transitions between oxygen intermediates in cytochrome *c* oxidase. *Proc. Natl. Acad. Sci. U. S. A.* **93**:12235-12239.
197. Verkhovsky MI, Tuukkanen A, Backgren C, Puustinen A, Wikström M (2001) Charge translocation coupled to electron injection into oxidized cytochrome *c* oxidase from *Paracoccus denitrificans*. *Biochemistry* **40**:7077-7083.
198. Vernon LP, White FG (1957) Terminal Oxidases of *Micrococcus Denitrificans*. *Biochimica Et Biophysica Acta (BBA)* **25**:321-328.
199. Voet, Voet, Pratt (1999) *Fundamentals of Biochemistry*, John Wiley & Sons, Inc., New York.
200. Vygodina TV, Konstantinov AA (1988) H_2O_2-Induced Conversion of Cytochrome *C* Oxidase Peroxy Complex to Oxoferryl State. *Ann. N. Y. Acad. Sci.* **550**:124-138.
201. Walker JE, Dickson VK (2006) The peripheral stalk of the mitochondrial ATP synthase. *Biochimica et Biophysica Acta (BBA) - Bioenergetics* **1757**:286-296.
202. Warburg O (1924) Über Eisen, den sauerstoffübertragenden Bestandteil des Atmungsfermentes. *Biochemische Zeitschrift* **Bd. 152**:479-494.
203. Weng LC, Baker GM (1991) Reaction of Hydrogen-Peroxide with the Rapid Form of Resting Cytochrome-Oxidase. *Biochemistry* **30**:5727-5733.
204. Wiertz FGM, Richter O-MH, Cherepanov AV, MacMillan F, Ludwig B, de Vries S (2004) An oxo-ferryl tryptophan radical catalytic intermediate in cytochrome *c* and quinol oxidases trapped by microsecond freeze-hyperquenching (MHQ). *FEBS Lett.* **575**:127-130.
205. Wiertz FGM, Richter OMH, Ludwig B, de Vries S (2007) Kinetic resolution of a tryptophan-radical intermediate in the reaction cycle of *Paracoccus denitrificans* cytochrome *c* oxidase. *J. Biol. Chem.* **282**:31580-31591.
206. Wikström M (1981) Energy-dependent reversal of the cytochrome oxidase reaction. *Proc. Natl. Acad. Sci. U. S. A.* **78**:4051-4054.
207. Wikström M (1989) Identification of the Electron Transfers in Cytochrome-Oxidase That Are Coupled to Proton-Pumping. *Nature* **338**:776-778.
208. Wikström M (2000) Mechanism of proton translocation by cytochrome *c* oxidase: a new four-stroke histidine cycle. *Biochimica et Biophysica Acta (BBA) - Bioenergetics* **1458**:188-198.
209. Wikström M (1998) Proton translocation by bacteriorhodopsin and heme-copper oxidases. *Curr. Opin. Struct. Biol.* **8**:480-488.
210. Wikström M (1988) Protonic sidedness of the binuclear iron-copper centre in cytochrome oxidase. *FEBS Lett.* **231**:247-252.
211. Wikström M (1984) Pumping of protons from the mitochondrial matrix by cytochrome oxidase. *Nature* **308**:558-560.
212. Wikström M, Bogachev A, Finel M, Morgan JE, Puustinen A, Raitio M, Verkhovskaya M, Verkhovsky MI (1994) Mechanism of Proton Translocation by the Respiratory Oxidases - the Histidine Cycle. *Biochimica Et Biophysica Acta (BBA) - Bioenergetics* **1187**:106-111.
213. Wikström M, Krab K, Saraste M (1981) Proton-Translocating Cytochrome Complexes. *Annu. Rev. Biochem.* **50**:623-655.
214. Wikström M, Morgan JE (1992) The dioxygen cycle. Spectral, kinetic, and thermodynamic characteristics of ferryl and peroxy intermediates observed by reversal of the cytochrome oxidase reaction. *J. Biol. Chem.* **267**:10266-10273.
215. Wikström M, Ribacka C, Molin M, Laakkonen L, Verkhovsky M, Puustinen A (2005) Gating of proton and water transfer in the respiratory enzyme cytochrome *c* oxidase. *Proc. Natl. Acad. Sci. U. S. A.* **102**:10478-10481.
216. Wikström M, Verkhovsky MI (2007) Mechanism and energetics of proton translocation by the respiratory heme-copper oxidases. *Biochimica et Biophysica Acta (BBA) - Bioenergetics* **1767**:1200-1214.
217. Wikström M, Verkhovsky MI (2002) Proton translocation by cytochrome *c* oxidase in different phases of the catalytic cycle. *Biochimica et Biophysica Acta (BBA) - Bioenergetics* **1555**:128-132.
218. Wikström MKF (1977) Proton pump coupled to cytochrome *c* oxidase in mitochondria. *Nature* **266**:271-273.

219. Witt H, Ludwig B (1997) Isolation, analysis, and deletion of the gene coding for subunit IV of cytochrome *c* oxidase in *Paracoccus denitrificans*. *J. Biol. Chem.* **272**:5514-5517.
220. Witt H, Malatesta F, Nicoletti F, Brunori M, Ludwig B (1998) Cytochrome-*c*-binding site on cytochrome oxidase in *Paracoccus denitrificans*. *Eur. J. Biochem.* **251**:367-373.
221. Witt H, Wittershagen A, Bill E, Kolbesen BO, Ludwig B (1997) Asp-193 and Glu-218 of subunit II are involved in the Mn^{2+}-binding of *Paracoccus denitrificans* cytochrome *c* oxidase. *FEBS Lett.* **409**:128-130.
222. Witt SN, Chan SI (1987) Evidence for a Ferryl Fea_3 in Oxygenated Cytochrome *c* Oxidase. *The Journal of Biological Chemistry* **262**:1446-1448.
223. Yonetani T, Anni H (1987) Yeast Cytochrome-*C* Peroxidase - Coordination and Spin States of Heme Prosthetic Group. *J. Biol. Chem.* **262**:9547-9554.
224. Yonetani T, Ray GS (1965) Studies on Cytochrome *C* Peroxidase I. Purification and Some Properties. *J. Biol. Chem.* **240**:4503-&.
225. Yoshikawa S, Muramoto K, Shinzawa-Itoh K, Aoyama H, Tsukihara T, Ogura T, Shimokata K, Katayama Y, Shimada H (2006) Reaction mechanism of bovine heart cytochrome *c* oxidase. *Biochimica et Biophysica Acta (BBA) - Bioenergetics* **1757**:395-400.
226. Yoshikawa S, Shinzawa-Itoh K, Nakashima R, Yaono R, Yamashita E, Inoue N, Yao M, Fei MJ, Libeu CP, Mizushima T, Yamaguchi H, Tomizaki T, Tsukihara T (1998) Redox-Coupled Crystal Structural Changes in Bovine Heart Cytochrome *c* Oxidase. *Science* **280**:1723-1729.
227. Yoshikawa S, Shinzawa-Itoh K, Tsukihara T (1998) Crystal Structure of Bovine Heart Cytochrome *c* Oxidase at 2.8 Å Resolution. *J. Bioenerg. Biomembr.* **30**:7-14.
228. Zaslavsky D, Gennis RB (2000) Proton pumping by cytochrome oxidase: progress, problems and postulates. *Biochimica et Biophysica Acta (BBA) - Bioenergetics* **1458**:164-179.

6 Appendices

6.1 Models of the catalytic mechanism

6.1.1 Classical model

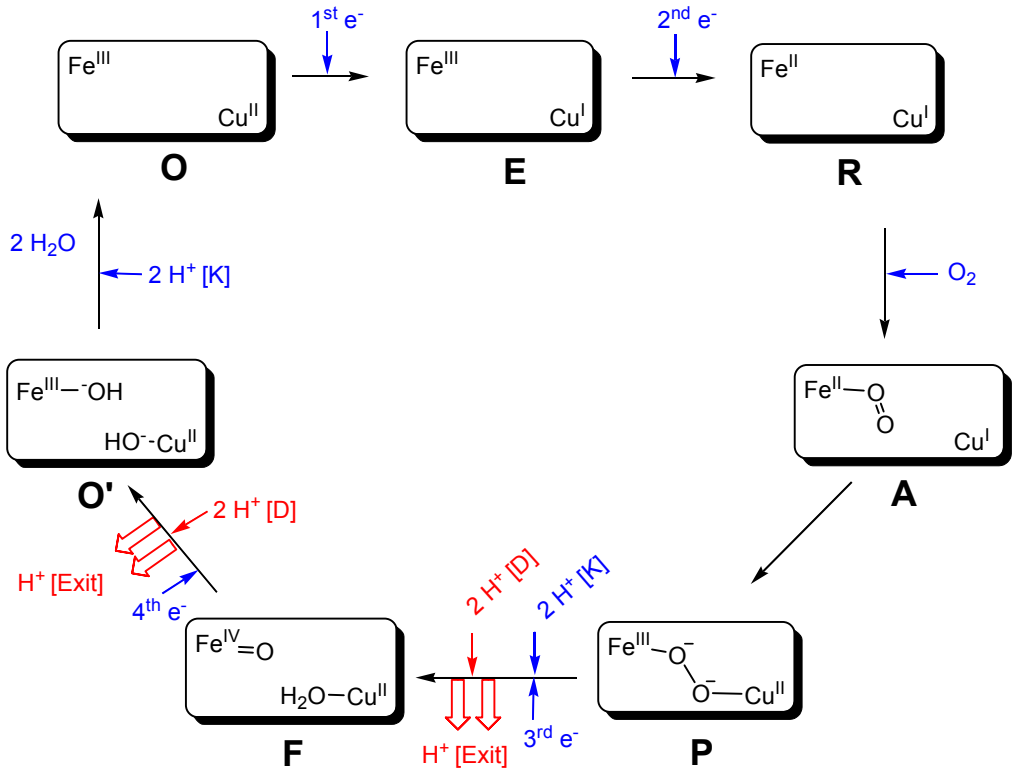

Figure 6.1-1 Classical model of C*c*O catalytic cycle. Fe and Cu represent haem Fea_3 and Cu_B. Intermediates are represented below the boxes as O, E, R, A, P, F **and** O´ **states. The binuclear centre receives electrons during the reductive phase, forming the two-electron reduced** R **state. Dioxygen binds to the ferrous haem a_3 generating the** A **state. Electronic rearrangements form the** P **state, which is a peroxy intermediate. Further electron input leads to the** F **state having an oxoferryl intermediate. After receiving the next electron the introduced** O´ **state has two bound OH^- groups. The bound OH^- groups are protonated; two H_2O molecules are released. Proton pumping occurs at the** P → F **and** F → O´ **transitions with two pump steps each. Small arrows indicate e^- or H^+ uptake (blue = substrate electrons/protons, red = pumped protons), red big arrows represent the pumping steps via an exit channel. It was suggested that substrate protons use the K-pathway, whereas pumped protons use the D-pathway (Iwata *et al.*, 1995). The proton pathways are labelled [D], [K] for substrate or pumped protons or [Exit] for the exit pathway of the pumped protons, respectively.**

6.1.2 Michel, 1999

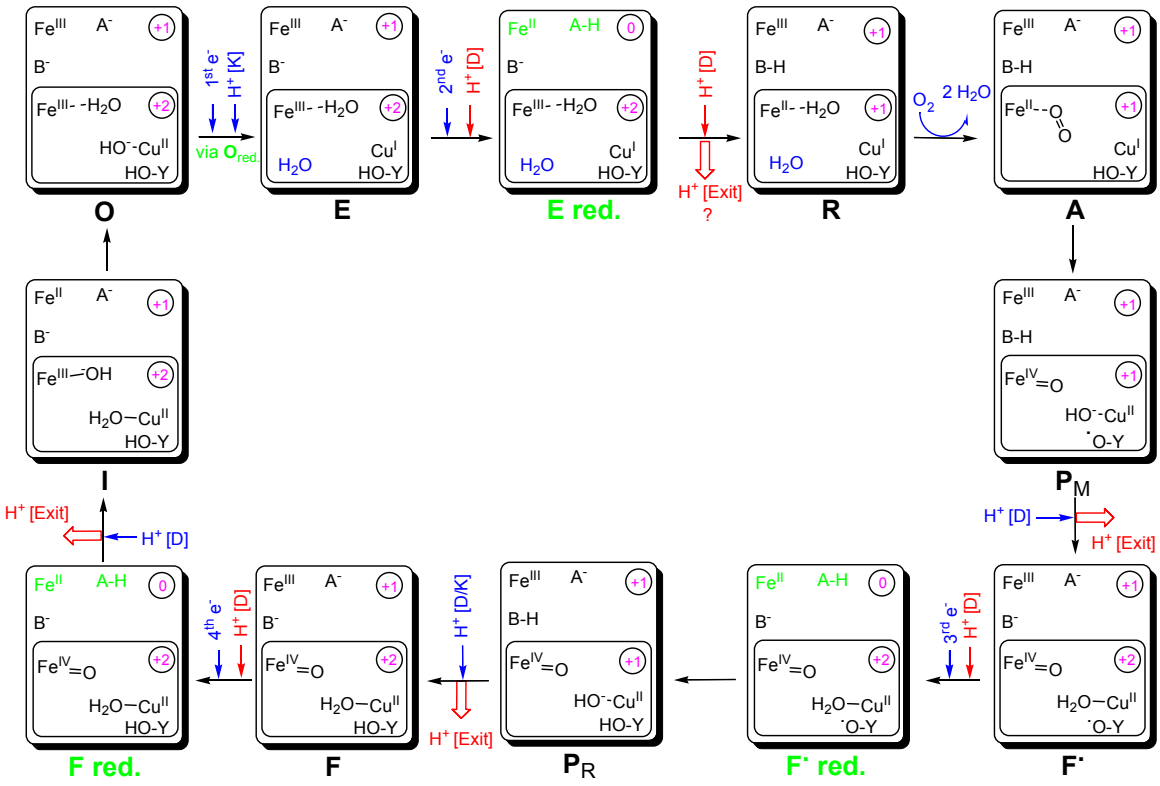

Figure 6.1-2 Model of C*c*O catalytic cycle (Michel, 1999). Boxes represent redox and protonation states of the intermediates; inner boxes describe the reaction within the binuclear site (haem a_3-Cu_B binuclear centre plus Y280). The intermediates are represented below the boxes as O, E, R, A, P_M, F˙, F, P_R, **and** I **states. Reduced haem *a* in a respective intermediate is labelled red. (reduced). The model introduces proton pumping by electrostatic repulsion. A and B are protonatable groups at the haem *a* propionates or a protonation site near the binuclear centre, respectively. The overall net charge of the centres for each state is shown in magenta (charge of porphyrin group = - 2, oxoferryl = 0, A and B site not regarded). Small arrows indicate e^- or H^+ uptake (blue = substrate electrons/protons, red = pumped protons); red big arrows represent the pumping steps via an exit pathway. Proton pathways are labelled [D], [K] for substrate or pumped protons or [Exit] for exit pathway of the pumped protons, respectively.**

6.1.3 Wikström, 2000

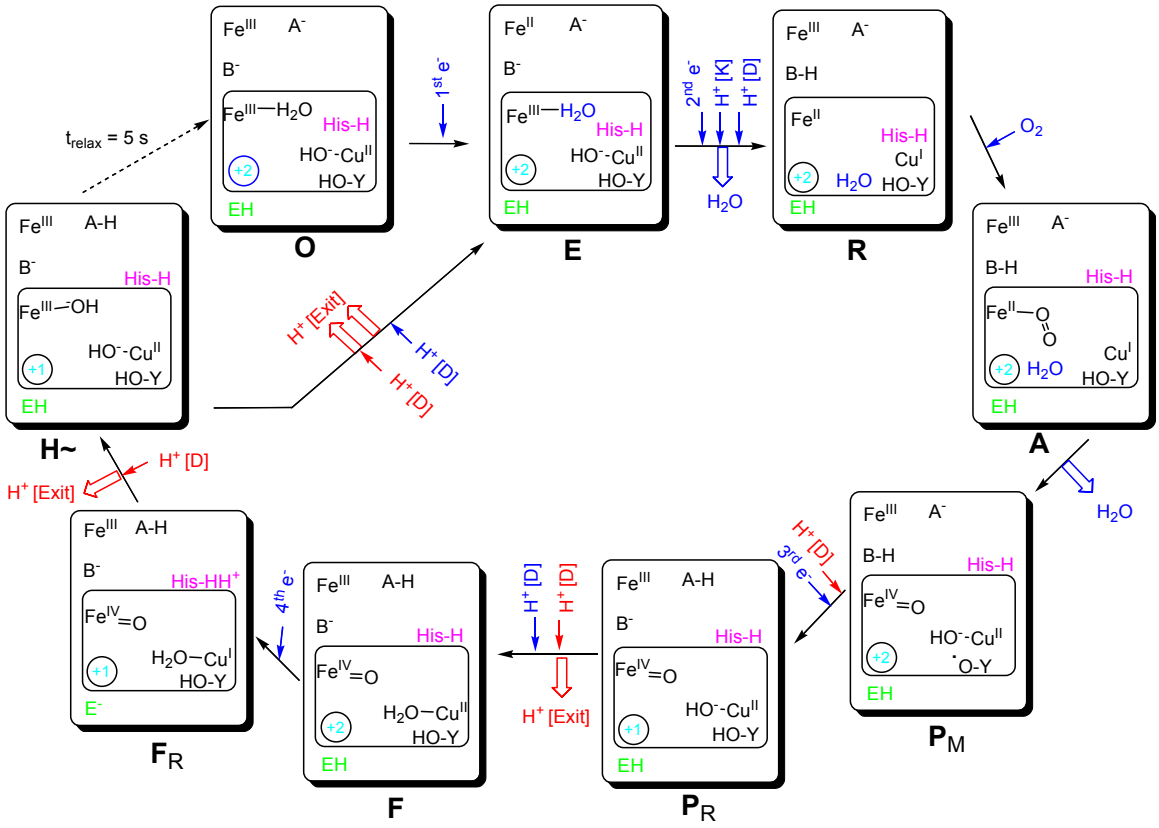

Figure 6.1-3 Model of CcO catalytic cycle (Wikström, 2000). Boxes represent redox and protonation states of the intermediates; inner boxes describe the reaction within the binuclear site (haem a_3-Cu_B binuclear centre plus Y280 and the histidine ligand of Cu_B (magenta)). Intermediates are represented below the boxes as O, E, R, A, P_M, P_R, F, F_R, **and** H~ **states. The formal charge of the binuclear centre is depicted in light blue (Porphyrin = -2, oxoferryl = 0).** E **stands for the residue E278 (green).** H **stands for a state with an OH^- bound to ferric haem a_3.** H~ **is an occluded "high-energy" state with potential for proton translocation. A and B are protonatable groups at the haem *a* propionates or a protonation site near the binuclear centre, respectively. Histidine imidazole (ImH) can dissociate from Cu_B and be protonated to imidazolim cation ($ImHH^+$). Small arrows indicate e^- or H^+ uptake (blue = substrate electrons/protons, red = pumped protons), red big arrows represent the pumping steps via an exit pathway. Proton pathways are labelled [D], [K] for substrate or pumped protons or [Exit] for the exit pathway of the pumped protons.**

6.2 Sequence of *cta*DIIβ and sequencing of the mutated *cta*DIIβ

6.2.1 ORF of *cta*DIIβ

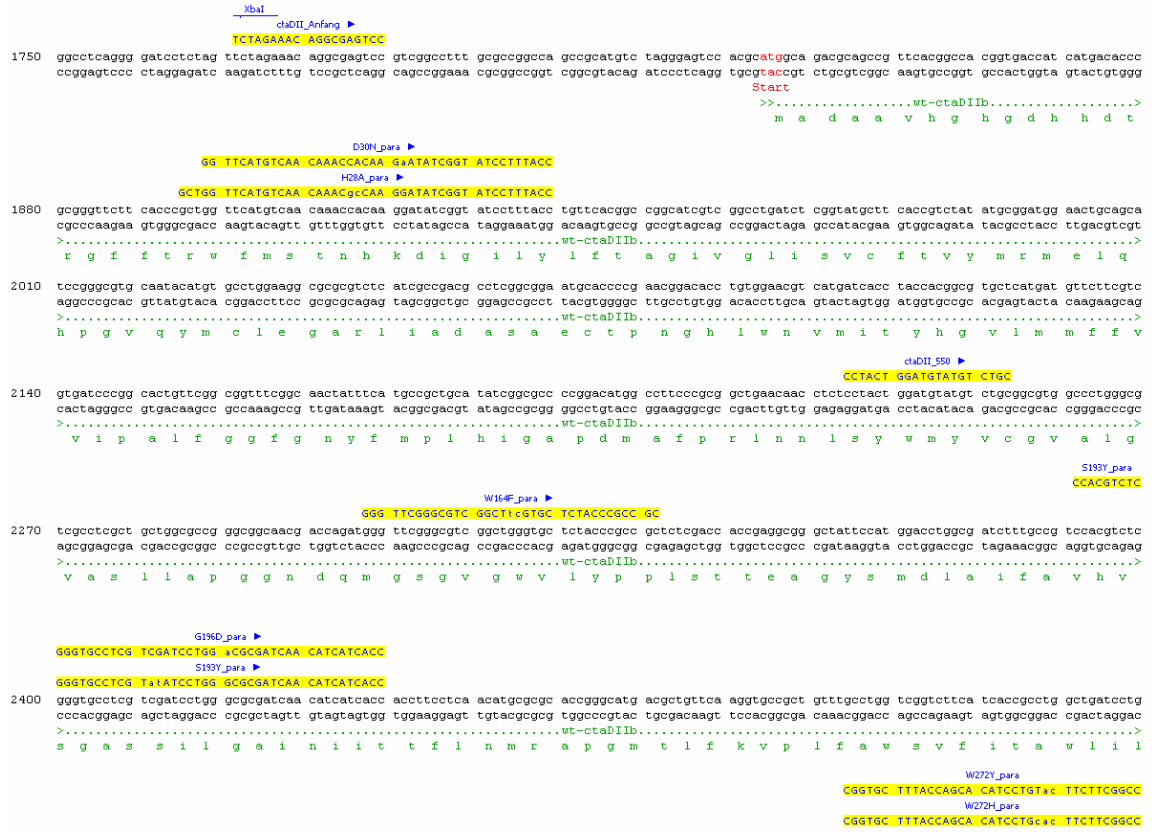

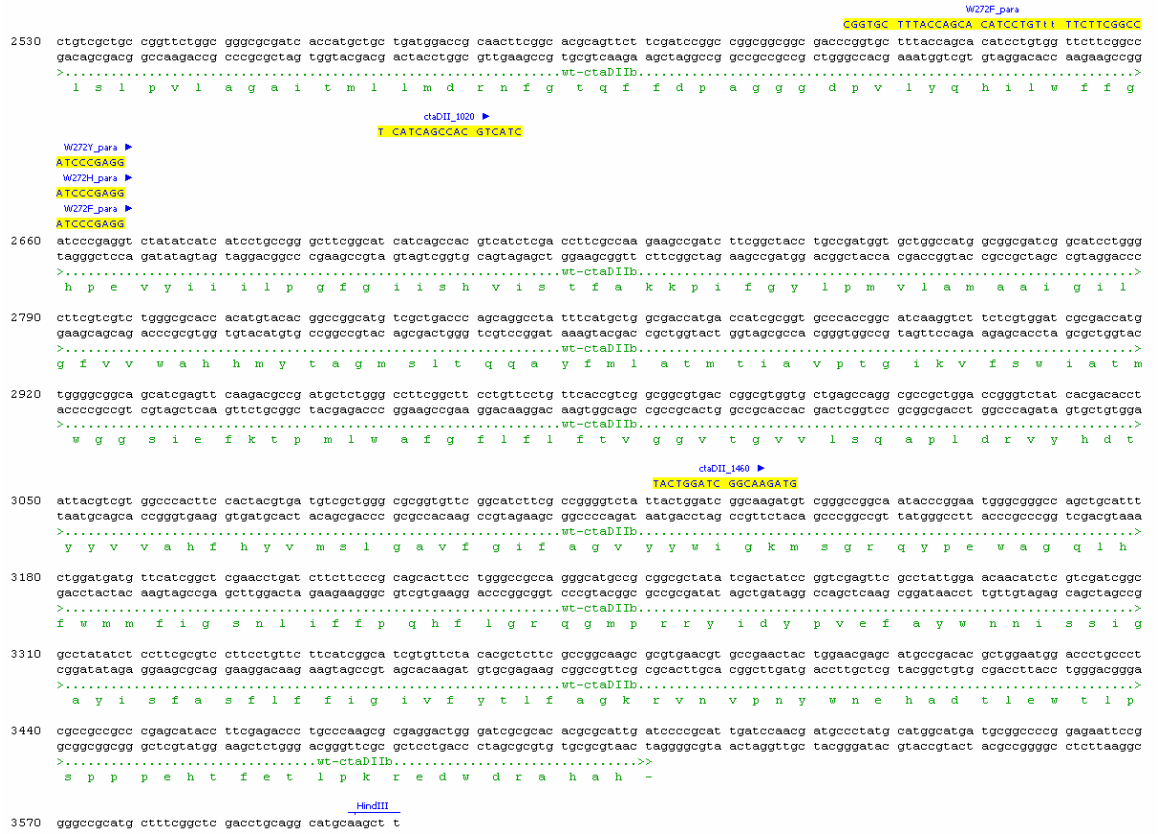

6.2.2 Seqlab sequencing

H28A

TCCCCGCTGGTTCATGTCAACAAACGCCAAGGATATCGGTATCCTTTACCTGTTCACGGCCGGCATCGTCGGCCTGATCTCGGTATGC
TTCACCGTCTATATGCGGATGGAACTGCAGCATCCGGGCGTGCAATACATGTGCCTGGAAGGCGCGCGTCTCATCGCCGACGCCTCG
GCGGAATGCACCCCGAACGGACACCTGTGGAACGTCATGATCACCTACCACGGCGTGCTCATGATGTTCTTCGTCGTGATCCCGGCA
CTGTTCGGCGGTTTCGGCAACTATTTCATGCCGCTGCATATCGGCGCCCCGGACATGGCCTTCCCGCGGCTGAACAACCTCTCCTACT
G

D30N

CTTCCCCGCTGGTTCATGTCAACAAACCACAAGAATATCGGTATCCTTTACCTGTTCACGGCCGGCATCGTCGGCCTGATCTCGGTATG
CTTCACCGTCTATATGCGGATGGAACTGCAGCATCCGGGCGTGCAATACATGTGCCTGGNAAGGCGCGCGTCTCATCGCCGACGCCC
TCCGGCGGAATGCACCCCAACGACACTGTGNACGTCATGATCACTTACACGGGTGCTCATGATGTNCTTCGCCTGATCCCGNNCTGTT
CGCGGTTTCGGNAAANNTTTNTGNCNNTTANAATTGGGGCCCCCGNAATTGGNTTTCCCGGGNNNGAAAAAACCCCCCCNNNCNNNN

W272Y-Y167F

TGGGGCGTCGCCTCGCTGCTGGCGCCGGGCGGCAACGACCAGATGGGTTCGGGCGTCGGCTGGGTGCTCTTCCCGCCGCTCTCGA
CCACCGAGGCGGGCTATTCCATGGACCTGGCGATCTTTGCCGTCCACGTCTCGGGTGCCTCGTCGATCCTGGGCGCGATCAACATCA
TCACCACCTTCCTCAACATGCGCGCACCGGGCATGACGCTGTTCAAGGTGCCGCTGTTTGCCTGGTCGGTCTTCATCACCGCCTGGCT
GATCCTGCTGTCGCTGCCGGTTCTGGCGGGCGCGATCACCATGCTGCTGATGGACCGCAACTTCGGCACGCAGTTCTTCGAT

TTCNGCACGCAGTTCTTCGATCCGGCCGGCGGCGGCGACCCGGTGCTTTACCAGCACATCCTGTACTTCTTCGGCCATCCCGAGGTC
TATATCATCATCCTGCCGGGCTTCGGCATCATCAGCCACGTCATCTCGACCTTCGCCAAGAAGCCGATCTTCGGCTACCTGCCGATGG

TGCTGGCCATGGCGGCGATCGGCATCCTGGGCTTCGTCGTCTGGGCGCACCACATGTACACGGCCGGCATGTCGCTGACCCAGCAG
GCCTATTTCATGCTGGCGACCATGACCATCGCGGTGCCCACCGGCATCAAGGTCTTCTCGTGGATCGCGACCATGTGGGGC

H28A-N131D

CTTNCCCGCTGGTTCATGTCAACAAACGCCAAGGATATCGGTATCCTTTACCTGTTCACGGCCGGCATCGTCGGCCTGATCTCGGTAT
GCTTCACCGTCTATATGCGGATGGAACTGCAGCATCCGGGCGTGCAATACATGTGCCTGGAAGGCGCGCGTCTCATCGCCGACGCCT
CGGCGGAATGCACCCCGAACGGACACCTGTGGAACGTCATGATCACCTACCACGGCGTGCTCATGATGTTCTTCGTCGTGATCCCGG
CACTGTTCGGCGGTTTCGGCAACTATTTCATGCCGCTGCATATCGGCGCCCCGGACATGGCCTTCCCGCGGCTGGATAACCTCTCGTA
CTGGATGTATGTCTGCGGCGTGGCCCTGGGCGTCGCC

6.2.3 X-Highperform sequencing (in house)

G196D

```
  1 CAACGACAGA TGGGTCGGGC GTCGGCTGGG TGCTCTACCG CCGCTCTCGA
 51 CACCGAGGCG GGCTATTCCA TGGACcTGGC GDTCTTTGCC GTCCACGTCT
101 CGGGTGCCTC GTCGATCCTG GACGCGATCA ACATCATCAC CACCTTCCTC
151 AACATGCGCG CACCGGGCAT GACGCTGTTC AAGGTGCCGC TGTTTGCCTG
201 GTSSGTVCTC ATCACCGCCT GGCTGATCCT GCTGTCGCTG CCGGTTCTGG
251 CGGGCGCGAT CACCATGCTG CTGATGGACC GCAACTTCGG CACGCAGTTC
301 TTCGATCCGG CCGGCGGGGC GAACCCGGTG CTTTACCAGC ACATCCTGTG
351 GTTCTTCGGC CATCCCGAGG TCWAAATCAT CATCCTGCCG GGCTTCGGAT
401 CATCAGCCAC GTCATCTCGR MCTTCGCcAA AAaGCCGATC TTCGGCWAaC
451 CTGCCGRAtG GTGCTGGCCA TGGCGGCrAT YGGMATCCTG GGCTTCGTCG
501 TCTGGGCGMA CCMMaTGTAA mCGGCCGGAA TGTCGCTGAA CCMGMAGGCC
551 WAWTTHAWGC TGGSRACMAw GACCATCSCG GTKGCCACCG GVATCAAAGG
601     TCTTCTCGTG GARTYSVRMC MTGTGGGGCG GMAMATCs
```

W272F

```
  1 GCCGCCTGAB TWRATCCTAG CTCGTWCGCT AGCCCGGTWb CTAGGCGGGC
 51 KCGAWTCACC ATGGCTGGCT GATGGACCGC AACTTCGGCA CGCAGTTCTT
101 CGATCCGGCC GGCGGCGGCG AACCCGGGTG CTTTACCAGC CACATCCTGT
151 TTTTCTTCGG CCATCCCGAG GTCTGAKRKG CRGGGKCCTG CCGGGCTTCG
201 GCATCATCAG CCACGTCATC TCGAGCTTCG CCAAGAAGCC GATyTTYGSX
251 TACCTGCCGA aTGGTGCTGG CCATGGCGGC GATCGGCATC CTGGGCTTCG
301 TCGTCTGGGC GCACCACATG TACACGGCCG GCATGTCGCT GACCCAGCAG
351 GCCTATTTCA TGCTGGCGAC CATGACCATC GCGGTGCCCA CCGGCATCAA
401 GGTCTTSKCG TGGATCGCGA CCATGTGGGG CGGCAVATCG AGTTCAAGAC
451 GCCGATGCTC TGGGCCTTCG GCTTCCTGTT CCTGTTCACC GTCGGCGGCG
501 TGACCGGCGT GGTGCTGAGC CAGGCGCCGC TGGACCGGGT CTATCACGAC
551 ACCTATTACG TCGTGGCCCA CTTCCACTAC GTGATGTCGC TGGGCGCGGT
601 GTTCGGCATC TTCGCCGGGG TCTATTACTG GATCGGCAAG ATGTCGGGCC
651 GGCAAWAMCC GGAATGGGCG GGCCAGCTGC AWTTCTGGAT GADG
```

W272F-Y167F

```
  1 TXXXcTTCCG CGGCTGAWCA ACCTCTCCTA CTGGATGTAT GTCTGCGGCG
 51 TGGCCTGGGC GTCGCTCGCT GCTGGCGCCG GGCGCAACGA CcAGATGGGT
101 TCGGGCGTCG GCTGGGTCCT CTTCCCGCCG CTCTCGACCA CCGAGGCGGG
151 CTATTCCATG GACCTGGCGA TCTTTGCCGT CCACGTCTCG GGTGCCTCGT
```

201 CGATCCTGGG CGCGATCAAC ATCATCACCA CCTTCCTCAA CATGCGCGCA
251 CCGGGCATGA CGCTGTTCAA GGTGCCGCTG TTTGCCTGGT CGGTCTTCAT
301 CACCGCCTGG CTGATCCTGC TGTCGCTGCC GGTTCTGGCG GGCGCGATCA
351 CCATGCTGCT GATGGACCGC AACTTCGGCA CGCAGTTCTT CGATCCGGCC
401 GGCGGSGGCG ACCCGGgTGC TTTACCAGCA CATCCTGTTT TTCTTCGGCC
451 ATCCCGAGGT CTATATCATC ATCCTGCCGG GCTTCGGCAT CATCAGCCAC
501 GTCATCTCGA CCTTCGCCAA GAAGCCGATC TTCGGCTACC TGCCGATGGT
551 GCTGGCCATG GCGGCGATYG GCATCCTGGG CTTCSTCGTC TGGGCGCACC
601 ACATGTWCAC GGGCcGGGAT GTCTSCTGAM CCAGCAAGGC CTAATTCAAG
651 CCGGCGACCA WGACCATCGC GGTGCCCACC GGCATCAARG gTCTTCTCGT
701 GGATCGCGAC CATWGTGGGG GCGGCACAHT CGARATT

D124N-D30N

1 XACACCGCGG VTHCTTCACC GCTGGTTCAT GTCAACAAAC CACAAGAATA
51 TCGGTATCCT TTACCTGTTC ACGGCCGGCA TCGTCGCTGA TCTCGGTATG
101 CTTCACCGTC TATATGCGGA TGGAACTGCA GCATCCGGGC GTGCAATACA
151 TGTGCCTGGA AGSGCGCGTC TCATCGCCGA CGCCTCGGSG AATGCACCCC
201 SRCCAAAACT GTGGAACGTC MTGATCASCT ACCACGGCGT GCTCATGATG
251 TTCTTCGTCG TGATCCCGGC ACTGTTCGGC GGTTTCGGCA ACTATTTCAT
301 GCCGCTGCAT ATCGGCGCGC CGAACATGGC CTTCCCGCGG CTGAACAACC
351 TCTCCTACTG GATGTATGTC TGCGSGCGTG GCCCTGGGCG TCGCcTCGCT
401 GCTGGCGCCc GGGCGCGAAC GACCAGATGG GTTCGGGCGT CGGCTGGGTG
451 CTCTACCCGC CGCTCTCGAC CACCGAGGCG GGCTAATTCA WGGACCTGGC
501 GATCTTGGCc GTCCACGTCT CCGGGTGCCT CCGKCGATHM CYKGGCGCGG
551 WwCAAAMaCA TCACCACCTT tCTTCAACAT GCGCGCGACC GGGCAHTGAC
601 GCTGKTTCAA rGTGgCCGCT GTTTTCCYYG GTYCGGTCTy CATCAACGCT
651 TGGCTTGTAC CACG

S193Y

1 CATGGCTTCC GCGGCTGAAC AACcTCTCCT ACTGGATGTA TGTCTGCGGC
51 GTGGCCTGGG CGTCGCTCGC TGCTGGCGCC GGGCGCAACG ACcAGATGGG
101 TTCGGGCGTC GGCTGGGTGC TCTACCCGCC GCTCTCGACC ACCGAGGCGG
151 GCTATTCCAT GGACCTGGCG ATCTTTGCCG TCCACGTCTC GGGTGCCTCG
201 TATATCCTGG GCGCGATCAA CATCATCACC ACCTTCCTCA ACATGCGCGC
251 ACCGGGCATG ACGCTGTTCA AGGTGCCGCT GTTTGCCTGG TCGGTCTTCA
301 TCACCGCCTG GCTGATCCTG CTGTCGCTGC CGGTTCTGGC GGGCGCGATC
351 ACCATGCTGC TGATGGACCG CAACTTCGGC ACGCAGTTCT TCGATTCGGG
401 CcGGCGGGGC GAACCCGGTG gCTTTACCAG CACATCCTGT GGGTTCTTCG
451 GCCATCCCGA GGTCTATAWC MTCATCCTGC CGGGCTTYGG ATWYAWCAGA
501 GCACGTTYAT ATCGAGMYCT CGCSCAaGAA aRCCGATTTT CGGKAAACYC
551 GCGAGAGGKK GCTSGGCMHW GGGGGCGAWW BGSRmTACYG GGGCTTYCBC
601 cGTCTYGGGG SgCACMMCAT GTDTCACcGG GCCGGSATGT CKCTGACCCC
651 AGCAGRGGCT CWTTTCAWCT GTGGGGGAGC MWGAVCMMTC KSGGGKGGSC
701 cMCMGGGATW HAAGGKKTTT CYCGTGGRKH GYGgRCCATG TGGGGSGGGA

W272H

1 GGCTGGACAA CCTCTCCTAC TGGATGTATG YCTGCGGCGT GGCCTGGGCG
51 TCGCTCGCTG CTGGCGCCGG GCGGCAACGA CcAGTATGGG TTCGGGCGTC
101 GGCTGGGTGC TCTACCGCCG CTCTCGACTA CcGRGCGGGC TATCCATGGA
151 CTGGCGATCT TTGCCGTCCA CGTCTCGGGT GCCTCGTCGA TCCTGGGCGC
201 GATCAACATC ATCACYWCTT CCTCAACATG CGCGCACCGG GCATGACGCT

251 GTTCAAGGTG CCGCTGTTTG CCTGGTCGGT CTTCWACACG CcTGGCTGWT
301 CcTGCTGTCG CTGCCGGTTC TGGCGGGCGC GATCACCATG CTGCTGATGG
351 ACCGCAACTT CGGCACGCAG TTCTTCGATC CGGCCGGCGG GGCGAMCCGG
401 TGCTTTACCA GCACATCCTG CACTTCTTCG GCCATCCCGA GGTCTAWAWC
451 ATCATCCTGC CGGGCTTCGG CATCATCAGC CACGTCATCT CGACCTTCGC
501 CAARAAGCCG ATCTTCGGST AACCTGCCGR aTGGTGCTGG CCATGGCGGC
551 GATYGGCATC CTGGGCTTCG TCGTCTGGGC GCMCCMCATG TWMMCGGCCG
601 GCATGTCGCT GAMCCCAGCA GGCCTATTTC ATGCTGGCGA CCATGRMCAT
651 CGCGGTGCCC ACCGGSATCA AaGGTCTTCT CGTGGATHGC GRCCATGTGG
701 GGSGGCAVAT CGAGTTCAAR ACGCCGaTGC TCCTGGGC

W272H-Y167F

1 TTCCGCGGCT GAACAACcTC TCCTACTGGA TGTATGTCTG CGGCGTGGCC
51 TGGGCGTCGC TCGCTGCTGG CGCCGGDDCG GCAACGACCA GATGGGTTCG
101 GGCGTCGGCT GGGTGCTCTT CCCGCCGCTC TCGACCACCG AGGCGGGCTA
151 TTCCATGGAC CTGGCGATCT TTGCCGTCCA CGTCTCGGGT GCCTCGTCGA
201 TCCTGGGCGC GATCAACATC ATCACCACCT TCCTCAACAT GCGCGCACCG
251 GGCATGACGC TGTTCAAGGT GCCGCTGTTT GCCTGGTCGG TCTTCATCAC
301 CGCCTGGCTG ATCCTGCTGT CGCTGCCGGT TCTGGCGGGC GCGATTCACC
351 ATGCTGCTGA TGGACCGCAA CTTCGGCACG CAGTTCTTCG ATtCcGGCCg
401 GgCGGGGCGA CCCGGTGCTT TACCAGCACA TCCTGCACTT CTTCGGCCAT
451 CCCGAGGTCT ATATCATCAT CTGGCGGGCT TCGGVATCAT tCAGCCACGT
501 CATYTCGACC TTCGGCMAGA AGCGGTTCTC CGCTAACCTG CcSRaTGTKG
551 CTGGCCAWGS SGSGATTCGG AWCCTGGGCT TCSGTCGCTY TGGCGCGCCC
601 CATATGWCAC ACGGCCGGCA WWKCTCGYKA SCCAGCGCAG GCCCTWTtYA
651 CTGCKCGGGG AGCACAKAGM TMTGCGGGGK GSCMCMCGGA THTMAAGGST
701 TYTCCGCGGG RTHKCCGAGC MMDKTGKGGG SGGSAGCAKM YGMGTTTCAC
751 RACGCCGCAT GYGCTKGGGG sS

W164F

1 GCGGCTGAAC AACCTCTCCT ACTGGATGTA TGTCTGCGGC GTGGCCTGGG
51 CGTCGCTCGC TGCTGGCGCC GGTCGCAWCG ACCAGATGGG TTCGGGCGTC
101 GGCTTCGTGC TCTACCCGCC GCTCTCGACC ACCGAGGCGG GCTATTCCAT
151 GGACCTGGCG ATCTTTGCCG TCCACGTCTC GGGTGCCTCG TCGATCCTGG
201 GCGCGATCAA CATCATCACC ACCTTCCTCA ACATGCGCGC ACCGGGCATG
251 ACGCTGTTCA AGGTGCCGCT GTTTGCCTGG TCGGTCTTCA TCACCGCCTG
301 GCTGATCCTG CTGTCGCTGC CGGTTCTGGC GGGCGCGATC ACCATGCTGC
351 TGATGGACCG CAACTTCGGC ACGCAGTTCT TCGATTCGGC CGGCGGGGCG
401 AaCCCGGTGC TTTACCAGCA CATCCTGTGg TTCTTCGGCC ATCCCGAGGT
451 CTATATCATC ATCCTGCCGG GCTTCGSATt CATCAGCCAC GTCATCTCGA
501 CCyTCGCCAA GAAGCCGATY TTCGGTAACC TGCCGATGGT GCTGGCcATA
551 GGCGGCGATY GGCATCCYGG GgCTTCGTCS TCTGGGCGCA CCACATGKDC
601 ACGGGCcSGC ATGTGCTGAC CCmGCAGGCC TATTTCATHG CTKGGCGACC
651 AaKACCAaTC GCGGGkCGCc ACCGGGCATH AAGRGTCTyT CGCGtGAWYG
701 CGACcMTGTT KGGSGCGCAC ATCTCRKSTC WWGDMVCCcG KMTCcYYTGG

W272Y

1 TGCTGTCGCT GCCGGTTCTG GCGGGCGCGA TCACCATGCT GCTGATGGAC
51 CGCAACTTCG GCACGCAGTT CTTCGATCCG GCCGGCGGSG GCGAACCCGG
101 gTGCTTTACC AGCACATCCT GTACTTCTTC GGCCATCCCG AGGTCTATAT
151 CATCATCCTG CCGGGCTTCG GCATCATCAG CCACGTCATC TCGACCTTCG
201 CCAAGAAGCC GATCTTCGGC TACCTGCCGA BGGTGCTGGC CATGGCGGCG
251 ATCGGCATCC TGGGCTTCGT CGTCTGGGCG CACCACATGT ACACGGCCGG

301 CATGTCGCTG ACCCAGCAGG CCTATTTCAT GCTGGCGACC ATGACCATCG
351 CGGTGCCCAC CGGCATCAAG GTCTTCTCGT GGATCGCGAC CATGTGGGGC
401 GGCAVATCGA GTTCAAGACG CCGATGCTCT GGGCCTTCGG STTCCTGTTC
451 CTGTTCACCG TCGGCGGCGT GACCGGCGTG GTGCTGAGCC AGGCGCCGCT
501 GGACCGGGTC TATCACGAMA CCTATTACGT CGTGGCCCAC TTCCACTACG
551 TGATGTCGCT GGGCGCGGTG TTCGGMATCT TCGCCGGGGT CTATTAaCTG
601 GRTCGGCMAA AWGTCGGGCC GGCAAWACCC GGAATGGG

6.3 Proton pumping experiments

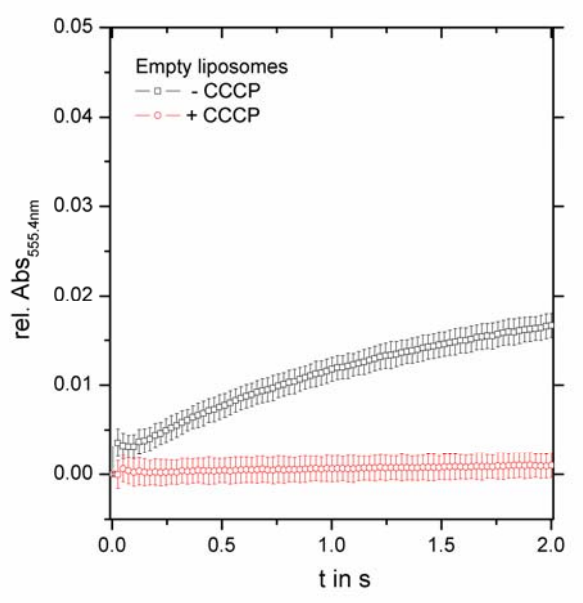

Figure 6.3-1 Control stopped flow kinetic proton pumping experiment of empty liposomes at λ = 555.4 nm. Unbuffered empty liposomes plus valinomycin and phenolred were mixed 1:1 with 20 μM reduced cyt *c* at a pH of 7.30 and recorded for 2 s. CCCP was added to the same vesicles and again mixed 1:1 with 20 μM reduced cyt *c* and recorded for 2 s.

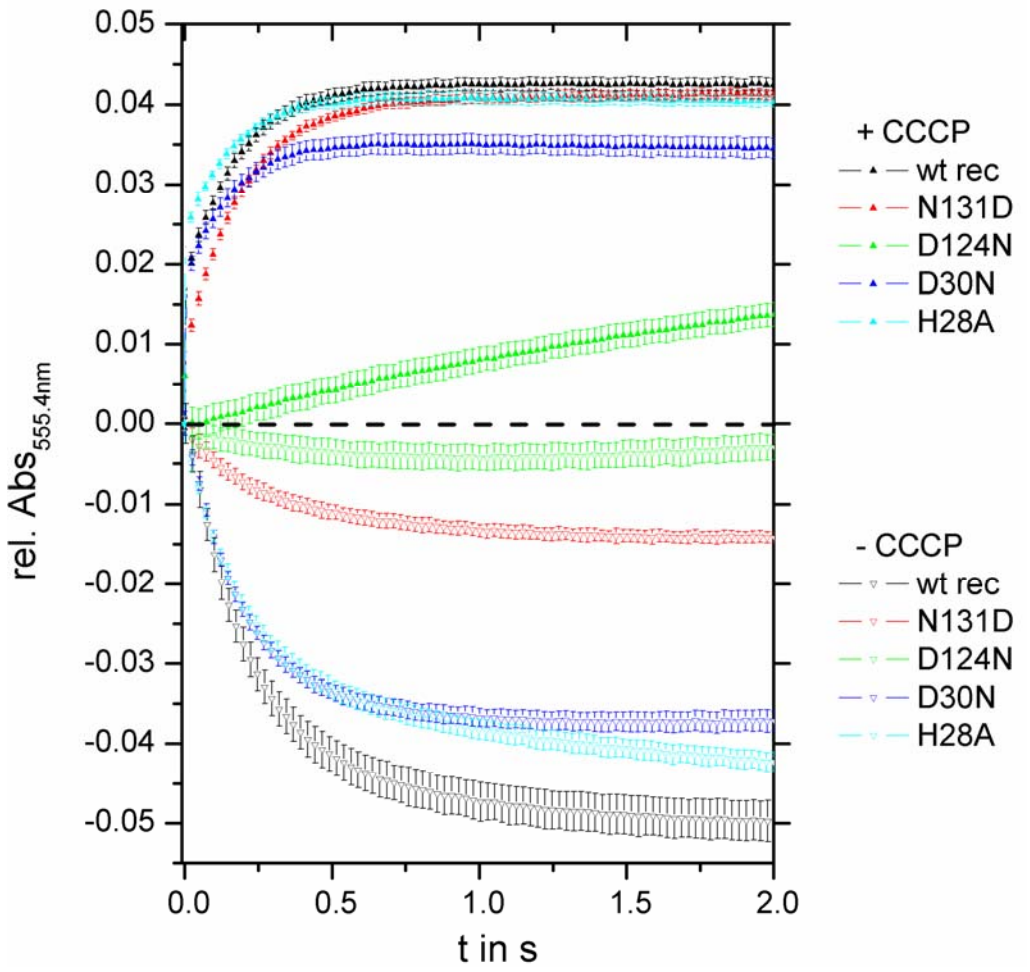

Figure 6.3-2 Stopped flow kinetic proton pumping experiments of the 4 SU-wt rec C*c*O and the variants N131D, D124N, D30N and H28A at λ = 555.4 nm. 400 nM unbuffered C*c*O reconstituted into proteoliposomes plus valinomycin and phenolred were mixed 1:1 with 20 μM reduced cyt *c* at a pH of 7.30 and recorded for 2 s (negative part of the figure, the background signal of empty liposomes is subtracted from the curves). CCCP was added to the same C*c*O proteoliposome samples and again mixed 1:1 with 20 μM reduced cyt *c* and recorded for 2 s (positive part of the figure).

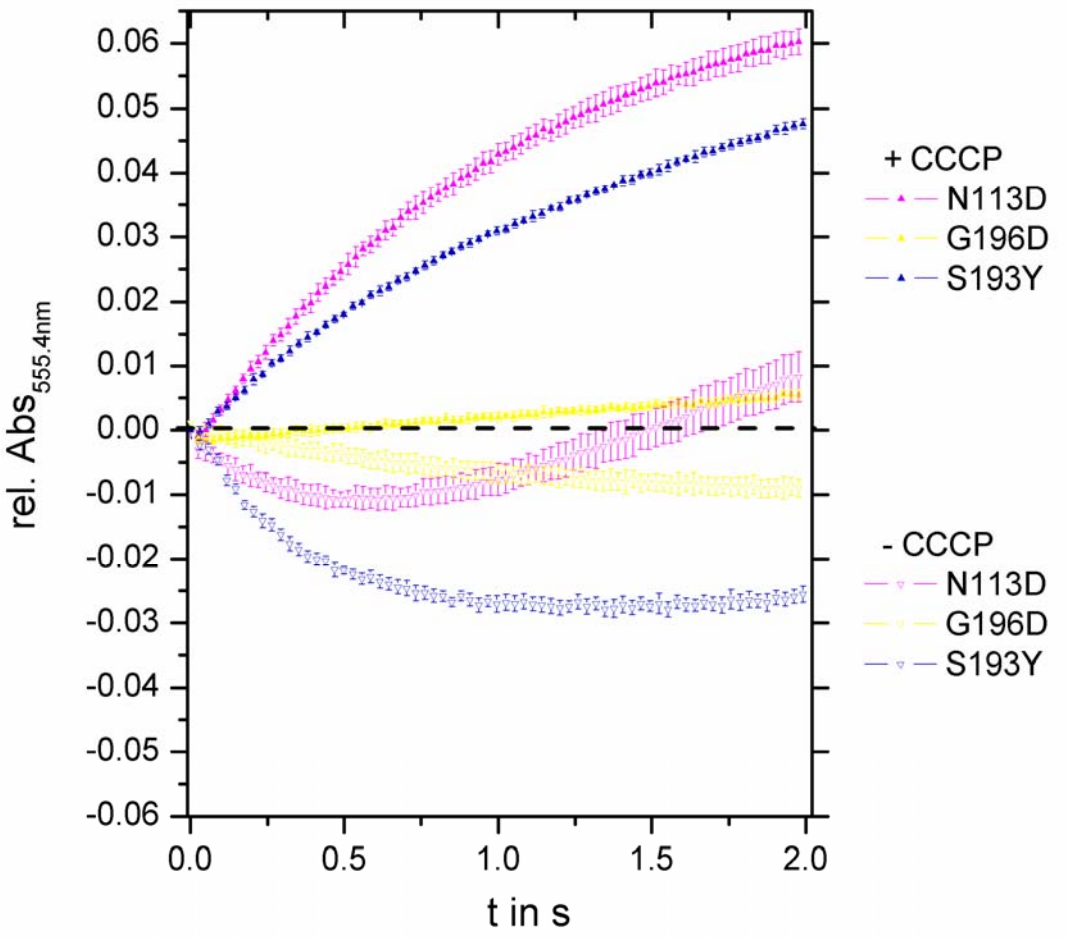

Figure 6.3-3 Stopped flow kinetic proton pumping experiment of the C*c*O variants N113D, G196D and S193Y at λ = 555.4 nm. 400 nM unbuffered C*c*O reconstituted into proteoliposomes plus valinomycin and phenolred are mixed 1:1 with 40 μM reduced cyt *c* at a pH of 7.30 and recorded for 2 s (negative part of the figure, the background signal of empty liposomes is subtracted from the curves). CCCP was added to the same C*c*O proteoliposome samples and again mixed 1:1 with 40 μM reduced cyt *c* and recorded for 2 s (positive part of the figure).

Curriculum Vitae

Date of birth	27th February 1978
Place of birth	Frankfurt am Main, Germany
Institutional address	Max-Planck-Institut für Biophysik Molekulare Membranbiologie Max-von-Laue Straße 3 60438 Frankfurt am Main, Germany email: heike.angerer@mpibp-frankfurt.mpg.de

Current Position

2008	Graduate student at the Max Planck Institute of Biophysics in the group of Prof. Hartmut Michel in Frankfurt am Main, Germany

Education

2005 – 2008	*PhD thesis* "Functional and structural studies on the *Atmungsferment* cytochrome *c* oxidase from *Paracoccus denitrificans*" Max Planck Institute of Biophysics in the group of Prof. Hartmut Michel in Frankfurt am Main, Germany
2005	*1st Degree (Diploma)*
October 2004 – March 2005	*Diploma thesis* "Production of recombinant terminal aa_3- and ba_3-cytochrome *c* oxidases from *Aeropyrum pernix* K1 in *Paracoccus denitrificans* and purification of wild type aa_3- and ba_3-cytochrome *c* oxidases from *Aeropyrum pernix* K1" Max Planck Institute of Biophysics in the group of Prof. Hartmut Michel in Frankfurt am Main, Germany
2000 – 2005	*Study of Biochemistry* Goethe University in Frankfurt am Main, Germany
February 2000 – September 2000	*Employment as Chemical Assistant* Aventis Pharma GmbH in Frankfurt am Main, Germany
January 2000	*Certification* by the German Chamber of Industry and Trade (D-IHK) as „Chemielaborantin" (chemical assistant)
1997 – 2000	*Practical Training as Chemical Assistant* Hoechst AG in Frankfurt am Main, Germany Provadis GmbH in Frankfurt am Main, Germany Aventis Pharma GmbH in Frankfurt am Main, Germany Clariant GmbH in Frankfurt am Main, Germany InfraServ in Frankfurt am Main, Germany Paul Ehrlich Berufsschule in Frankfurt am Main, Germany
1997	*Abitur*
1994 – 1997	*Oberstufe* Friedrich-Dessauer-Gymnasium, Frankfurt am Main
1988 – 1994	*High School* Leibniz-Gymnasium, Frankfurt am Main
1984 – 1988	*Elementary School* Karl-von-Ibell Schule, Frankfurt am Main

Acknowledgements

I am grateful to Prof. Hartmut Michel for his support and giving me the opportunity to work on such a challenging project. I also wish to thank Prof. Bernd Ludwig (JWG University of Frankfurt) for his help and supervision of this work.

Further, I would like to acknowledge Hannelore Müller and Cornelia Münke for their excellent technical assistance. I am also grateful to Dr. Fraser MacMillan (University of East Anglia) for collaboration on the oxidase project and for his motivations to improve my work. I am thankful to Dr. Guohong Peng and Dr. Jürgen Köpke for the determination of the structure from wild type oxidase.

I would like to thank Tobias Beckhaus, Sergiu Amarie and Claudia Rittmeyer (JWG University of Frankfurt) for MALDI-TOF/TOF mass spectra, UV-vis spectroscopic or TXRF measurements.

I am grateful to Prof. Petra Hellwig (University of Strasbourg) for collaboration on this project and for FTIR spectra of different states of the oxidase.

I thank all members of the Max Planck Institute of Biophysics especially the staff of the Department of Molecular Membrane Biology for the immediate help, when I had questions about practical work. Thanks to Ulrike Wedemeyer, Adriana Rycovská and Steven Marino for the correction of this thesis. In this context I would like to thank Christian Bamann for fruitful discussions and the introduction in the stopped-flow measurements. I would like to thank all members of the group from Prof. Bernd Ludwig for the organisation of the “oxidase club” and further discussions on the oxidase.

I thank my parents, my friends and Yunus Kürtbağı for their existence in my life.